Analysis and modelization of local hydrodynamics in bubble columns

Pedro Maximiano Raimundo

UNIVERSITÉ GRENOBLE ALPES

THÈSE

Pour obtenir le grade de

DOCTEUR DE L'UNIVERSITÉ GRENOBLE ALPES

Spécialité : **Mécanique des fluides, Procèdes, Energétique**

Arrêté ministériel : 7 août 2006

Présentée par

Pedro Maximiano Raimundo

Thèse dirigée par **Alain Cartellier** et
codirigée par **Davide Beneventi**

préparée au sein du **Laboratoire des Ecoulements Géophysiques et Industriels**
dans **l'École Doctorale I-MEP2**

Analyse et modélisation de l'hydrodynamique locale dans les colonnes à bulles

Thèse soutenue publiquement le **14 Octobre 2015**,
devant le jury composé de :

Mme, Eveline MAURET
Professeur, Université Grenoble Alpes, Présidente
M., Dominique LEGENDRE
Enseignant-chercheur, Université de Toulouse III, Rapporteur
M., Romain VOLK
Maître de conférences, ENS Lyon, Rapporteur
M., Daniele MARCHISIO
Professeur, Politecnico di Torino, Membre
M., Alain CARTELLIER
Directeur de recherche, Université Grenoble Alpes, Membre
M., David BENEVENTI
Chargé de recherche, Université Grenoble Alpes, Membre

Remerciements

En préambule à ce mémoire, je souhaitais adresser mes remerciements les plus sincères à tous ceux qui m'ont apporté leur aide et qui ont contribué à l'élaboration de ce mémoire de thèse.

Je tiens à remercier sincèrement Alain CARTELLIER, mon Directeur de thèse, qui s'est toujours montré disponible tout au long de la réalisation de cette étude, ainsi que pour l'aide et le temps qu'il a bien voulu me consacrer, surtout dans la phase de rédaction.

Je remercie vivement Davide BENEVENTI, co-directeur de thèse, qui m'a toujours encouragé et donné des conseils pertinents.

Je tiens tout particulièrement à remercier Ann CLOUPET et Frédéric AUGIER qui m'ont fait confiance dès le début pour porter ce sujet de thèse. Pendant les 3 ans passés à IFPEN, ils ont toujours été disponibles pour m'aider à résoudre les problèmes inhérents au travail de doctorant.

Je voudrais également adresser mes remerciements à toute l'équipe de techniciens R124, et tout particulièrement à Robert BEAUMONT, pour leurs aides et leurs encouragements pendant toute ma période d'expérimentations.

Je tiens à remercier le Professeur Dominique LEGENDRE et M. Romain VOLK pour avoir accepté d'être les rapporteurs de ce travail.

Je remercie aussi tous mes amis que j'ai eu l'opportunité de rencontrer à Lyon pendant ces trois années. Ils ont su me motiver et m'encourager. J'ai partagé avec eux de vrais moments de bonheur.

Finalement, je remercie ma famille, ma mère, mon père, ma petite sœur et ma compagne qui m'ont mené jusqu'ici car sans eux je n'aurais jamais réussi.

Table of Contents

Notations

1C	Mono-fiber conical optical probe
A	Adjustment factor
Ac	Column cross-section
Ai	Injector cross-section
C	Bubble chord
C_{10}	Arithmetical averaged chord
CARTP	Computer automated radioactive tracking particle
CC	Cross-correlation
CCD	Charge-coupled device
C_D	Drag coefficient
CFD	Computer fluid dynamics
C_L	Lift coefficient
C_{TD}	Turbulent dispersion coefficient
C_{VM}	Added mass coefficient
D	Column diameter
d	Distance between probes
D_{32}	Bubble Sauter mean diameter
d_{eq}	Equivalent diameter
De	Bubble equivalent diameter
Dh	Bubble horizontal diameter
D_{op}	Diameter of the optical fiber
d_{SM}	Mean Sauter diameter
Dv	Bubble vertical diameter
Ecc	Bubble eccentricity
E-L	Euler-Lagrange
Eo	Eötvös number
ERT	Electric resistance tomography
$f^{(1)}$	Product density function
fb	Bubble arrival frequency
Fgl	Interfacial momentum exchange

F^d	Drag force
F^L	lift
F^{VM}	Added mass
g	Gravitational acceleration
H	Column height
h	Height in the column
h	Swarm factor
H_0	Column bed static height
H_D	Column bed dynamic height
HFA	Hot Film Anemometer
i.d.	Inner diameter
jg	Local gas flux
l	Length
l_{12}	Distance between tips of a double optical probe
LDA	Laser doppler anemometry
LDV	Laser doppler velocimetry
LED	Low energy diode
LES	Large eddy simulations
ls	Sensible tip length
M	Modified webber number
Mo	Morton number
P	Pressure
P(C)	Bubble chord distribution of the system
Pc	Detected chord distribution
Pd(Rh)	Probability distribution of detected bubble radius
PDF	Probability density function
Phi 1000	1 m diameter column
Phi 150	0.15 m diameter column
Phi 3000	3 m diameter column
Phi 400	0.4 m diameter column
PIV	Particla imaging velocimetry
Q	Flowrate
R	Column radius

r	Distance to the bubble centre
Re	Reynolds number
Rh	Horizontal radius
Rv	Vertical radius
s	Variance of bubble population
$Signal_A$	Signal of probe A
$Signal_B$	Signal of probe A
t	Time
ta	Time to bubble arrival
tm	Time to reach the top of the tip cone
T1	Bubble signature from which is possible to infer a velocity
T2	Bubble signature from which is not possible to infer a velocity
ta	Time of bubble arrival
t_{exp}	Experimental duration
tg	Time of gas
tm	Rising time
u	Axial liquid velocity
ul	Axial liquid velocity
$\bar{u}$	Mean liquid velocity
u’	Axial liquid velocity fluctuation
u'^2	Axial liquid turbulent kinetic energy
u’v’	Stress tensor
URANS	Unsteady Reynolds averaged Navier-Stokes
v	Radial liquid velocity
v’	Radial liquid velocity fluctuation
v'^2	Radial liquid turbulent kinetic energy
Vb	Bubble velocity
v_{b1}	Bubble velocity (relative to the probe) before the contact with the probe have occurred
Vi	Injection velocity
Vl	Liquid velocity
Vl(0)	Centreline liquid velocity

Vmp	Most probable velocity
VOF	Volume of fluid
Vsg	Superficial gas velocity
x	Spatial position
x_k	Characteristic phase presence function
Δh	Height difference
ΔP	Pressure difference
$P(C\|Rh)$	Probability of detect a chord C on a bubble with a radius Rh

Greek letters

εg	Gas hold-up
<εg>= εg	Average gas hold-up
ρ	Density
μ	Viscosity
σ	Surface tension
τ	Stress tensor
θ	Inclination angle of a bubble
ε	Turbulent kinetic energy dissipation
φ	Integration constant
α	Bubble rotation angle

Exponents

D	Drag
VM	Virtual mass
L	Lift
P	Pressure

Indices

l	Liquid
g	Gas
32	Sauter mean
v	Vertical

h	Horizontal
b	Bubble
k	Fluid phase
lam	Laminar
tur	Turbulent
BIT	Bubble induce turbulence

Introduction

Bubble column reactors are widely used in the chemical and biological industry, as e.g. Fischer-Tropsch reactors, α-olefins oxidation reactors and as aerobic fermenters. They typically consist in a cylindrical vessel filled with liquid at the bottom of which gas is injected. The industrial advantages of such a configuration mainly rely on the good liquid-gas mixing and on the high interfacial area densities achieved without any moving parts. Therefore, bubble columns are suitable to carry strongly exothermic and/or mass transfer limited reactions. Typical scales of industrial reactors are 2-8m in diameter and 2<H/D<5. They are commonly operated at superficial gas velocities, defined as the ratio of the injected gas flow rate to the column cross-section, about 5-30cm/s, leading typically to void fractions in the range of 10% to 35%.

Figure 1 – Snapshot of the Fischer-Trospch pilot unit of IFPEN-ENI in Sannazzaro. (Copyright: © ENI)

Despite their common utilization, the scale-up of bubble columns is still a very "experimental" process that requires a posteriori verification of the predicted performance several scales. Indeed, the hydrodynamics of such bubbly flows is expected to be strongly dependent on the column diameter and on the superficial gas velocity but existing scale-

up correlations were mainly developed in small columns or at low gas hold-up conditions: thus their extrapolation to larger sizes and/or larger flow rate is a somewhat risky process. A possible solution to identify the correct scaling properties could be to exploit CFD simulations. However, nowadays no model is able to directly resolve all the interactions occurring in these flows, except when considering a very limited number of inclusions and small systems. Alternately, two-fluid Eulerian approaches that provide an averaged view of the flow, are frequently used in industry, and notably at IFPEN, for the simulations of these two-phase flows. This framework is well adapted to handle large systems and high gas content, but it requires the implementation of closure laws, such as those concerning the representation of turbulence or of interphase momentum exchanges. So far, and despite significant progress, these closures are not indisputably established: either their range of validity is not well known or some mechanisms are not properly accounted for. That situation is especially critical when considering industrial-like conditions (i.e. high gas hold-up and large columns) which are poorly documented. Consequently, more refined investigations are required to increase the reliability of the models and in fine to build fully predictive tools.

In this framework, the main objective of the present work is to improve our knowledge on gravity driven bubbly flows as the ones found in bubble columns, by building and analyzing of a wide experimental database of local flow characteristics including void fraction, bubble size distributions, velocity statistics on both phases… With respect to the scaling issue, these measurements should be obtained over a large range of column diameters.

Anticipating on the detailed work program presented in the next chapters, in the present work, the columns diameter has been varied from 0.15m up to 3 m, i.e. spanning a 1:20 factor. In the same perspective, and for each column, the range of superficial gas velocities has been varied from 3 cm/s up to 35 cm/s, i.e. corresponding to a 1:10 factor. Moreover, in order to ease the analysis of hydrodynamic phenomena, to help the identification of scale-up rules and also to facilitate the test of simulations, the chosen strategy was to carry out experiments in the best controlled conditions possible. In particular, the following objectives were set:

- The gas injection must be homogeneous over the column cross-section in order to avoid the formation of high gas concentration zones and consequently the appearance of instabilities in the vicinity of the injection.

- The injected bubble size must be as stable as possible when changing the column or the flow rates in order to ensure comparable experimental conditions.
- Coalescence must be avoided.

The manuscript is organized as follows.

A detailed review of the existing experimental studies, measuring methods and modeling approaches is presented in chapter 1, and the precise work program is defined accordingly.

Chapter 2 presents the study of the gas injector design and the final choice of the gas distributor for each column. Furthermore, the bubble size in the vicinity of gas injection is analyzed for several columns.

In chapter 3, the measurement methods adopted to access the various hydrodynamics properties are discussed. Their performances are analyzed by comparison with other methods or with literature data. In addition, a new method dedicated to the measurement of the average horizontal size of bubbles is proposed and tested.

Chapter 4 presents the experimental data collected. The evolutions of the hydrodynamics properties with the column dimension and with the superficial gas velocity are analyzed. Some flow behaviors are then deduced from these observations including the probable presence of concentration fluctuations at meso-scale, and their possible consequences on the modeling are evoked.

In chapter 5, a preliminary approach aimed at accounting for the observe dynamics in averaged two-fluid models is presented using a 1D balances as well as a 3D URANS simulations.

Finally, a general conclusion synthetizes the main results and provide some perspectives.

1 Bubble columns hydrodynamics

A bubble column is a vertical cylindrical vessel containing a liquid phase where a gas phase is injected at the bottom. This injection is made by a gas distributor those orifices are distributed all over the cross-section of the column. This gas phase thus produces rises through the liquid, escaping from it at the upper free surface. Excepted at very low gas flow rate or in specific experimental setup involving capillary tubes as gas injectors, the hydrodynamics of the liquid phase exhibits an important recirculation at the center of the column (Forret et al., 2003). Such gas-liquid flows are characterized by very strong couplings between the dynamics of the two phases. Similar situations also arise for gas-liquid flows in ducts, such as in gas lift systems (Guet and Ooms, 2006) or when the forced liquid flow remains weak enough compared to gravity forcing (Mudde, 2005; Riviere et al., 1999[a,b]). All such gravity driven bubbly flows remain difficult to model without resorting to empirical information.

Bubble columns encompass a wide variety of internal technologies as draft tubes, plates or packing, those improve some aspect of the flow as mass transfer or mixing (Deckwer, 1992). The Figure 1.1 presents some examples of bubble column internals. In the present study a focus is done on empty bubble columns.

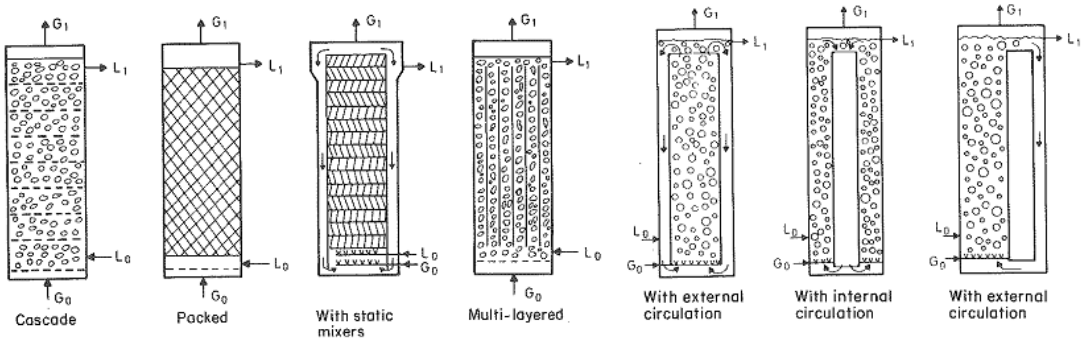

Figure 1.1 - Typical internals in bubble columns.

In the first part of this bibliographic study, available results on global and local parameters gathered in bubble columns for various operating conditions are summarized. Main global quantities are for example the average gas hold up that quantifies the amount gas present in the column or the flow regime. Local variables typically concern the local void fraction, bubble size, bubble and liquid velocity and turbulence.

In a second part, available measuring techniques are described. Bubble size and liquid velocity measurements are considered in particular.

Different modelling approaches are then briefly presented and their predictive capabilities on bubble columns are discussed. Finally, we identify key open questions on the dynamics of such flows and we then define an adapted work program.

1.1 Hydrodynamics

Global hydrodynamics

Gas Hold Up and flow regimes

The flow regimes in a bubble column are strongly related with the superficial gas velocity, v_{sg}, and gas hold up, ε_g.

Three flow regimes can typically be found in literature: homogeneous (or bubbly flow), transition and heterogeneous (or churn-turbulent) (Krishna et al., 2001), as shown in Figure 1.2. The homogeneous regime is present at low values of v_{sg} and is characterized by a quasi-linear behaviour of the global void fraction ε_g versus the gas superficial velocity v_{sg}. The bubble population is equally dispersed in the column, and it is characterized by somewhat narrow bubble size distribution. The radial profiles of ε_g and mean velocities are flat. Bubble break up and coalescence phenomena are negligible in these conditions because bubbles are dispersed and have quasi-rectilinear paths.

With a further increase in v_{sg}, the increasing trend of ε_g with v_{sg} is reduced and goes through a local maximum, which is a characteristic of the transition regime. For these conditions, larger bubbles start to appear mostly in the centre of the column and their path become helical or wobbling.

The heterogeneous regime occurs at larger v_{sg} conditions, where ε_g experiences a slower increase with v_{sg} than in the homogeneous regime. This regime is characterized by an agitated flow, where the bubbles movement is more chaotic. In the heterogeneous regime, two major classes of bubbles are identified by some authors (Urseanu et al., 2003). The *large bubbles*, found mostly in the centre, possess high velocities that lead to a quick rise through the column. The second class corresponds to small bubbles, normally found in the wall region, and that are entrained by the down coming flow of the liquid. This liquid recirculation is induced by the movement of the *large bubbles* in the core of

the column generating an upcoming flow of liquid. Once it reaches the top of the bed the liquid descends through the wall region. As consequence of this heterogeneous bubble concentration in the column, the gas hold up and the bubble velocity radial profiles become more parabolic. However, there is no consensus in the systematic presence of coalescence since some authors such as Chaumat et al. (2005) have not detected the presence of *large bubbles* in the heterogeneous regime. As a conclusion, it is not clear that the appearance of large bubbles determines the formation of a liquid recirculation. Both phenomena may also share a common cause as the increase of void fraction. Besides that, the picture below is not universal since in some conditions of gas injection, the relationship between the global void fraction and the superficial gas velocity does not exhibit any maximum. Instead, it could be monotonous with a continuous increase of the ε_g versus v_{sg} slope. Clearly, the passage from the homogenous regime to the heterogeneous regime is still poorly understood.

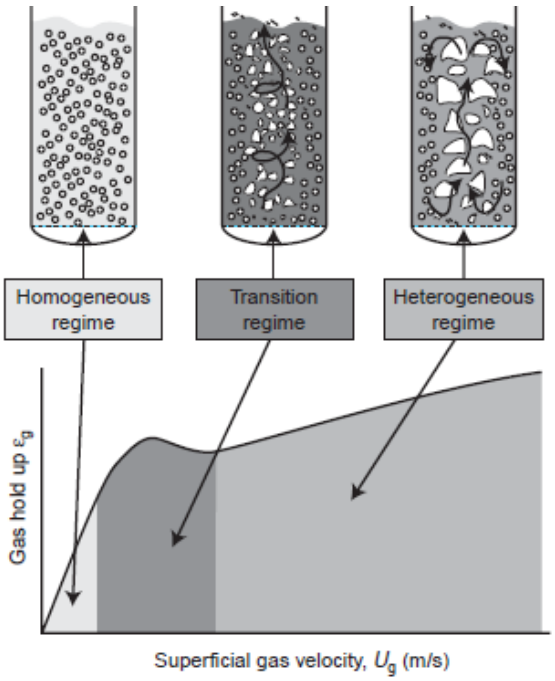

Figure 1.2 - Schematic representation of the flow regimes in a bubble column. (Forret et al., 2006)

As a preliminary basic view of the hydrodynamics of bubble columns, it seems that one can distinguish two limiting cases. In the dilute limit and for well controlled injection conditions, the back flow of liquid occurs around each inclusion, and the swarm of bubbles remains globally spatially homogeneous (Garnier et al., 2002, Riboux et al., 2014). When increasing the void fraction, the flow tends to structure itself into ascending

zones gathering most bubbles and descending zones with a weaker gas content (such a structuration process is also observed in sedimentation). Radial in-homogeneities become then significant. Even more, convective type instabilities can arise due to differential buoyancy forcing. This situation is typical of operating conditions of industrial bubble columns.

In addition to the above hydrodynamic processes, coalescence may affect the bubble size and therefore the spatial distribution of buoyancy forcing. Yet, coalescence may not always be the driving mechanism of the homogeneous-heterogeneous transition usually observed in bubble columns, and the origin of the transition needs to be clarified.

Impact of the gas injector design on gas hold up

A gas hold up evolution, as showed in Figure 1.2, is not always possible to obtain. Ruzicka et al. (2001) and Kuncová et al. (1995) showed that the gas injector design has a determinant impact on the hold up. A perforated plate with small and closely spaced orifices is pointed as a design capable of generating homogeneous bubbling regimes. In a design with larger orifices the gas injection has a 'non-uniform' spatial distribution all over the column cross-section, creating local heterogeneous bubble concentration even at small v_{sg}. Figure 1.3 shows the typical evolution of ε_g for a non-homogeneous gas injector.

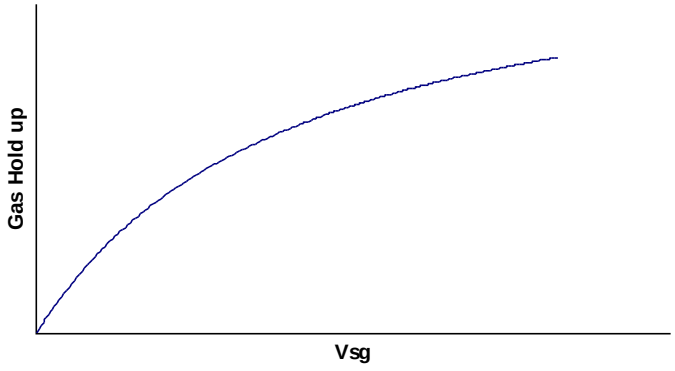

Figure 1.3 - Schematic representation of the flow regimes in a bubble column. Adaptation from Ruzicka et al. (2001)

When such a gas holdup trend is obtained, it is not possible to identify the transition between regimes. Moreover, there is no real linear evolution of ε_g even at low v_{sg}, suggesting that a liquid recirculation appears at very low gas velocity. As described by Ruzicka et al. (2001), regardless the gas injection device, the reached heterogeneous

regime is always similar; it is characterized by wide bubble size distributions with a strong presence of coalescence and liquid recirculation.

Forret et al. (2006) have found that the distributor effect on the gas hold-up profile is only significant at an elevation lower than one diameter from the gas distributor.

As a conclusion, the gas injector has a strong impact on global hydrodynamics, as it conditions the transition between homogeneous and heterogeneous regime. But when heterogeneous regimes are considered, the impact of the gas injection is negligible on global hydrodynamics.

Impact of liquid phase properties on gas hold up

The properties of liquid phase, such as surface tension and viscosity, have an important impact on the bubble formation and on bubble-up break/coalescence processes.

The literature (Kuncová et al., 2006; Kantarci et al., 2005; Thorat et al., 2008; Fransolet et al., 2005) indicates that a liquid phase with a higher viscosity yields a lower ε_g than one with a lower viscosity. This decrease in ε_g is related to an increase of the coalescing nature of the liquid phase, favouring the formation of larger bubbles in the near injector zone of the column. In the other hand, the viscosity of the liquid may decrease the relative velocity between fluids, which indicated how complex is the coupling between phenomena inside bubbles. The larger bubbles travel faster in the column than smaller bubbles, thus yielding a smaller ε_g. (Kuncová et al., 2006). Changes in the bubble population affect also the flow regime. Figure 1.4 shows the results of the study of the impact of liquid phase viscosity on the void fraction made by Kunková et al. (2006) in a 0.154 m diameter column equipped with a perforated plate with 0.5 mm i.d. holes. The viscosities were tested in a range from 1 mPa.s for distilled water to 110 mPa.s for the saccharose solution of 64,5wt%. On this figure the transition between regimes is clearly observed for distilled water, but tends to disappear when the viscosity increases.

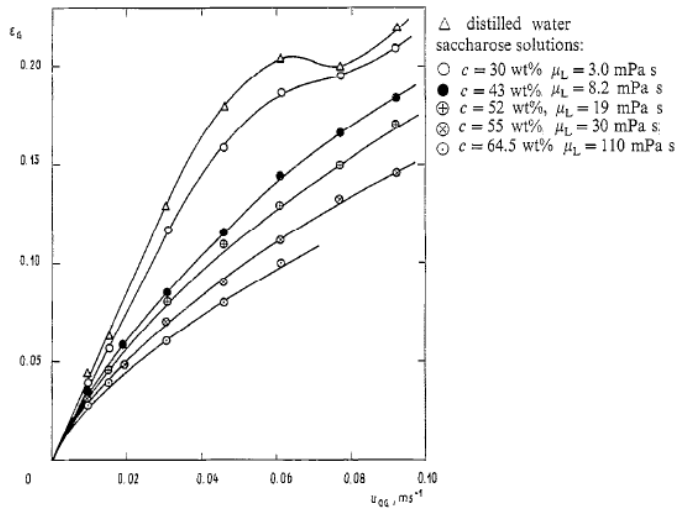

Figure 1.4 – Gas holdup versus superficial gas velocity for Saccharose solutions with different concentrations (Kuncová et al., 2006).

The surface tension is also a property that has an important impact on the flow regime. The addition of surfactants reduces the surface tension between the liquid and gas phases, usually decreasing coalescence. As a consequence, the bubbles will be smaller which means that they will rise slower and a higher ε_g will be yield (Kantarci et al., 2005; Thorat et al., 2008; Mouza et al., 2005; Chaumat et al., 2005). These phenomena were also observed by Veera et al. (1999) in a 38 cm diameter and 3.2 m height bubble column. A perforated plate with 623*1 mm diameter holes was used as the gas distributor. The void fraction was measured using gamma ray tomography in an air/water system. In order to change the gas-liquid surface tension, several solutions of n-butanol, from 0.02 %v/v up to 0.5% v/v, have been used as can be seen in Figure 1.5 A.

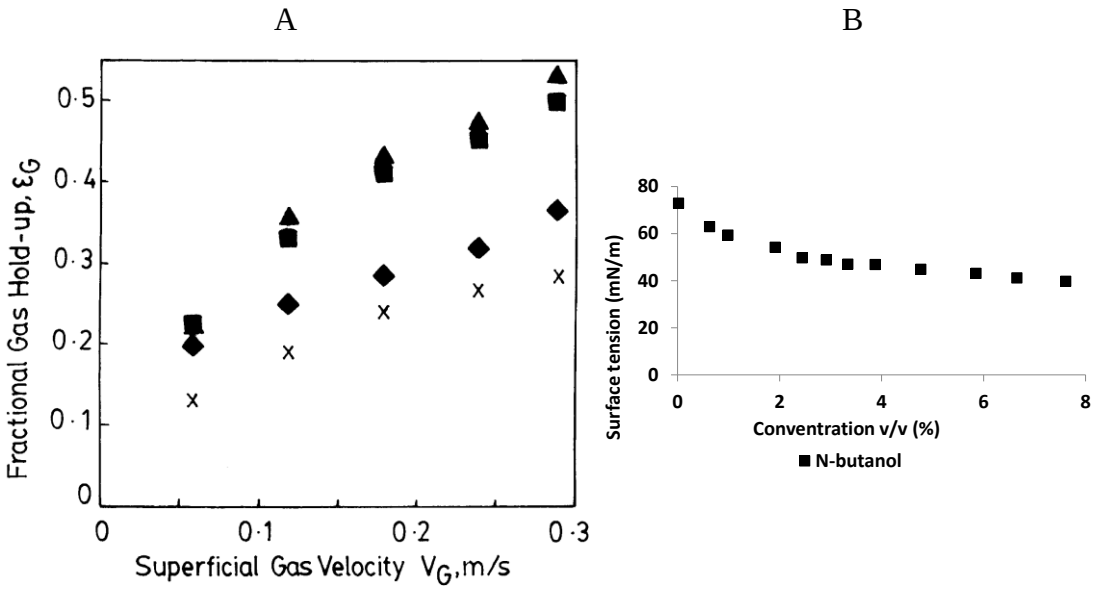

Figure 1.5 – A) Effect of n-butanol concentration on the average gas hold-up (Symbols: crosses- water; rhombus – 0.02 % v/v; squares – 0.2 % v/v; triangles – 0.5 % v/v) (Veera et al., 1999); B) Variation of the surface tension of n-butanol with the concentration (Hey and Kippax, 2005)

As can be seen in Figure 1.5 B, the range of concentrations used in the experiments is placed in the zone where the surface tension has an important reduction with the concentration. The results show that, as already mentioned, a decrease in surface tension leads to higher void fractions. However, the 0.5 % v/v solution showed similar void fractions to the 0.2% v/v solution. Probably the bubble coalescence has been completely blocked at 0.2% v/v of n-butanol, so a further addition did not have an impact on the global gas hold-up (although this surfactant concentration remains below the maximum interface coverage limit according to Figure 1.5 B).

Impact of the pressure level on gas hold up

Elevated pressure changes the behavior of the two phases and the way they interact. Increasing the pressure in a bubble column increases the global gas hold up in the heterogeneous regime and delays the transition from homogeneous to heterogeneous flow regime to higher superficial gas velocities (Wilkinson, 1991; Colombet, 2012; Urseanu et al., 2003). This phenomenon is linked with the decrease of mean bubble diameter, which may be caused by an effect of pressure on the bubble formation and/or on the breakage and coalescence. The reduction of the number of large bubbles also limits the propagation of instabilities in the column explaining the delay on the transition

between flow regimes (Urseanu et al., 2003). Authors studied the impact of pressure in the gas hold up for several liquids as can be seen in Figure 1.6. A 1.22 m high and 0.15 m diameter column has been used with a perforated plated with 0.001 m holes.

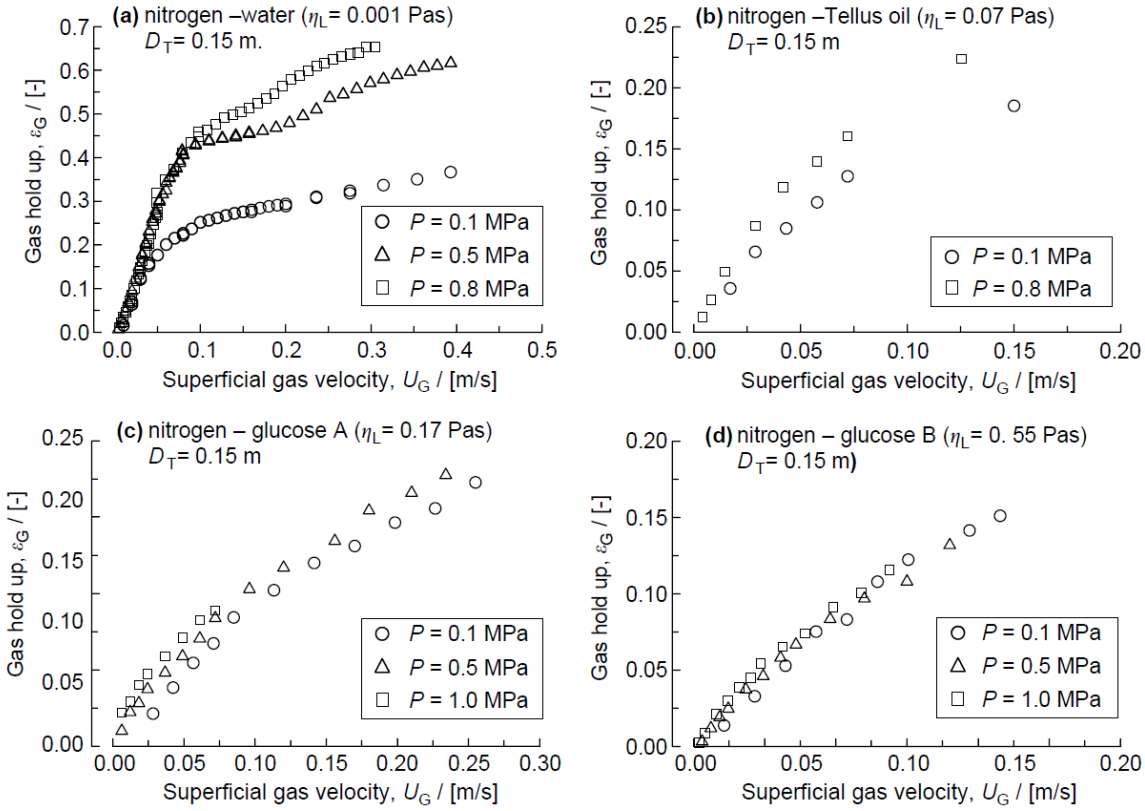

Figure 1.6 – Variation gas hold up with pressure and liquid viscosity in a bubble column (Urseanu et al., 2003)

The results show that for the water/nitrogen system, the gas hold up strongly increases with the pressure level but for the heterogeneous regimes only. The sensitivity to pressure diminishes with an increase in viscosity, as can be seen for the Tellus-oil/nitrogen system. In the case of the glucose solutions, the effect of the pressure level becomes insignificant. Clearly, large viscosities systems are not sensitive to the absolute pressure. Urseanu et al. (2003) argued that the promotion of bubble coalescence by viscosity overcome the bubble break-up phenomena due to elevated pressure. This argument is not convincing as coalescence is not expected to be promoted by viscosity. Even if effects on break-up and coalescence, it is more likely that the gas density modification due to the pressure level affects the injected size distribution itself, producing more smaller bubbles and thus increasing the void fraction. In addition,

injection conditions may change in these experiments as, for a given gas superficial velocity, the gas velocity inside the injectors evolves with the pressure level.

An increase of the gas phase molecular weight is also associated with an increase in the gas hold up. This phenomenon is linked with an increase in the gas density that is the physical cause responsible for the effect of molecular weight and pressure on gas hold up (Kantarci et al., 2005; Wilkinson et al., 1994).

The study of bubble size, its path and velocity along the column will be discussed in detail in the chapter 4 through the study of local hydrodynamic parameters.

Column geometry effect on the gas hold-up

Forret et al. (2006) have measured the evolution of the global gas hold-up with the gas superficial velocity in bubble columns with diameter ranging from 0.15 m up to 1 m (system air/water). Gas injections devices are similar in term of size of holes and global porosity. As can be seen in Figure 1.7, the gas hold-up shows no dependency in the column diameter for all the tested superficial gas velocities.

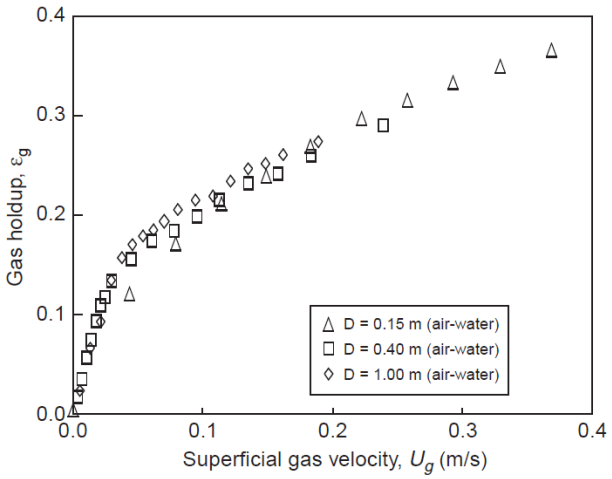

Figure 1.7 – Global gas hold-up variation with the superficial gas velocity. (Forret et al., 2006)

Considering the knowledge on global hydrodynamics allows to identify several open question as:

- What mechanism is responsible for the transition?

- What is the role of the bubble size distribution on it? Is the coalescence the main cause of the transition?

Local hydrodynamics

Local gas holdup

Forret et al. (2006) have showed that, for gas superficial velocities higher than 10 cm/s, the radial profiles of the local gas hold-up ε_g normalized by the global void fraction $\overline{\varepsilon_g}$ overlap regardless of the column diameter and the superficial gas velocity, as shown in Figure 1.8. Hence, these profiles can be predicted as a function of the global gas hold-up by the correlation developed by Schweitzer et al. (2001):

$$\varepsilon_g\left(x/R\right) = \langle\varepsilon_g\rangle\left[-1.7889\left(x/R\right)^6 - 1\right) + 1.228\left(x/R\right)^4 - 1\right) - 0.939\left(x/R\right)^2 - 1\right)\Big] \quad (1.\ 1)$$

Where x/R represents the dimensionless radial position, $\varepsilon_g\left(x/R\right)$ the local gas hold-up at this position, and $\langle\varepsilon_g\rangle$ represents the global gas hold-up.

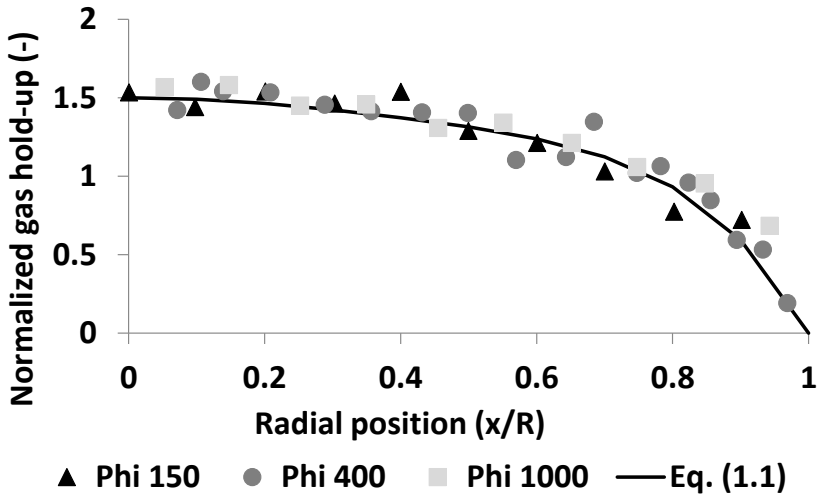

Figure 1.8 – Normalized gas hold-up radial profiles for several column diameters. (Forret et al., 2006)

The similarity between gas holdup profiles has been validated on a wide range of column diameter and superficial gas velocity, as long as the heterogeneous regime is achieved (v_{sg}>10cm/s).

Bubble size

The knowledge of the bubble size in large bubble columns is still a recurrent question in today's research due to the lack of accurate experimental information and also due to its importance for the modelling of both hydrodynamics and mass transfer in such bubbly flows. There are two main aspects that determine the bubble size. The first one is the bubble formation process, as the bubble population at the bottom of the column is set by injection conditions. The second one is related with coalescence/break-up phenomena, as the equilibrium between these two processes determines how the bubble sizes evolve along the column.

The shape of the bubble changes as a function of the flow conditions and can be roughly predicted using bubble regime maps as the one shown in Figure 1.9 (Clift et al., 2005). The shape of bubbles is strongly linked to the their volume and relative velocity. It is thus linked also to the physical properties of the system. This map relates three non-dimensional numbers, namely the bubble Reynolds number (Re_b), the Eötvös number (Eö) and the Morton number (Mo). The Reynolds number represents a ratio between the inertial and viscous forces and can be calculated by:

$$Re_b = \frac{\rho_l {V_b}^2 d_{eq}}{\mu_l} \qquad (1.\ 2)$$

where ρ_l and μ_l are respectively the liquid density and viscosity, V_b is the bubble velocity relative to the liquid and d_{eq} is the diameter of an iso-volume spherical bubble.

The Eötvös number compares the hydrostatic pressure at the scale of an inclusion and the capillary pressure, it is evaluated as follows,

$$Eo = \frac{\Delta\rho g {d_{eq}}^2}{\sigma} \qquad (1.\ 3)$$

where $\Delta\rho$ is the density difference between the liquid and the gas phase, g represents the gravitational acceleration and σ the surface tension.

The Morton number that characterises the gas/liquid system and gravity is calculated as follows,

$$Mo = \frac{g {\mu_l}^4 \Delta\rho}{{\rho_l}^2 \sigma^3} \qquad (1.\ 4)$$

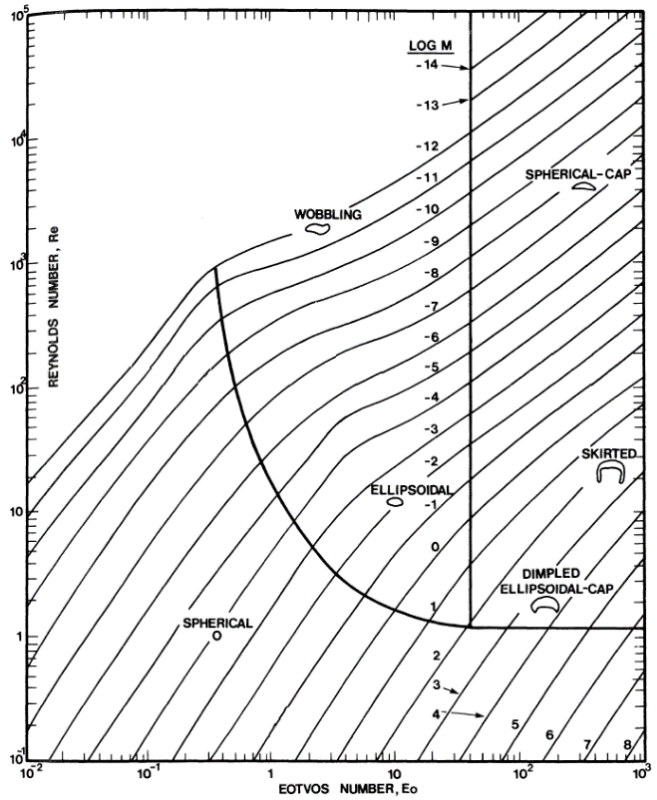

Figure 1.9 - Bubbles shape regimes for bubbles in unhindered gravitational motion. (Cliff et al., 2005). The map provides also the terminal velocity of bubbles.

Figure 1.9 provides the bubble shape and its relative velocity (included in the Reynolds number) as a function of Eö (i.e. the bubble volume) and the Morton number. This map has been established for a single bubble in a stagnant liquid. Note that interfacial contamination should also be accounted for as it affects the relative velocity especially in the ellipsoidal and wobbling regions.

Another issue is related with the type of statistics considered. Some techniques sample frozen bubbles (such as standard imaging techniques) while others account for fluxes (such as some local probes). These two approaches are not equivalent unless the relative velocities between any bubble classes remain negligible. This is another difficulty for performing sound comparisons between various contributions.

Last, regarding coalescence and/or break-up, it must be emphasized that no conclusion can be drawn when comparing mean sizes only. Indeed, the size pdf (probability density function) and thus their moments can change simply because of transport and dispersion (in particular, it will be shown below that strong size segregation can occur in bubble columns) even in absence of coalescence/break-up. To ascertain the presence of coalescence, one needs to consider fluxes per size classes. Alternately, one can examine

the evolution of the minimum and maximum sizes in the system to decide whether or not coalescence/break-up processes are likely to be present. Despite these difficulties, we will analyse the data on bubble size that are available in the literature.

The previous results as an important part of the work done in this subject were carried either in 2D columns (Mouza et al., 2005; Kazakis et al., 2006, Simmonet et al, 2007; De Swart et al. 1996) or in small bubble columns (diameter < 0.15 m) at low gas hold-up due to measurement methods limitations. However, this study aims to study the bubble size in large bubble columns and at high void fractions. Consequently, only the studies done in similar conditions will be further detailed. As the present study is clearly focused on the scale-up of industrial bubble columns, a particular attention is paid to data acquired in "large" columns at high gas velocity.

Impact of superficial gas velocity on bubble size

Xue et al. (2008 B) have studied the evolution of the mean chord with the gas superficial velocity using a four point optical probe. This technique measures bubble chords, as it will be detailed in Chapter 3. The measurements were made in a 2.30 m height and 0.16 m diameter column using two different perforated plates in a tap water/air system. Spargers of different open area and hole diameter have been used. In the centre of the column (r/R=0), the results show an increase in the mean bubble chord from 2.5 mm at 2 cm/s up to 6 mm at 30 cm/s. At higher superficial gas velocities, the mean bubble chord remained constant, with similar volume based bubble chord distribution.

Though, in the wall region (r/R=0.9), the mean bubble chord remained constant around 3 mm for all the tested conditions, as can be seen in Figure 1.10. This information is in agreement with what was previously referred, in the churn-turbulent regime at high v_{sg}: the larger bubbles quickly rise through the column centre. The smaller bubbles, already existent in the homogeneous regime, recirculate in the wall region explaining the difference between the two sets of measurements. There is thus a strong lateral segregation effect.

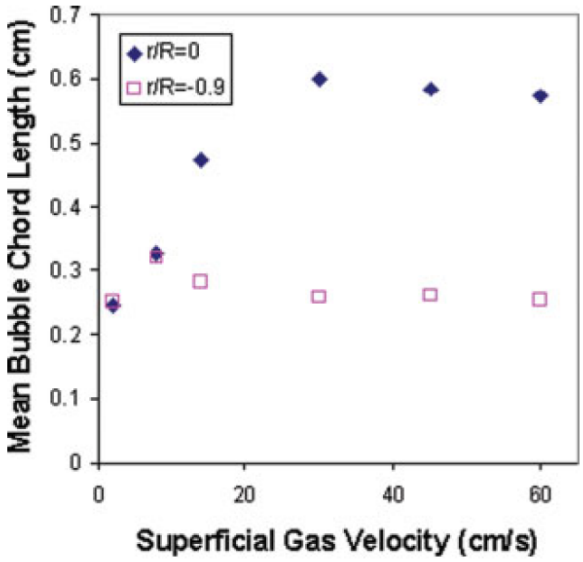

Figure 1.10 – Evolution of mean chord lengths with gas superficial velocity at the column center and near the wall (Xue et al., 2008 B). (z/D=5.1).

Colombet et al. (2014) also addressed the impact of gas superficial velocity on the bubble equivalent diameter. The measurements were made using a photographic method, meaning that bubbles were only measured in the wall zone. The experiments were carried in a 0.15 m squared bubble column and 1m high. The gas distributor is composed by 841 capillaries 15 cm long and with an inner diameter of 0.2 mm. Filtered tap water was used as liquid phase and air as gas phase. The measurements were made by two different imaging methods and a double tip optical probe. The bubble equivalent diameter is plotted as a function of the gas hold up, as shown in Figure 1.11. As previously referred, the gas hold up increases with gas superficial velocity. The results show that the equivalent diameter strongly increases with the gas hold-up up to 5%. Above this value, the bubble equivalent diameter presents a smaller increase with the gas hold-up.

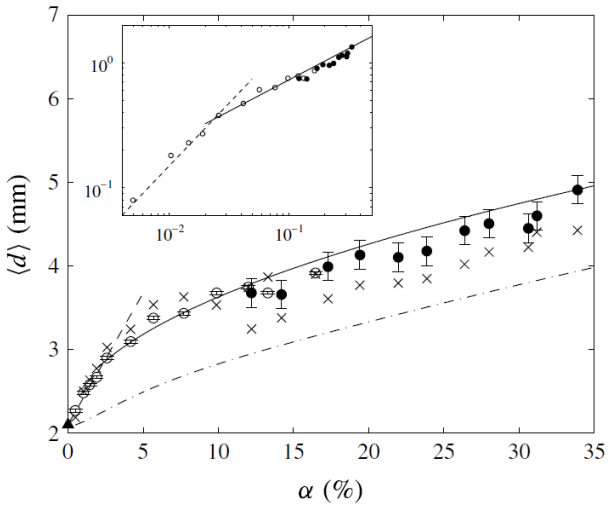

Figure 1.11 – Evolution of bubble equivalent diameter with gas hold up (symbols: filled circles – imaging method with a telecentric lens, empty circles - imaging method with a fixed lens, crosses – double tip optical probe). (Colombet, 2014).

Colombet et al. (2014) have calculated the bubble equivalent diameter from the mean bubble chord, under the assumption of a mono dispersed bubble population with a null angle of attack when approaching the probe. Since there is no information about the bubble eccentricity in the work of Xue et al. (2008), it is impossible to compute the bubble equivalent diameter from the mean bubble chord. Consequently only a qualitative comparison can be done between both results. The results of Xue et al. (2008) present a steeper bubble size increase than Colombet et al. (2014), this could be due to the different configurations of the gas distributors. Colombet et al. (2014) stated that the capillary gas distributor assured an homogenous injection of 2 mm diameter bubbles, allowing to yield 30% of gas hold-up without changing the flow regime (homogeneous regime). A more heterogeneous bubble injection can change the flow organization, and promote coalescence/break-up rates in the flow, which could explain the larger bubbles measured by Xue et al. (2008 B).

Impact of pressure level on bubble size

In his PhD thesis, Wilkinson (1991) studied the bubble sizes in 0.15 m diameter and 1.5 m height bubble column. The statistic information was obtained using a photographic method through visualisation windows present at different heights of the columns. In his work he studied several gas/liquid systems at different pressures, as can

be seen in Figure 1.12. The obtained bubble size distributions at the wall were fitted with a log-normal distribution as follows.

$$f(d_{eq}) = \frac{1}{s \times d_{eq} \times \sqrt{2}} exp^{\left(-\frac{1}{2}\left(\frac{\ln(d_{eq}/\overline{d_{eq}})}{s}\right)^2\right)} \quad (1.5)$$

Where s represents the variance of the bubble population and $\overline{d_{eq}}$ represents the mean bubble equivalent diameter.

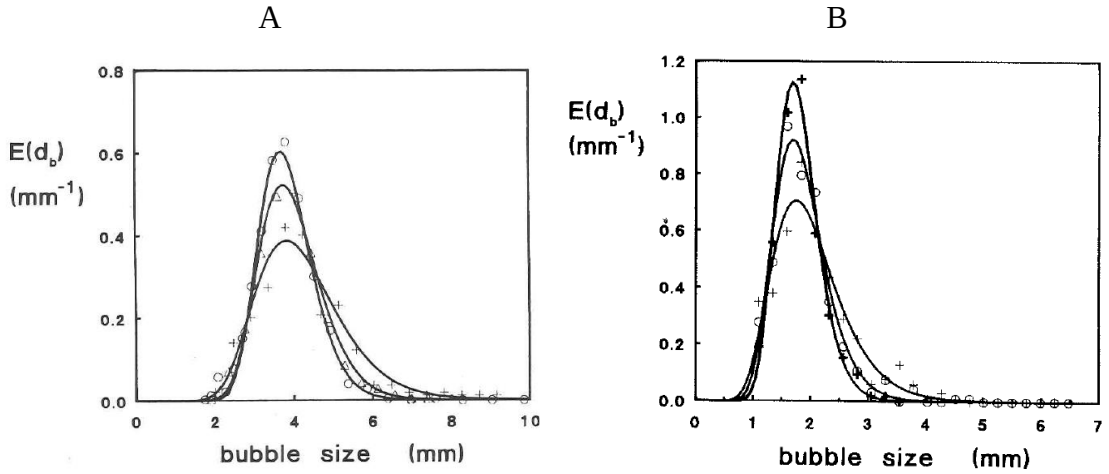

Figure 1.12 – Bubble size distributions in different systems at different pressures A) water-air B) N-heptane-N_2 Legend: circles – 1.5 MPa triangles – 1 MPa Plus signs – 0.5 MPa (Wilkinson, 1991).

The results show that the pressure level affect the mean bubble size for both organic and aqueous media. It is visible that when the pressure rises, the larger sizes are not detected or are not present anymore. The disappearance of larger bubbles was also verified with the substitution of nitrogen by gases of higher density showing that the effect of pressure is a direct effect of density (Wilkinson et al., 1994). The limited range of pressure (from 0.5 to 1.5 MPa) and the fact that these measurements were achieved in the wall zone could explain the small effect of the pressure level on the bubble size distributions.

The effect of pressure was also studied by Schafer et al. (2002) using 19 capillaries of 25 mm in length and inner diameter of 0.15 mm in a 1 m height and 0.054 m internal diameter column. The results are presented in the form of the mean Sauter diameter d_{32},

which represents the diameter of a mono dispersed spherical bubble population with the same volume/surface ratio as the one studied. The d_{32} can be calculated as follows,

$$d_{32} = \frac{\sum d_v^3}{\sum d_s^2} \qquad (1.\ 6)$$

where d_v is the diameter issued from the bubble volume and d_s is the diameter from the bubble surface calculation. Shafer studied the effect of pressure for aqueous and organic systems as can be seen in Figure 1.13.

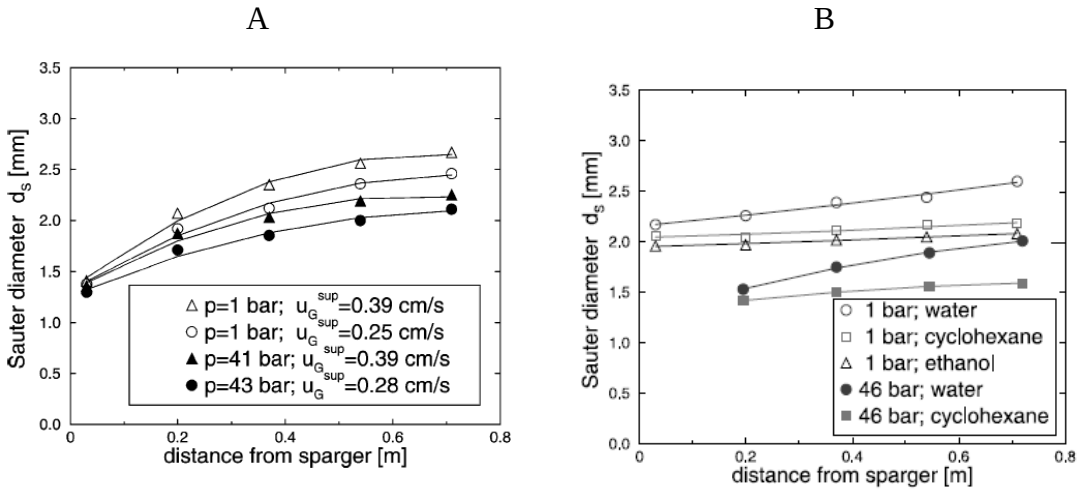

Figure 1.13 – Evolution of mean Sauter diameter along the column in different mediums A) air-water B) Comparison of water, cyclohexane and ethanol at v_{sg}=0.39cm/s (Schafer et al., 2002).

Figure 1.13 A shows that the mean Sauter diameter decreases with the pressure level all along the column, except near the sparger.

Impact of liquid properties on bubble size

Surface tension

The impact of liquid-gas superficial tension on the mean Sauter diameter of bubbles is recurrently studied in experiments using water and cyclohexane as liquid phases (Chaumat et al., 2007 A, Colombet et al. 2012). Indeed, these two liquids have similar viscosities (around 0.9 mPa.s at 25ºC) but different surface tensions, 24.4 mN/m for cyclohexane and 72 mN/m for water (at 25°C). In literature, it is recurrent to associate the decrease in surface tension with a stabilization of the interfaces and consequently a

reduction of bubble coalescence rate. This trend can be found in Figure 1.13 B where the mean Sauter diameter is measured along the column for several liquid phases. The results show that smaller surface tension leads to smaller bubble sizes. It is also demonstrated that the effect of surface tension is present all along the column and also at different pressures.

Chaumat et al. (2007 A) have studied the impact of surface tension in a range of superficial gas velocities up to 0.2 m/s in water and cyclohexane systems. The 0.2 m diameter column used was operated in a continuous mode for the liquid and the gas phases. The bubbles were generated using an annular sparger with holes of 0.001 m. The measurements were made using a bi-optical probe located 0.65 m above the sparger. To perform the mean Sauter diameter calculation, a spherical form for the bubbles was assumed and the computation was made through the following equation,

$$d_s = \frac{3V_{mp}\varepsilon_g}{2f_b} \qquad (1.\ 7)$$

where V_{mp} is the most probable detected velocity and f_b is the bubble arrival frequency. The reduction of the d_s with the decrease of the surface tension is visible in all the tested range of v_{sg} and for different liquid velocities, as illustrated in Figure 1.14.

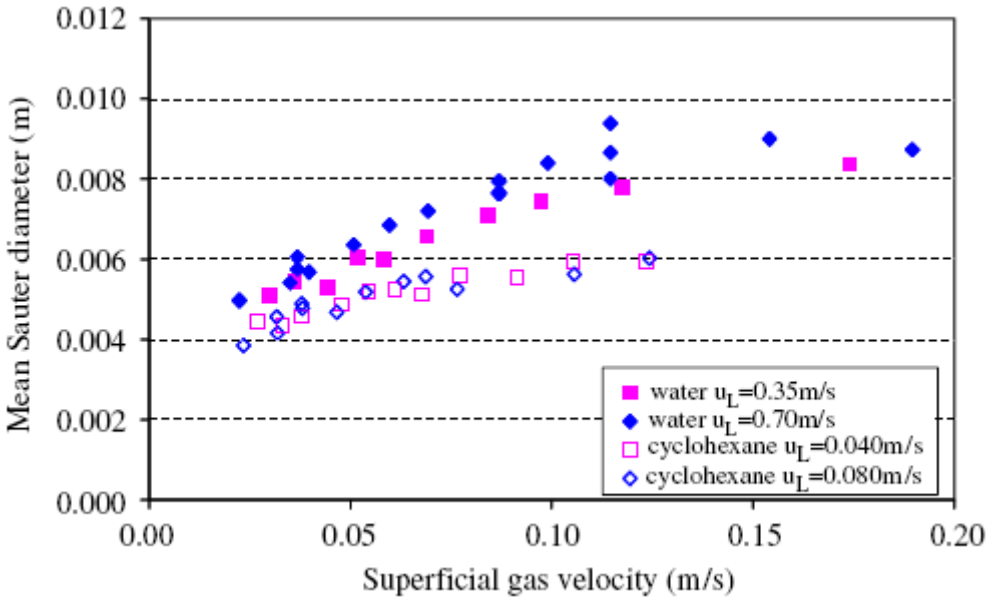

Figure 1.14 – Evolution of mean Sauter diameter with superficial gas velocity. (Chaumat et al., 2007 A) U_L is the liquid superficial velocity.

This effect is also visible in Figure 1.12, where smaller bubble sizes and a more narrow size distribution were detected for an N-heptane/nitrogen system (surface tension

=20 mN/m) in comparison with the water/air system. This phenomenon is also well supported by the higher gas hold-up values reported with N-heptane than with water (Wilkinson et al., 1991). Indeed, smaller bubbles ascend slower in the column, leading to higher gas retention.

Viscosity

Kazakis et al. (2006) have studied the impact of the liquid viscosity on the bubble size distribution at the sparger region. A square cross-section column with 0.04 m side has been used, using metal porous disk as injector. The measurements were made using a photographic method. Two glycerine solutions (50% and 66.7% v/v) were used as an alternative liquid phase with a viscosity of 6.2 mPa.s and 16.6 mPa.s and a superficial tension of 69 mN/m and 67 mN/m at 25°C. Two different porous sizes of the gas distributor (porous of 40 and 100 µm) were tested and in both cases the increase of viscosity leads to a decrease in the bubble size, as illustrated in Figure 1.15. Furthermore, in the case of the porous plate with 100 µm holes, a bi-modal population was detected for the three tested systems (water and the two glycerine solutions). These results show how difficult it is to generate a homogeneous bubble size distribution when viscous liquids are involved. They also tend to prove that an increase of viscosity decreases the primary bubble size mean diameter. This result, also coherent with those of Mouza et al. (2005), tends to invalidate the arguments of Kuncova (1995) to explain the decrease of gas holdup with the viscosity of liquid.

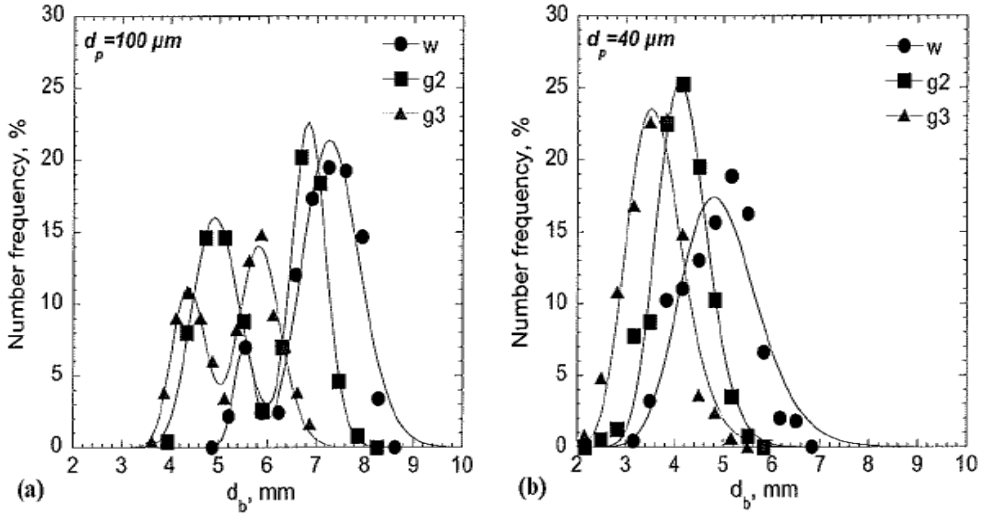

Figure 1.15 – Bubble size distributions for two different porous plates with 100 µm (a) and 40 µm (b) porous sizes (Kazakis et al., 2006).

Impact of gas distributor on bubble size

Chaumat et al. (2006) studied the impact of the sparger on the bubble columns hydrodynamics. The experiments were carried out in a 0.2 m diameter and 1.6 m height bubble column equipped with two annular spargers with 0.5 mm and 1 mm hole diameters, respectively.

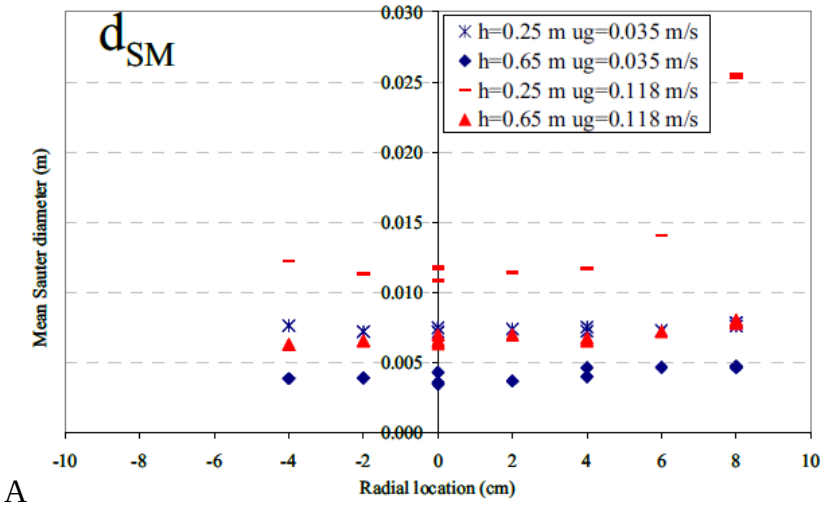

A

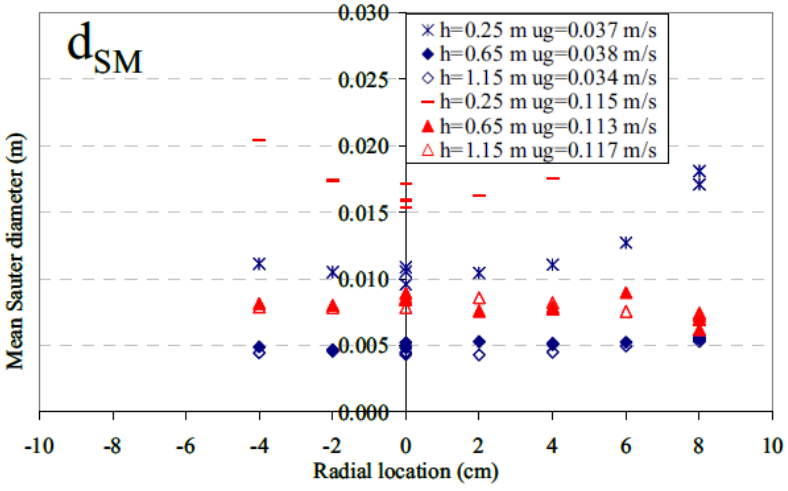

B

Figure 1.16 – Mean Sauter diameter radial profiles obtained at different elevations for: A) 0.5 mm diameter holes sparger; B) 1 mm diameter holes sparger (Chaumat et al., 2006).

As can be seen in Figure 1.16, in the sparger zone (0.25m above the distributor), a larger mean Sauter diameter was measured for the sparger with the larger holes. This trend is visible for both superficial gas velocities. However, in the fully developed zone (h=0.6m) no difference was found in the mean Sauter diameter between the bubbles generated by both spargers.

These results are supported by the results of Xue et al (2008), where a cross sparger with 2.5 mm holes (sparger 1) and two perforated plates with 0.5 mm (sparger 2) and 1.2 mm (sparger 3) diameter holes were used in a 2.30 m high and 0.16 m diameter column. Measurements were taken at 0.27 m from the sparger in the column center, with a superficial gas velocity of 30 cm/s. Figure 1.17 shows, similarly to the results of Chaumat et al. (2006), that the size of generated bubbles increases with the diameter of the gas injectors.

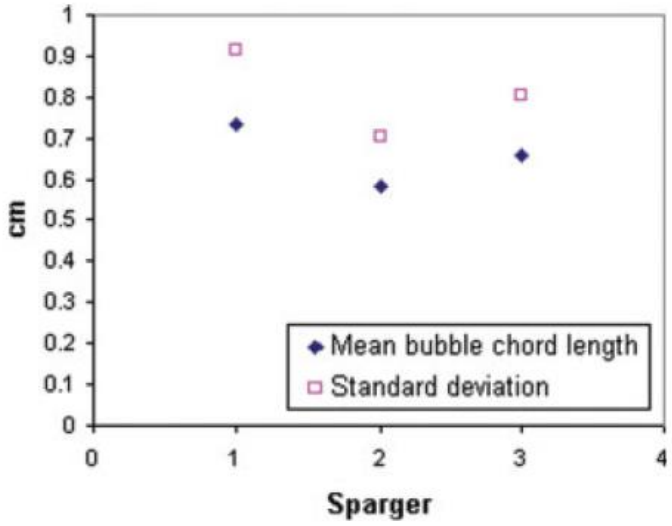

Figure 1.17 – Mean bubble chord and standard deviation of the bubble chord distribution for three different spargers, at the center of the column with a v_{sg} of 30 cm/s and at 0.27 m from the sparger (Xue et al., 2008).

As a short synthesis concerning the bubble size in the bubble columns, following trends have been identified:

- The gas sparger impacts the primary bubble distribution
- The impact of the sparger disappears in the heterogeneous regime when going up in the column.
- Gas density affects breakage and/or coalescence and leads to larger bubbles, but does not affect clearly the bubble formation.

- The role of the liquid viscosity is not clear but tends to enlarge the bubble size distribution at the gas injection.
- The superficial gas velocity increases the bubble size.

Bubble velocity

Similarly to what has been referred to the study of bubble size, the measurement of bubble velocity is also an active vector in research nowadays. Although it has been studied for years, information about bubble velocity in large bubble columns and at high void fraction is still scarce. Most of the existing work has been done in 2D columns or in small columns in the homogeneous regime.

The absolute bubble velocity is an important parameter, necessary to calculate the relative velocity, which is a key point to understand the interaction between gas and liquid phases and the global hydrodynamics of the columns.

Impact of superficial gas velocity on bubble velocity

Xue et al. (2008 B) studied the bubble rising velocity using a four point optical probe in a 0.16 m diameter column. One characteristics of this technique is the ability to measure bubbles moving upward and downward (although with a selection of large sizes, thus a bias). As a consequence, the presented velocity values are mean values obtained by:

$$\overline{V_b} = \frac{\overline{V_{b,up}} \times N_{up} + \overline{V_{b,down}} \times N_{down}}{N_{up} + N_{down}} \qquad (1.\ 8)$$

where $\overline{V_b}$ represents the bubble velocity and N the number of detected bubbles while the subscripts represents the bubbles moving upward and downward.

At very low v_{sg} (≈ 2cm/s), the radial profiles of the bubble mean velocity were flat, as expected since such superficial velocities generally correspond to an homogeneous regime. The increase of v_{sg} changed the flow regime and the velocity radial profile became parabolic as a result of liquid recirculation, as can be seen in Figure 1.18. As typical in the churn-turbulent regime, the bubbles have a negative mean velocity value in the wall zone due to the downward direction of the liquid velocity. The experiments

carried out by Xue (2004) go up to gas superficial velocities of 60 cm/s, however his measurement technique has been only validated in a 2D column at low ε_g (values unknown).

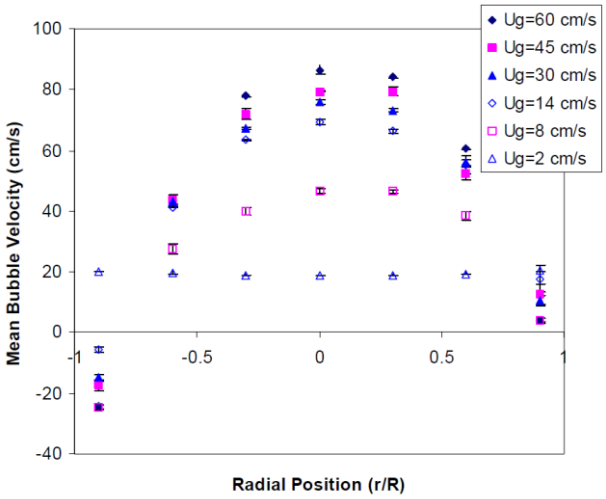

Figure 1.18 – Bubble velocity radial profiles for several gas superficial velocities. Xue et al. (2008 B)

Chaumat et al. (2007 A) also studied the bubble velocity in a 0.2 m diameter column using a double tip optical probe for a water/nitrogen and cyclohexane/nitrogen system. The measuring method presented some limitations, as reported by the authors, especially at high superficial gas velocities. Namely the mean bubble velocity was dependent of the post-treatment calibration. The most probable velocity, that represents the maximum of the velocity distribution, was pointed as the more adequate variable to describe bubble velocities. Figure 1.19 shows the most probable velocity radial profiles for several superficial gas velocities. Contrarily to what have been seen in Figure 1.18, at low superficial gas velocities the profile is parabolic, indicating the presence of an heterogeneous flow. This parabolic shape is also found on the profiles at higher v_{sg}. Since the above authors have reported different properties of the velocity distribution, it is not possible to compare the reported values.

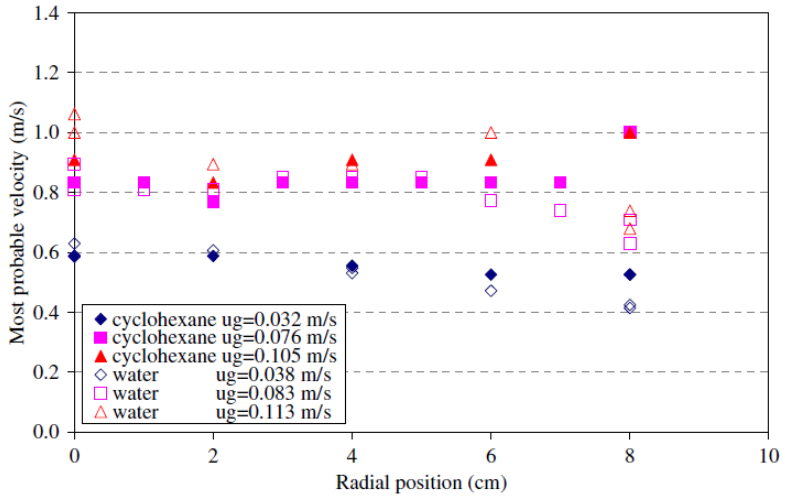

Figure 1.19 - Effect of superficial gas velocity in bubbles velocity radial profiles. (Chaumat et al., 2007 A)

At 3.8 cm/s the velocity radial profile for hexane is flat, contrarily to the one obtained in water. This fact can be due to the reduction of coalescence in the medium, as shown in Figure 1.14. Hence, the flat shape of the bubble velocity profile is still present at higher v_{sg}, which could indicate that the flow never reached the transition regime in the tested conditions (v_{sg} up to 0.11m/s).

Impact of pressure on bubble velocity

The impact of pressure on bubbles velocity is also addressed in Xue et al (2008 B), as can be seen in Figure 1.20. The results show that the bubble velocity slightly increases with the pressure level in the core of the column, and decreases in the wall region. As previously referred, an increase of the pressure leads to smaller bubble size and higher gas hold-up. These two parameters affect the bubble velocity along opposite ways. Smaller bubbles rise slower on the column than the larger ones. However, the liquid recirculation is enhanced by the void fraction (Fan and Cui, 2005). Since the bubble velocity is the sum of the bubble relative velocity and the liquid velocity, the effect of increasing the pressure depends on the radial position in the column. In the column core the liquid presents the highest rising velocity. However, the larger bubbles also rise in the column centre. When the pressure increases, the bubbles in the centre are smaller and have a smaller relative velocity, but the liquid velocity will also increase, leading to a

small increase in the bubble velocity. Closer to the column wall, the liquid exhibits its highest average downwards velocity and the bubbles are smaller. Hence, when the pressure level increases the bubbles are smaller, resulting in a lower relative velocity. Consequently, the bubbles are easier to be dragged down by the liquid.

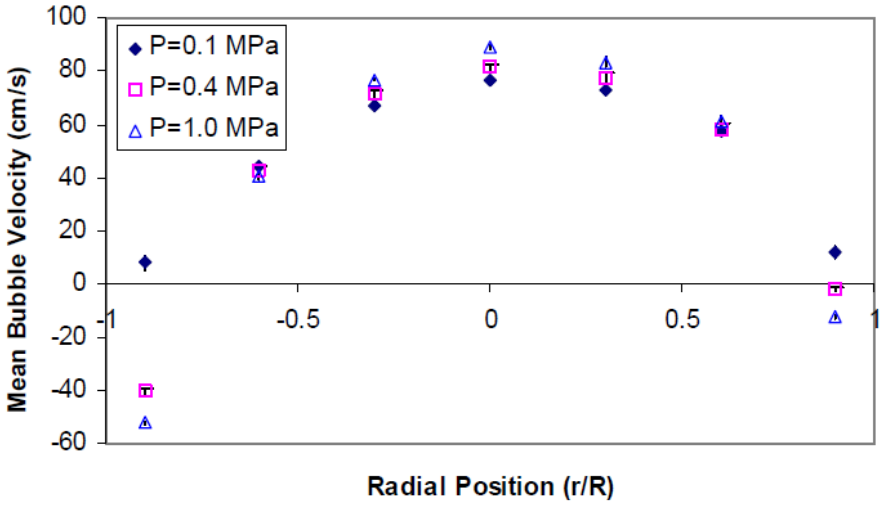

Figure 1.20 - Mean bubble velocity for a superficial gas velocity of 30cm/s in the center of the column at 80cm from the sparger (Xue et al., 2008 B)

Impact of gas distributor on bubble velocity

In the study of Xue et al. (2008B), three different spargers were used: a cross sparger with 2.5 mm holes and two perforated plates with 0. 5 mm diameter holes and 1.2 mm diameter holes. As can be seen in Figure 1.21, the sparger configuration did not affect the bubble velocity PDF (measurement with a four point optical probe). However, as shown in the chapter 2.2.1, the gas distributor affects the bubble size.

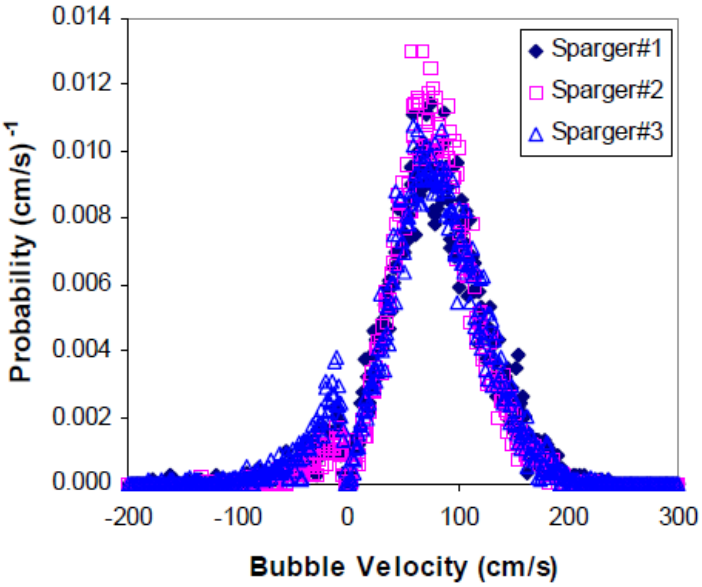

Figure 1.21 - Sparger effect in bubble velocity distribution for a superficial gas velocity of 30cm/s in the center of the column at 80cm from the sparger. (Xue et al., 2008 B)

Impact of liquid properties on bubble velocity

In Figure 1.19 can be seen the impact of surface tension on bubble velocity done by Chaumat et al (2007 A). The results show that the decrease in surface tension did not affect considerably the velocity, although in cyclohexane the bubbles were smaller than the ones generated in the water, as shown Figure 1.14. Generally, smaller bubbles are associated with a lower velocity: this was not observed in this study.

The absolute bubble velocity results from different parameters as the liquid velocity the bubble size, the properties of the system and so on. It is therefore difficult to analysis independently from the other parameters of interest.

Liquid velocity

The hydrodynamics of the liquid phase has a strong effect on mixing, heat and mass transfer and therefore plays an important role in the performance of a bubble column.Industrial bubble columns are often operated in a continuous mode for liquid and gas phases. However, the ratio of gas/liquid throughput is so high that it is possible to consider semi-batch operation conditions (batch operation for liquid and continuous for

gas). Studies performed in continuous and batch mode for the liquid phase can be found in the literature, although, in this study only the batch mode operated columns will be considered.

The studies of the liquid hydrodynamics in bubble columns found in literature can be divided in two categories:

- Studies of the liquid velocity field through the measuring of local instantaneous liquid velocities $V_L(r,z)$.
- Study of the recirculation dynamics that govern the macro mixing in the column, by the study of residence time distribution and diffusivity in the liquid phase.

Since the objective of the present work is the study of local hydrodynamics, only the studies of liquid velocity field will be discussed. As previously referred, there is no liquid throughput to the column, so the liquid velocity in a bubble column is a result of the interfacial momentum transfer from the gas phase to the liquid phase. As a consequence, as it was already shown for the gas phase, it also depends on the column design, on physical-chemical properties and on the operation conditions.

Flow organization

Several studies (Forret et al., 2003 A, 2003 B, Menzel et al. 1990, Devanathan et al., 1990) show that the global organization of the liquid flow in the column can be defined as a core-annular flow. In the core of the column the liquid have an uprising direction with the gas phase, once at the top the degasing will occur and the flow path will change to the wall direction. In the near wall region the flow goes downwards to bottom on the column where, due to the momentum of the gas injection, the liquid will converge to the column centre closing the recirculation loop.

Forret et al (2006) have measured liquid velocity profiles in 0.15 m, 0.4 m and 1 m diameter bubble columns with a perforated plate with 2 mm diameter holes at several distances from the gas distributor for an air water system using a Pavlov tube, as shown in Figure 1.23. Similarly to void fraction profile, the radial profile of the mean liquid velocity is parabolic and axisymmetric with its maximum in the centre of the column. The point of the flow direction inversion is reported by different authors to be around the dimensionless radial position x/R=0.7. That indicates that, in average, the upflow region occupies 70% of the column radius, also equal to 50% of the column cross-section. Forret

et al. (2006) have also reported that when the radial profile of the axial liquid velocity ($V_l(x)$) is normalized by the axial liquid velocity in the column center ($V_l(0)$) , the same profile is obtain regardless of liquid properties or column design, as can be seen in Figure 1.25 B. Furthermore, this normalized axial liquid velocity $V_l(x)/V_l(0)$ is only function of the velocity on the axis $V_l(0)$ and its radial distribution can be approximated by the correlation of Schweitzer et al. (2001):

$$V_l(x) = \frac{V_l(0)}{a-c}\left[ae^{(-bx^2)} - c\right] \qquad (1.\ 9)$$

Where a=2.976, b=0.943 and c=1.848. However, this correlation is only valid in the fully heterogeneous regime and in column diameters up to 1 m.

Degaleesan et al. (2001) also measured liquid velocity in a 0.44 m diameter column using a computer-automated radioactive-particle tracking (CARPT) method.

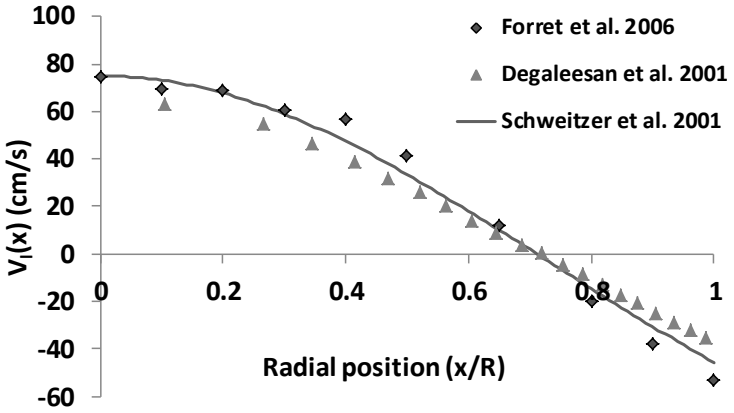

Figure 1.22 – Liquid velocity radial profile in a 0.4 m diameter column at superficial gas velocity of 9 cm/s.

Figure 1.22 shows that liquid velocity radial profiles obtained by Degaleesan et al. (2001) and Forret et al. (2006) have a good agreement with the empirical correlation of Schweitzer et al. (2001).

Gas distributor effect

Degaleesan et al. (2001) have studied the impact of the gas injection on the liquid flow, using a computer-automated radioactive-particle tracking (CARPT) technique with an air-water system in 0.14 m and 0.44 m diameter columns. In the 0.14 m column, the gas injection was made using a perforated plate with 0.4 mm diameter holes, arranged in 3 concentric circles achieving a 0.05% of porosity. In the 0.44 m diameter column, the gas injection was also made through a perforated plate but in this case with 0.7 mm diameter holes arranged in 14 concentric circles achieving a porosity of 0.077%. In this work it is reported that in a 14 cm diameter column there was no impact of the gas injection in the liquid velocity field at an elevation of 50 cm (H/D =3.57) from the gas distributor. A similar result is reported for the 0.44 m diameter column where the injection effect was detected up to 1.32 m (H/D =3) from the injection. This may show that the "height of gas effect" is perhaps not scalable with the column diameter.

This subject was also address in the work of Forret et al. (2006), the perturbation made by the gas distributor was measured through the axial evolution of the liquid velocity. Figure 1.23 shows that there are two different zones in the column, as similarly reported by Degaleesan et al. (2001). However, Forret et al. have found that the zone of flow acceleration is only detecTable 1. up to h/D=1, where lower velocities have been measured. Above h/D≈1, the liquid velocity was no longer evolving with the height, as can be seen in Figure 1.23. This discrepancy can also be related to the fact that Degaleesan et al. (2001) used the radial and azimuthal components of the liquid velocity to verify the evolution of the flow regime and Forret et al. (2006) have only analysed the axial component of the flow velocity.

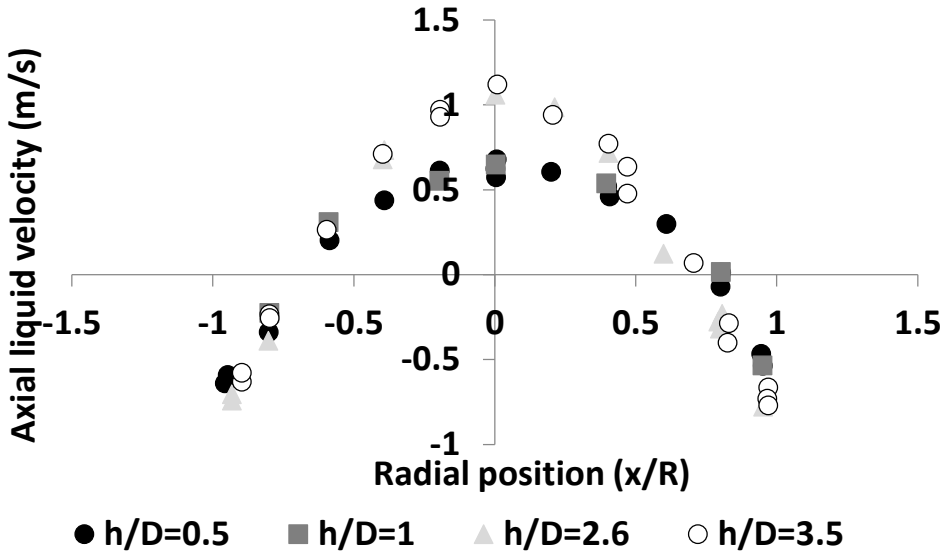

Figure 1.23 – Axial and radial liquid velocities profiles in a 1 m diameter bubble column (Forret, 2006)

Impact of liquid properties on liquid velocity

The impact of viscosity on the liquid velocity was studied by Krishna et al (2001) using a Pavlov tube method in a 0.38 m diameter column. Figure 1.24 presents the radial profiles of the axial liquid velocity obtained for water and Tellus oil (viscosity 75 times higher than water). The results show that liquid viscosity has no effect on the axial liquid velocity, since the profiles are overlapping over the column radius.

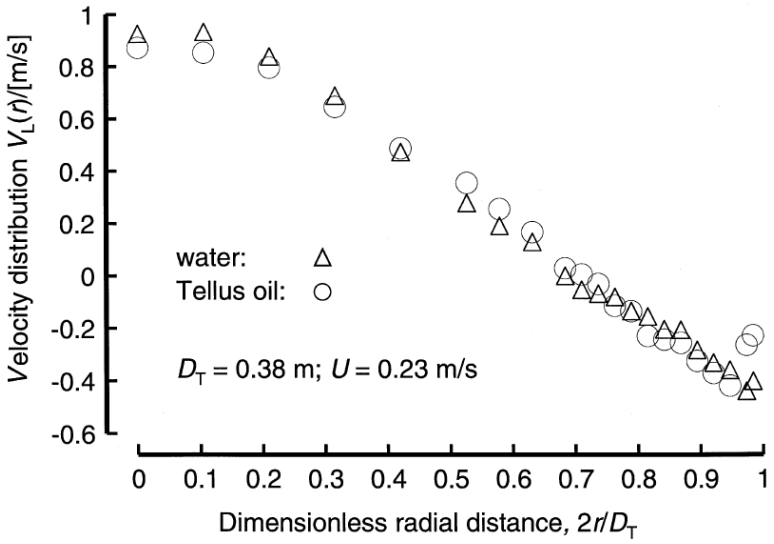

Figure 1.24 - Radial profile of liquid velocity for water and Tellus oil. (Krishna, 2001)

Impact of column geometry on liquid velocity

In literature, an increase in the column diameter is commonly associated to an increase of the liquid recirculation. Krishna et al (2001) measured a center-line liquid velocity more than doubled in a column with a diameter of 0.63 m than in 0.18 m diameter's column filled with water.

Forret et al. (2006) measured the center-line liquid velocity in several columns sizes (up to 1 m) in a wide range of v_{sg}. The increase of liquid velocity with v_{sg} was observed in all tested conditions (Figure 1.25 A).

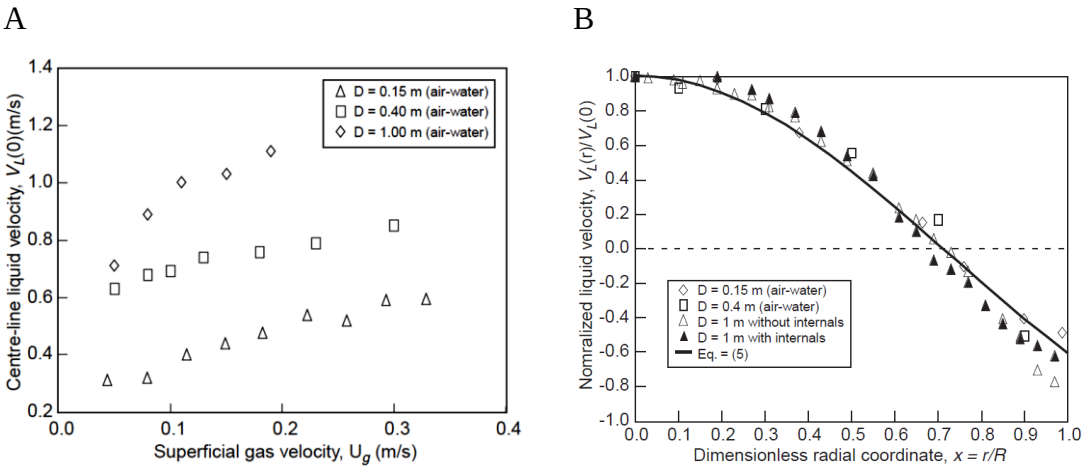

Figure 1.25 – A) Centre-line mean liquid axial velocity for several bubble column sizes. B) Normalized mean liquid velocity profiles for several bubble column sizes (Forret, 2006)

Miyauchi and Shyu (1970) proposed a correlation to predict the liquid velocity in the center of the column ($V_l(0)$) as a function of the v_{sg} and the column diameter (D):

$$V_l(0) = 2.47 \times vsg^{0.5} \times D^{0.28} \qquad (1.\ 10)$$

This correlation was validated by Forret et al. (2006) in columns ranging from 0.15 m up to 1 m diameter and in superficial gas velocities up to 30 cm/s.

Liquid velocity fluctuations

The information on liquid velocity fluctuations in the churn-turbulent regime is very scarce. Figure 1.26 presents the radial profile of liquid velocity fluctuations in a 1m diameter column, from Forret et al. (2006). These data were obtained with a Pavlov tube with a resolution frequency of 50 Hz for a superficial gas velocity of 15 cm/s.

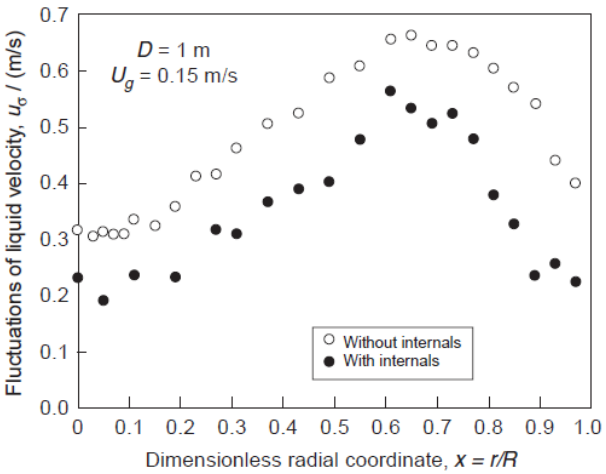

Figure 1.26 – Radial profiles of axial velocity fluctuations in the liquid for a 1 m diameter column with and without internals.

The results show that the axial liquid velocity fluctuation (u') profile is roughly parabolic and have the highest fluctuations in the zone of the mean flow inversion (namely x=0.7, as can be seen in Figure 1.25 B). Degaleesan et al. (2001) have measured the liquid turbulence intensity with a CARPT method in the axial direction (u'^2) and in the radial direction (v'^2) at superficial gas velocity of 10 cm/s in a 0.44 m diameter column, as can be seen in Figure 1.27.

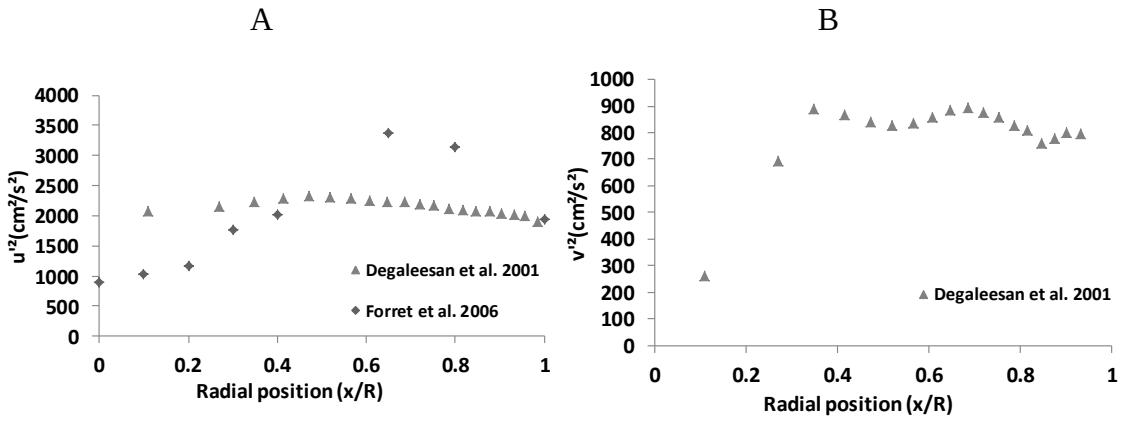

Figure 1.27 – Radial profile of liquid turbulence intensity in the: A) axial direction; B) radial direction.

The u'² measurements of Degaleesan et al. show a flat profile along the column axis, contrarily to the parabolic profile of Forret et al. (2006). The v'² is reported to be constant from the column wall up to x/R=0.3. Further from this point there is a strong reduction in the turbulence intensity, which is in agreement with the assumption that in the column core the liquid is raising in the upward direction.

Reynolds stress

Menzel et al. (1990) have measured the Reynolds stress in a 0.6 m diameter bubble column using a hot film anemometry probe at superficial gas velocities up to 10 cm/s. Devanathan et al. (1990) have also measured the Reynolds stress in a 0.3 m diameter column using a CARPT method up to 10 cm/s. Finally, Degaleesan et al. (2001) have also reported the Reynolds stress in a 0.4 m diameter with a CARPT method. All the results are shown in the Figure 1.28.

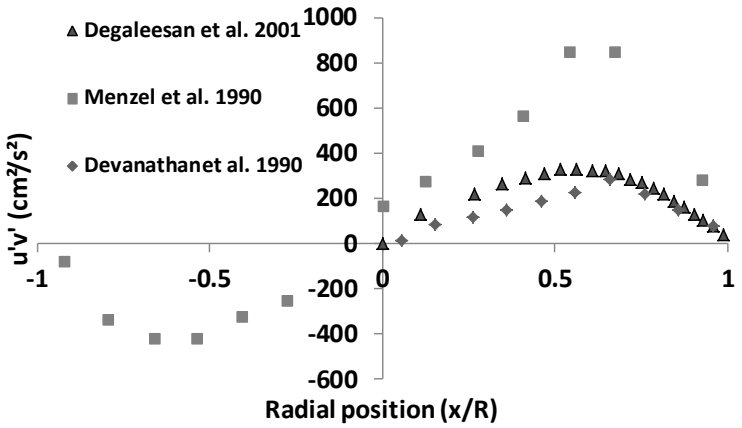

Figure 1.28 – Radial profiles of the Reynolds stress u'v' at superficial gas velocity of 10 cm/s Menzel et al. (1990) D=0.6m, Devanathan et al. (1990) D=0.3m; Degaleesan et al. (2001) D=0.4m.

The results show that despite the measurements have been made with different methods and different column diameters, they all have the same shape. Hence, the amplitude of the peak of the Reynolds shear is increasing with the column diameter, for a given superficial gas velocity. As previously stated, the liquid velocity profiles become steeper with the increase in the column diameter. As a consequence the velocity gradient and the turbulence increases also, which is in agreement with the results presented in Figure 1.28. Menzel et al. (1990) reported the Reynolds stress in all column diameters, and results show that the profile is asymmetric. This could be related to the large scale eddies rotating in opposite directions. Since the liquid rises in the core of the column and descends near the wall, the large eddies from each side of the column should be rotating in opposite directions.

The analysis of liquid phase velocity profiles raises different remarks and questions. As for the gas holdup analysis, the transition between regimes is still not clear. The role of bubble coalescence is still under debate. Otherwise, the effect of scale-up on liquid average liquid velocity profiles has been characterized, but involved mechanisms are not really clear. The effect of turbulence is not yet well understood, and as existing data have been acquired without characterization of bubble diameter, is it not possible to discriminate clearly the effect of coalescence and turbulence on the regime transition and the flow structure.

1.2 Measurement techniques

The study of local properties in a bubble column requires the characterization of continuous phase (liquid) and dispersed phase (gas). The experimental work will be conducted in different columns with different sizes (from 0.15 m to 3 m of diameter) and in a large interval of v_{sg}. The final choice of measurement technology should take into account the ability to measure the local hydrodynamics in all desired range but also if it is possible to apply the technology at every scale.

Hold up

Global gas hold up

The global gas hold up can be directly calculated by the visual observation of the expansion of liquid height by:

$$\bar{\varepsilon_g} = 1 - \frac{H_0}{H_D} \qquad (1.\ 11)$$

Where $\bar{\varepsilon_g}$ represents the global void fraction, H_0 represents the non-aerated liquid height and H_D the aerated liquid height. This is a very simple method but it is not very accurate and only gives a mean value of global gas hold up (Forret, 2006).

The global hold up can also be measured by pressure drop across a layer of aerated liquid. The mean gas hold-up is measured by the variation of the static pressure and assuming that axial variation of the gas hold up has a small dependency of acceleration and friction phenomena and there is no pressure gradient on the column radius (De Swart, 1996; Chilekar, 2005). In this case the global gas hold up can be calculated by:

$$\bar{\varepsilon_g} = \frac{(\frac{\Delta P}{\Delta h})}{g(\rho_l - \rho_g)} \qquad (1.\ 12)$$

Where ΔP represents the differential pressure, Δh represents the difference of heights where the pressure probes are placed, g represents the gravitational acceleration, ρ_l represents the liquid phase density and ρ_g the gas phase density.

Local gas hold up

ERT

Electrical resistance tomography (ERT) is a technology able to measure the local gas hold up. This technique is a non-intrusive method that consists in measuring the electrical resistance distribution in a section of the column. Electrodes placed in the column walls, as shown in Figure 1.29 A, are connected to a tomograph that converts the electrical signal into a gas hold up cross-section profile (Jin, 2007, Fransolet, 2001; Toye, 2005).

A B

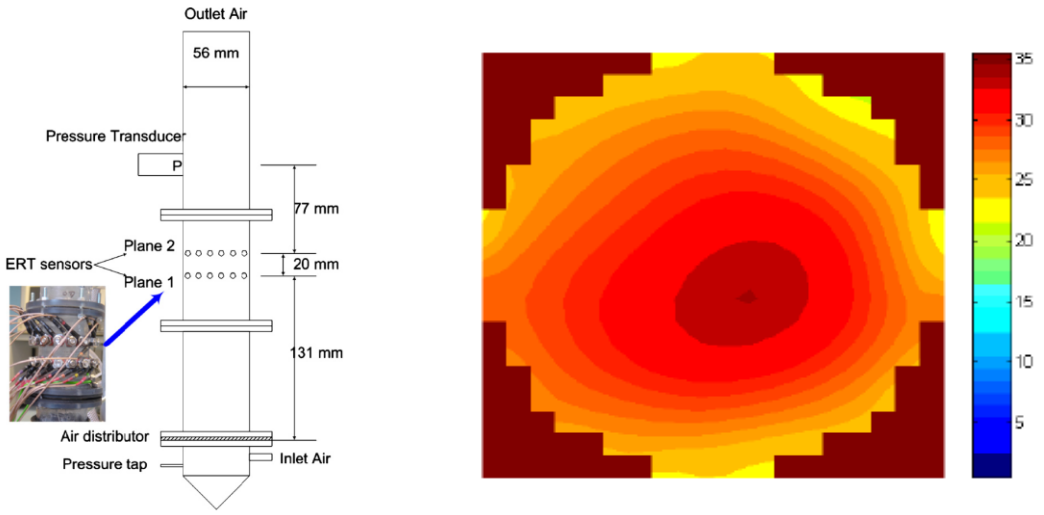

Figure 1.29 – A) A schematic representation of ERT system. B) A hold up cross-section profile measured by ERT. (Fransolet, 2001)

Time and spatial resolution are still not enough to measure local void fraction in churn turbulent regime. Moreover, since the electrodes should have a tenth of diameter of the column it is very difficult to apply it in big scales (Toye, 2005).

X-ray tomography/γ-ray tomography

The gas hold-up in a bubble column can also be measured by X-ray tomography, as can be seen in Figure 1.30 A (Hubers et al. 2005). Through the attenuation caused by the transmission of the X-ray or γ-ray in a heterogeneous medium is possible to compute the mass density distribution on the beam path. If the measure of these distributions is performed at different angles in the same plan, an image reconstruction procedure can provide a spatial density distribution of phases in a high spatial resolution (Chaouki, 1997). As shown in Figure 1.30 B, the measuring system is composed by a radioactive source outside of the column and a set of collimated sensors on the opposite side of the column. Hence, in order to obtain a completed image of the cross-section the complete system rotates around the column (Chaouki, 1997). Hubers et al (2005) have applied this method in a 30 cm diameter column at superficial gas velocities up to 18 cm/s.

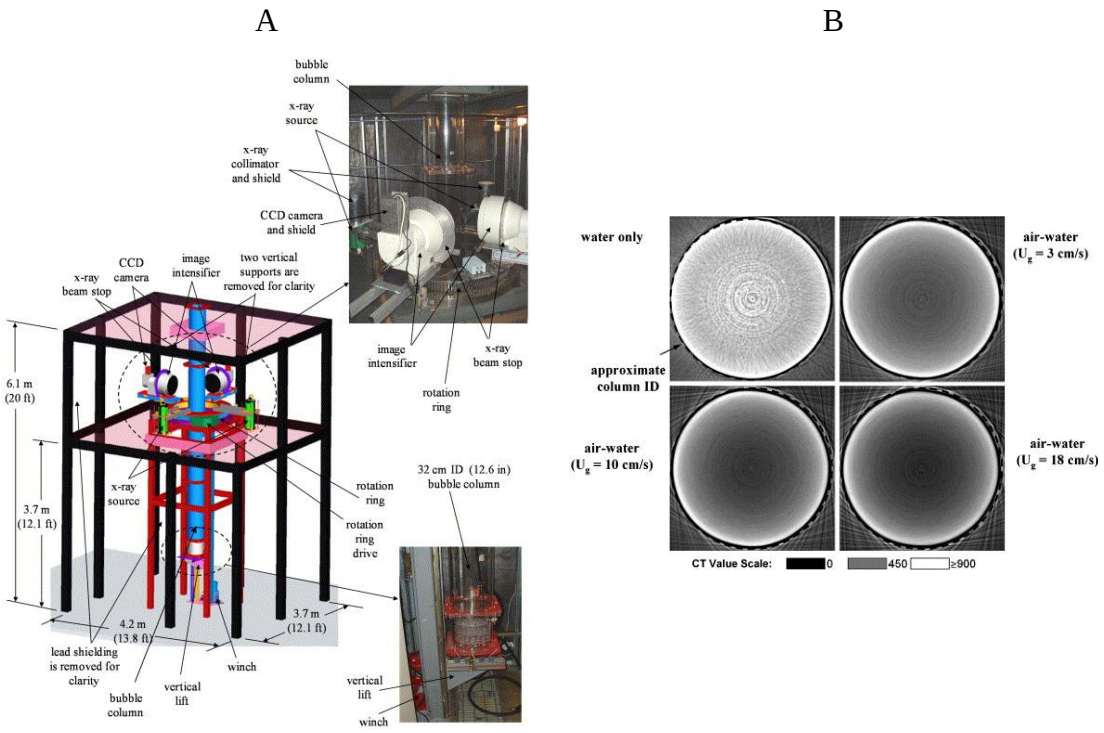

Figure 1.30 – A) A schematic representation of X-ray tomography system. B) Hold up cross-section profiles measured by of X-ray tomography (Hubers, 2005)

Resistivity probe

Another suiTable 1. technology to measure the local gas hold up is the resistivity probe, an intrusive technique, where at least one wire in placed inside the column. The electrical resistivity of the fluid present in the tip of wire is measured and registered as shown in Figure 1.31 A.

A

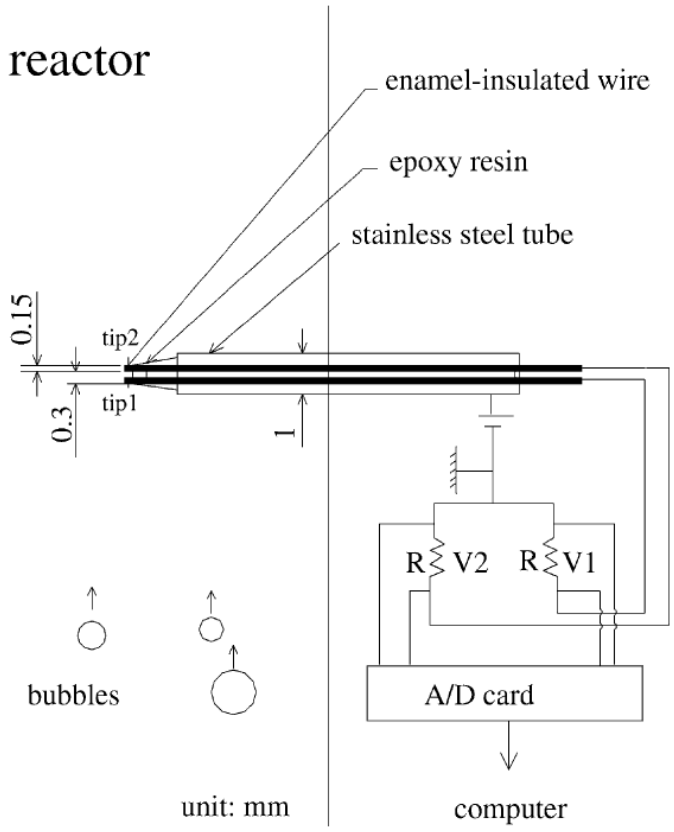

B

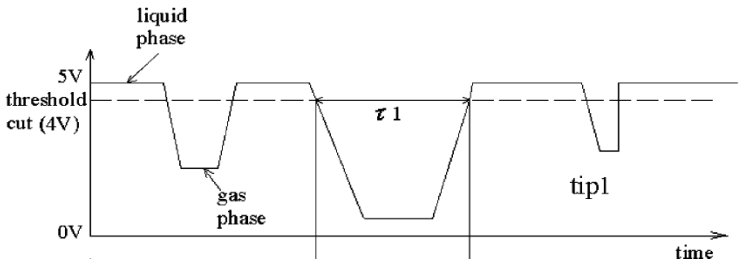

Figure 1.31 – A) A scheme of resistivity probe installation in a bubble column. B) A schematic representation of the signal treatment (Lo, 2003)

A post treatment based on a threshold convert the probe signal into a phase detection function, as shown in Figure 1.31 B. Adding the time that the probe detected the gas phase, the hold up can be determined by the following equation.

$$\varepsilon_g = \frac{Gas\ time}{Experimental\ time} \quad (1.\ 13)$$

However this technique can only be applied in conductive flows which excludes the organic flows. An optical probe achieves a much higher signal-to-noise ratio than a resistivity probe (Xue, 2008)

Optical probes

Very common and intrusive methods to measure local gas hold up are the optical probes. In literature, there can be found light transmission optical probes (Kuncova, 1993) and light reflective optical probes (De Swart, 1996; Cartellier, 1990; Guet, 2003).

In a light transmission probe, a light beam is sent through the liquid phase to a detector. If there is a bubble in the light path, the beam will be deflected and not detected, indicating to the probe is the presence of a bubble.

In a light reflective probe, the beam is generated by a laser or led and is sent through glass fiber to the point of the probe. If the probe is in contact with the liquid phase, the light beam is refracted through the liquid media. Otherwise, if the probe tip is in contact with the gas phase, the light beam is reflected by the bubble into the probe tip and then detected by a photodiode where the light beam intensity is converted into voltage.

The reflective probes have been more often used due to its smaller size and higher accuracy and capacity to be used in non-conductive media (e.g. organic liquids) (J. Xue, 2004). The post treatment of the signal used to measure the local gas hold up is usually alike the one already presented for the resistivity probe.

Bubble velocities

Optical probes

Different configurations of reflective optical probes can be found according to the number of fibers. The most common type is the bi-probe where two fibers are set apart at a small elevation distance l_{12} (normally 1 or 2 mm) (Colombet, 2012) in the macroscopic flow direction, as can be seen in Figure 1.32.

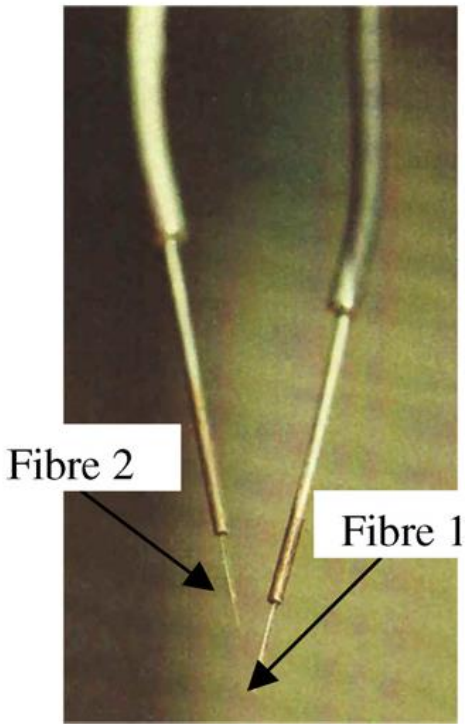

Figure 1.32 – A double optical probe (Chaumat, 2005)

The raw signal of an optical probe is the detected voltage as a function of time. A post treatment based on a threshold, that will mark the transition from one phase to the other, can convert the probe signal into a phase detection function. In the case of a bi-probe, there will be two independent signals. The velocity's calculation is done by association of both signals. In the case of a single bubble rising on the axis of the probe, the bubble will be pierced two times. First by the probe tip 1 and later by the probe tip 2, therefore, generating a pulse on each signal that will be delayed in time. This time delay (t_{12}) represents the time taken by the bubble interface to travel from tip 1 to tip 2. Once this time is determined, the bubble velocity (v_b) can be found by Revankar and Ishi (1992):

$$v_b = \frac{l_{12}}{t_{12}} \quad (1.\ 14)$$

Once the velocity has been measured, the pierced chord can be found by the multiplication of the bubble velocity with its own gas time. The described post-treatment is based on the assumption that the bubble rising velocity is strictly vertical and only one bubble shape is present in the flow (spheres or ellipsoids). The pure ascending flow can be a very restricting condition as reported by Xue et al. (2003) that stated that even in a 2D bubble column only 1% of the bubbles have a pure ascending rising direction.

Signals association is a crucial step to the determination of a bubble velocity. So even in a bubbly flow with only vertical movement it is necessary to assure that the signals associated are generated by the same bubble. Meaning that a time window should be defined in way to ensure that the second pulse is sufficiently distant in time from the first pulse, to be sure that the bubble has reached the second tip. Moreover, this window should be sufficiently narrow to rule out the detection of a second bubble. These conditions should become even more difficult to define at higher void fractions. This process can limit the range of bubble velocity detected by the probe, as reported by Chaumat et al. (2005).

In a bubble column operated in heterogeneous regime, bubbles will have a chaotic movement and they are expected to present a significant transversal velocity. In this case, if a bubble approaches the probe in a certain angle relatively to the probe axis, the measured t_{12} will not be physically linked to the bubble axial velocity. However, it will be interpreted as a measurement of the axial bubble velocity, leading to an overestimation of the mean bubble velocity. Xue et al. (2003) have calculated that for an ellipsoid bubble this overestimation can grow from 50% for an angle of 30° up to 300% for a bubble with an angle of 60°.

These phenomena have been experimentally verified by Chaumat et al. (2005), through the comparison of bubble velocity measurements obtained by an optical bi-probe and a visualization technique. The experiments were conducted in a 0.25m x 0.25m square tank filled with water. Nitrogen was used as a gas phase and was injected in the bottom by two 1 mm diameter nozzles. The experiments were carried out in moderate conditions with a bubble frequency ranging from 4.6 up to 9.9 bubbles/s. In a bubble column at superficial gas velocity of 35 cm/s, the bubble frequency is above 100 bubbles/s. Even at these conditions the bi-probe has always measured higher mean bubble

velocity than the velocity measured by the flow observation, reaching a deviation of 32% for the higher bubble frequency.

An optimization of the time window, where the second pulse is searched, has been proposed by Kamp (1996) and has been successfully used by Chaumat et al. (2005) to minimize the deviation between the mean bubble velocities. However, this procedure is done by comparing two bubble velocity distributions coming from different sources. Meaning that it cannot be performed *a priori* and requires a second method to measure the bubble velocity. Moreover, this time window is characteristic of the flow, so it should be necessary to repeat it for each flow condition in order to prevent the increase of the detection of a second pulse originated by a second bubble. Consequently, the chord estimation by a bi-probe cannot be realistic because it is based on the velocity measurement. Chaumat et al. (2005) showed that for a cyclohexane/nitrogen system, 15% of the detected chords were bigger than the biggest diameter detected by image analysis. In the case of a bubble in a horizontal position (as is assumed in the signal treatment) the bigger vertical chord that can be detected is the bubble vertical diameter, despite the bubble shape. This deviation can be originated either by a bubble that slowed down during the piercing or a piercing done in a non-vertical direction.

A different probe configuration with four fibers has been developed by Saito and Mudde (2001), Guet et al. (2003) and Xue et al. (2003). Like a bi-probe, this probe configuration consists in the aggregation of four independent optical probes, as can be seen in Figure 1.33. The main probe has a central and lower position and the other three probes are placed in a triangular shape.

The void fraction is measured, likely on a bi-probe, using the signal coming from the main tip. However, to measure the bubble velocity, four different bubble pulses must be associated. If the bubble is rising aligned with the center of the probe and in a pure ascending movement, the main probe signal will have the first pulse. Then, in function on the bubble shape, orientation and movement direction, the other three probes will later detect the bubble. However, if the bubble is rising with a considerable offset from the probe axis, this time delay for the detection of the bubble by one of the secondary probes can be significantly different. Similarly to what have been described to the bi-probe, it is necessary to add a criteria limiting the accepTable 1. time window, where all the four bubble pulses must be, in order to the bubble velocity to be taken into account (Guet et al 2003). Guet et al. (2003) have found a good agreement between the imposed flow and the measured flow by limit this time window to ±25% of the mean time delay. However,

these experiments have been conducted in an air-lift mock-up with a 7.2 cm diameter column, operated in a gas superficial velocity up to 4 cm/s with a gas injection being done through a porous plate. Meaning that, despite the high void fraction achieved (28%), the flow would be homogeneous and follow mostly unidirectional path likewise, contrarily to the turbulent flow typical from a bubble column operated in industrial relevant conditions.

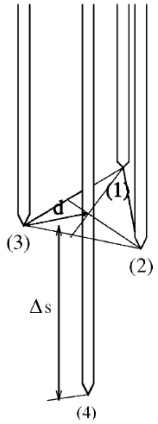

Figure 1.33 – A scheme of a four point optical fiber probe (Guet, 2003)

A signal process algorithm for a four-point optical probe has been proposed by Xue et al. (2003) based in the association of bubble pulses in the different probe tips. The authors affirm that the bubble ascending velocity (v_b) can only be known when the bubble velocity vector is aligned with the probe axis. When it is not, the probe can only detect the vertical component of the velocity (v') that is a function of the angle (θ) between the bubble velocity vector and the probe normal vector.

Xue et al. (2003) assumed that the angle θ would have the maximal value of 30° which implies a maximal velocity measurement error of 13%. However, this assumption was based on the results of Lim and Agarwal (1992) in a 2D fluidized bed flow and on the results of Kataoka et al. (1986) obtained in 6 cm diameter bubble column operated in the bubbly flow regime and the slug flow regime. Contrarily, in a large bubble column operated in the heterogeneous regime, bigger bubble angles can be detected, as will be later presented in this work.

Xue et al. (2008A) tested the performance of the previous referred algorithm in different conditions such as single bubble experiment, 2D bubble column and Taylor flow in a 5.5 cm diameter column. The validation was performed through a comparison of results coming from the optical probe and from a visualization technique. The single-bubble experiments showed that the piercing of the bubble by the probe tip caused no

deceleration. This is an important observation because, if the bubble decelerates when it is being pierced, a systematic error will be added to the velocity measurements. However, this effect has only been verified for the case where the velocity vectors of bubbles are aligned with the probe axis. Nevertheless, in the presence of a substantial angle between the bubble velocity vector and the probe axis the chances of occurrence of this phenomenon increase.

Xue et al. (2008B) performed experiments in a 16 cm diameter bubble column using a four-point optical probe with a tap water/air system for superficial gas velocities up to 60 cm/s. A detailed characterization of detected bubble chords and velocity has been made through radial profiles obtained at different elevations of the column. However, the performance of the algorithm has only been verified in a 2D bubble column for low void fraction (Xue et al. 2008A). In the 3D bubble column at a gas superficial velocity of 60 cm/s, high gradients of bubble and liquid velocity from the core of the column to the wall region are expected, leading to a chaotic movement of bubbles. Moreover, the bubble will be more deformed and will arrive at the probe with significant angles, meaning that further validation is needed.

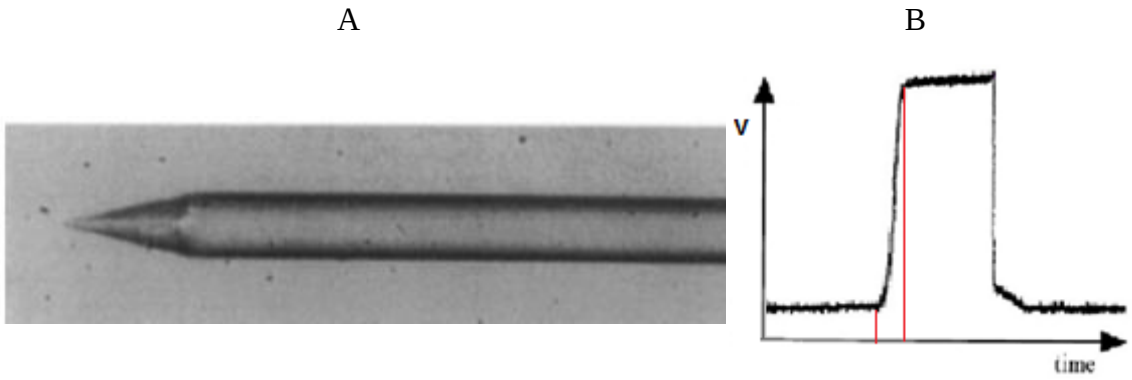

Figure 1.34 – The 1C mono-fiber optic probe: A)The shape of tip; B) 1C typical bubble signal (Cartellier, 1998)

Cartellier (1998) has developed a mono-fiber conical optical probe that is able to measure void fraction, bubble velocity and consequently the pierced chord due to its shaped point. The point of the probe is produced by an etching technique and several probe tips have been tested. The chosen probe for this work has a 30 μm length cone in the tip (1C probe), as can be seen in Figure 1.34 A. Due to its shape, the probe signal has a curvature in the rise of the pulse when a bubble interface perambulates through the probe tip. Once the bubble is pierced, as shown in Figure 1.34 B, the signal starts to

increase. Using a low threshold, corresponding to the signal level when the probe tip is wet, the time of bubble arrival (ta) to the probe tip is detected. Using a high threshold that corresponds to the signal level when the probe is dry, the time when the bubble surface reach the top of the cone (tm) is detected. Knowing the length of the sensible tip (ls), the bubble velocity (vb) can then be calculated by:

$$v_b = \frac{(tm - ta)}{ls} \qquad (1.\ 15)$$

When the probe tip pierces out the bubble, the signal falls back to the liquid level and, using again the low threshold, the total time passed by the probe inside the bubble (tg) can be detected. The pierced chord can then be calculated by the product of the bubble velocity v_b and the gas time tg. (Cartellier and Barrau, 1998) The best feature of a conical mono-fiber optical probe is that only one detection is needed to obtain the time of gas, bubble velocity and the pierced chord. Since there is no pulse association, the error coming from multi-bubble detection in high void fractions flows does not exist.

Single bubble-probe interactions have been carried out by Barrau et al. (1999) by comparing the probe results with an imaging technique. The authors report a 10% error in the detected chord, for ellipsoidal bubble with a 2 mm horizontal diameter and 1.4 mm vertical diameter, when the bubble is pierced along its axis of symmetry. However, the authors alert for the fact that these values have been obtained for stagnant liquid conditions and larger errors should be found in two-phase flows with three dimensional and unsteady structures. The principal sources of error in mono-optical probes have already been identified by Cartellier et al (1999) and are explained by three different mechanisms:

1. The blinding effect: the probe only detects the deformed surface of the bubble. In this case the detected chord will be smaller than the real on, as shown in Figure 1.35 A.
2. The drifting effect: the trajectory of the bubble is altered leading to a smaller detected chord or no chord detected, as shown in Figure 1.35 B.
3. The crawling effect: the bubble is decelerated and/or deformed during the probe-bubble interaction as shown in Figure 1.35 C.

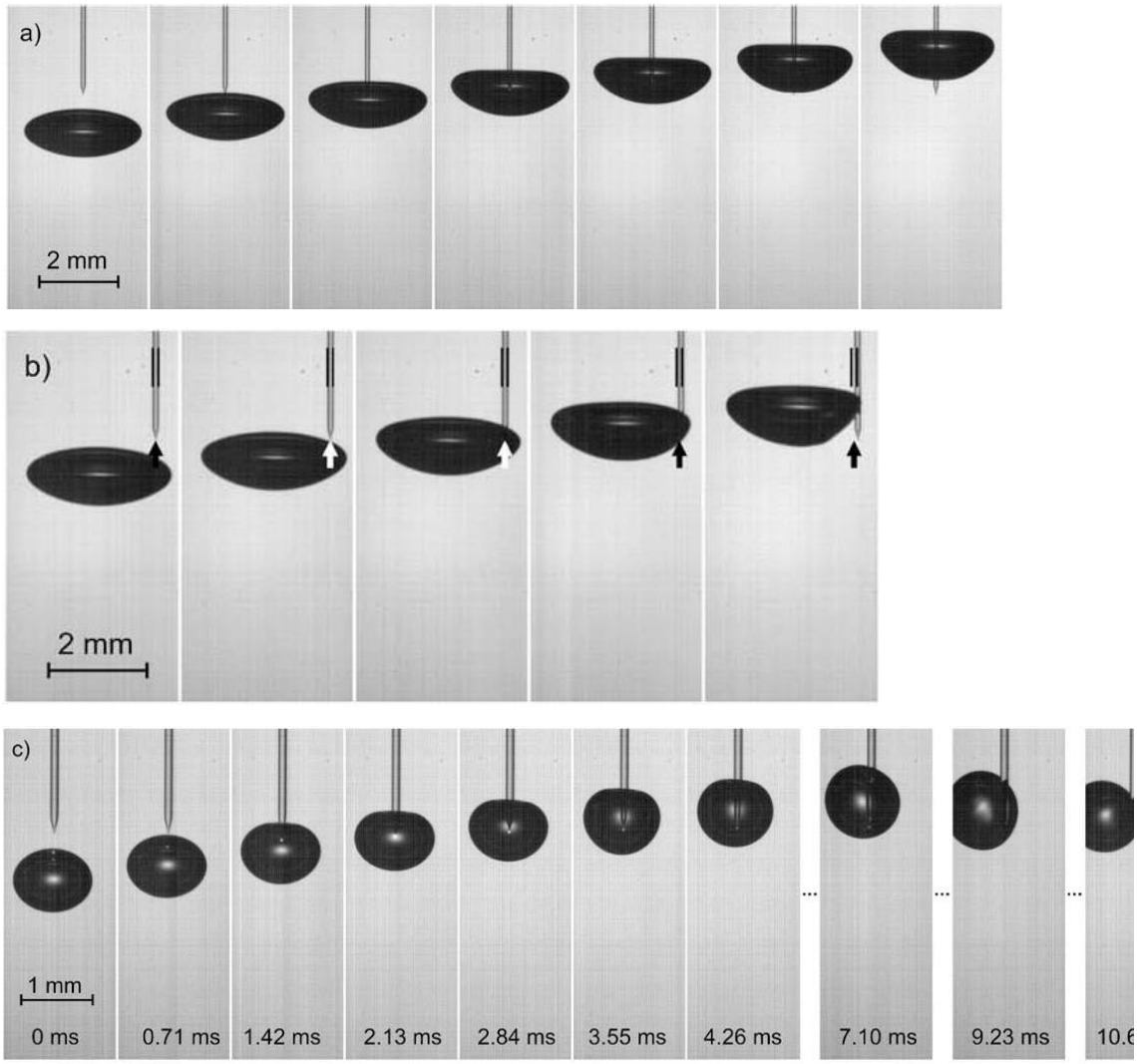

Figure 1.35 – Illustration of three phenomenon leading to error in mono-optical probe measures. A)the blinding effect b)the drifting effect c) the crawling effect (Vejrazk, 2010)

Vejrazka et al. (2010) have studied these mechanisms contributing for errors on optical probes measurements and therefore their impact on the probe performance. Errors on the measurements were reported in function of a modified Webber number (M), which is the ratio of the bubble momentum to the impulsion of the surface-tension from the probe, and characterizes the ability of the bubble to overcome the surface tension from the probe. It is reported that in case of an M number higher than 50, the void fraction and maximal chord measurement error should be less than 10%, and in the experiments carried out in our study the M number has been always greater than 100. Similarly to what have already be stated for other studies, one should mind that these values have been obtained for single bubble-probe interactions and in the absence of turbulent flows.

A second probe tip has been developed that is formed by cone + cylinder + a cone (3C probe). The signal generated by this probe has, in addition to curvature coming from the cones, an intermediate level due to the cylinder, as shown in Figure 1.36 B. In this case, the velocity will be calculated dividing the length of the cylinder by the period of time that the signal remains at the intermediate level (marked by the red lines in Figure 1.36 B).

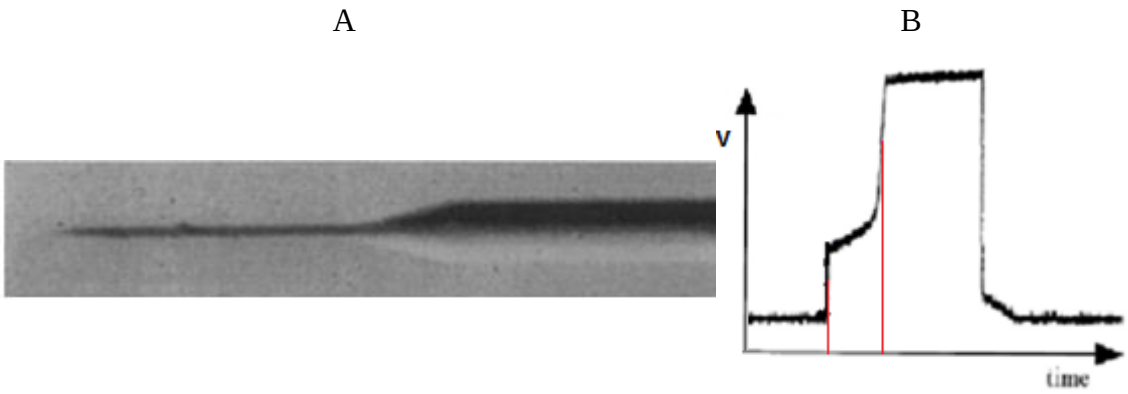

Figure 1.36 – The 3C mono-fiber optic probe: A) Shape of the probe tip. B) 3C typical bubble signal (Cartellier, 1998)

Another mono-fiber optical probe have been developed by Mizushima and Saito (2012).This probe have the particularity of having edge tip with 35° angle, as shown in Figure 1.37, which according with the authors generated a pre-signal when the bubble is pierced in the center which allows the differentiation between bubble chords and diameter (Mizushima et al., 2013). Apart from that, the signal post-treatment is identical to the one previously described for the 1C mono-fiber optical probe.

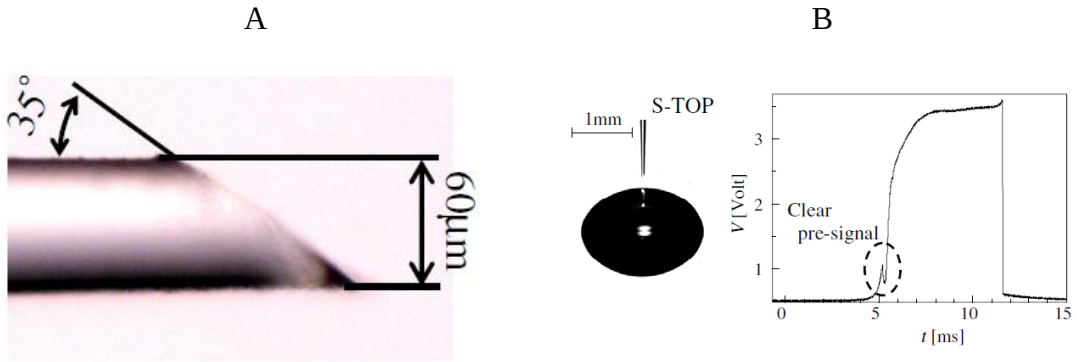

Figure 1.37 – The S-TOP mono-fiber optic probe: A) Shape of the probe tip. B) Typical bubble signal (Mizushima et al. 2013)

Acoustics probes

Al Mashry et al. developed a technique that is based in the measuring of pressure pulsation caused by bubbles passing nearby the sensor. A methodology has been applied to measure bubbles velocities using the autocorrelation function. However this technique has been applied only until 12% of void fraction and in with a superficial gas velocity of 4 cm/s. It will be very challenging to apply this technique in the turbulent conditions desired in this work.

Bubble size

Imaging

Imaging was one of the first methods employed to measure bubble size. Usually a photographic camera (Wilkinson et al. 1994, Lage and Esposito 1999) or a high speed camera (Colombet 2012, Kazakis et al. 2006, Ferreira et al.2012) is used to take images of the flow from the outside of the column and a strong light source is placed on the opposite side. This technique requires a transparent wall column and can only be employed in 2D bubble columns or close to wall regions of a 3D bubble column, since it is dependent of light's penetration in the flow. With the increase of the gas flow rate, the bubble velocity will increase, meaning a faster image capture will be necessary and consequently, a higher light intensity. Hence, with the increase of the flow rate, the void fraction will also increase and as a result the obstruction to the light path will also grow. The same problem can be expected when the column diameter is increased.

In order to avoid the light obstruction problem, a solution has been found by performing an *in situ* image technique through an endoscope (Maas et al., 2011). Contrarily to the previously presented imaging methodologies the endoscope is an intrusive technique. The endoscope works like a very thin and long lens than can be inserted in the column allowing to take images close to the flow point of interest. The high speed video camera stays in the outside of the column reducing the flow perturbations. In some cases, endoscopes are equipped with optical fiber that can conduct a light beam from an exterior source to the measurement point. Moreover, since these are local measurements it is possible to analyze the radial evolution of bubble size. The velocity measurement can also be possible by particle tracking in an Eulerian frame.

Optical probes

The optical probes are also able to measure bubble sizes through measurement of bubble chords[39]. As previously mentioned, the optical probes measure two properties: bubble velocity V_b and the time of detection of each bubble t_g. So it is possible to compute the bubble pierced chord (l) by the following equation.

$$l = V_b \times t_g \qquad (1.\ 16)$$

This bubble chord represents the path traversed by the probe inside the bubble. So for one bubble size, there will be a distribution of bubble chords. This distribution will change not only with bubble diameter but also with the shape of the bubble and its trajectory.

In literature, different approaches are proposed to transform the chord distribution in to a diameter information. Cartellier et al (1999) developed an analytical procedure to reconstruct the distribution of bubble sizes from the detected chord distribution, assuming a spherical shape and ascendant flow path. This procedure is divided in two different cases, the one where there is no chord-velocity correlation and another one if there is.

If no chord-velocity correlation have been detected in the measurements the detected chord distribution can be directly used for the reconstruction of the bubble diameters distribution. The procedure is based on the fact that, in the chord distribution generated by a single spherical bubble, the larger chord corresponds to the bubble diameter. Therefore, in the bubble chord distribution issued from an optical probe measurement in a polydispersed bubble population, the larger detected chord is the diameter of the larger bubble. Moreover, the frequency of detection this chord indicates the number of bubbles with this size that have been detected. So the typical chord distribution of a spherical bubble with this size can be calculated and multiplied by the number of this class of bubbles present in the flow. At this point, the contribution of this bubble class to the chord distribution have been computed and then can be subtracted from the original chord distribution. Consequently, the larger bubble chord on the remainder chord distribution correspond to the second largest bubble class. So the procedure can be repeated, until the all the bubble chord distribution have been deconstructed.

Otherwise if there is a chord-velocity correlation, the chord distribution need to be divided in several different distributions, corresponding to each class of bubble velocity. The procedure to reconstruct the detected diameter distribution remains the same, so at the end it will be a diameter distribution by each bubble velocity class.

However, such interpretation for ellipsoidal bubbles is quite more challenging, especially in the presence of important angles of attack. Moreover, even in the case of spherical bubbles this method requires a very detailed and converged bubble chord distribution.

Clark and Turton (1988) have proposed a numerical backward transform to find the bubble diameter distribution from the detected chord distribution for several bubble shapes, in a homogenous flow.

Liu et al. (1995) deduced the quantitative relationships of the mean and the standard deviation values for bubble chords and diameters for ellipsoidal bubbles. The bubble diameter distribution can be calculated by adjusting the gamma probability distribution to the detected chord distribution.

Disengagement gas technique

The dynamic gas disengagement technique is method to study bubble groups. The principle involves tracing the pressure drop in the column after the gas flow has been shut off. The resulting disengagement profile can be used to separate the contributions of the small bubbles and large bubbles to the total gas hold up (Kantarci, 2005; Fransolet, 2005). This technique can only show how many size classes of bubbles are present in the flow and their contribution to the flow.

Chemical method

The chemical method has been used in early studies to determine the interfacial area in bubble columns using reactions as the sulphite oxidation, hydrazine oxidation, glucose oxidation and hydrogen peroxide degradation (Pinelli et al., 2010). Usually the reaction involves a chemical species present in the liquid phase that will react with the oxygen coming from the gas phase. Assuming that the reaction happens fast enough it is possible

to affirm that the reaction rate is controlled by the mass transfer (Shultz and Elmer 1956, Akita and Yoshida 1974). Hence, if the oxygen concentration is known on the air inlet, air outlet and in the liquid, it is possible to calculate interfacial area and the mean Sauter diameter (Popovic and Robinson, 1987).
This method requires very controlled conditions in order to assure that the mass transfer coefficient and the reaction rate are constant and within the assumed range, which can be very difficult to achieve in large bubble columns. Moreover, through this method only a global mean Sauter diameter can be calculated.

Liquid velocities

In this chapter will be presented some of the available technologies to measure liquid velocity in a bubble column. However, as previously referred, the chosen technology should be able to be used in a large range of columns and in a wide v_{sg} range.

LDV, LDA

The laser Doppler velocimetry (LDV) or laser Doppler anemometry (LDA) is used to measured local mean and fluctuation velocity of the liquid phase in biphasic systems (Toye, 2005; Mudde, 1997). This technology is based on the Doppler effect that states that one particle in movement lighted by a light bean diffuse a different beam with a shifted frequency. The diffused frequency is linked with the frequency of the used light beam and the particle velocity.

Particles with a sufficient small size to follow all liquid flow dynamics are placed inside the column. These particles are lighted with a laser and the diffused radiation is measured. This technique can measure all desired components of the velocity; but for each velocity component, a different laser beam is needed. Fransolet et al (2005) were able to apply this technology in flows with void fractions up to 30%. However, a 2D column has been used. Since optical access is mandatory, this technology could be difficult to apply in large columns.

PIV

Another available technique called particle image velocimetry (PIV) is also described in the literature (Liu, 2005; Lindken, 2002). For PIV method is also necessary to use small particles to follow the flow dynamics. The used particles are fluorescents and they are excited by a laser beam and then followed with a CCD camera. As LDA, this technology depends on the optical access to the flow, which restricts the range of gas hold up where it can be applied up to 5% (Lindken, 2002).

Pavlov tube

Forret[26] has measured mean and fluctuation liquid velocity in large scale bubble columns (up to 3m) and with void fraction up to 25% using a Pavlov tube, with reported errors in the scale of 10%. The Pavlov tube is a cylindrical tube, in which two opposite 0.5 mm holes, as shown in Figure 1.38. Each one of this holes is in a different section of the tube, and both sections are connected to a single differential pressure sensor. The path between the pressure sensor and the holes is filled with water, in order to assure the transmission of the pressure fluctuations from the flow to the pressure sensor. So the Pavlov tube is used to measure instantaneous differential pressure ΔP and consequently the instant liquid velocity V_L is calculated by following equation.

$$V_L(r) = \frac{\sum_{i=1}^{N} u_i(r)}{N} \quad \text{with} \quad u_i = \begin{cases} \sqrt{\dfrac{2.\Delta P_i}{\rho_L}} & \text{if } \Delta P_i \geq 0 \\ -\sqrt{\dfrac{-2.\Delta P_i}{\rho_L}} & \text{if } \Delta P_i < 0 \end{cases} \tag{1. 17}$$

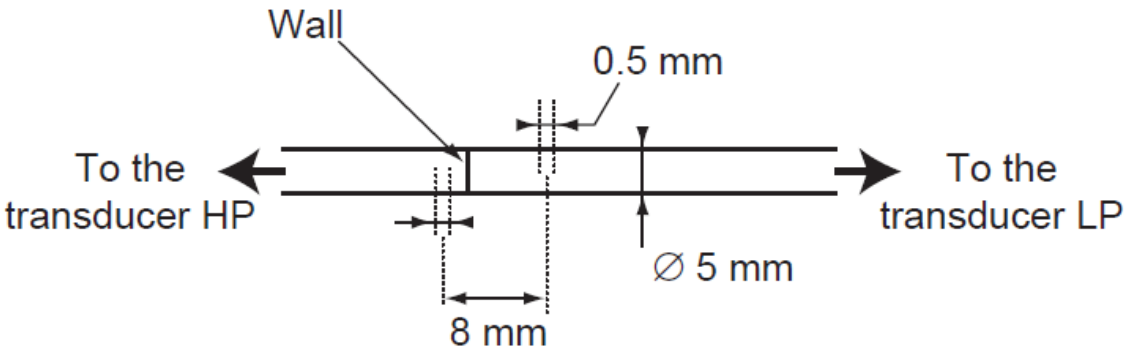

Figure 1.38 – Schematic representation of a Pavlov tube (Forret, 2006)

Contrarily other liquid velocity measurement techniques, the Pavlov tube is well adapted to high void fraction flows and large bubble columns. However, have a limited time resolution; as will be detailed in section 3.

CARPT

The computer-automated radioactive particle tracking (CARPT) is a non-invasive measurement method which consists in the tracking of a radioactive particle that is moving with the continuous phase in the flow. This particle, that is neutrally buoyant, is tracked recurring to the intensity measurement of the radiation emitted by the particle. The raw information of this method is the position of the particle in function of time, which enables a Lagrangian tracking of the particle. Using the particle position is possible to compute the particle velocity and velocity fluctuations from which several turbulence proprieties can be computed (i.e. turbulence intensity, Reynolds shear tensor, etc…) (Devanathan 1990, Y. Pan 2001, Degaleesan 2001).

This method have been applied to columns with diameters up to 44 cm and in gas superficial velocities up to 12 cm/s. However, this method was not retained for the present work because it will be very challenging to adapt this technique to a 1 m and 3 m diameter bubble columns.

Hot wire / hot film anemometer

The Hot-Wire Anemometer measures a fluid velocity by noting the heat convected away by the fluid. The core of the anemometer is an exposed hot wire either heated up by a constant current or maintained at a constant temperature. In either case, the heat lost to fluid convection is a function of the fluid velocity. By measuring the change in wire temperature under constant current or the current required to maintain a constant wire temperature, the heat lost can be obtained. The heat lost can then be converted into a fluid velocity in accordance with convective theory, considering the electrical power input equal to the power lost to convective heat transfer:

$$I^2.R_w = h.A_w\left(T_w - T_f\right) \qquad (1.\ 18)$$

where I is the input current, R_w is the resistance of the wire, T_w and T_f are the temperatures of the wire and fluid respectively, A_w is the projected wire surface area, and h is the heat transfer coefficient of the wire, function of fluid velocity. The link between the heat transfer coefficient and the fluid velocity is obtained by calibration.

The advantages of this technique is the high spatial and time resolution, that make it an appropriate tool to measure turbulent fluctuations. The drawbacks are its fragility (wire diameter generally between 1 to 10 µm, so difficult to apply in large bubble columns) and the limitation of the measurement to only one velocity component.

Based on hot wire anemometry, different configurations are proposed, such as hot film anemometers. In this case, the wire is replaced by a coating on a conical, beveled or spherical support (see the following figure).

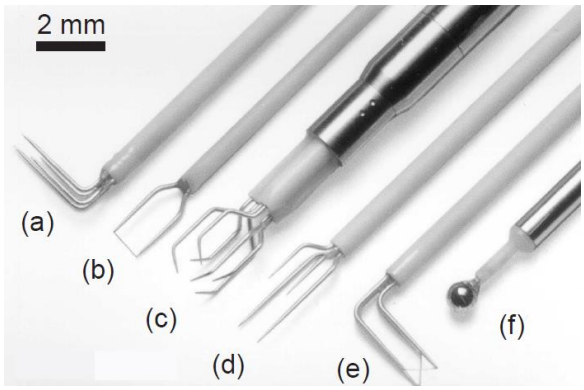

Figure 1.39: (b): simple hot wire, (a) and (e): double hot wire, (c): triple hot wire, (f): spherical hot film anemometer

Suzanne et al. (1998) report that the hot film anemometer (HFA) had two major drawbacks: the difficulty to obtain a sTable 1. calibration curve, and the unknown effect of the bubble crossings on the film heat transfer. The HFA output voltage recorded in bubbly flow presents a drop of the signal that is characteristic of the presence of a bubble on the film and sometime a larger rear peak just after the passage of the bubble is observed. According to Suzanne et al. (1998), up to now, it was not admitted that this rear peak is representative of a real velocity in liquid phase.

Roig and de Tournemine (2007) have developed a method for analyzing and interpreting the conditional statistics of the velocity in the liquid phase of a bubbly flow. By combining hot-film measurements and phase discrimination they were able, with a conditional averaging, to measure the perturbation induced in the liquid velocity in the

vicinity of a test bubble in a swarm. They have observed the attenuation of the length of its wake when the void fraction increases.

1.3 Modeling of bubble columns

The gas-liquid flow present in bubble columns is characterized by a combination of inherently unsteady flow interactions that are very heterogeneous in the time and space scales. Hence, modeling all these interactions poses a large number of problems to be solved. In a simplified manner there are 4 mechanisms that govern the bubble entrainment in the column. The first one concerns the movements induced by the density difference between the phases. The second one is the deceleration and the deviation of a bubble movement towards a vortex. The third one is the dispersion on the bubbles spatial arrangement by the liquid turbulence. The last one is the turbulence caused by bubbles (pseudo-turbulence). Presently there is no model that can resolve all the interactions in all the time and length scales excepted in small configurations. However, there are different models that are adapted to solve the hydrodynamics phenomena at different scales.

Interface reconstruction methods

Several CFD models are based on the principle to reconstruct the interface between gas and liquid, as Front Tracking, Level Set or Volume of Fluid methods. The latter approach is a very detailed solution that does not require empirical closure laws. In this method both phases are represented by "theoretical" phase where physical properties (density, viscosity, etc.) vary continuously in the passage of one phase to the other one. The instantaneous Navier-Stokes equations are solved to obtain the gas and liquid flow field in a very thin space resolution. This method has a spatial resolution in an order of 10^{-4} m and is suiTable 1. to obtain bubble-liquid interactions, bubble shapes and interfacial closure laws. However, the simulation is very costly in time and limited in number of inclusions that can be simulated (<100) (Zhang, 2007; Lance, 1996). Furthermore, interfacial reconstruction algorithms are needed to limit the diffusion of interface to a small number of cells (1-3), and a compromise has to be chosen between

accurate but unsTable 1. algorithms and more diffusive and sTable 1. ones. Different authors have used VOF methods to simulate bubbly flows (Van Sint Annaland et al., 2005; Swapna et al., 2010), but only small calculation domains are involved due to the CPU-time consumption of these methods.

Euler-Lagrange

The Euler-Lagrange (E-L) or Discrete bubble model is a model where the liquid is described as a continuous phase and the gas is defined as discontinuous phase. The liquid field is resolved in a eulerian framework. The gas phase is described by a tracking of several inclusions randomly distributed in the space by the resolution of a force balance for each inclusion This model assumes that the hydrodynamic forces acting on each bubble is known. The model has a two-way coupling for the exchange of momentum between gas and liquid phase. This method is limited in the number of inclusions that could be followed (order of magnitude 10^6), so it is commonly applied in low gas hold up conditions or small vessels (Lance, 1996; Colombet, 2012).

Two-fluid model (Euler-Euler)

The Eulerian approach of modeling a biphasic mixture consists in converting it in equivalent homogeneous fluid with specific physical properties and behaviour laws. This "homogenization" of the biphasic flow is done by averaging the phase properties. The phases are represented by their characteristic function $x_k(x,t)$ that takes the value of 1 when point *x* is in phase *k* at the time *t* and 0 when it is in the other phase. Hence, the gas retention rate ε_g is defined by the time-average of the gas phase characteristic function.

$$\varepsilon_g(x,t) = < x_g(x,t) > \qquad (1.\ 19)$$

and the same could be written for the liquid phase, knowing that $\varepsilon_g + \varepsilon_l = 1$. The mean of the velocity of the phase weighted by the mass can be defined by:

$$\overline{\boldsymbol{u}_k} = \frac{< x_k \rho_k \boldsymbol{u}_k \geq}{< x_k \rho_k >} \qquad (1.\ 20)$$

The mass and momentum conservation laws for each phase are conditionally obtained by the local and instantaneous phase characteristic function and by applying the mean operator, so the obtained equations are

$$\frac{\partial \varepsilon_k \rho_k}{\partial t} + \nabla.(\varepsilon_k \rho_k \mathbf{u}_k) = 0 \tag{1. 21}$$

$$\frac{\partial}{\partial t}(\varepsilon_k \rho_k \boldsymbol{u}_k) + \nabla.(\varepsilon_k \rho_k \boldsymbol{u}_k \boldsymbol{u}_k) = -\varepsilon_k \nabla P + \varepsilon_k \rho_k \boldsymbol{g} \pm \boldsymbol{F}_{gl} + \nabla.(\varepsilon_k \boldsymbol{\tau}_k) \tag{1. 22}$$

Assuming that $\varepsilon_g + \varepsilon_l = 1$. $\boldsymbol{F}_{gl}$ is the interfacial momentum exchange. $\dot{\sigma_k}$ is the stress tensor that can be calculated by:

$$\tau_k = \mu_{eff,k}\left(\nabla \boldsymbol{u}_k + \nabla \boldsymbol{u}_k^T - \frac{2}{3} Ik\right) \tag{1. 23}$$

The advantage of this approach is to treat both fluids in a symmetric way, making it less costly in time than the Lagrangian approach. However, it poses closure problems especially in the Reynolds stress tensor and in the terms of interphase exchanges. To solve it authors resort to additional laws that are usually semi-empirical and dependent on flow parameters (Zhang, 2007; Lance, 1996). The topology of the dispersed phase is also required (size and shape of bubbles), or may result from breaking and coalescence coupled models.

Interfacial momentum transfer

The term of momentum transfer between phases is usually described as a sum of the contributions of drag force, lift, and added mass:

$$\boldsymbol{F}_{gl} = \boldsymbol{F}^d + \boldsymbol{F}^L + \boldsymbol{F}^{VM} \tag{1. 24}$$

Each term can be calculated as follows:

$$\boldsymbol{F}^d = \frac{3\varepsilon_g C_d}{4 D_b}\left|u_g - u_l\right|\left(u_g - u_l\right) \tag{1. 25}$$

$$\boldsymbol{F}^L = \varepsilon_g \rho_l C_L\left(u_g - u_l\right)(\nabla \times u_l) \tag{1. 26}$$

$$F^{VM} = \varepsilon_g \rho_l C_{VM}\left(\left(\frac{\partial}{\partial t} + \nabla \times u_g\right)u_g - \left(\frac{\partial}{\partial t} + \nabla \times u_l\right)u_l\right) \tag{1. 27}$$

where the C_d represents the drag coefficient, C_L represents the lift coefficient, C_{VM} represents the coefficient of added mass and the C_p represents the pressure coefficient.

As previously referred, the described forces are calculated with the mean velocities of both phases.

Drag force coefficient for single bubbles

The drag force is the most important force to consider in the modelling of bi-fluid flows[11].In the case of a bubble that ascends in a stationary way through the column, the drag force is the opposite force to the buoyancy force. The C_d will be reviewed in detail since it impacts the relative velocity of the bubbles when comparing to the liquid velocity. Hence, it impacts the void fraction in the column.

The C_d can be experimentally obtained by the measure of velocity of a bubble and the liquid, or can be obtained by simulation. In literature several correlations can be found for a C_d of a spherical bubble, as showed in Figure 1.40, in function of the bubble Reynolds number Re_b.

Table 1. 1.1 –Correlations for C_d of a single and spherical bubble (Brahem, 2013; Colombet, 2012)

Conditions	Correlation	Authors
$Re_b \ll 1$	$\frac{24}{Re}$	Stokes (1851)
$Re_b \ll 1$	$\frac{16}{Re_b}$	Hadamard (1911)
$Re_b \leq 1000$	$\frac{24}{Re}\left(1 + 0.15{Re_b}^{0.687}\right)$	Schiller Naumann (1933)
$Re_b > 1000$	0.44	
$Re_b \leq 1$	$\frac{16}{Re_b}\left(1 + \frac{Re_b}{8} + \frac{{Re_b}^2}{40}\ln(Re_b) + O(Re_b)\right)$	Taylor et al. (1964)
$Re_b \gg 1$	$\frac{48}{Re_b}$	Levich (1962)
$Re_b > 50$	$\frac{48}{Re_b}\left(1 - \frac{2..211}{{Re_b}^{0.5}}\right)$	Moore (1963)
-	$\frac{16}{Re_b}\left(1 + \frac{Re_b}{8 + 0.5(Re_b + 3.315{Re_b}^{0.5})}\right)$	Mei et al.(1994)
	$C_D = \frac{24}{Re}(1 + 0.9135\ Re^{0.6305})$	Fdhila and Duineveld, 1996
	$C_D = 0.44 + \frac{24}{Re} + \frac{1}{1 + \sqrt{Re}}$	Zhang and Vanderheyde (2002)

However, a bubble is deformable, as already discussed in chapter 2.2, and its velocity will depend on the adapted shape under the flow conditions. It is possible to find in the literature specific correlations to compute the C_d for deformed bubbles, as described in . In the case of deformed bubbles the authors add the Eotvos number and Morton number to the Re_b to describe the C_d.

Table 1. 2 –Correlations for C_d of a single and deformed bubble (Brahem, 2013).

Correlation	Authors
$C_D = \frac{8}{3}(1-\varepsilon_g)^2$	Ishii and Zuber (1979)
$\begin{cases} for\ Eo \le 7.12 & min\left\{\frac{4}{3}\frac{Eo}{We_c}, \frac{8}{3}Eo^{2/3}\right\} \\ for\ Eo > 7.12 & \frac{8}{3}\frac{4Eo}{(9.5+Eo)} \end{cases}$	Maxworthy et al. (1996)
$We_c = \max(0.517\ln(Mo) + 7.624, 2.326)$	
$\sqrt{{C_d}^2(Re_b) + {C_d}^2(Eo)}$	
$C_d(Re_b) = \frac{16}{Re_b}\left(1 + \frac{Re_b}{8 + 0.5\left(Re_b + 3.315{Re_b}^{0.5}\right)}\right)$	Dijkhuizen et al. (2010)
$C_d(Eo) = \frac{4Eo}{(9.5+Eo)}$	
$max\left\{min\left\{\frac{16}{Re_b}\left(1 + 0.15{Re_b}^{0.687}\right), \frac{48}{Re_b}\right\}, \frac{8}{3}\frac{Eo}{(4+Eo)}\right\}$	Tomiyama (1998)
$\frac{2}{3}\sqrt{Eo}$	Zhang et al (2006)
$\sqrt{{C_d}^2(Re_b) + {C_d}^2(Eo)}$	
$C_d(Re_b) = \frac{16}{Re_b}\left(1 + \frac{Re_b}{8 + 0.5\left(Re_b + 3.315{Re_b}^{0.5}\right)}\right)$	Dijkhuizen et al. (2010)
$C_d(Eo) = \frac{4Eo}{(9.5+Eo)}$	
$C_D = \frac{8}{3}\frac{Eo}{E^{\frac{2}{3}}(1-E^2)^{-1}Eo + 16E^{\frac{4}{3}}}F^{-2}$	Tomiyama et al. (2012)
$F = \frac{sin^{-1}\left(\sqrt{1-E^2}\right) - E\sqrt{1-E^2}}{1-E^2}$	

$$E = \frac{1}{1 + 0.163Eo^{0.757}}$$

Several correlations are represented as a function of Re except for the range of Re number from 100 to 1000 the correlations predictions are very similar.

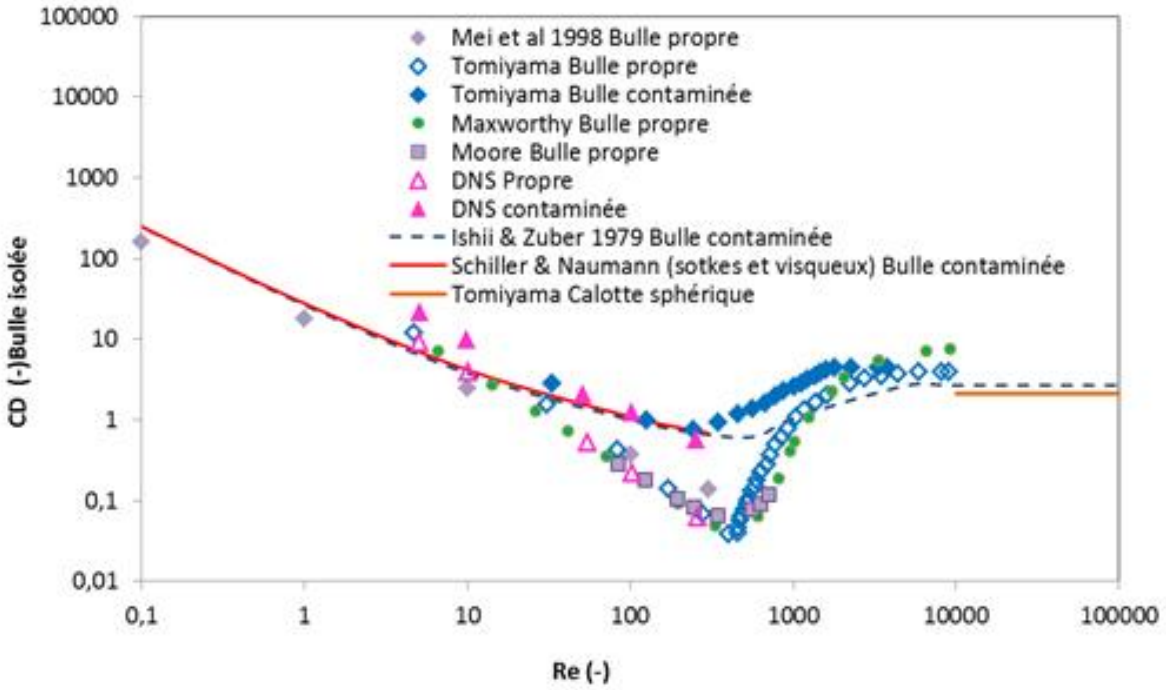

Figure 1.40 – Representation of the drag coefficient in function of the Reynolds number (Brahem, 2013)

Drag coefficient for a bubble swarm

The presented correlations were developed for a single bubble ascending in the column. These correlations are only adapted for much diluted flows (low ε_g). In the studied cases the gas hold up can achieve more than 30% so the C_d should be adapted to these conditions. One of the strategies to resolve this problem is to use a swarm factor *h* that corrects the drag coefficient by:

$$h = \frac{C_d}{C_d{}^{\infty}} = \left(\frac{V_r{}^{\infty}}{V_b}\right)^2 \qquad (1.\ 28)$$

Where $C_d{}^{\infty}$ and C_d represent the drag coefficient for a single bubble and for a swarm of bubbles respectively and $V_r{}^{\infty}$ and V_r represents the terminal velocity of a single bubble

and a bubble in a swarm. Several correlations are available in the literature to compute the h factor, as shown in the following Table 1..

Table 1.3 – Correlations for the h factor for a bubble swarm (Colombet, 2012; Zhang, 2007).

Conditions	Correlation	Authors
$n = 1.39$ $Ecc < 1$	$\frac{1}{(1-\varepsilon_g)^{2n}}$	Bridge et al (1964)
$n = 1$ $Ecc < 1$		Wallis (1969)
-	$\frac{1}{\sqrt{\varepsilon_l}}$	Ishii-Zuber (1979)
$Ecc < 1$ $0\% \leq \varepsilon_g \leq 45\%$ $27 \leq Re_b \leq 960$	$e^{(3.64\varepsilon_g)} + {\varepsilon_g}^{0.4864}$	Rusche & Issa (2000)
$Ecc \approx 0.5$ $0\% \leq \varepsilon_g \leq 30\%$ $300 \leq Re_b \leq 500$	$\frac{1}{(1-{\varepsilon_g}^{1/3})^2}$	Garnier et al (2002)
$Ecc < 1$ $0\% \leq \varepsilon_g \leq 45\%$ $150 \leq Re_b \leq 1200$ $1 \leq Eo \leq 5$ $4 \times 10^{-12} \leq Mo \leq 2 \times 10^{-9}$	$1 + \frac{18\varepsilon_g}{Eo}$	Roghair et al (2011)

Simmonet et al. (2008) developed a drag law from local velocity measurements of gas and liquid performed directly in bubble and air-lift columns operated in the heterogeneous regime. The resulting swarm factor is written as follows:

$$h = (1-\varepsilon_g)\left[\left(1-\varepsilon_g\right)^{25} + \left(4.8\frac{\varepsilon_g}{1-\varepsilon_g}\right)^{25}\right]^{-\frac{2}{25}} \quad (1.\ 29)$$

It has the particularity to increase slightly in the range of ε_g [0-15%], and then to decrease quickly to zero, as presenter in chapter 5.

Other coefficients for bubble swarms

The lift coefficient for a single bubble was studied by Tomiyama (2004) that concluded that it could be computed as:

$$C_L = min(0.288\tanh(0.121Re), f(Eo_d)) \quad (1.30)$$

where Eo_d represents the modified Eotvos number that can be calculated by:

$$Eo_d = \frac{Eo}{Ecc} \quad (1.31)$$

and $f(Eo_d)$ can be calculated by:

$$f(Eo_d) = 0.00105{Eo_d}^3 - 0.0159{Eo_d}^2 - 0.0204Eo_d + 0.474 \quad (1.32)$$

Behzadi et al. (2004) studied the variation of the lift coefficient in a bubble swarm and concluded that it could be computed as:

$$C_L = min\left(0.5, \frac{6.51\times10^{-4}}{\varepsilon_g}\right) \quad (1.33)$$

The vector of added mass coefficient was also studied by Tomiyama (2004), that states it has the form of $(C_{VM,h}, C_{VM,v}, C_{VM,h})$. In the case of a spherical bubble, both components (horizontal and vertical) take the value 0.5. For an ellipsoidal bubble, the horizontal ($C_{VM,h}$) and vertical ($C_{VM,v}$) coefficients are computed as follows:

$$C_{VM,h} = \frac{Ecc \times cos^{-1}(Ecc) - \sqrt{1-Ecc^2}}{Ecc \times \sqrt{1-Ecc^2} - Ecc \times cos^{-1}(Ecc)} \quad (1.34)$$

$$C_{VM,v} = \frac{cos^{-1}(Ecc) - Ecc \times \sqrt{1-Ecc^2}}{(2Ecc^{-1} - Ecc) \times \sqrt{1-Ecc^2} - cos^{-1}(Ecc)} \quad (1.35)$$

However, to be applied in high void fraction conditions it should be corrected (Wijngaarden, 1976) using:

$$C_{VM,Swarm} = C_{VM,bubble}(1 + 2.89\varepsilon_g) \quad (1.36)$$

Turbulence modeling

In the phase k, the stress tensor can be described (Zhang, 2007) as:

$$\tau_k = -\mu_{eff}\left(\nabla u_k + (\nabla u_k)^T - \frac{2}{3}I\nabla u_k\right) \quad (1.37)$$

where I represents the unit tensor and μ_{eff} is the effective viscosity, that for the liquid phase can be computed as:

$$\mu_{L,eff} = \mu_{L,Lam} + \mu_{L,Tur} + \mu_{BIT} \quad (1.\ 38)$$

The term $\mu_{L,Lam}$ represents the liquid molecular viscosity, $\mu_{L,Tur}$ represents the liquid shear induced turbulence, and μ_{BIT} the bubble induced turbulence. The shear induced turbulence is resolved through turbulent models, in this chapter will be described the k-ε model and the sub grid model (SGS). According to Jakobsen et al (1997) the effective viscosity for the gas phase ($\mu_{g,eff}$) can be computed as:

$$\mu_{g,eff} = \frac{\rho_g}{\rho_l}\mu_{L,eff} \quad (1.\ 39)$$

In the SGS model proposed by Vreman (2004) the shear induced turbulence in the liquid phase can be calculated as:

$$\mu_{L,Tur} = 2.5\rho_l C_s^2 \sqrt{\frac{B_\beta}{S_{ij}S_{ij}}} \quad (1.\ 40)$$

Where S_{ij} and B_β can be calculated as:

$$S_{ij} = \partial u_j/\partial x_i \quad (1.\ 41)$$

$$B_\beta = \beta_{11}\beta_{22} - {\beta_{12}}^2 + \beta_{11}\beta_{33} - -{\beta_{13}}^2 + \beta_{22}\beta_{33} - {\beta_{23}}^2 \quad (1.\ 42)$$

$$\beta_{ij} = \Delta_i^2 S_{ij}S_{ij} \quad (1.\ 43)$$

Where Δ_i represents the filter in the i direction and C_s is a model constant that is valid within the range from 0.08 to 0.22. In the bubble column modeling carried by Zhang (2007), the C_s had the fixed value of 0.1.

Sato (1975) propose to modeling the bubble induced turbulence through:

$$\mu_{L,BIT} = \rho_l \alpha \varepsilon_g C_{\mu,BIT} D_b \left|u_g - u_l\right| \quad (1.\ 44)$$

Where $C_{\mu,BIT}$ in a model constant with the value of 0.6.

The extended k-ε model proposed by Pfelger and Becker (2001) considers that the liquid turbulence is influenced by the bubble induced turbulence. Hence, the term of the liquid bubble induced viscosity ($\mu_{L,BIT}$) is set to zero. The shear induced turbulence is calculated by:

$$\mu_{L,Tur} = C_\mu \rho_l \frac{{k_T}^2}{\varepsilon_T} \quad (1.\ 45)$$

where k_L represents the turbulence kinetic energy and the ε_L represents the turbulence dissipation rate and C_μ is a model constant. The conservation equations for k-ε model are given by:

$$\frac{\partial(\varepsilon_l \rho_l k_T)}{\partial t} + \nabla\left(\varepsilon_l \rho_l k_T u_l - \varepsilon_l \left(\mu_{L,Lam} + \frac{\mu_{L,Tur}}{\sigma_k}\right)\nabla k_T\right) = \varepsilon_l (G_l - \rho_l \varepsilon_T) + S_{k,BIT} \quad (1.\ 46)$$

$$\frac{\partial(\varepsilon_l \rho_l k_T)}{\partial t} + \nabla\left(\varepsilon_l \rho_l \varepsilon_T u_l - \varepsilon_l \left(\mu_{L,Lam} + \frac{\mu_{L,Tur}}{\sigma_\varepsilon}\right)\nabla \varepsilon_T\right) = \alpha_l \frac{\varepsilon_T}{k_L}(C_{\varepsilon 1} G_l - C_{\varepsilon 2} \rho_l \varepsilon_T) + S_{\varepsilon,BIT} \quad (1.\ 47)$$

where $S_{k,BIT}$ and $S_{\varepsilon,BIT}$ are source terms due to bubble presence and can be computed (Pfleger, 2001) by:

$$S_{k,BIT} = \varepsilon_l C_k |M_l| \times |u_g - u_l| \quad (1.\ 48)$$

$$S_{\varepsilon,BIT} = \frac{\varepsilon_T}{k_T} C_\varepsilon S_{k,BIT} \quad (1.\ 49)$$

The values of the model constants are still in ongoing debate on the scientific community. In Table 1. 4 is possible to see the ones presented by Pfelger (2001).

Table 1. 4 – Table 1. of values of k-ε model constants.

Constant	Value
$C_k = C_{\varepsilon 1}$	1.44
$C_\varepsilon = C_{\varepsilon 2}$	1.92
C_μ	0.09
σ_k	1
σ_ε	1.217

Many turbulent models have been developed following the RANS approach, and they will not be details here. Commonly used turbulence models in bubbly flows are k-ε, realizable k-ε, RNG-k-ε and k-ω models. RNG-k-ε is commonly used at IPFEN for the simulations of bubbly flows.

About the use of two-fluid models

The two-fluid Eulerian model is presently the only model usable in R&D for the simulation of industrial columns. For a given operating condition and a given geometry, the model has proven its ability to perform reasonable estimations of local average fluid

velocities and volume fractions. But despite the huge number of studies on the subject, many questions are still under debate as:

- What are the forces really to be taken into account? Is the drag force sufficient?
- What is the expression of the drag force? and the other forces, if any?
- How to model turbulence in bubbly flows? Is the RANS (k-ε or similar) approach sufficient or do we need resolution at smaller scales? How to account for pseudo-turbulence?
- In a polydispersed bubble size distribution, what bubble size should be used? Should we use an averaged bubble size, transport all the moments of the bubble size distribution (Marchisio and Fox, 2013) or transport all the bubble classes individualy?

Of course the question depends on the application and cannot found universal answers. Pourtousi et al. (2014) details the different variables and parameters that may affect the simulations of bubble columns, this illustrates the complexity of the problem.

The question of the turbulence model is crucial but it is not the objective of the present study, and only low time-resolved metrology is used to characterize the liquid velocity fluctuations. Furthermore, different studies show rather satisfactory results with the RANS turbulence modelling in bubble columns, as Ekambara et al. (2005).

Concerning the momentum exchange between phases, and especially concerning the drag force formulation, two difficulties make the subject very complex. First, usable data for drag law formulation are scarce and mostly acquired in the homogeneous regime. The use of resulting drag laws in heterogeneous regime is not validated. The lack of data is due to the difficulty to measure properly the velocity of both phases and the bubble size in chaotic flows, i.e. when bubbles have non vertical trajectories.

Secondly, the studies concerning the validation of the drag law on bubble columns are often based on a narrow domain of operating conditions, and does not prove that identified formulations can be successfully used for scale-up. For instance, Krishna and Van Baten (2001) used CFD simulations validated on a 0.38 m diameter column, and validated a drag force formulation based on the discrimination between “small” and “large” bubbles. Ekambara et al. (2005) validated a drag law empirically fitted as a linear function of the gas holdup and the relative velocity, based on comparisons with experiments in various columns with a diameter ranging between 0.15 m and 0.6 m, but

only at low gas velocity (vsg < 0.1 m/s). More recent works of Xing et al. (2013) and McClure et al. (2015) provide drag law validation on a single column diameter of 0.19 m and 0.39 m, respectively. Note that the later one validates a swarm factor based on the formulation of Simmonet et al. (2008), as it will be discussed in chapter 5.

It appears this clearly that the lack of data in large columns (i.e. D>0.4 m), is a major limitation to the validation of CFD for bubble column modeling. In particular the bubble size and velocity are necessary in the heterogeneous regime.

1.4 Conclusions

As presented in this chapter, the main parameters of the local hydrodynamics of bubble columns are the bubble size and shape, bubble velocity and concentration and liquid velocity statistics. These parameters are expected to be strongly interrelated, and depend on the liquid and gas physical properties, interface contamination, injection conditions, column design (H/D) and operating conditions (flow regimes). In addition, some key phenomena are still poorly known, namely the impact of bubble coalescence and of gas injection on the bubble columns hydrodynamic. The bubble coalescence can be avoided recurring to surfactants, which stabilize the interfaces and partially control the evolution of bubble size on the column. However, the gas injection conditions are inherent to the choice of gas injector and flow throughput. In the literature, different configurations of gas distributors can be found (e.g. porous plates, capillary injectors, perforated plates, single-hole spargers, etc…). Nevertheless, the gas injection can impact not only the primary bubble population but also other phenomena, as for example the bubble size evolution on the flow, the spatial gas distribution and liquid recirculation. Hence, experimental results are difficult to be comparable, causing the creation of consensus on the key phenomena to be a difficult task. This is why there is a lack of reliable scale-up correlations, which compels to an empiric procedure. Therefore, the main parameters have to be measured in cold mock-ups of different scales, in order to understand their evolution with the column scale.

A possible alternative to improve the scale-up procedures can be the CFD simulations. The modeling of “industrial” scale bubbly flows requires 3D simulations that accounts for the unsteady and turbulence characteristics of the flow. Due to the size of the

simulation domains, DNS simulations are not a viable possibility. Therefore, these simulations can be performed recurring to URANS or LES models. In the present work only the URANS model will be studied, since the LES simulations are still very time demanding. As it was presented in section 1.3, the implementation of URANS models for the simulation of heterogeneous bubbly flows has two major setbacks: the correct prediction of the turbulence and accurate closing laws governing the interfacial momentum exchanges. However, in the present work only the latter will be discussed. In bubbly flows, the buoyancy force is the driving force, so to compute it is necessary to know the mean bubble size and concentration. The buoyancy force and the bubble drift velocity are linked by the drag force, which has a major role since it controls the gas hold-up. However, the development of an adapted drag force for heterogeneous and turbulent flows is still an open question on research. In section 1.3, several drag forces are presented, mostly for single bubbles in diluted flows. Although, one should question if those correlations are still valid to be used in different flow regimes. Since the URANS models solve the turbulence in a scale larger than the size of a bubble, it is also questionable if the drag force should not also account for the unsolved turbulence scales (e.g. eddies smaller than a bubble) that could affect the bubble drift velocity. So, to be able to compute the drag force it is necessary to know locally the size and velocity of the bubbles and the liquid velocity and its fluctuations.

The aim of the present work is to construct a detailed data base of the hydrodynamics properties obtained in bubble columns with different diameters and in a wide range of superficial gas velocities. The experiments will be carried out in columns with a diameter of 0.15 m, 0.4 m, 1m and 3 m, achieving a scale factor of 20. Since the measurements are carried out in a wide range of conditions and in different columns, it is necessary to ensure that the same bubble population is generated in the columns. As mentioned in chapter 1.1, the gas distributor configuration can impact not only bubble size but also the flow regime. Consequently, the air injection in the column is addressed by the study of a gas distributor that could be applied in the different columns. The objective is to ensure a homogenous gas distributor in all the columns assuring a known and controlled bubble generation. Moreover, one should mind the spatial arrangement of injectors on the gas distributor in order to avoid the interactions between jets. The pressure fluctuations on the air feeding system can also impact the gas injection on the column. The column must have a large air chamber before the gas distributor to serve as buffer to the pressure fluctuations, assuring a constant gas rate in the column. Beside the injection

aspects, the bubble coalescence should be ideally avoided, either by the choice of a non-coalescence liquid/gas system or by the use of surfactants.

Once one has ensured that all experiments are carried out in similar conditions, a wide database characterizing the flow should be build. The bubble size, velocity and concentration as the instantaneous and time averaged liquid velocities should be locally measured. These parameters should be characterized radially and axially on the columns, at a wide range of superficial gas velocities from 3 cm/s up to 35 cm/s. Assuring that the experiments are carried out both in homogenous and heterogeneous regimes, achieving a global gas hold-up up to 30%. Moreover, the meso-scale structures (clusters and voids), that are visible on the column walls, can have an important role on the momentum exchange. Therefore, they should be identified and their size and periodicity should be characterized on the flow.

Since the flow properties that need to be measured have been identified, it is necessary to select adapted measurement methods. As the experiments will be carried out in large bubble columns, at high gas holdup, several technical constraints must be overcome. The size of the column and the gas concentration make it impossible to observe directly from the outside of the column, eliminating some visual techniques. Also the size of the column will generate high signal loss, which can be problematic for some non-invasive methods. Additionally, due to the strong liquid recirculation, at high gas hold-up, the bubble movement is “chaotic”, generating strong fluctuations, of liquid velocity and of gas concentration. These conditions are very challenging for several intrusive methods that should be able to perform reliable measurements in the presence of such conditions. The discussion of which methods should be used and their validation will be further detailed in chapter 3.

2 Experimental strategy

In this chapter the cold mockups, which will be used in the experimental part of this work, will be presented in detail. The experiments will be carried out in bubble columns of different internal diameters, namely 0.15 m, 0.4 m, 1 m and 3 m respectively, corresponding to a scale-up factor of 20. As mentioned in chapter 1, the bed should have a ratio of static height of water/column diameter of at least 4 in order to ensure the existence of a fully developed flow zone. Besides, the experiments will be carried out in different flow regimes, since the superficial gas velocity will wary over a 10:1 range, yielding a global void fraction from 13 % up to more than 30 %.

Also, and as seen in chapter 1, the configuration of the bubble gas distributor can impact the bubble size and the flow dynamics. Thus, in order to ease the comparison between the data collected on each column, a first objective was to ensure that the same (or at least very similar) bubble population were injected in all the experiments, and with a uniform injection of gas over the entire cross-section. Uniformity holds here both for the size distribution and for the flux. For this reason, a study of gas injection was carried out to characterize the impact of the injector design parameters such as the injector internal diameter and the injector length on the bubble population over a large range of gas injection velocities. From this analysis, presented in section 2.1 here below, an optimal ideal injector geometry was determined. Yet, technical constraints lead us to depart from this solution for some columns: adaptations and final choices are discussed at the end of section 2.1. In section 2.2, the four bubble columns used in this work are described in detail. As a last step, it was necessary to check the spatial homogeneity of injection over the columns cross-sections, the homogeneity being relative to bubble size but also to fluxes in particular to avert the generation of instabilities in the injection's vicinity. Another issue concerns the impact of coalescence on the characteristics of injected bubbles, notably because of interacting gas jets and/or of liquid recirculation at the bottom of the columns. These questions are addressed in section 2.3. We then conclude on the quality of gas injection in our experimental set-up.

2.1 - Gas distributor design

In this PhD work local hydrodynamic properties will be studied over a large range of superficial gas velocities and column diameters. As stated in Chapter 1, it is necessary to ensure similar bubble populations at injection in all tested conditions, in order to collect comparable data in columns of various dimensions. Hence, a necessary preliminary step was to design adapted gas distributors. The objective of this section is to find a gas distributor that could be applied in every studied scale, with the capacity to generate the same bubble size over a range of superficial gas velocity from 3cm/s up to 35 cm/s, and using an "industrial" design i.e. perforated plates with millimetre size holes and low hole density. The design parameters analysed in this study were: injection internal diameter (i.d.), injection velocity and the ratio injector length/inner diameter (l/i.d.). The presence of coalescence near the gas distributor was also checked through the measurement of bubble size at different distances from the gas distributor. All these experiments were achieved in a 0.15 m diameter column.

Impact of injector diameter on the bubble size distribution

In order to study the effect of the injector diameter on the initial bubbles size, several experiments were performed with a single injector located in the centre of the column, as depicted in Figure 2.1.

A B

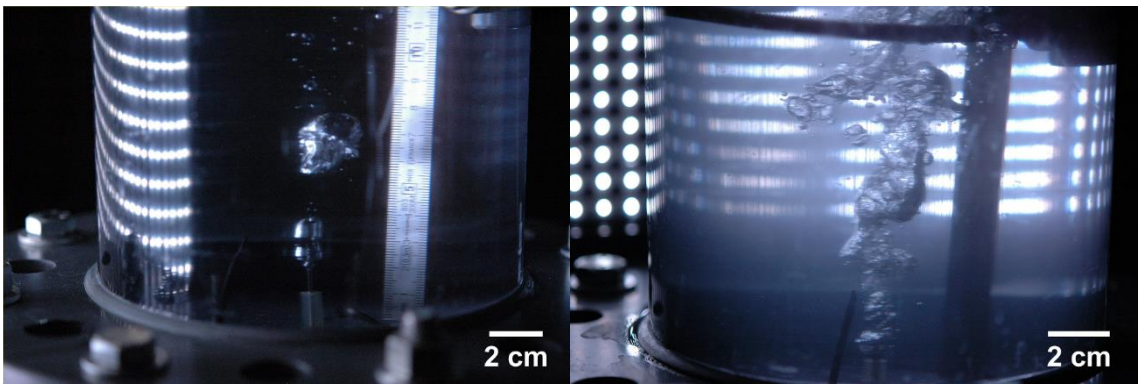

Figure 2.1- A) 1.2 mm i.d. injector (Vi=29 m/s) B) 1.7 mm i.d. injector (Vi=61 m/s)

A range of inner diameters from 0.6 mm up to 9 mm, with a l/i.d. ratio of 10, were tested for a gas injection velocity (V_i) in the range 9.8 m/s up to 83 m/s. The gas injection velocity is the ratio of the gas flow (Q_g) to the injector exit cross section (Ai), as can be seen in the following equation.

$$V_i = \frac{Q_g}{A_i} \qquad (2)$$

Conical optical probes, which characteristics and performances are presented in Chapter 3, were used to measure bubble chords and velocities as well as local void fractions. In particular, the bubble dimension is characterised either by a mean vertical chord, or by a mean horizontal diameter (see Chap.3 for details). The experiments consisted in measuring 7000 bubbles with an optical probe located at the centre of the column and at a given distance from the injector. The convergence of the mean chords and velocities was ensured to be within a range of ±5%, as can be seen in Figure 2.2, to allow the validation of each measurement.

A

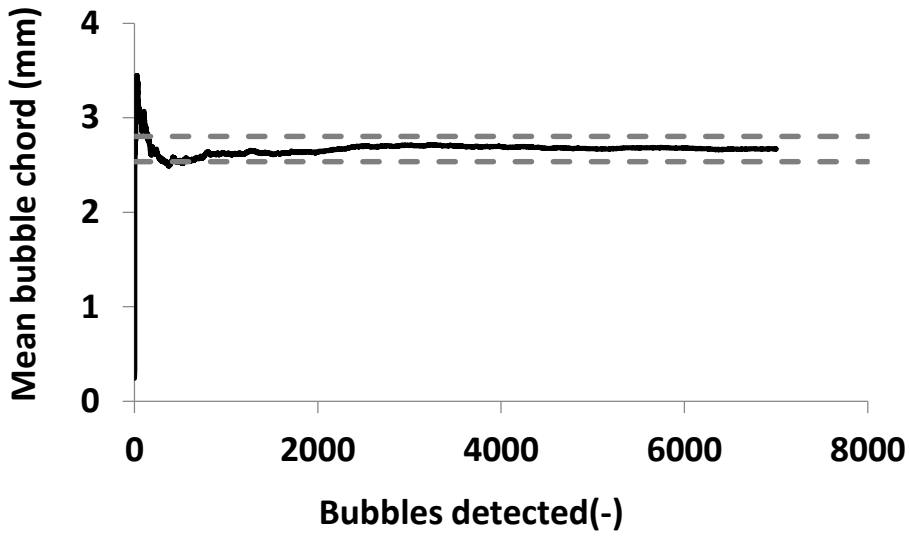

B

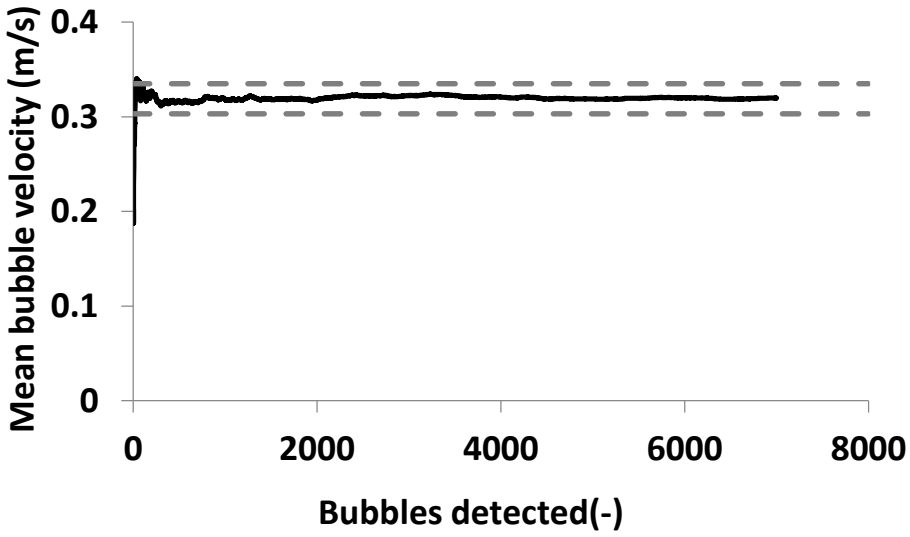

Figure 2.2 – Convergence of the cumulative average of: A) bubble chord B) bubble velocity. (Dashed lines- ±5% convergence)(I.d. injector =1.2 mm at 0.16 m from the injector and Vi=17 m/s)

In the case of the injectors with inner diameter of 0.6 mm, 1.2 mm, 1.7 mm and 4 mm, the probe was located 0.16 m above the injector exit. In the case of 9 mm i.d. injector (for all the l/i.d. ratios tested), the probe was located at 0.41 m from the injector. The distance was changed in order to gather data outside the gas jet region where bubble break up phenomenon is still very active and where the bubble size is not yet stabilized.

To study the same injection range in different injector diameters a wide range of gas flow was used, with gas injection velocities ranging from 10 to 80m/s. Since all the measurements were carried out in a 0.15 m diameter column, the experimental conditions

can be compared through the superficial gas velocity (vsg) that is computed through the following equation.

$$V_{sg} = \frac{Q_g}{A_c} \quad (3)$$

W

where Q_g represents the gas flow and A_c represent the column cross-section. As can be seen in Table 2.5 and in Figure 2.3 a wide range of superficial gas velocities and local gas hold-up were scrutinized during these experiments.

Table 2.5 – Superficial gas velocities in cm/s as a function of injector diameter and velocity of gas injection.

Injector Diameter (mm)	Velocity Injection (m/s)					
	9.8	**17**	**29**	**49**	**61**	**83**
0.6	0.015	0.02	0.04	-	-	-
1.2	0.06	0.11	0.18	0.3	-	-
1.7	0.12	0.22	0.37	0.6	0.7	1.06
4	0.7	1.2	2.1	3.5	4.3	5.9
9	3.5	6.1	10.4	17.6	22	31

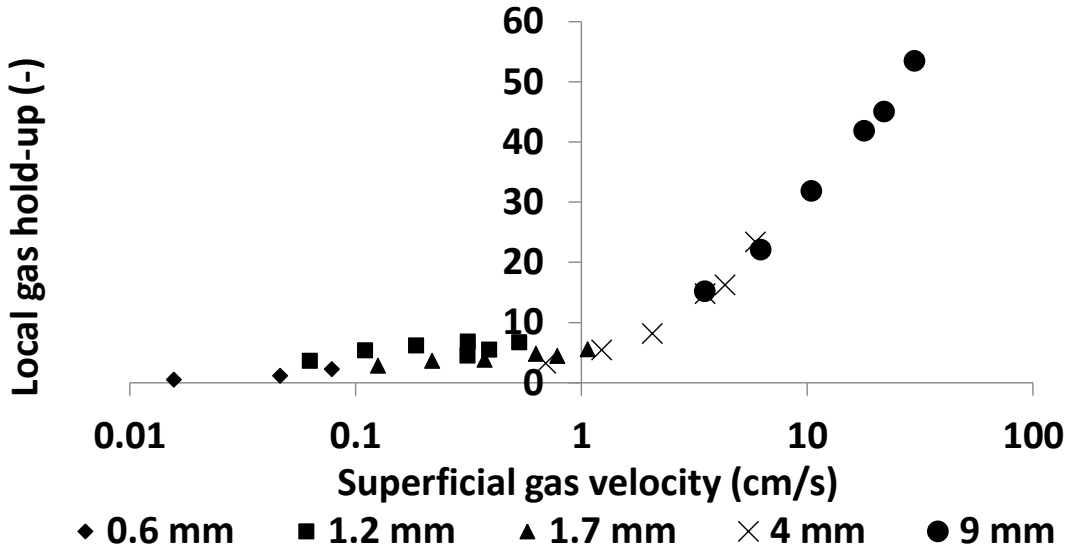

Figure 2.3- Evolution of local gas hold-up measured by optical probes with the gas superficial velocity for different injector sizes. (l/i.d.=10)

Figure 2.3 shows that the experiments for the 4 mm and 9 mm inside diameter injectors were carried at much higher gas superficial velocities than for the smaller i.d. injectors. In these conditions, significant liquid and gas recirculation can occur that does not appear, or remain less drastic in more dilute conditions: this will be confirmed thereafter by bubble velocity measurements. Therefore, one should bear in mind that the characterisations of injected bubbles were not achieved in strictly identical conditions for "small" (namely 0.6 mm, 1.2 and 1.7 mm i.d.) and "large" (namely 4 mm and 9 mm i.d.) injectors.

Figure 2.4 A and Figure 2.5 A present the evolution of the mean vertical chord (measured by 1C optical probe) with the gas injection velocity for each tested injector. The results show that the 0.6 mm diameter injector always produces bubbles smaller than 2 mm, compared to the 1.2 mm and 1.7 mm diameter injectors that produce intermediary size bubbles between 2 and 3 mm. The 4 mm and 9 mm i.d. injectors produce somewhat larger bubbles, in a range 3 to 4mm, at the tested elevation.

A

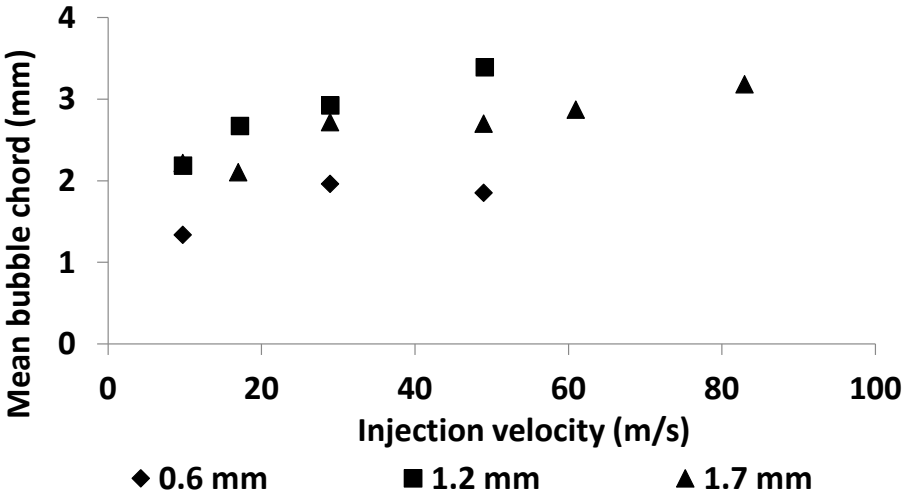

B

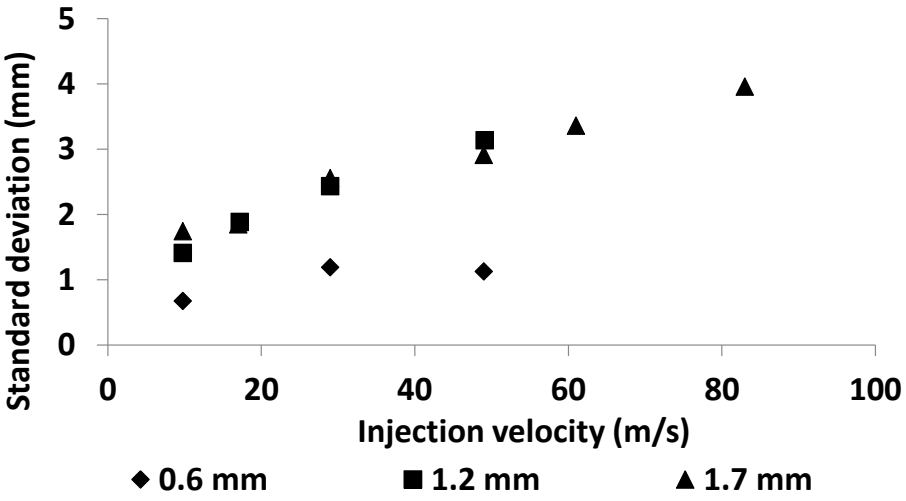

Figure 2.4 – A) Evolution of bubbles mean chord with the gas injection velocity B) Evolution of the standard deviation of the bubble chord distribution with the gas injection velocity. Measurements for several injector with internal diameters ranging from 0.6 mm to 1.7mm, measurements at an elevation of 0.16m from the injector.

A

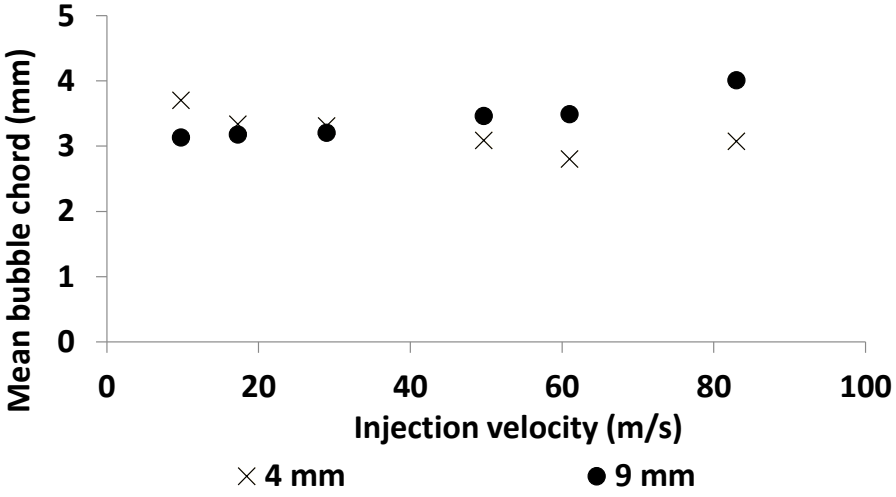

B

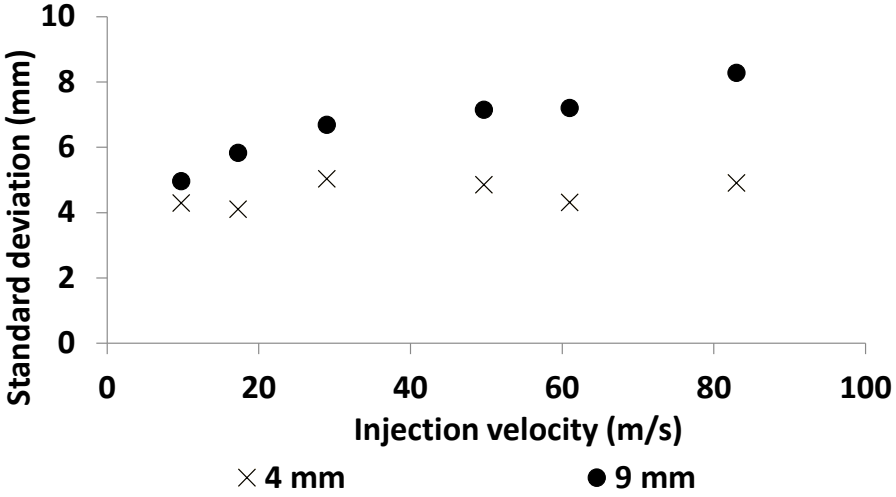

Figure 2.5 – A) Evolution of bubbles mean chord with gas injection velocity B) Evolution of the standard deviation of the bubble chord distribution with the gas injection velocity. Measurements for injectors with internal diameter of 4 mm and 9 mm. Measurements taken at an elevation of 0.16 m and 0.5 m from the injector, for the 4 mm and 9 mm diameter injectors, respectively.

Figure 2.4 B and Figure 2.5 B show the evolution of the standard deviation of the detected chord distributions in the previously detailed measurements. The standard deviation is always of the order of the mean values, but it can be much higher as for the 9 mm i.d. injector or for the largest gas injection velocities. The results also show that the standard deviation neatly increases with the injector internal diameter. This is clearly seen in Figure 2.6 drawn at a fixed gas injection velocity of 50 m/s: the mean chord happens to be poorly sensitive to injector i.d. above about 1mm but the standard deviation

drastically increases, leading to a widely dispersed size distribution for injectors of large inner diameter.

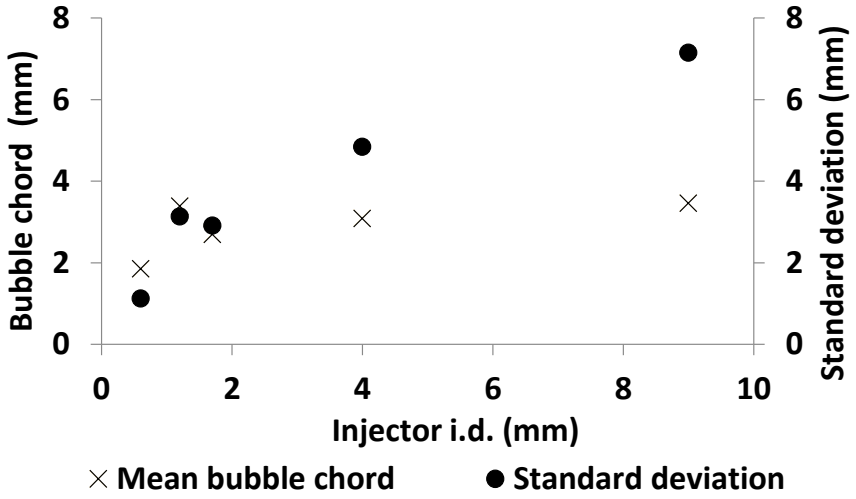

Figure 2.6– Evolution of the mean bubble chord and standard deviation with the injection inner diameter for an injection velocity of 50 m/s

Impact of injection velocity on bubble size distribution

As can be seen in Figure 2.4 A and Figure 2.5 A, the injection velocity does not impact the functioning of the different injectors in the same way. For the "small" injectors with an inner diameter of 0.6 mm, 1.2 mm and 1.7 mm, the bubble size experiences a steep increases at low gas velocities, say below 20-30m/s. Thereafter the increase is smoother, with a slope of the mean chord versus velocity of the order 0.01 s. For the larger injectors (4 and 9 mm i.d.), the sensitivity to the injection velocity remains low (slope ≈ 0.04 s) over the entire velocity range tested. Note that the slope is negative for the 4 mm i.d. injector (which is odd) but it has a similar magnitude. Thus, for "large" injectors and for "small" injectors above 20-30m/s injection velocity, the characteristic bubble size is weakly affected by the injection velocity. This behaviour is quite advantageous as similar bubble sizes can be produced over a large range of gas superficial velocities with the same injector.

As it will be further detailed in chapter 3, the 1C mono-fibre optical probe can measure the bubble velocity projected along the probe axis. The arithmetical averaged

bubble velocity and the standard deviation of the bubble velocity distribution, for the 0.6 mm, 1.2 mm and 1.7 mm inside diameter injectors, are presented in Figure 2.7 A and B, respectively. The results for the 4 mm and 9 mm inside diameter injectors are presented in Figure 2.8 A and B.

A

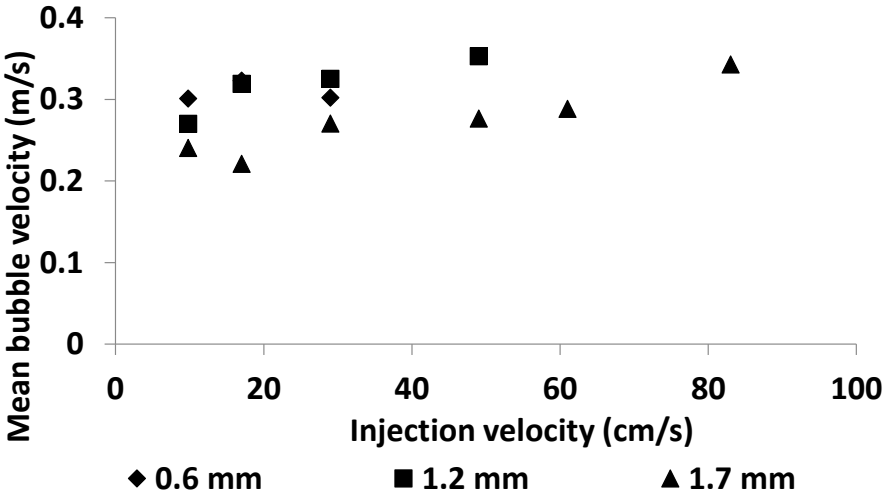

B

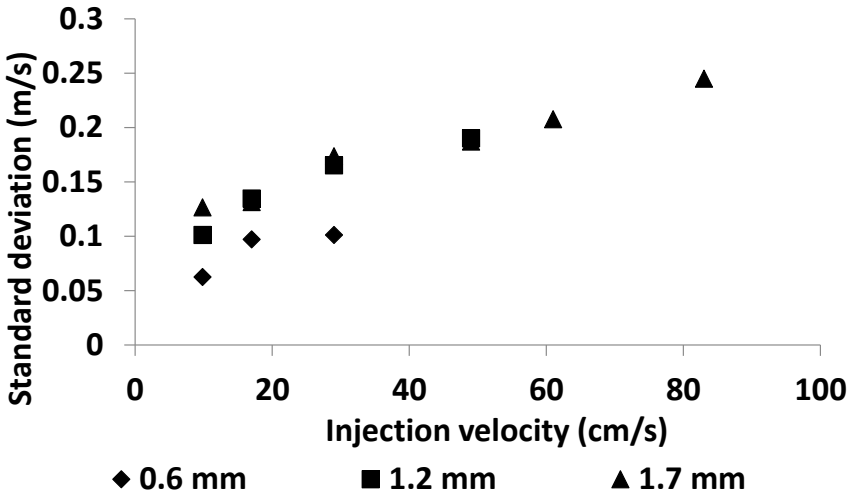

Figure 2.7 - A) Evolution of bubbles mean velocity with gas injection velocity B) Evolution of the standard deviation of the bubble velocity distribution with gas injection velocity. Measurements for several injector with internal diameters ranging from 0.6 mm to 1.7mm, measurements at an elevation of 0.16m from the injector.

A

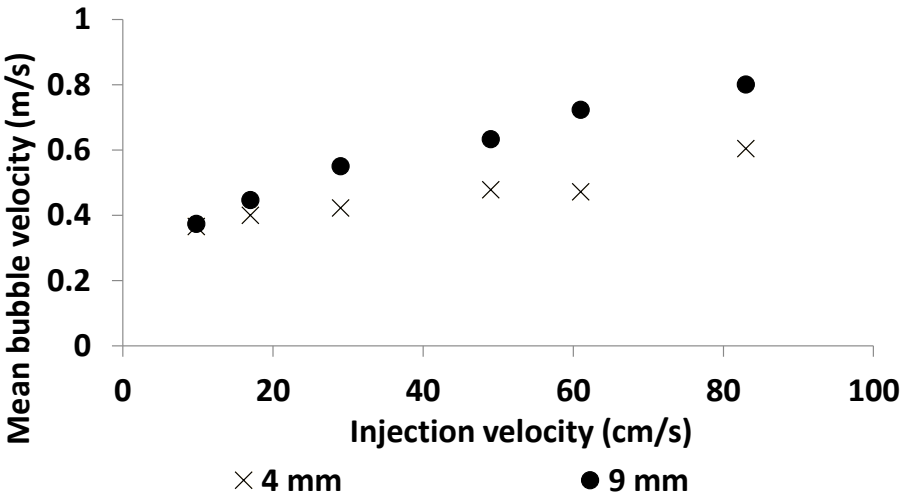

B

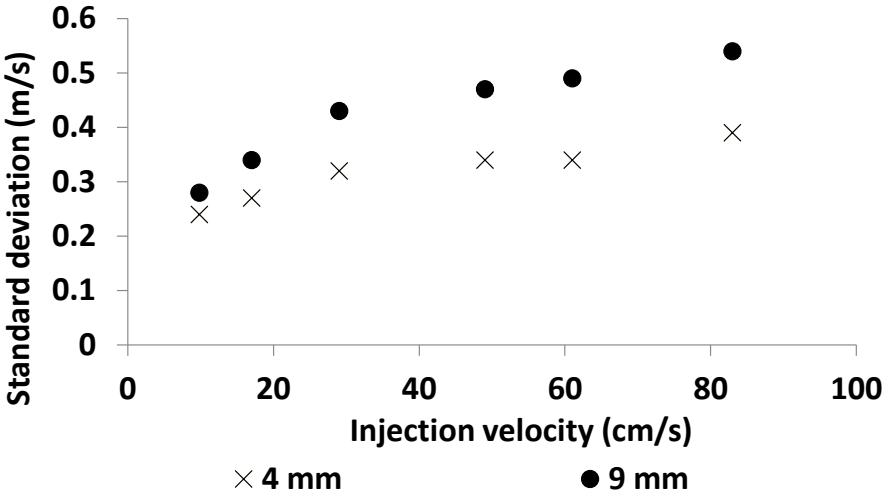

Figure 2.8 – A) Evolution of bubbles mean velocity with gas injection velocity B) Evolution of the standard deviation of the bubble velocity distribution with the gas injection velocity. Measurements for injectors with internal diameter of 4 mm and 9 mm. Measurements take at an elevation of 0.16 m and 0.5 m from the injector, for the 4 mm and 9 mm diameter injectors, respectively.

For a given injection velocity, the results show similar mean bubble velocities for the 0.6 mm and 1.2 mm diameter injector, and lower ones but still comparable for the 1.7 mm diameter injector. The three injectors show a slight increase of the mean bubble velocity with the injection velocity, as can be seen in Figure 2.7. However, the 4 mm and 9 mm inside diameter injectors exhibit a very distinct behaviour: for these injectors, it is observed a stronger increase with the injection velocity when compared with the 1.7 mm inside diameter injector. In addition, the bubble velocity neatly increases with the injector inside diameter. Furthermore, the mean bubble velocities are much higher (from 0.4 to

0.8 m/s) than the terminal velocities (≈0.2-0.3m/s) for this type of bubbles (Clift et al., 1978). Taking everything into consideration, it is clear that, in the experiments with the 4 mm and 9 mm i.d. injectors, the bubbles were entrained by the liquid recirculation so that the detected characteristic sizes are not due to the injection dynamics alone.

Impact of injector l/i.d. ratio on bubble size distribution

The pressure drop in each hole can work as a buffer to avoid the effects on injection velocity caused by pressure fluctuations in the gas circuit before the column, or those due to bubble formation. Moreover, it is important to ensure a sufficient pressure drop through the gas distributor to guarantee that all the injectors will be working, even at low gas velocities. The length of the injector (l) has a direct impact on the pressure drop, and this is the reason why the l/i.d. ratio was also studied. The 1.7 mm diameter injector was studied for l/i.d. ratio of 15, 10 and 5. The 4 mm injector was tested for l/i.d. ratio of 10, 5 and 2. Finally, the 9 mm injector was studied with l/i.d. ratio of 10 and 2. For these different l/i.d. ratios, the mean bubble chords are shown in Figure 2.9.

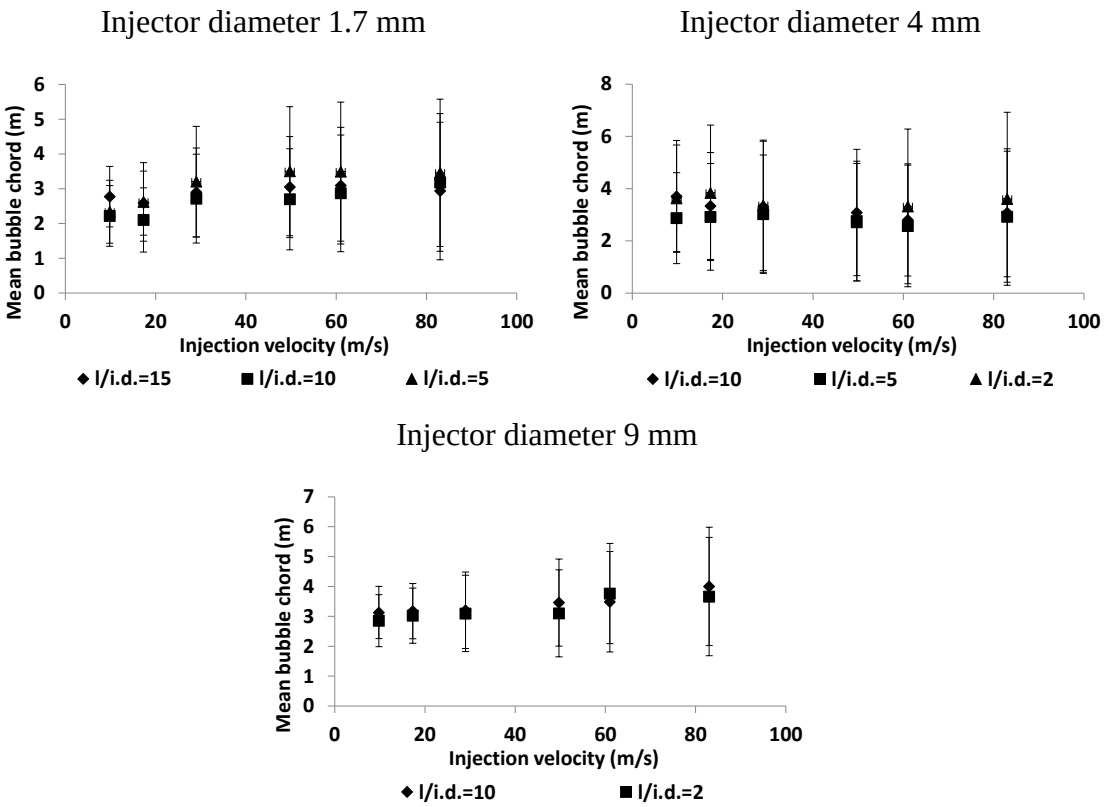

Figure 2.9 - Mean bubble chord for 1.7 mm, 4 mm and 9 mm injectors for several l/i.d. ratios in function of the injection velocity. Measurements at an elevation of 0.16 m for the 1.7 mm and 4 mm injectors and 0.5 m for the 9 mm injector (Vertical bars represent the standard deviation of each bubble chord distribution).

The presented data suggests that the l/i.d. ratio has no significant impact on mean bubble chord (typical deviations are at most about 1mm), and that for each injection velocity all the mean chords are inside the standard deviation (vertical bars) intervals. Figure 2.10 presents the PDF of the bubble chord distributions for all the tested injectors at velocities injections of 30 m/s and 80 m/s.

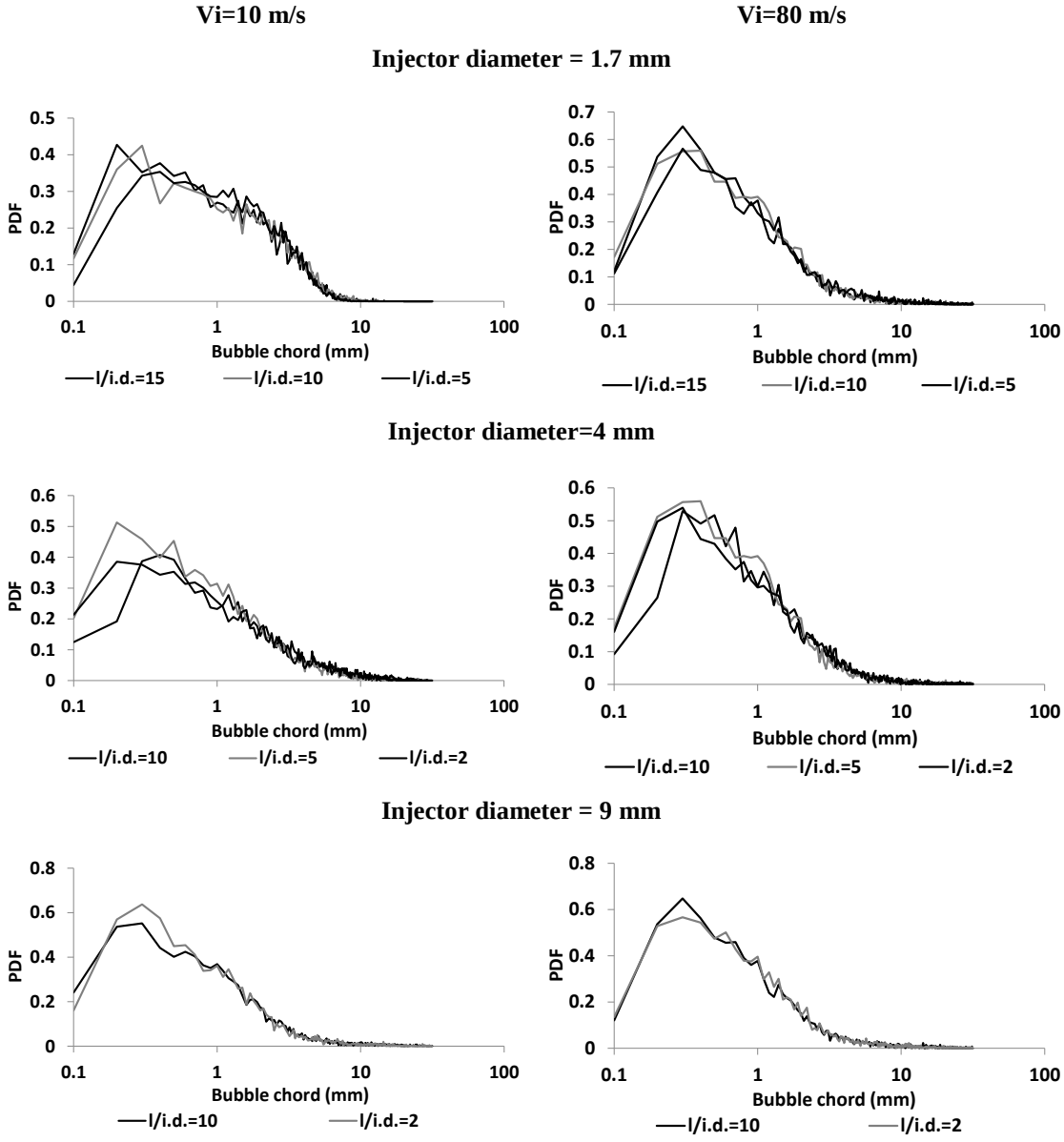

Figure 2.10 - Bubble chords probability density of bubble chords for 1.7 mm, 4 mm and 9 mm injectors for several l/d ratios.Measurements at an elevation of 0.16 m for the 1.7 mm and 4 mm injectors and 0.5 m for the 9 mm injector

The PDF of the 1.7 mm inside diameter injector, visible on Figure 2.10, demonstrates that the injectors with the l/i.d. ratio of 15 and 10 have very similar bubble chord distributions for both injection velocities. The injector with the smallest l/i.d. ratio, namely 5, exhibits lower probabilities of detecting small chords, but this affects chords below 0.8 mm only. In all cases, the chords larger than 0.8mm exhibit similar probabilities for either injection velocities. Very similar conclusions can be drawn for 4 mm and 9 mm i.d. injectors, despite some peculiarities. In particular, for the 4 mm i.d. injector, the largest l/i.d. ratio corresponds to a lowest probability of detection of smaller chords, but

the pdfs remain unaltered for chords above ≈ 0.8-0.9 mm. Also, the injector of 9 mm i.d. leads to very similar PDFs whatever the l/i.d. ratio and the injection velocities.

Therefore, as previously mentioned, no significant impact of the l/i.d. ratio was found on bubble chord distributions. This could mean that the velocity profile is already established inside the injectors, even for the smallest tested l/d ratios.

Impact of the height of measurement on bubble size distribution

In order to study the impact of the height of the measurement on the detected bubble size distribution, the optical probe was located at higher distances from the injector (h) and measurements were repeated. These experiments were performed to verify whether the previous results have been collected outside the gas jet region. So doing, the presence of coalescence can also be tested by checking if bubbles larger than those detected near the injector are seen or not further downstream.

As in the previous experiments the probe was located in the column centre. When using the 1.7 mm and 4 mm injectors, the probe was placed at 0.40 m above from the injector. In the case of the 9 mm injector the probe was placed at 0.75 m above from the injector. Figure 2.11 presents the variation of the mean chord with the distance from the injector for two injection velocities (61 m/s and 83 m/s)).

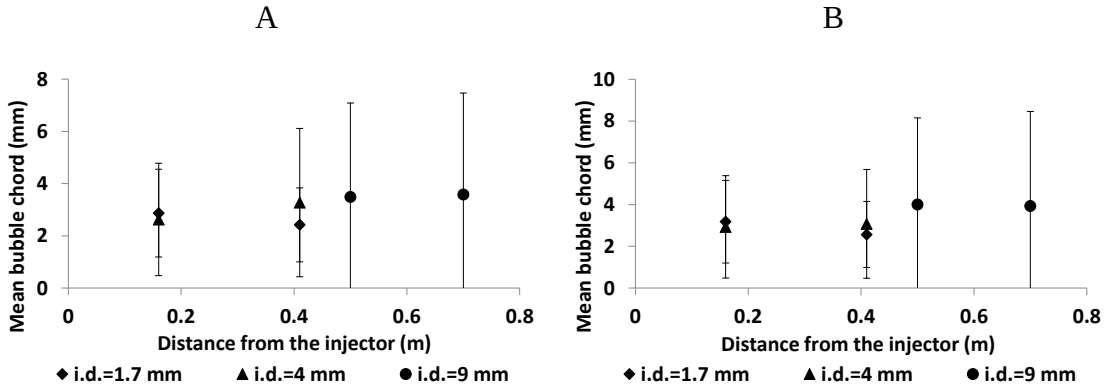

Figure 2.11 – Evolution of the mean bubble chord with the distance from the injector for an l/d=10: A) injection velocity of 61 m/s; B) injection velocity of 0.83 m/s. (vertical bars represent the standard deviation of the bubble chord distribution)

The results show that, for a given injection velocity, the mean chord differences are quite small (less than 0.5 mm). The PDFs of bubble chords corresponding to these measurements are presented in Figure 2.12.

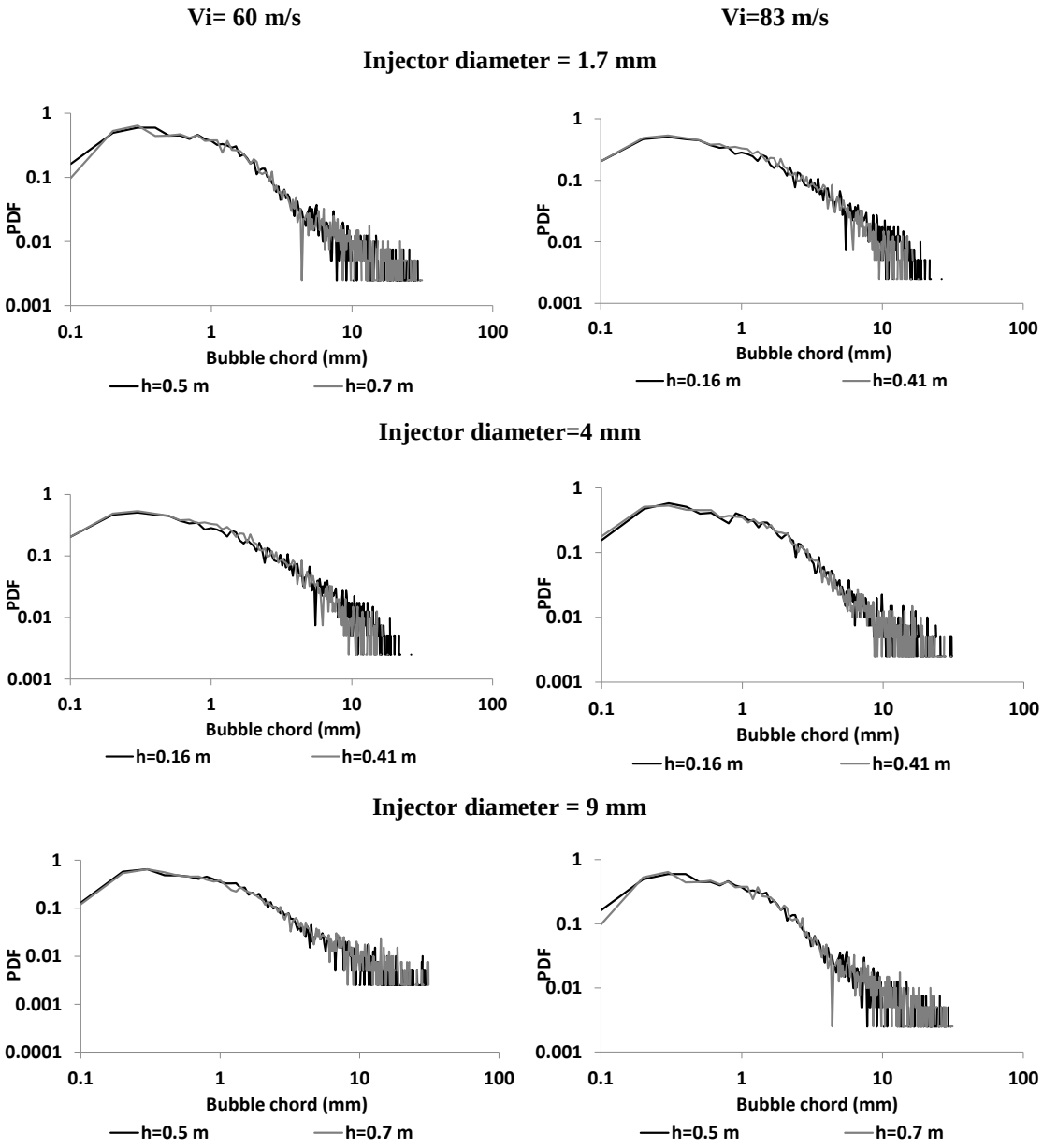

Figure 2.12- Bubble chords probability density functions for l/d ratio of 10.

Figure 2.12 shows that all the PDFs from the three injectors on the two injection velocities considered are overlapping. So, based on these results and on the results of Figure 2.11, is possible to affirm that the distance to the injector has no significant influence on the bubble chord distribution. Consequently, this demonstrates that all the measurements presented in the previous sections were indeed performed outside the gas jet, that is in a zone where the break-up processes related with injection are terminated. Moreover, there is no indication of the presence of coalescence in these flows, since the larger bubbles have the same size at both distances.

In order to further confirm that the measurements were made out of the exit jet, one can analyse the arithmetic average bubble velocity at both distances from the injectors, as presented in Figure 2.13 A and B.

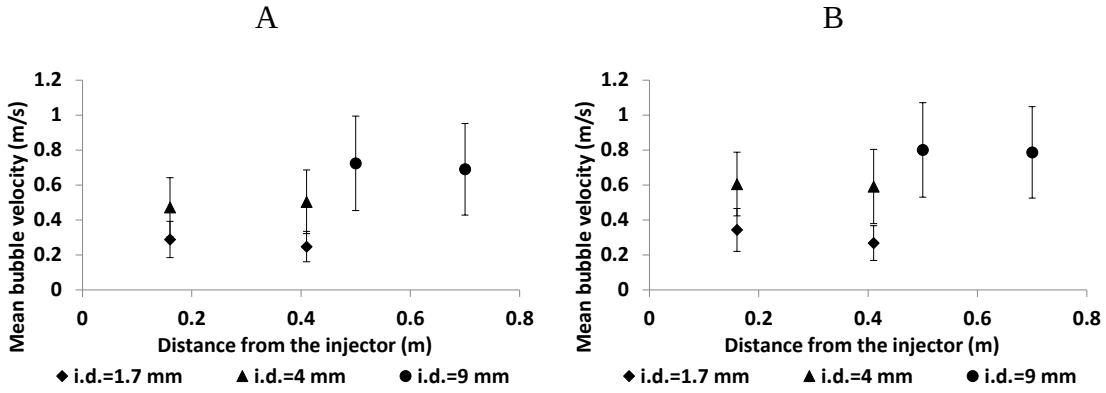

Figure 2.13 - Evolution of mean bubble velocity with the distance from the injector: A) injection velocity of 60 m/s B) injection velocity of 83 m/s (vertical bars represent the standard deviation of the bubble velocity distribution, injectors with a l/i.d. ratio of 10)

Figure 2.13 A and B show that the average bubble velocity was indeed stable along the column axis, for both injection velocities. These results bring further evidence that all measurements were made outside the gas jet region, validating thus the experiments.

Injector designs: ideal solution and practical choices

In the perspective of an injector design able to produce similar bubble size distributions over a wide range of superficial velocities, the above analysis leads to the following conclusions:

- The l/i.d. ratio was studied and the results prove that there is no significant impact on the bubble size distribution in the range of injection velocities considered.
- no evidence was found of the existence of coalescence at injection in the conducted experiments.
- for “large” injectors and “small” injectors above 20-30m/s injection velocity, the mean bubble chord is weakly affected by the gas injection velocity.

- Standard deviations increase with injection velocity. Yet, they are significantly stronger for “large” injectors than for “small” injectors.

Owing to these trends, selecting “small” injectors appeared as the best solution to ensure similar mean bubble sizes over a large range of injection velocity together with a restricted extent of their size distribution. In that view, the chosen configuration was 1 mm internal diameter injectors. The ratio internal diameter/length was set to 10, large values of this ratio being favorable for damping any pressure fluctuations. The number of injectors must then be chosen with the aim of achieving the desired flow rate with an injection velocity at the injector within the tested range. In addition, the spacing between injectors should be large enough to avoid (or limit) the interactions between the existing gas jets and thus to avoid coalescence at injection. Moreover, the spatial arrangement should ensure a homogeneous injection over all the column section and to avert the generation of instabilities in the injection’s vicinity.

These ideal objectives should then be matched with practical constraints. Here below we detail the choices made for the injectors of the four columns.

A perforated plate was the chosen configuration of gas distributor, since it was suitable for the several columns used in the study. In addition, it ensures (at least in principle) an homogeneous injection over the column section since it allows an even distribution of injectors over the whole cross-section. The 0.15 m and 0.4 m diameter columns (Phi 150 and Phi 400) have perforates plates 10 mm thicknen with 55 and 391 injectors of 1 mm diameter, respectively. The plate porosity on both gas distributors is 0.2 %. Low plate porosity is important to ensure enough pressure drop to allow that all orifices are injecting gas even at lower superficial gas velocities. For the 1 m diameter column (Phi 1000), we selected a perforated plate with 613 injectors with a 2 mm diameter, instead of 1 mm diameter injectors, due to technical manufacturing difficulties. However, the plate porosity was kept constant (0.2%) in order to ensure the same injection velocity by orifice than the other gas distributors (at iso-v_{sg}). The difference on the injectors inner diameter, of 1 mm to 2 mm, is expected to have no influence on the bubble size population in the columns. Since the 1.2 mm and 1.7 mm injectors presented similar bubbles populations (c.f. Figure 2.4 A). Nevertheless, the homogeneity of the bubble size in all the columns will be further verified in the section 2.3.

Another parameter considered in the gas distributor design was the injectors pitch. The use of a sufficiently large pitch was important in order to avoid the bubble coalescence at the injection/bubble formation. However, a pitch exceedingly large can

induce heterogeneities and instabilities on the flow, contrary to the objective of having a homogeneous injection on the column section. Moreover, a large pitch will limit the number of injectors on the column surface. Therefore, the chosen pitch was a compromise between the number of injectors, the column cross-section and the bubble size, knowing that ideally the pitch should be at least the size of a bubble. The injectors were arranged in a triangular pitch of 15 mm for the 0.15m and 0.4 m diameter column, and of 38 mm for the 1 m diameter column.

For the 3 m diameter column (Phi 3000), the gas distributor has not been changed because of the cost and of the technical difficulties involved. The existing one is a sparger comprising 164 injectors with 9 mm i.d. orifices, arranged in a 200 mm pitch.

Let us now discuss the expected bubble sizes. Recurring to a method that will be presented in chapter 3, the information gathered on the average bubble chord C_{10} is transformed into a Sauter mean diameter along the vertical $\left(Dv_{32} = \frac{\sum_0^n Dv_i^3}{\sum_0^n Dv_i{}^2}\right)$ using $C_{10} = \frac{2}{3} Dv_{32}$. This transformation is based on the assumptions that the bubbles have rectilinear motion and that all the bubbles have the same shape, later being either spheres or ellipsoids with the same eccentricity. Thus the expected Dv_{32} was estimated for the lowest and highest gas injection velocities considered in the single jet experiments. The resulting superficial gas velocity was calculated taking into consideration the gas distributor configuration (size and number of injectors) for each column. Indeed, for a given gas injection velocity and a number of injectors, the gas flow rate injected in the column is evaluated, and it is transformed into a superficial gas velocity by diving the flow rate by the column cross-section. For the columns Phi 150, Phi 400 and Phi 1000, the Dv_{32} was estimated from the mean chord detected for the 1.7 mm i.d. single injector. This estimation was made under the assumption that a 1 mm and 2 mm i.d injectors produce the same bubble populations, an assumption supported by the quite similar results obtain for the 1.2 mm and 1.7 mm i.d. single injectors, as presented above. The estimation of the bubble Dv_{32} for the Phi 3000 column was made from the results obtained for the 9 mm i.d. single injector The estimation of the bubble size in each column, which are presented in Table 2.6: in terms of v_{sg} the table covers nearly the whole range of conditions that will be considered in our experiments.

Table 2.6 – Prediction of expected the Dv_{32} of the bubble population at injection and for all the columns.

		Phi 150	Phi 400	Phi 1000	Phi 3000
	Injectors i.d. (mm)	1	1	2	9
Injection velocity (m/s)	**Number of injectors**	55	391	613	164
9.8 m/s	**Superficial gas velocity (cm/s)**	2			1.5
	Dv_{32} (mm)	2.8			4.9
83 m/s	**Superficial gas velocity (cm/s)**	20			12
	Dv_{32} (mm)	4.9			6.3

The two configurations of gas distributors installed on the Phi 150, 400 and 1000 columns are expected to generate equivalent bubble populations, with a vertical Sauter mean diameter evolving with the superficial gas velocity from 2.8 to 4.9 mm. In the Phi 3000 column, larger size of bubbles are expected, the latter evolving from 4.9 to 6.63 mm: at a given superficial gas velocity, these sizes are somewhat larger than those expected on three other columns. This trend is especially neat at very low superficial gas velocities.

2.2 Experimental set-up

In the present work four different columns with 0.15 m, 0.4 m and 1 m and 3m inner diameters were tested. The diameter tolerance on the columns is ±0.5 mm, ±0.8 mm, ±1.2mm, ±2 mm for the 0.15 m, 0.4 m and 1 m and 3m diameter columns, respectively. Moreover, the verticality of all the columns was verified a bubble level.

All the experiments were conducted with compressed air, which had been dried and cooled, as the gas phase and with water, with no net liquid flow rate, as the liquid phase. In the 0.15 m, 0.4 m and 1 m diameter columns the water came from the public system. However, due to its volume (45 m^3), in the 3 m diameter column was used untreated water coming from a water well. This water source was not analyzed, so there is no information about the possible contaminants on the water. In addition, the 0.15 m, 0.4 m and 1 m diameter columns were operated with a liquid static height/column

diameter ratio of 4. On the other hand, the 3 m diameter column has operated with 2.2 liquid static height/diameter ratio because the column is only 12 m height.

0.15 m diameter column (Phi 150)

The smaller bubble column used in this study was 0.15 m in diameter and 1 m high (Figure 2.14 A), in which it is easy to change the air distributor. For the experiments where a single orifice injector was used, it was always placed in the centre of the column bottom (c.f. Figure 2.1). In the remainder experiments, a perforated plate was used as a gas distributor. The perforated plate was 10 mm thick and has 55 holes of 1 mm inner diameter, spaced in a 15 mm triangular pitch, yielding a porosity of 0.24%. The air enters in the column by way of a 2 litres gas chamber located under the perforated plate. The air flow is controlled by two Brooks mass flow controllers in the range from 0 to 1 Nm^3/h and 0 to 60Nm^3/h with a flow rate resolution of 0.01 Nm^3/h and 0.1 Nm^3/h. The superficial gas velocity was measured with an uncertainty of ±5%.

.

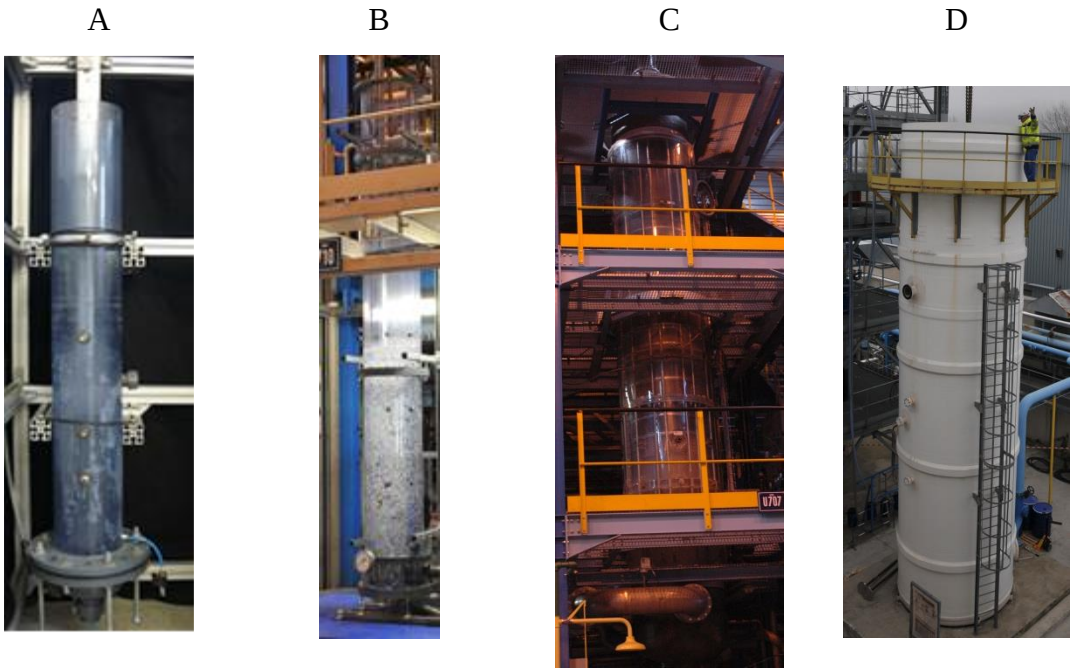

Figure 2.14 – A) 0.15 m diameter column; B) 0.4m diameter column; C) 1 m diameter column; D) 3m diameter column

0.4 m diameter column (Phi 400)

The second bubble column studied in this work had 0.4 m inner diameter and was 3.25 m high, as can be seen in Figure 2.14 B. Also constructed in Plexiglas, this column is equipped with a perforated plate with 391 holes of 1 mm diameter, arranged in a 15 mm triangular pitch, yielding a plate porosity of 0.2%.The perforated plate has 10 mm thickness and it is located on top of a 25 liters air chamber. The air flow is controlled by three Brooks mass flow controllers in a range from 0 to 60 Nm^3/h with a resolution of 0.1 Nm^3/h. The superficial gas velocity was measured with an uncertainty of ±7%.

1m diameter column (Phi 1000)

The third column had 1 m inner diameter and was 5.7 m high, as depicted in Figure 2.14 C. The gas distributor was a perforated plate made of stainless steel, contrarily to the gas distributors used in the Phi 150 and 400 columns that were constructed in PMMA. As a consequence, it was technically challenging to perforate 1 mm holes, so the solution was to use 2 mm diameter holes. However, the distributor was 20 mm thick, which kept the same l/d ratio of the injectors, and also 0.2% of porosity. The final design consists in 613 holes of 2 mm in diameter, arranged in a 38 mm triangular pitch. The air flow was controlled by four rotameters with capacities of 60 Nm^3/h, 300 Nm^3/h and two of 600 Nm^3/h, and a resolution of 5 Nm^3/h, 20 Nm^3/h and 50 Nm^3/h, respectively. The superficial gas velocity was measured with an uncertainty of ±12%. In addition, the air entered into the column through a 780 liters air chamber, located under the gas distributor.

3m diameter column (Phi 3000)

The largest column studied in this work had 3 m in diameter and 12 m height. It was not possible to change the gas distributor on this column. The one available for this column was a tubular sparger with 164holes of 9 mm i.d. and 5 mm thick arranged in a 200 mm square pitch, yielding a porosity of 0.15%. The air flow is controlled by mass flow controllers in a range from 0 to 10200 Nm^3/h which uncertainty was measured recurring to a standard flow meter to be of ±10%. Moreover, due to technical difficulties this column was only operated in the superficial gas velocity range between 5 cm/s and 15 cm/s.

The main design parameters of four injectors are listed in the following table.

Table 2.7- Injectors design parameters for all the columns.

Column	h/D column	h_{water}/D	Injector	N° of injectors	Pitch (mm)	Porosity (%)	Injection velocity range (m/s)	Superficial gas velocity (cm/s)	Thickness (mm)
Phi 150	6	4	1	55	15 (triangular)	0.2	13-140	3-35 ±5%	10
Phi 400	8	4	1	391	15(triangular)	0.2	13-140	3-35 ±7%.	10
Phi 1000	6	4	2	613	38(triangular)	0.2	13-140	3-35 ±5%.	20
Phi 3000	4	2.2	9	164	200(squared)	0.15	37-103	5-15 ±10%	5

2.3 Injection conditions in the various columns

Characterization of bubble size

After designing the gas distributors it was necessary to verify if the bubble size was stable for all the superficial gas velocities and for all the columns, and if the bubble injection rate was constant over the columns cross-sections. In addition, the bubble size measured in the columns were also compared to the single injector results, detailed in section 2.1 on a single injector.

To do so the bubble size was measured at an elevation 16 cm above the perforated plates, in the three columns (Phi 150, Phi 400 and Phi 1000), using the 1C mono-fiber optical probe. Such measurements were not done in the Phi 3000 column, the adaptation of the probe holder being complex and also far too time consuming.

The PDFs of the bubble chords detected in the column center, at vsg of 3 cm/s, 16 cm/s and 25 cm/s are presented in Figure 2.15 A, B and C, respectively.

A

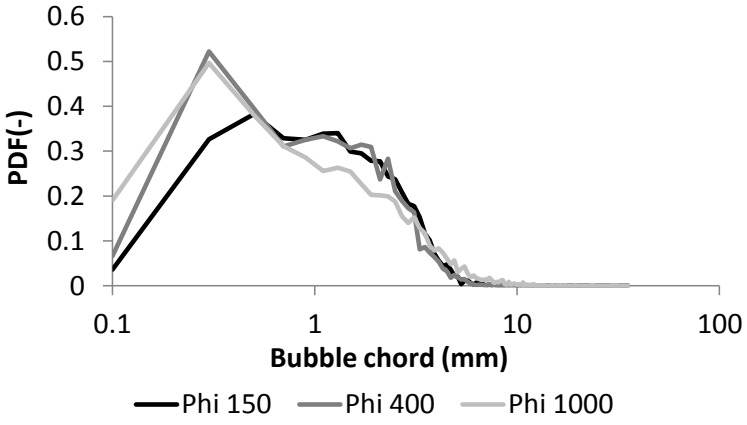

B

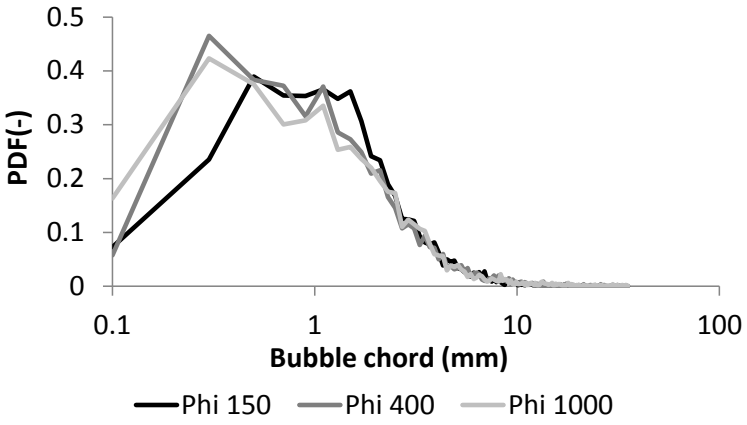

C

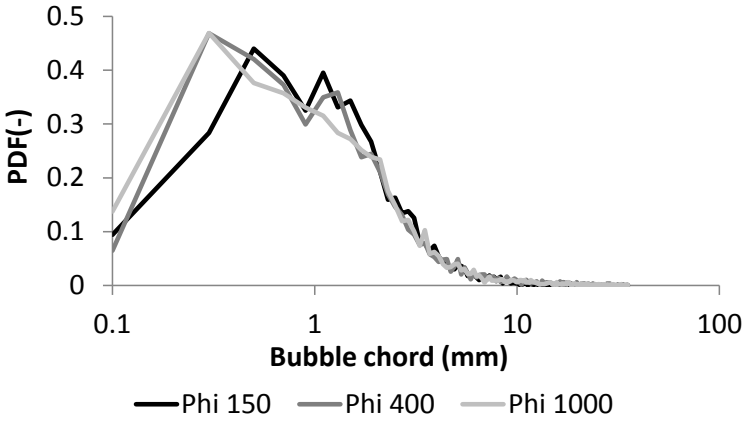

Figure 2.15 – Bubble chords PDFS in different columns at superficial gas velocities of: A) 3cm/s, B) 16 cm/s, C) 25cm/s. (measurements made at 16 cm from the gas distributor, in the center of the column)

Figure 2.15 A shows that for each of the three superficial gas velocity investigated, namely 3 cm/s, 16 cm/s and 35 cm/s, the chord distributions detected on the axis of the

columns Phi 400 and Phi 1000 are nearly identical or at least very close. The chord distributions detected in the Phi 150 columns happen to be slightly different, with the maxima of the PDFs shifted to higher chords. Yet the difference is slim (the shift is from 0.4 mm to 0.5 mm). Besides, the maximum values of the chords are identical in all the columns.

The same data have been reorganized in Figure 2.16 to illustrate the evolution of cord PDFs with the superficial gas velocity for each column. These distributions are insensitive to v_{sg} in the Phi 1000 column. The same trends holds for the Phi 150 and Phi 400 for superficial gas velocities higher than 10 cm/s. The deviations observed at the lowest v_{sg} correspond to the disappearance of the largest cords (Figure 2.16).

A

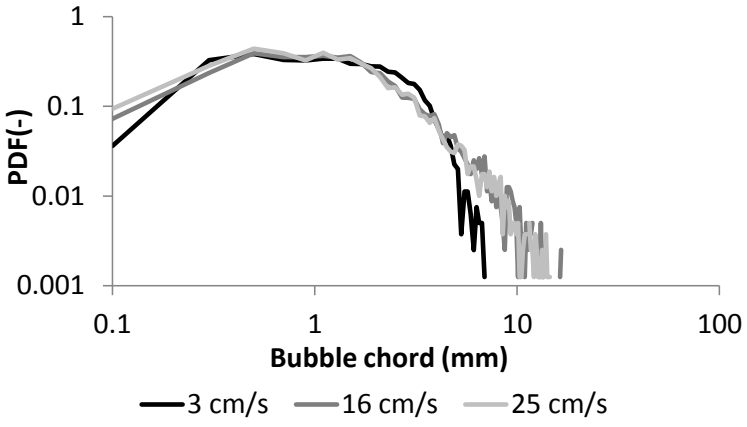

B

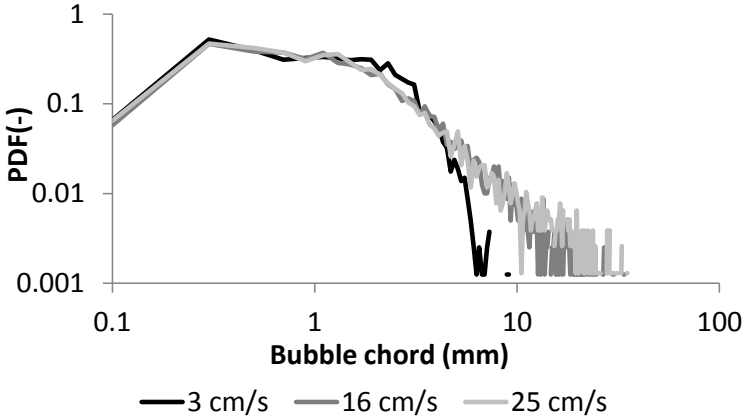

C

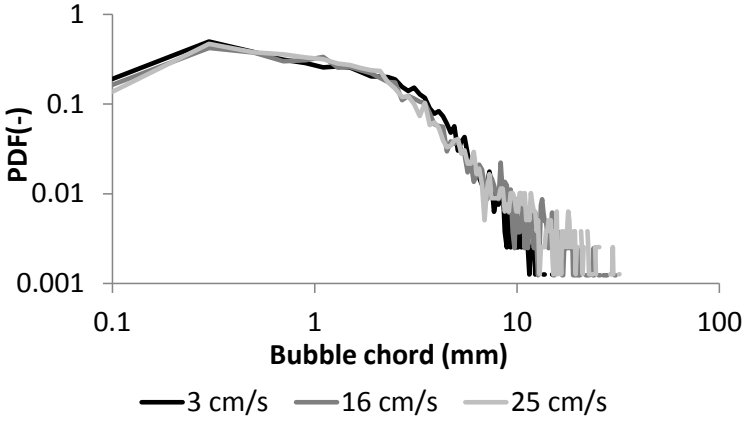

Figure 2.16 - Bubble chords PDFS in different superficial gas velocities in the columns: A) Phi 150, B) Phi 400, C) Phi 1000. (measurements made at 16 cm from the gas distributor, in the center of the column)

Accordingly, the standard deviations, shown in Figure 2.17, are in a range from 4 mm up to 6 mm for superficial gas velocities higher than 10 cm/s, in the Phi 400 an Phi 1000 columns. For all the other conditions, the standard deviations present smaller values, about 2 mm.

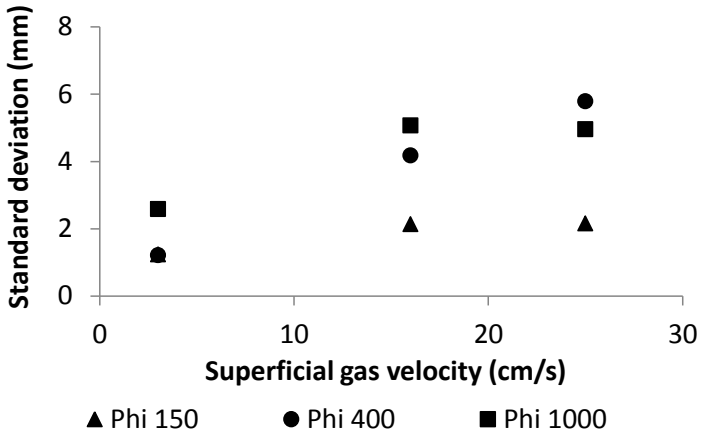

Figure 2.17 – Standard deviations of the bubble chords distributions for several superficial gas velocities and column diameters. (measurements made at 16 cm from the gas distributor, in the center of the column)

To further analyze the bubble size population, the Sauter mean vertical diameter (Dv_{32}) was deduced from the mean detected chord, using the same method as in section 2.1. Measurements were obtained at 3, 16 and 25 cm/s: the radial profiles of the mean vertical diameter are given in Figure 2.18 A, B and C, respectively. The measurements were obtained at a superficial gas velocity of 3 cm/s, 16 cm/s and 25 cm/s: the radial profiles are shown in Figure 2.18 A, B and C, respectively. The measurements were only made up to a dimensionless radial position x/R=0.8 due to the size of the probe support. The vertical bars plotted in Figure 2.18 represent the standard deviation of the bubble chord distributions for each measurement.

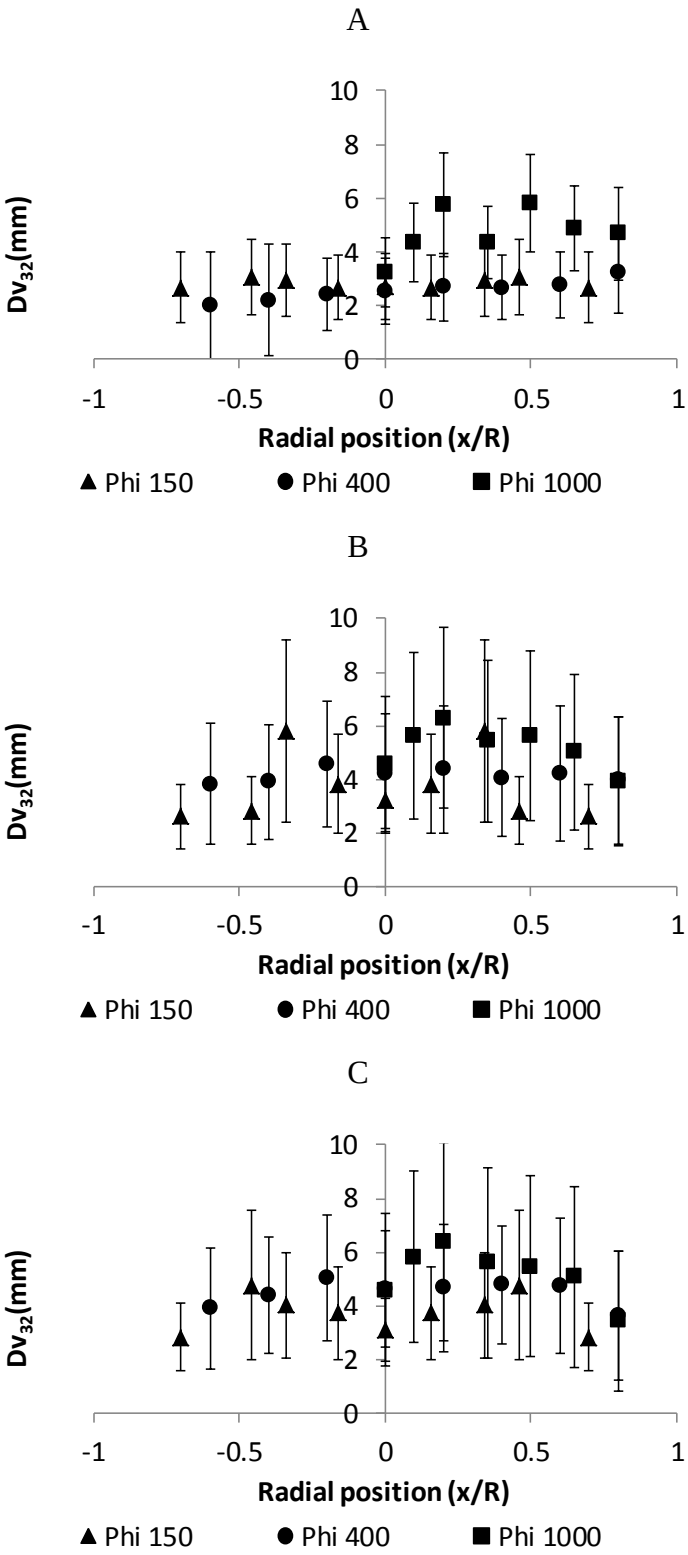

Figure 2.18 – Radial profiles of the Sauter mean vertical diameter in different columns at superficial gas velocities of: A) 3cm/s, B) 16 cm/s, C) 25cm/s. (measurements made at 16 cm above the gas distributor, vertical bars represent the standard deviation of the bubble chord distributions)

By analyzing Figure 2.18 A, it is possible to conclude that at the superficial gas velocity of 3 cm/s the bubble vertical diameter evolve between 3 and 6 mm along the column diameter. Both the Phi 150 and Phi 400 columns presented both a constant $Dv_{32}\approx$ 3 mm along the column diameter. For the Phi 1000, the Dv_{32} varies from 4 mm in the column center, up to 6 mm at x/R=0.4, and, decreases to 5 mm at larger radial distances.

Figure 2.18 B represents the radial profiles of the Dv_{32} at vsg=16 cm/s. It shows that the Phi 150 column has a flat profile around 3 mm. The same holds for the Phi 400 column, but in this case with $Dv_{32}\approx$4 mm. In the Phi 1000 column, and like it has been seen in Figure 2.18 A, the bubble size evolves between 4 mm and 6 mm, along the column radius.

At 25 cm/s (Figure 2.18 C), the Phi 150 and Phi 400 columns present flat profiles around 4 mm and 5 mm, respectively. Again, the Phi 1000 column presents a similar radial evolution of the bubble size, as seen at lower superficial gas velocities, with Dv_{32} ranging from 4 mm up to 6 mm.

Concluding, the Phi 150 and Phi 400 columns present flat radial profiles of bubble size in all the tested conditions, but with an increase on the of Dv_{32} with the superficial gas velocity from 3 mm to 4 mm and from 4 mm to 5 mm, respectively. Let us note that, the final injection configuration presents a weaker bubble size evolution with the superficial gas velocity than the one observed for a single injector (namely 2.8mm – 4.9 mm, see section 2.1). Despite the small variations in the bubble Dv_{32} (typically 1 mm), it is possible to affirm that the goal of having a stable and homogenous bubble size between the columns was obtained for the Phi 150 and Phi 400 columns.

Contrarily to the above mentioned columns, the bubble size evolves along the column radius in the Phi 1000 column, with Dv_{32} ranging from 4 mm up to 6 mm. The profiles are all close to a parabola with a maximum in size at x/R= 0.4. Such a shape may results from the lateral motions due to the recirculating liquid. Indeed, the measurements are performed at h=16 cm, i.e., a low h/D value and more homogeneous conditions may be reached at larger distances from injection: this question will be addressed in chapter 4where the experimental data are analyzed. Note that, as h is fixed, the ratio h/D is not the same for the other columns diameters, and that may explain the flatness of the profiles for the Phi 150 and Phi 400 columns. Also, and compared with a single injector conditions, much larger size are detected in the Phi 1000, possibly due to some coalescence in the vicinity of the injector (that question will be revisited in the chapter 4).

Nevertheless, for the Phi 1000, there is no significant evolution of the bubble size with the superficial gas velocity.

A resume of the estimated Dv_{32} from single injector experiments (c.f. section 2.1) and the measured Dv_{32} in the final gas distributor configurations is presented in Table 2.8

Table 2.8- Estimated and measured Dv_{32} for the Phi 150, Phi 400 an Phi 1000 columns.

					Measured Dv_{32} (mm)	
Vsg (cm/s)	**Column**	**Estimated Dv_{32} (mm)**	**Vsg (cm/s)**	**Column**	**Min detected**	**Max detected**
2	**Phi 150**	2	**3**	**Phi 150**	2.6	3
	Phi 400			**Phi 400**	2.6	3.2
	Phi 1000			**Phi 1000**	3.2	5.8
20	**Phi 150**	4.9	**16**	**Phi 150**	2.6	5.8
				Phi 400	3.8	4.6
	Phi 400			**Phi 1000**	3.9	6.3
	Phi 1000		**25**	**Phi 150**	2.8	4.8
				Phi 400	3.6	5
				Phi 1000	4	6.3

The results show that for a superficial gas velocity of 3 cm/s, the Dv_{32} in the Phi 150 and Phi 400 column ranges between 2.6 mm and 3.2 mm. These result are in a good agreement with the estimated Dv_{32} (≈2 mm) issued from the single injector experiments. Yet, larger bubbles were detected on the Phi 1000 column with Dv_{32} up to 5.8 mm. Yet, superficial gas velocities (16cm/s and 25 cm/s), the bubble size in the three columns becomes quite close with a Dv_{32} ranging between 3 mm and 6 mm. The predicted Dv_{32} for a superficial gas velocity of 20 cm/s was 5 mm, showing the good agreement with single injector experiments.

Concluding, the objective of injecting similar a bubble size in the three columns at all superficial gas velocities was fulfilled in most cases. Indeed, and except of the Phi 150 the Phi 400 columns at the smallest superficial gas velocity (3cm/s), the Sauter mean vertical diameter evolves between 3.4 mm (±0.6mm) and 5.5 mm (+0.8/-0.9 mm) in all the tested conditions and over the column cross-sections. In additions, the width of the size distributions are similar (standard deviation ≈ 5 mm) in the Phi 400 and in the Phi 1000 provided that the superficial gas velocity is higher than 3 cm/s. For all other conditions, the standard deviations are comprised between 1 and 3 mm.

The experimental data are adapted and reported in Figure 2.19 that depicts a map of bubble shape regimes as a function of Eötvos, and Morton numbers. The equivalent diameter, that represents the diameter of a iso-volume sphere, is here computed through the Dv32, assuming a bubble eccentricity of 0.7, which is the mean value in the experimental conditions (c.f. section 3.4). The corresponding Eötvös number (Eq. (1.2)) evolves from 2 (Dv32= 3 mm and De= 3.8 mm) to 7.9 (Dv32= 6 mm and De= 7.6 mm)and for a Morton number (Eq.(1.13)) of 2.63×10^{-11} (air/water system). The grey lines on Figure 2.19 represent the range of the experimental conditions: in all cases the bubbles correspond to wobbling ellipsoidal bubbles. That conclusion will be confirmed in section 3.4, by *in situ* optical measurements.

Besides, the particulate Reynolds (Eq. (1.2)) number can be deduced from this map. It ranges from 1200 to 2500, corresponding to terminal velocities in still fluid comprised between 31 cm/s and 33 cm/s. It should be notice that the contamination is not precisely accounted for here, however it is not expected to have a drastic impact in this regime.

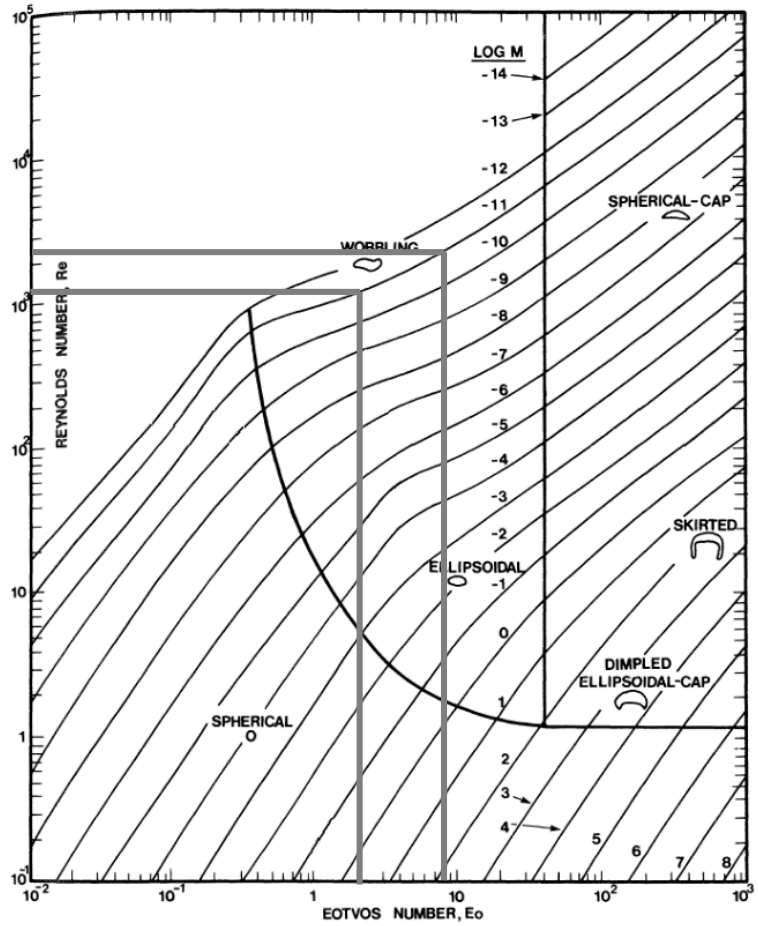

Figure 2.19 – Shape regimes for bubbles in unhindered gravitational motion trough liquids (Clift et al., 1978) (Vertical grey lines represents the range of Eötvös number for this work)

Characterization of the bubble flux

As already, said, aside bubbles sizes, the second objective of the gas distributor design was to obtain a uniform gas injection gas over the entire cross-section of the column. The 1C mono-fibre optical probe can measure the local gas hold-up (εg) and the local gas flux (j_g), as it will be detailed in section 3.3.

Further investigation of the gas distribution in the column can be achieved by the study of the gas hold-up profiles in the vicinity of the injection. Therefore, Figure 2.20 A, B and C presents the gas hold-up profiles obtained by the 1C mono-fibre optical probe in the Phi 150, Phi 400 and Phi 1000 columns, respectively.

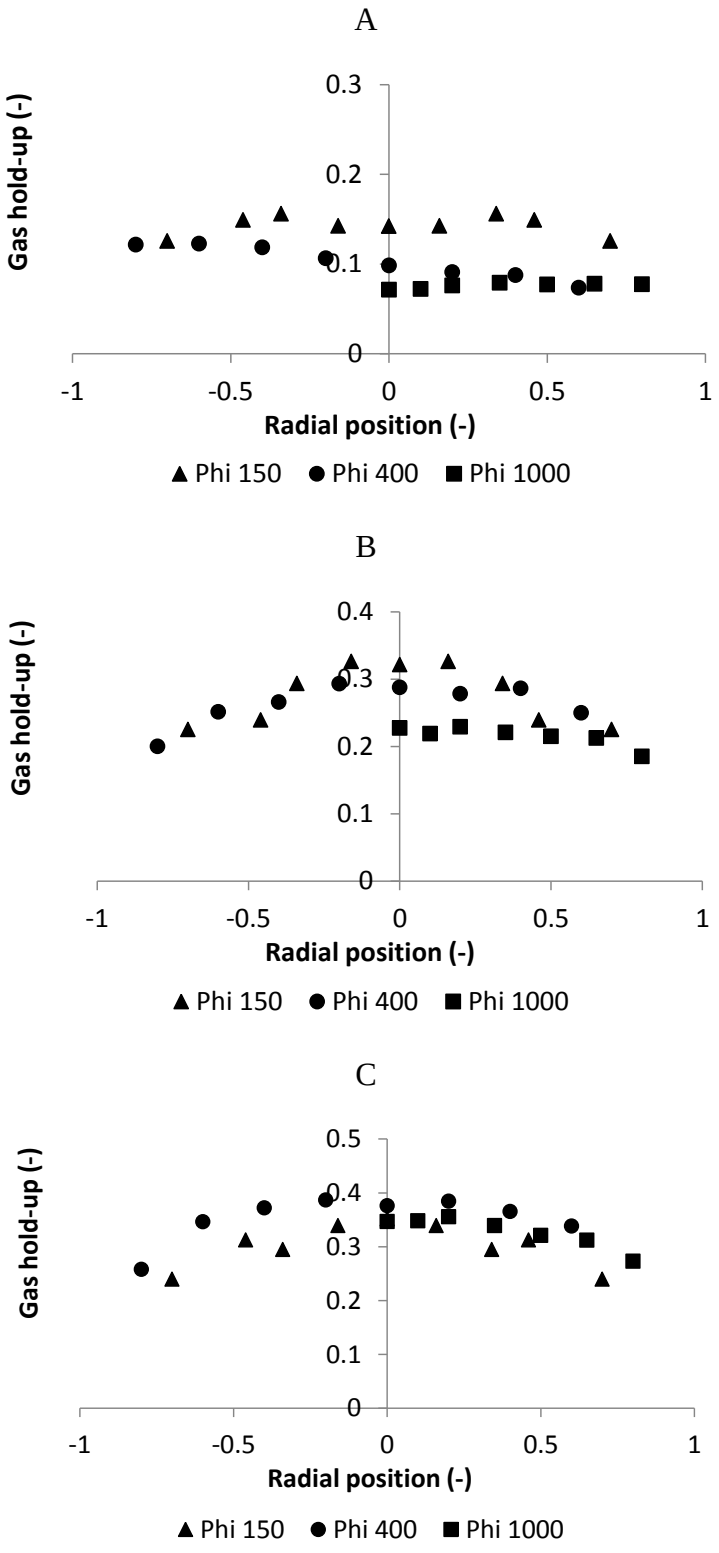

Figure 2.20 – Radial profiles of the gas hold-up in Phi 150, Phi 400 and Phi 1000 columns: A) 3 cm/s; B) 16 cm/s; C) 25 cm/s (measurements taken at 16 cm from the gas distributor)

Figure 2.20 A shows that the local gas hold-up radial profiles are neatly flat, suggesting that the bubble concentration is uniformly distributed along the column cross-

section. At higher superficial gas velocities, the local gas hold-up radial profiles become slightly parabolic, especially for the Phi 150 and Phi 400 columns. However, for the profiles for the Phi 1000 column are quite flat, even at superficial gas velocity of 25 cm/s. This phenomenon can be linked with the liquid recirculation in the columns. Indeed, the zone of establishment of the liquid flow roughly corresponds to h/D≈1 (elevation on the column/column diameter ratio), as presented in chapter 1. Since the distance from the injector is fixed to 16 cm (to ensure that the measurements are made outside of the coherent region of the gas jets), the ratio h/D is decrease from small to large columns. In that view, it is probable that the measurements performed in the smaller columns were made far enough from the injector, to perceive the entrainement by the liquid recirculation, and thus the start of the formation of a parabolic-type void fraction profile. In the Phi 1000 column the measurements were made at h/D=0.16, i.e. in a zone where the entrainment is not yet efficient, leading thus to flat profiles. The axial evolution of the gas hold-up profiles will be analysed in the chapter 4. Whatever the reasons of these differences, it happens that, at iso-vsg, similar local gas hold-up values were measured in the three columns in the tested conditions. So, it is possible to conclude that, the objective of ensuring an even gas concentration distribution over the various columns cross-section and in the whole considered range of superficial gas velocity was reached.

A better check would consist in considering the gas flux instead of the gas hold-up profile. As referred in the beginning of this section, the 1C mono-fibre optical probe can also measure the local gas flux. However, it should be notice that these measurements were performed in the bottom of the column, a zone where the liquid flow reversal takes place. Consequently, strong transversal liquid and gas velocities are to be expected, that represent very challenging conditions to perform velocity measurements with the 1C mono-fibre optical probe. Indeed, the velocity measurements using conical optical probes are reliable for angles between the probe axis and the bubble trajectory typically comprised between ±30° (Cartellier and Barrau, 1998 A). Additionally, significant errors on the gas flux estimation on the cross-section of the column were found at higher elevations in the column (c.f. section 3.5) even though the mean flow orientation is more favourable for a correct probe functioning. For all these reasons, the flux measurements performed in the three columns and at an elevation of 16 cm above the gas distributor should be considered with care. The radial profiles of the local volumetric gas fluxes are presented in Figure 2.21 A,B and C, for superficial gas velocities of 3 cm/s, 16 cm/s and 25 cm/s respectively.

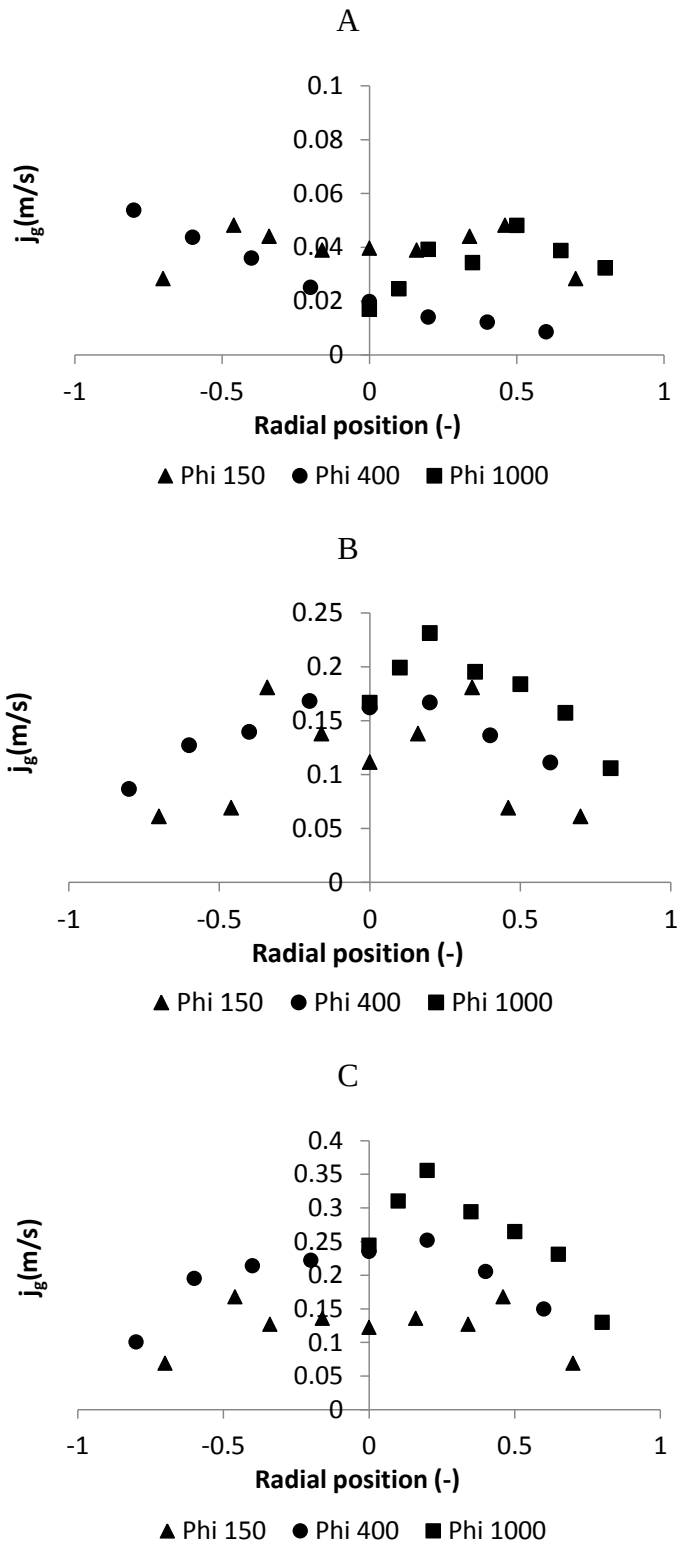

Figure 2.21 – Radial profiles of the local gas volumetric flux sense in the Phi 150, Phi 400 and Phi 1000 columns: A) 3 cm/s; B) 16 cm/s; C) 25 cm/s (measurements taken at 16 cm from the gas distributor)

Figure 2.21 A shows that at 3 cm/s the local gas flux (j_g) is constant at around 0.04 m/s in the Phi 150 and Phi 1000 columns. However, in the Phi 400 column there is a misdistribution of gas, since on the left hand size of the image the j_g reaches values up to six times higher than in the right hand side of the image (j_g max= 0.05 m/s; j_g min= 0.008 m/s). One possible cause for this phenomenon may be the radial entrance of the gas flow in the gas chamber. Indeed, that gas entrance corresponds to the left hand size of the Figure 2.21 in the Phi 400 column. There is no such asymmetry the Phi 150 and Phi 1000 columns as the gas flow entrance in the gas chamber is achieved along the symmetry axis.

For a superficial gas velocity of 16 cm/s (Figure 2.21 B), Phi 400 column presents a parabolic profile of j_g with a value 0.16 m/s in the centre of the column and 0.09 m/s at x/R=0.8. The Phi 150 and Phi 1000 columns present a peak around x/R=0.2 (0.18 m/s and 0.23 m/s, respectively) and minimum value at further radial distances (0.06 m/s and 0.16 m/s, respectively). Furthermore, similar trends are found for the 25 cm/s experiments, with higher values of j_g. The Phi 150 and Phi 400 columns present parabolic profiles ranging from 0.12 m/s and 0.16 m/s in the column centre to 0.06 m/s and 0.10 at further radial distances. The Phi 1000 column, as discussed for the other superficial gas velocities, presents a maximum of 0.35 m/s at x/R=0.2 and a minimum of 0.13 m/s at the position x/R=0.8. Two different causes could explain these results: a higher flux of gas is being injected in the column centre rather than near the wall or the bubbles in the centre of the column are already being accelerated by the liquid recirculation. Since j_g increases with the column diameter and with the superficial gas velocity, as observed in the liquid velocity, this fact supports the latter hypothesis. For that reason, the detected characteristics of j_g are not due to the injection dynamics alone but are related with the hydrodynamics in the entire column.

In this chapter, the four experimental set-up have been presented. Attention has been paid to design optimised gas distributors for the Phi 150, 400 and 1000 columns while for technical reasons, the distributor for the Phi 3000 remained unchanged. These new distributors were able to generate relatively homogeneous conditions over the entire columns cross-sections, both in terms of bubble size distribution and of concentration (the homogeneity in terms of gas flux was not properly checked due to the limitations of the measuring techniques). If one sets aside the Phi 150 and Phi 400 columns operated at the lowest superficial gas velocity of 3 cm/s, the vertical mean Sauter diameters Dv_{32} range typically from 3.4 mm (±0.6 mm) and 5.5 (+0.8/-0.9 mm) in all the tested conditions and

over the columns cross-sections. Such bubbles correspond to Eö numbers in the range of 2 to 7.9: they all pertain to the wobbling ellipsoidal regime, with a the terminal velocity in a still fluid between 31 cm/s and 33 cm/s.

3 Measurement techniques

As presented in chapter 1, this study aims to locally measure the bubble velocity and size and the liquid velocity at high gas hold-up. These measurements will be performed in the experimental set-ups presented in chapter 2. In the present chapter the adopted measuring methods and their measuring capabilities will be detailed.

A Pavlov tube method, described in section 3.1, is used to measure the liquid velocity and its fluctuations. An endoscopic flow visualization technique, that will notably be used to validate optical probe measurements, is presented in section3.2. The chosen method to locally measure gas hold-up, bubble velocity and vertical size, namely the 1C mono-fiber optical probe, and its signal treatment are presented in section 3.3. An extension of the optical probe measurement capacities to measure a mean horizontal bubble diameter is described in detail in section 3.4. This new method is based on the spatial cross-correlation between the signals of two optical probes separated by a given distance. A theoretical model to interpret the variation of the cross-correlation value with the distance between probes for several bubble shapes and orientations is also illustrated in section 3.4. Finally, in section 3.5, the 1C mono-fiber optical probe and the cross-correlation are validated in different flow regimes by comparison with other measuring methods.

3.1 Pavlov tube

The Pavlov tube was the chosen method for liquid velocity measurements in the present work, due to its simplicity and its capacity to measure liquid velocity at high gas hold-up (Forret et al., 2003, 2006). The hot film anemometry was also a possibility, which is a method that is able to measure multiples velocity components. However, this method requires frequent recalibrations and its use in high gas hold-up can be very challenging.

Apparatus

The Pavlov tube used in this work is composed by four 5 mm diameter tubes, arranged as it is shown in the right-hand side of Figure 3.1. The four tubes are placed inside a 30 mm diameter tube, that crosses horizontally the column, in order to obtain rigidity and to allow horizontal displacement. The 5 mm diameter tubes are completely

closed, except for a 0.5 mm diameter lateral hole that assure that the pressure inside the tube is equal to the one in the column.

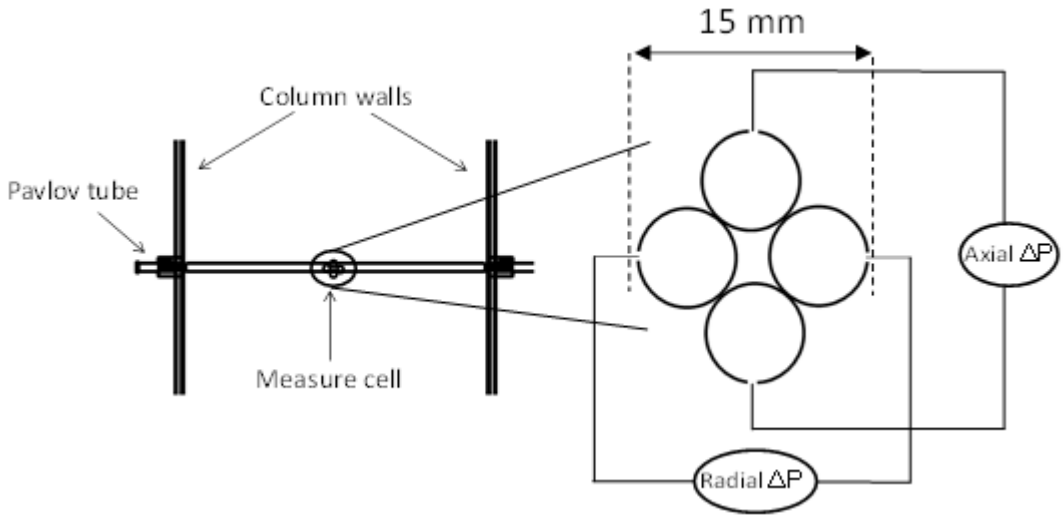

Figure 3.1 – Schematic representation of the Pavlov tube. (Axial measurements are performed along a vertical axis, radial measurements are performed along a horizontal axis)

The holes of the tubes on the vertical plan are placed in the same axis but in opposite directions, as can be seen in Figure 3.1. Additionally, each of the tubes on the vertical direction is connected to one of the chambers of a differential pressure sensor. These tubes serve to measure the axial pressure difference, since the holes on the tubes are aligned with the column vertical axis.

Similarly, the holes of the tubes on the horizontal plan are also aligned in the same axis but in opposite directions, as can be seen in Figure 3.1. Moreover, these tubes are also connected to a chamber of a second differential pressure sensor. The horizontally aligned tubes will measure the radial pressure difference, since the holes on the tubes will be aligned with the column radial axis. The four tubes are filled with water in order to assure quasi instantaneous response time.

The simultaneous measurements of the radial and axial pressure differences (ΔP) can be used to calculate the radial (v_l) and axial (u_l) liquid velocity recurring to the following equation.

$$vl(t) = \begin{cases} \sqrt{\frac{2\Delta P(t)}{\rho_l}} \; if \; \Delta P(t) \geq 0 \\ -\sqrt{\frac{-2\Delta P(t)}{\rho_l}} \; if \; \Delta P(t) < 0 \end{cases} \quad (3.\ 1)$$

Two different sets of pressure sensors were used, in the first configuration were used two Rosemount 3051T differential pressure transmitters that have a frequency of 8 Hz. The axial ΔP measurement was made with a differential pressure transmitter with a range of ±60 mbar and resolution of 0.01 mbar. The radial ΔP measurement was made with pressure transducer with a range of ± 7 mbar with a resolution of 0.001 mbar. Note that each branch was connected to one side of the sensor membrane: so doing these sensors were able to measure positive and negative values of ΔP, namely positive as well as negative velocities.

In order to reach a higher time resolution, the Rosemount pressure sensors were replaced by 100 Hz frequency Keller sensors. However, these sensors can only measure positive values of ΔP, making it necessary to connect each branch of the Pavlov tube to a separate sensor. The other connection of the pressure sensor was left open to the atmosphere, to measure the absolute pressure. The resulting ΔP was calculated during the signal post-treatment. In this configuration each branch dedicated to measure the axial ΔP was connected to a 0 - 500 mbar sensor with a resolution of 2.5 mbar. Likewise, the each of the radial branches was connected to a 0 - 200 mbar sensor with a resolution of 1 mbar. A resume of the characteristics of the four different pressure sensors is presented in Table 3.9.

Table 3.9 – Characteristics of pressure sensors used with the Pavlov tube.

Pressure sensor	Velocity component	Frequency (Hz)	Pressure range (mbar)	Pressure resolution (mbar)	Velocity range (m/s)	Velocity resolution (m/s)
Rosemount 3051T	Axial	8	±60	0.01	±3.5	0.04
	Radial		±7	0.001	±1.2	0.01
Keller Series PD23	Axial	100	0 - 500	0.2	±10	0.2
	Radial		0 - 200	0.08	±6.3	0.12

According to Table 3.9, with the 8 Hz frequency pressure sensors the Pavlov tube can be used to measure liquid velocities higher than 0.04 m/s on the axial direction and 0.01 m/s on the radial direction. When using the 100 Hz sensors, the Pavlov tube is able to measure liquid velocities from 0.2 m/s on the axial direction up to 0.12 m/s on the axial direction.

The second limitation of this method is a consequence of the fact that the Pavlov is a tube that crosses the column. Therefore, the measurements can only be acquired at

heights where it is possible to insert the tube in the column. The radial profiles are easily obtained by moving the measuring cell along the column radius. However, it is necessary to ensure a good alignment between the holes and the desired components of the velocity. Forret (2003) has shown that the velocity measured by the Pavlov tube changes with the angle between the measurement direction and the velocity direction. For angles up to 45°, the measured velocity decreased proportionally with the cosine of angle between the measurement direction and the velocity direction. In order to avoid the misplacement of the holes, the external tube had a mark that allowed to visually verify the verticality of the vertical holes. Since the radial holes are perpendicular to the vertical ones, only one verification is necessary.

Pavlov tube measurements

Before each measurement the differential pressure was registered during 30 s in a stagnant liquid (no gas or liquid throughput). The mean value of the differential pressure obtained during this period is considered as the "zero" of the sensor. Moreover, this procedure is repeated after the measurement in order to detect if any bubble has entered the tube. In case of presence of a bubble in the measurement chain, the differential pressure will not match the one acquired before the measurement. If the initial and final differential pressures diverge of more than 0.1 mbar, the whole measurement chain will be flushed, with water, in order to ensure that the gas bubble is removed and the measurement is repeated. The pressure measurement chain was calibrated in all the detectable range recurring to a dedicated Mensor standard pressure sensor.

In each measurement, both differential pressures are sampled and the instantaneous velocity components (u_l,v_l) are calculated by Eq. (1.15). The experiments were carried out over 300 s to assure ±10% of convergence on the average velocity, as shown in Figure 3.2.

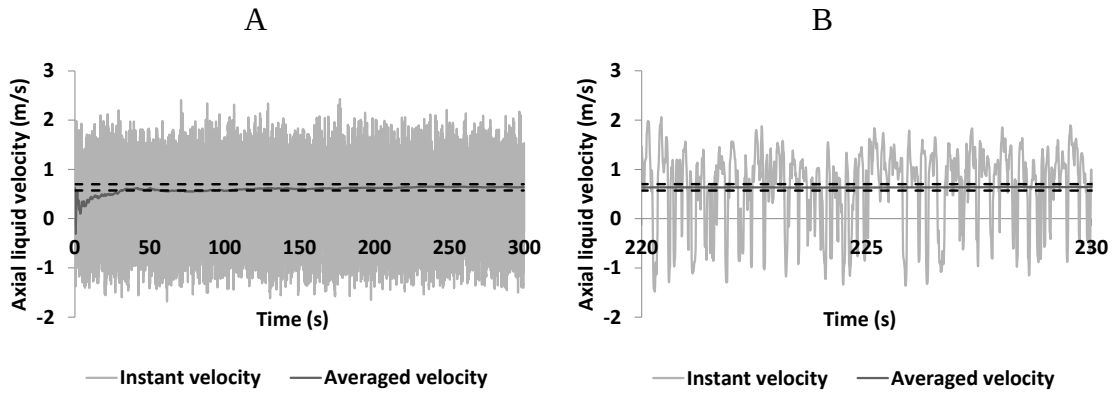

Figure 3.2 –A) An example of a Pavlov tube measurement; B) A zoom of the signal between 200 s and 230 s. (Dashed lines – 10 % convergence of the averaged velocity, acquisition rate: 100 Hz).

The velocity fluctuations (u' and v') can be calculated through the instantaneous and the averaged velocities, using Reynolds decomposition, as presented in the following equation.

$$u(x,t) = \overline{u(x)} + u'(x,t) \qquad (3.\ 2)$$

Where $\overline{u(x)}$ represents the mean liquid velocity, $u'(x,t)$ represents the liquid fluctuation velocity at the instant t and $u(x,t)$ represents the liquid velocity at the instant t. Therefore, using the velocities fluctuations it is possible to calculate the turbulent intensities (u'² and v'²) and the Reynolds stress (u'v'). However, it should be noticed that the pressure measurements were done over 15x15 mm window, as can be seen in Figure 3.1. This distance between the pressure measuring points is not taken into account in Eq. 3.1. Consequently, this method will not be able to measure velocity fluctuations inside structures smaller than the measurement window. Moreover, it is necessary to verify if the pressure range available with each pressure sensor is adapted to the velocity range that is intended to be measured. The 8 Hz frequency pressure sensors were only used in the Phi 150 and Phi 400 column. Since, the liquid velocity and turbulence is expected to increase with the column diameter the available velocity range for 8 Hz frequency sensor will be only compared with the maximum velocities detected on the Phi 400 column. The 100 Hz frequency sensor velocity range will be compared with the maximum velocities detected in the Phi 1000 column. The maximum detected velocities and the velocity range are presented in the next table.

Table 3.10 – Comparison between the available range of velocity and maximal detected velocity for each pressure sensors used with the Pavlov tube.

Pressure sensor	Velocity component	Frequency (Hz)	Velocity range (m/s)	Velocity resolution (m/s)	Maximum detected velocity (m/s)
Rosemount 3051T	**Axial**	**8**	±3.5	0.04	2
	Radial		±1.2	0.01	0.9
Keller Series PD23	**Axial**	**100**	±10	0.2	5
	Radial		±6.3	0.12	2.7

Table 3.10 shows that the maximal detected velocities are inside the available velocity range of all sensors. Therefore, it is possible to conclude that velocity detection it is not limited by the velocity range. Nevertheless, is should be noticed that the resolution on velocity measurement are not the same for all the sensors, as shown in Table 3.9. Under the limits indicated in Table 3.10, the velocity will be considered as zero. The 8 Hz frequency pressure sensors have high velocity resolution, namely 0.01 m/s and 0.001 m/s for the axial and radial velocity components. However, the 100 Hz frequency pressure sensor provides a velocity resolution of 0.2 m/s and 0.12 m/s for the axial and radial components of the velocity, respectively. Therefore, some limitations can be found in the measurement of low liquid velocities.

3.2 Endoscope

For in situ bubble size and shape measurements and also for the validation of the cross-correlation technique (that is presented hereafter), a flow visualisation methodology was required that could be applied in all columns and for all void fractions. An endoscopic technique was chosen because it does not require optical access through the column wall and also because its short working distance allows its usage inside bubbly flows. As a matter of fact, at high concentrations, only the bubbles in the wall region are visible (Mass et al., 2001).

Apparatus

A 0.7 m long and 8 mm diameter Sirius endoscope from the society Foretec was used to obtain images of the flow. These were captured with a high speed video camera Baumer HXC20, with a 2/3" captor, through the acquisition software StreamPix 5. A LED panel was installed in the opposite side of the column to supply the necessary light intensity to capture high speed videos.

In the experiments made in the Phi 150 column, a light source with a power 400 lm was placed outside the column, in front of the endoscope, as shown in Figure 3.3 A. In the Phi 400 and Phi 1000 columns, due to the increase of the column scale, it was necessary to place the light source close to the measurement point. A 50 mm diameter tube was inserted radially in the column, as shown in Figure 3.3 B, to guide the light beam from a 50 mm diameter spot light with a power of 500 lm, placed outside of the column, up to the measuring point.

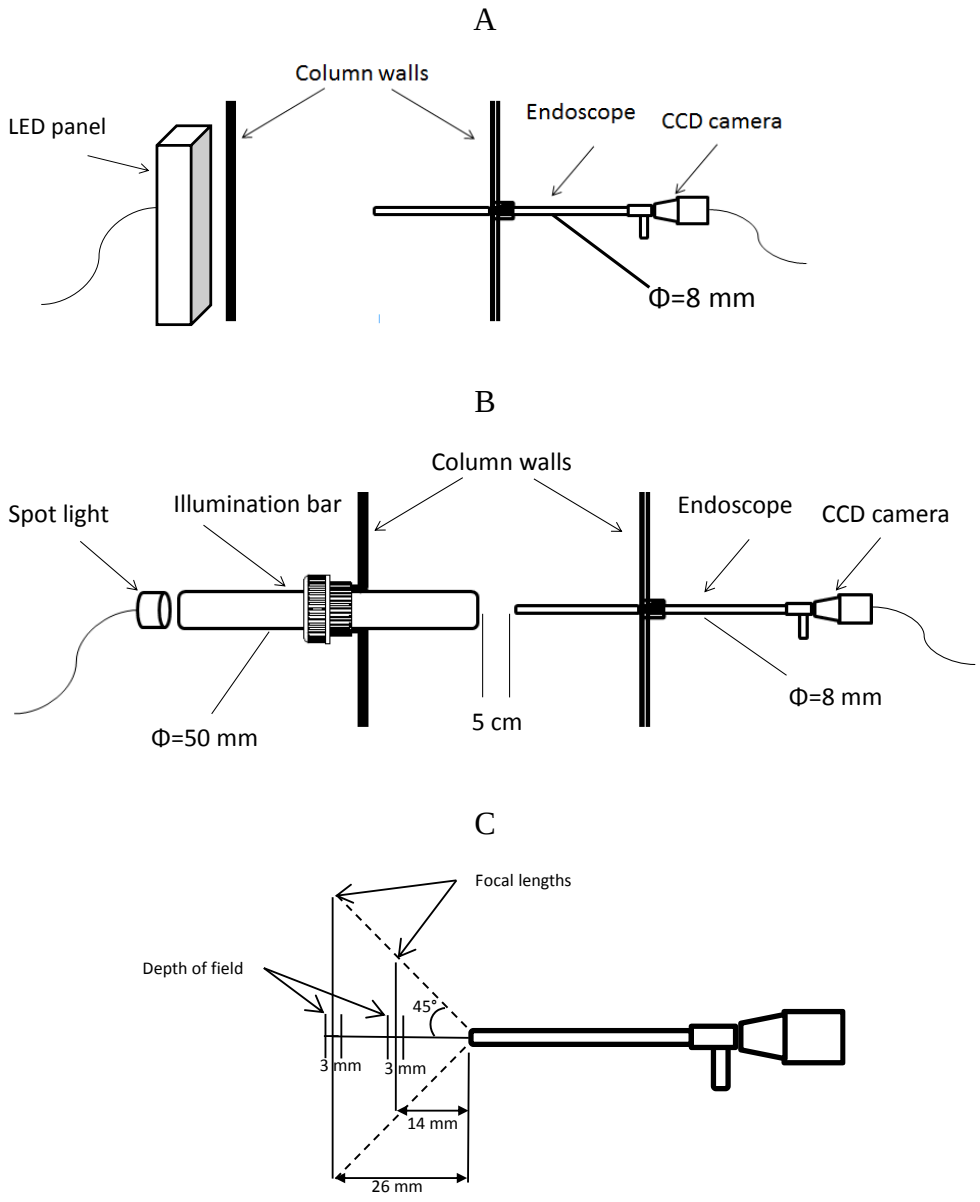

Figure 3.3 – Schematic representation of: A) the endoscope experiments on Phi 150; B) the endoscope experiments on Phi 400 and Phi 1000 C) Endoscope view angle and depth of field.

Endoscope measurements

The endoscope is equipped with a lens with 90° vision angle with a depth of field of 3 mm, the extension of the field of view is ≈25 mm, which should be larger enough compared with the bubble size. An object placed inside of this field can be measured with +/- 7% of uncertainty due to the variation of the magnification inside the depth of field. The high speed camera was configured to take images with 50 µs of exposure time to freeze the moving bubbles. The images had spatial resolution of 35 pixels/mm and the minimal detectable size was 0.3 mm. In the image analysis it was assumed that the

bubbles had an ellipsoidal shape. The bubbles were manually selected under somewhat subjective criteria based on sharpness. Also, bubbles overlapped by other bubbles or that were only partially visible in the field, were not considered. For each selected bubble, the horizontal diameter (big diameter), the vertical diameter (small diameter) and their angle, relatively to a horizontal axis, were measured. Figure 3.4 presents two examples of the images obtained by this method. Moreover, the solid line represents the measurement of the vertical diameter and the dashed line the horizontal diameter.

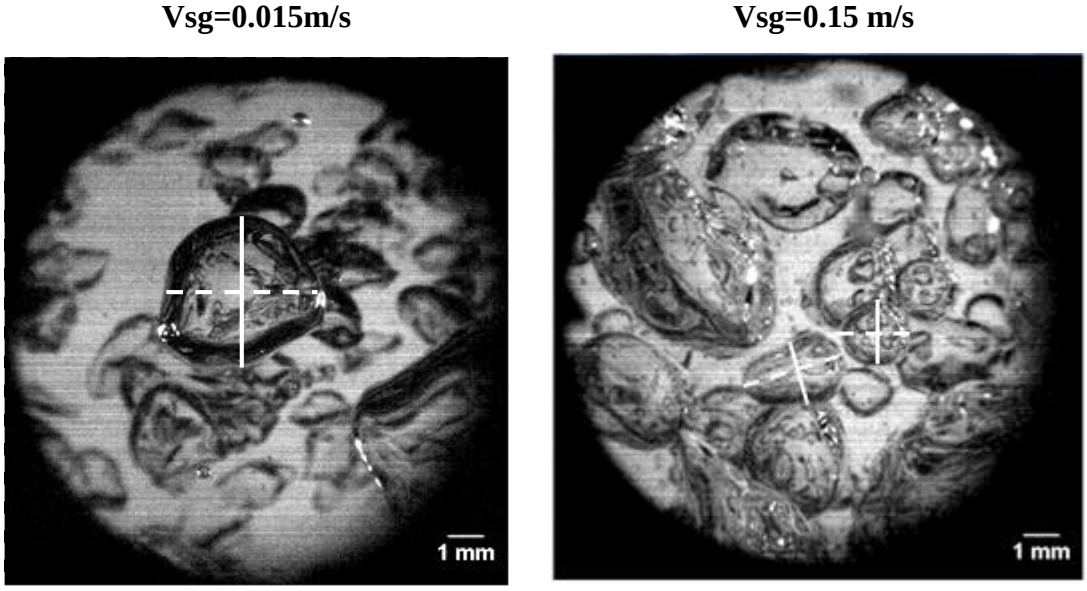

Figure 3.4 - Examples of endoscopic images (Measurements taken at the centre of the Phi 150 column, using an outside illumination).

The selection of the bubbles is also represented in the Figure 3.4. The bubbles that would be selected to be measured have a dashed line over their horizontal diameter and a solid line over their vertical diameter. The other bubbles would be considered to be either out of the depth of field or overlapped. The bubble eccentricity (Ecc), i.e. the ratio between the vertical diameter (Dv) and the horizontal one (Dh) was calculated for each bubble by the following equation.

$$Ecc = \frac{Dv}{\mathrm{Dh}} \qquad (3.\ 3)$$

Due to the image's small contrast it was not possible to develop an automatic measurement routine. Therefore, all measurements were hand-made, a laborious and time-consuming process, making it necessary to minimize the number of treated images.

The convergence of bubble horizontal and vertical diameter and eccentricity is depicted in Figure 3.5.

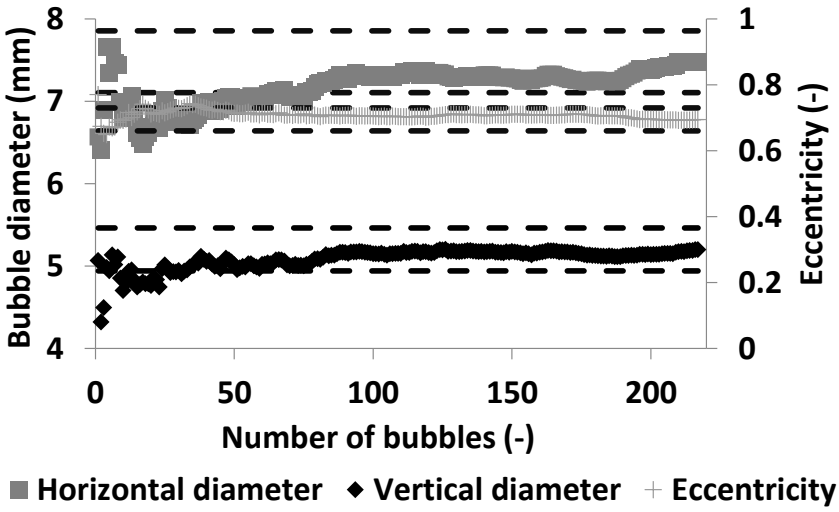

Figure 3.5 – Convergence of the mean values of eccentricity, horizontal and vertical diameters. (Measurements taken at the centre of the Phi 150 column, using an outside illumination, dashed lines represent the convergence range of each variable)

The results show that for 100 measured bubbles the three parameters are already inside a ±5% convergence range. Nevertheless, to assure that the convergence will be achieved, even in conditions were the bubble size population is more polydispersed, each measurement comprises 200 bubble detections. Moreover, the PDFs of vertical and horizontal diameters and of eccentricity are presented in Figure 3.6.

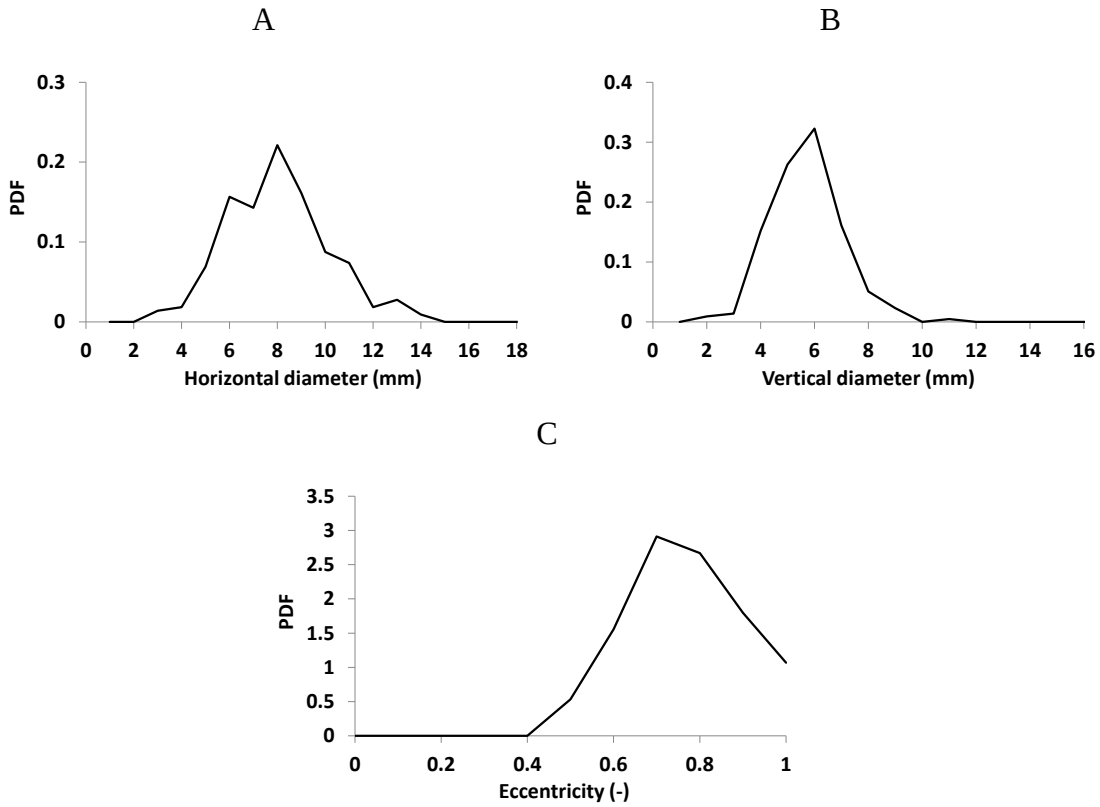

Figure 3.6 – PDFs from endoscopic measurements : A) Horizontal diameter; B) Vertical diameter; C) Eccentricity (Measurements taken at the centre of the Phi 150 column, using an outside illumination)

By analysing Figure 3.6 is possible to conclude that 200 bubbles are also enough to achieve a good convergence on the PDFs of horizontal and vertical diameter and eccentricity.

Two different focal lengths, namely 14 and 26 mm, were used to test if the working distance affects the size measurements. After selecting one focal distance, several gas superficial velocities were tested in a range between 1.5 and 15 cm/s in the centre of the Phi 150 column, as can be seen in Figure 3.7.

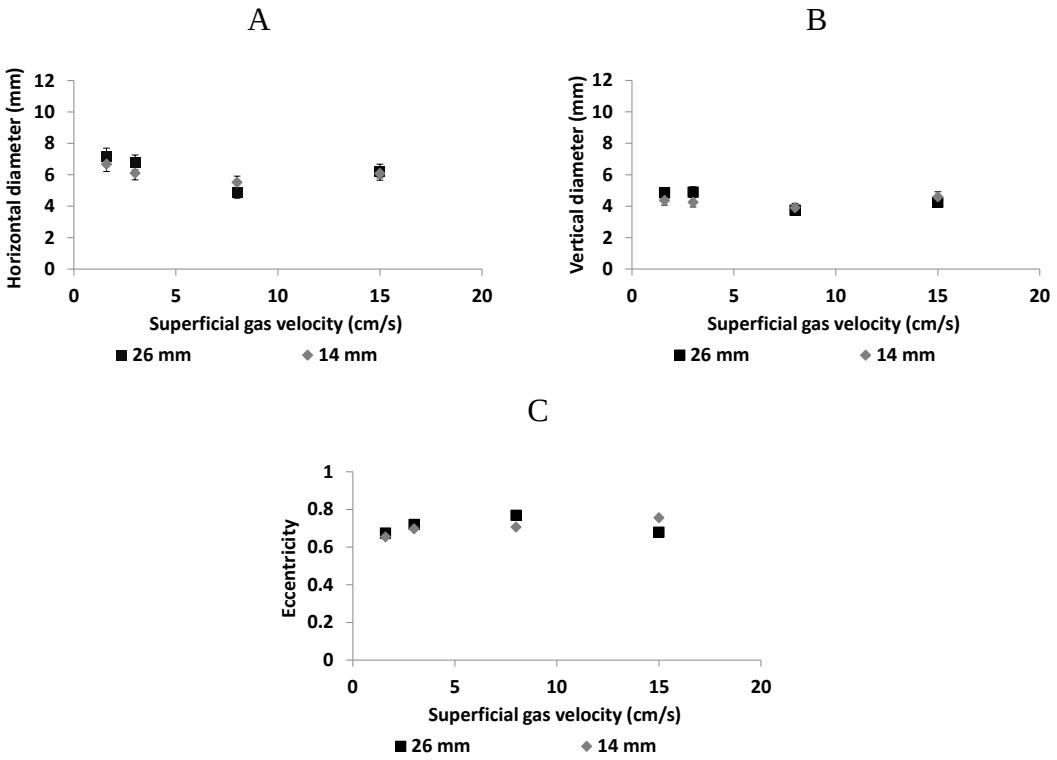

Figure 3.7– Effect of the focal length on: A) Mean horizontal diameter; B) Mean vertical diameter; C) Eccentricity (Measurements taken at the centre of the Phi 150 column, using an outside illumination)

By analysing the results it is possible to conclude that the focal distance does not have a significant impact on the mean bubble size measurements (mean deviation ± 1.8 %), regardless of the tested gas superficial velocity. The PDFs of the horizontal and vertical diameters are plotted in Figure 3.8 A and B, respectively.

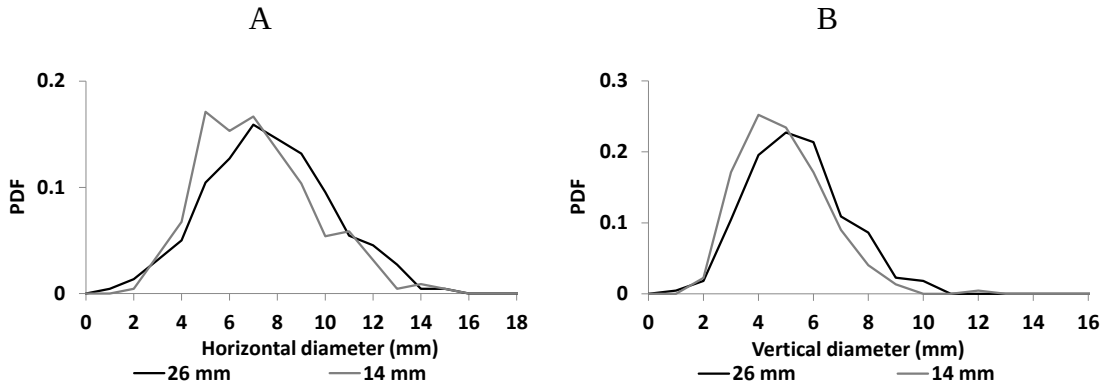

Figure 3.8– Effect of the focal lengths on: A) PDF of horizontal diameter; B) PDF of vertical diameter (Measurements taken at the centre of the Phi 150 column, using an outside illumination)

Figure 3.8 A and B show that similar PDF of the vertical and horizontal diameter are obtained for the focal distances of 26 mm and 14 mm. In agreement with the conclusion of the analysis of the averaged values, is possible to conclude that the focal distance does not have a significant impact on the measured diameter distributions. Therefore, the focal distance used in the measurements, that will be presented in further in this chapter and the chapter 4, was typically 20 mm.

Intrusive behaviour

As previously referred, the endoscope imaging is an intrusive method, especially when the illumination tube is also introduced in the column. Therefore, the impact of the endoscope and of the illumination bar on the bubble size was studied. In the Phi 400 column, the bubble size was measured by the spatial cross-correlation method (method further detailed in this chapter) by placing the optical probes in the focal plane of the endoscope. Afterwards, those measurements were compared with the ones acquired at the same location in the column but without the endoscope. These results can provide some information about the perturbation effect of the endoscope and of the illumination tube on the bubble characteristics inside the measurement volume.

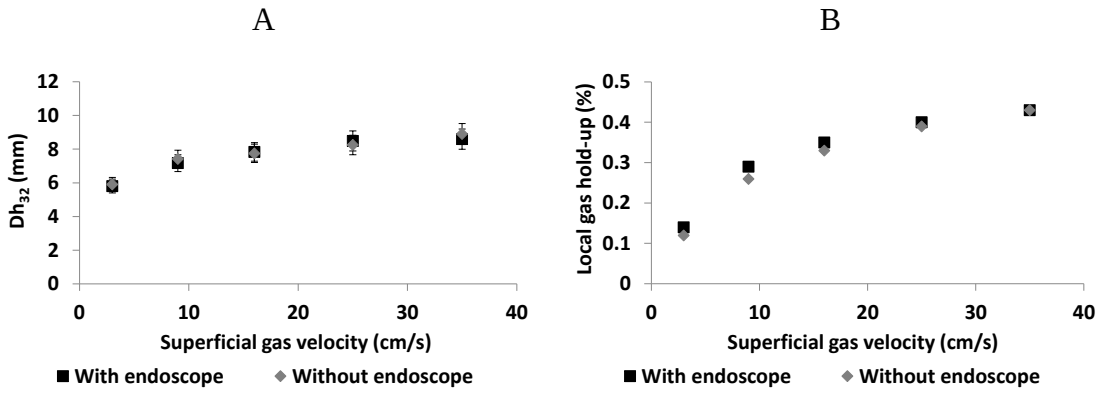

Figure 3.9 – Effect of the presence of the endoscope on: A) Dh_{32} (bubble size) measurements by the spatial cross-correlation method; B) Local gas hold-up (measured by the optical probe) (Measurements taken at the centre of the Phi 400 column)

By analyzing the results of Figure 3.9, it is possible to conclude that the endoscope and the illumination tube did not affect the measured bubble size. Similarly, Figure 3.9 B shows that the local gas hold-up does not significantly change with or without the presence of the endoscope. Hence, the endoscope imaging method will be used as a reference to test the size measurement performed using optical probes.

The Pavlov tube and the endoscope are radially inserted in the column and placed perpendicular to the flow, making their positions in the column fixed. The measurements were made at ratio height of the column/ column diameter of 2.5 and 3.75 in all of the columns in order to obtain comparable data. In the 0.15 m, 1 m and 3 m columns the probes were inserted axially, allowing its positioning at any height. In the 0.4 m column the probe was also inserted radially, meaning that, just as the endoscope and the Pavlov tube, its positions in the column were limited. Nevertheless, the optical probe measurements were also carried out at height of the column/ column diameter ratio of 2.5 and 3.75

3.3 Optical probes

As referred in the section 1.3, optical probes ideally provide the local gas hold-up as well as information on chord and velocity for each detected inclusion. Several optical probes configurations have been presented in the Chap.1. However, in this work, a 1C (conical) mono-fibre optical probe will be used. This type of probe has the advantage of allowing the access to the bubble velocity component along the probe axis with only one fibre (c.f. section 1.3). Beside, and compared with bi- or quadri-probes, no signals association is required, a feature that eliminates many, often subjective, processing parameters.

For single conical probes, developments in signal processing, in data post-treatment as well as validations of the technique have been presented in several publications (Cartellier, 1990, 1992, 1998; Cartellier and Barrau, 1998 A, 1998 B; Barrau et al. 1999 A, 1999 B; Vejrazka et al., 2010) that will be briefly detailed further in this section.

The bubble size, velocity and flux measurements by the 1C mono-fiber optical probes have been validated in bubbly flows with narrow bubble size distributions (see for ex. Andreotti, 2009), and also in various gas-liquid flows up to void fractions of 30%. The typical uncertainty on void fraction measurements using 1C mono-fiber optical probes was about -10%/+0% while the gas flux was determined with an uncertainty about ±15% Cartellier (1998). To quantify the range of proper probe functioning in bubbly flows, Vejrazka et al. (2010) have proposed a modified Weber number M, that represents the ratio between the bubble momentum ~ $\rho_l De^3 v_{b1}$ and the impulsion of the surface-

tension force arising from the probe dewetting $\sigma_l D_{op} De \ \ / v_{b1}$,.and that is thus computed from following equation:

$$M = \frac{\rho_l De^2 v_{b1}^2}{\sigma_l D_{op}} \qquad (3.\ 4)$$

Where ρ_l and σ_l represent the liquid density and surface tension, respectively, De represents the bubble equivalent diameter, v_{b1} represents the bubble velocity (relative to the probe) before the contact with the probe have occurred and D_{op} the diameter of the optical fiber. Vejrazka et al. (2010) have reported the errors of the gas hold-up and bubble chord measurements by the optical probe as function of M. For low viscosity fluids (such as water) and for M values higher than 50, the void fraction and the maximal chord measurement error should be less than 10%. In all bubble column experiments carried out in our study, the M number has always been greater than 100: our flow conditions were thus quite favorable for using monofiber probes.

However, most previous probe qualification were performed on quasi 1D flows such as bubble swarms or flows confined inside a tube, i.e. without liquid recirculation nor strong velocity fluctuations. In such flows, bubbles have an almost unidirectional movement, contrary to the flows that will be considered in this work. Whenever unsteady 3D structures are present, the probes performances are expected to be less reliable but it is not clear in what measure. For example, very severe measuring difficulties have been encountered using double-optical probes in dense bubble columns (Chaumat et al., 2007). The performance of monofiber probes in the conditions of our bubble columns, and notably at high gas hold up, deserves thus to be evaluated.

In subsequent sections, the principles of optical probes are initially summarized, followed by a proposition on how to extend their measuring capabilities to the detection of the horizontal dimension of distorted bubbles. In the section 3.5, the reliability of single probes to provide bubbly flow characteristics in bubbles columns at high void fractions is discussed.

Apparatus

The probe is placed in the flow and connected to an opto-electronic module by an optical fibre, as can be seen in Figure 3.10. As already mentioned in section 1.3, a laser beam is generated by this module, sent to the probe tip and, in case of gas detection, it is reflected back to the opto-electronic module. A photodiode converts it into an electrical signal and

sends it to an oscilloscope Picoscope 2000 series, built by Picotech. The oscilloscope has a USB connection with a computer, in which the signals are treated by the software SO6 from the society A_2 Photonic Sensors. Throughout this work a 1C conical mono-fibre optical probe from A_2 Photonics Sensors was used: the 130 µm outer diameter optical fibre is held by a 1.5 mm in diameter stainless steel tube. Its length outside the holder is about 6 mm. Its conical tip provides a sensing length about 12 µm.

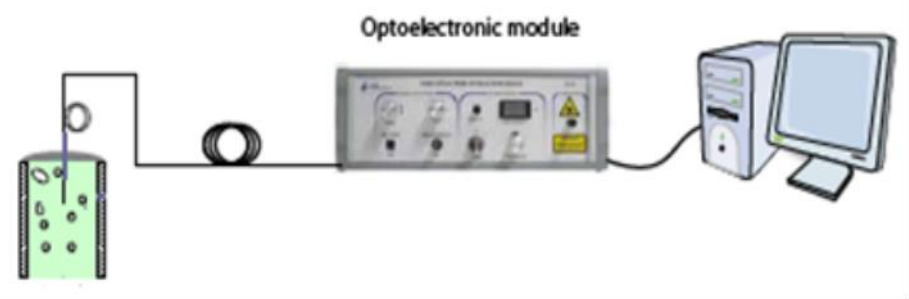

Figure 3.10 – Optical probes experiments apparatus.

Optical probes measurements

The SO6 software requires two preliminary adjustments before a measurement: a liquid level interval and the gas level. The liquid level interval corresponds to the signal voltage when the probe tip is wet, in which conditions the signal presents small fluctuations. Hence, an interval must be defined in a way that these fluctuations are contained within it: the later are represented by red lines in the lower part of the signal in Figure 3.11. The gas level is the signal voltage reached when the probe tip is completely dry (inside a bubble): it is represented by the upper (blue) line in Figure 3.11. The post treatment of the mono-fibre optical probes signal has been carefully detailed in several publications (Cartellier, 1990, 1992, 1998; Cartellier and Barrau, 1998A, 1998B) and only the main principles will be described hereafter.

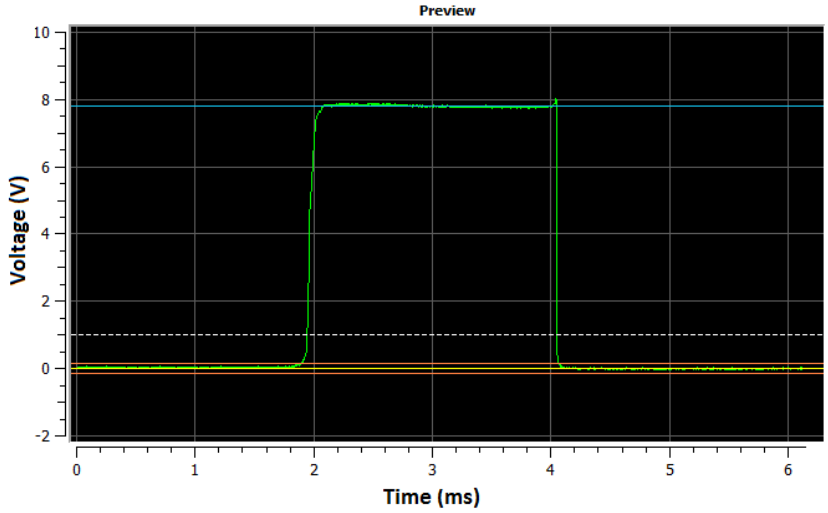

Figure 3.11 – Snapshot of gas and liquid voltages in SO6 software.

Local gas hold up measurement

Each time the signal voltage is higher than the liquid upper level, the signal treatment detects a bubble. The signal treatment considers the end of the bubble detection as the moment when the signal voltage drops neatly below the gas level. The *gas residence time*, which corresponds to the time that the probe tip stays in the bubble, is the time difference between the beginning and the end of the detection of each bubble. The local gas hold up is computed as the ratio between the sum of all detected *gas residence times tgi* and the total measurement duration texp.

Velocity measurement

The signal treatment detects the beginning and the end of the rising front of the signal as illustrated in Figure 1.33. This time difference is defined as the *rising time*: it characterises the probe de-wetting process that occurs when its tip enters a bubble. The velocity component along the probe axis is computed as the ratio between the sensing length of the probe (a parameter quantified before the measurements, see Cartellier (1989)) and the *rising time* of the bubble (Cartellier, 1992).

In some cases the bubble does not travel through the whole sensing tip of the probe, so the rising front of the signal is not well defined, as represented Figure 3.12. For this kind of signature, the *end of gas detection* occurs when the signal decreases sharply.

Also, for such signatures, it is not possible to directly obtain a reliable velocity measurement. The signal treatment can detect these two types of signatures and defines them as T1 bubbles, if a velocity information is directly available, or T2 bubbles, if not. When there is no direct velocity information, a software routine interpolates the velocity from the previous and the next T1 bubbles (Cartellier, 1998). Therefore, all the detected bubbles are associated with a value for the gas residence time and a value for the velocity. From these data, one can extract the velocity distribution and its various moments, including the arithmetic mean bubble velocity.

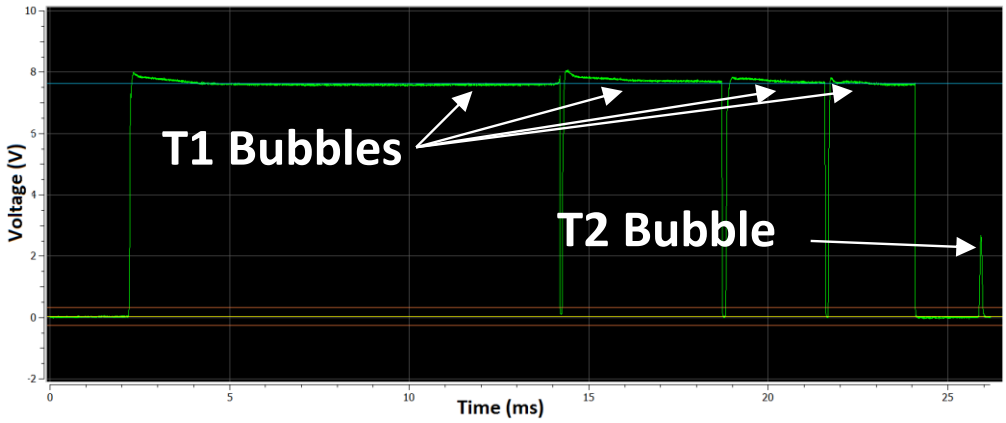

Figure 3.12 – A sample of 1C mono-fiber optical probe signal collected in the Phi 1000 bubble column vsg of 35 cm/s at the center of the column.

Chord calculation

The pierced chord corresponds to the length of the course made by the probe tip in the bubble. This information can be calculated by the product of the gas residence time with the bubble velocity. From the chord distributions, various quantities can be inferred, including a Sauter mean diameter. Therefore, the basic output from these probes is a product density $f^{(1)}$(Chord,Velocity) from which one can infer various variables of interest (Cartellier, 1999) including void fraction, joint chord-velocity distributions, local volumetric flux, number density and its flux, interfacial area density. The variables that will be exploited in the present work are given below.

Local volumetric flux

Assuming that the velocity in the gas phase and on all positions along the chord pierced by the probe equals the velocity detected on the interface (a very reasonable

assumption for bubbly flows), the local volumetric gas flux can be calculated by weighting each velocity by the bubble residence time, namely:

$$j_g = \frac{\sum V_{bi}^* \times t_{gi}}{t_{exp}} \ (m/s) \qquad \textbf{(3. 5)}$$

Where V_{bi}^* represents the ith bubble velocity (measured or interpolated), t_{gi} represents the ith bubble residence time and t_{exp} is the measuring duration. When using (3.5), all contributions have to be considered (namely populations T1 and T2). The gas flow rate on the column can be computed by integrating j_g over the column cross-section.

Shape estimation

According to Clark and Turton (1988), if the bubble population is composed of oblate ellipsoids, with a given eccentricity Ecc and a unidirectional ascending movement, the pierced chord (C) through a bubble is given by the equation:

$$C = 2Ecc\sqrt{Rh^2 - r^2} \qquad (3. 6)$$

Where C represents the bubble chord, Rh represents the horizontal diameter of the ellipsoid and r is the distance in the x, y plane between the bubble center and the probe tip. Moreover, Clark and Turton (1988) have established the mathematical relation between the chord distribution (P(C)) and the radius distribution of detected bubbles (Pd(Rh)):

$$P(C)dC = \int_{\frac{C}{2Ecc}}^{\infty} Pd(Rh)dRh \times Pc(C|Rh) \qquad (3. 7)$$

Where $Pc(C|Rh)$ represents the probability of detecting the chord C on a bubble with an horizontal radius Rh, and $Pd(Rh)$ represents the probability of detecting a bubble with an horizontal radius Rh. $Pc(C|Rh)$ can be defined as the surface ratio between the crown (i.e. the positions of bubble centers) where a chord C can be detected and the projected surface of the bubble (Figure 3.13):

$$Pc(C|Rh) = \frac{2\pi r dr}{2\pi Rh^2} \qquad (3. 8)$$

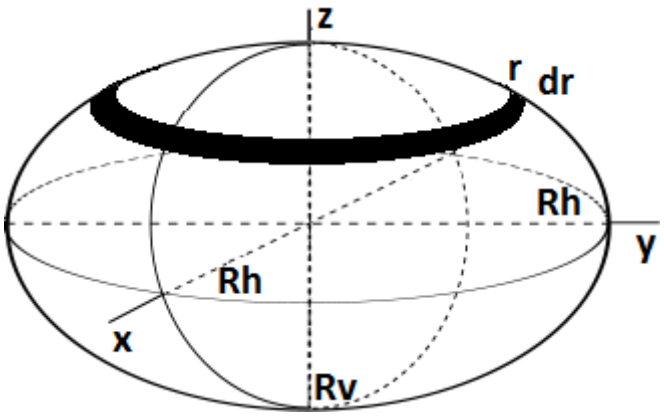

Figure 3.13 – Schematic representation of an oblate bubble.

Therefore, r and dr can be obtained from Eq. (3.6) and Eq. (3.8) can be rewritten as:

$$Pc(C|Rh) = \frac{C}{EccRh^2} \tag{3. 9}$$

In the above equations, Pd(Rh) represents the probability that the probe detects a bubble of size Rh. Pd(Rh) differs from the size distribution P(D) in the system since large bubbles are easier to be detected than small ones. Since the probability of detecting a bubble is proportional to its projected surface, the following relation is obtained:

$$Pd(Rh) = P(Rh) \times Rh^2 \times \varphi \tag{3. 10}$$

Where φ is a constant of normalization. Replacing Eq. (3.9) and (3.10) in Eq. (3.7):

$$P(C)dc = \frac{c}{Ecc}\varphi \int_{\frac{c}{2Ecc}}^{\infty} P(Rh)dRh \tag{3. 11}$$

The mean chord (C_{10}) can be found by

$$C_{10} = \int_0^{\infty} cP(C)dC = \int_0^{\infty} dC \int_{\frac{C}{2Ecc}}^{\infty} \frac{C^2}{\alpha}\varphi P(Rh)dRh \tag{3. 12}$$

Permuting dC and dRh

$$\begin{aligned} C_{10} &= \frac{\varphi}{Ecc}\int_0^{\infty} P(Rh)\int_0^{2EccRh} y^2 dCdRh \\ &= \frac{\varphi}{Ecc}\int_0^{\infty} P(Rh) \times \frac{8Ecc^3Rh^3}{3} dRh \\ &= \frac{\varphi 8Ecc^2 < Rh >^3}{3} \end{aligned} \tag{3. 13}$$

The normalization by φ must ensure that $\int_0^{\infty} P(C)dC = 1$, then

$$1 = \frac{\varphi}{Ecc}\int_0^{\infty}\int_0^{2EccRh} CP(Rh)dC\,dRh \Leftrightarrow 1$$
$$= \frac{\varphi}{\alpha} \times \frac{4Ecc^2Rh^2}{2} \Leftrightarrow \varphi = \frac{1}{2Ecc < Rh^2 >} \quad (3.\ 14)$$

Replacing in Eq. (3.13):

$$C_{10} = \frac{4Ecc}{3}\frac{< Rh >^3}{< Rh >^2} = \frac{2Ecc}{3}Dh_{32} \quad (3.\ 15)$$

Where Dh is the Sauter mean diameter evaluated using the size distribution P(Rh) in the system (and not the detected one). Note that, when using the detected size distribution Pd(Rh), one has:

$$C_{10} = \frac{2Ecc}{3}Dh_{detected} = \frac{2}{3}Dv_{detected} \quad (3.\ 16)$$

where $Dh_{detected}$ and $Dv_{detected}$ are the arithmetical mean diameters of the detected distributions. Beside, according to the definition of eccentricity Eq. (3.3), and assuming a constant eccentricity for all the bubbles present in the flow, Eq. (3.15) can be rewritten as:

$$C_{10} = \frac{2}{3}Dv_{32} \quad (3.\ 17)$$

where Dv32 is the Sauter mean of the vertical diameters again using the size distribution P(Rv) of the system.

Concluding, the Sauter mean vertical diameter (Dv_{32}) of the bubble population can be computed using Eq.(3.16), even if the eccentricity of the oblate bubble population is unknown.

Deconvolution of chord distribution into diameter distribution

Clark & Turton (1988) and Lui and Clark (1995) have proposed an algorithm to compute the distribution of bubble diameters on the flow from the distribution of the detected chords for a bubble population of various but fixed bubble shapes. In this work, the procedure to obtain the diameter distribution of an oblate shaped bubble population

with a known fixed eccentricity will be detailed. First, we rewrite the Eq. (3.9) by replacing Rh by Dh and by normalizing using $\langle Dh^2 \rangle$:

$$Pd(Dh) = \frac{P(Dh) \times Dh^2}{\langle Dh^2 \rangle} \tag{3. 18}$$

The relation chord diameter becomes:

$$Pc(C) = \frac{2C}{Ecc^2 \langle Dh^2 \rangle} \int_{\frac{C}{ECC}}^{\infty} P(Dh) dDh = \frac{2C}{Ecc^2} \int_{\frac{C}{ECC}}^{\infty} \frac{Pd(Dh)}{Dh^2} dDh \tag{3. 19}$$

$$=$$

The chord classes are already known, so it is only necessary to define the classes of Pd. Since the largest diameter cannot be bigger than the largest chord, the maximal limit is set as the largest chord. Therefore, diameter classes can be defined considering that their size is identical to the ones of chord classes. Eq. (3.18) is discretized by the method of finite sums:

$$Pc(i) = \frac{2C(i)Pd(i)}{Ecc^2 Dh(i)^2} dDh(i) + \frac{2C(i)}{Ecc^2} \sum_{j=i+1}^{N} \frac{Pd(j)}{Dh(j)^2} dDh(j) \tag{3. 20}$$

Solving for $P_d(i)$:

$$Pd(i) = \frac{Ecc^2 Dh(i)^2}{2C(i) dDh(i)} Pc(i) - \frac{Dh(i)^2}{dDh(i)} \sum_{j=i+1}^{N} \frac{Pd(j)}{Dh(j)^2} dDh(j) \tag{3. 21}$$

The calculus is initialized with i=N, and by looping i from N-1 to 1, the distribution of the detected diameter can be computed. Therefore, the diameter distribution can be found by solving Eq. (3.18). This process requires a well converged Pc curve in order to avoid negative probabilities in Pd. Typically, the Pc issued from optical chords measurements presents long tail with very low probability of detections, which can induce the negative probabilities in the calculated Pd. Therefore, the calculus should be applied preferentially to chord distributions issued from very long acquisitions (large number of detections) to avoid this problem. Nevertheless, the Pc can be smooth out by neglecting the higher chords and imposing a more linear increase of the detection probability of the chords.

3.4 Spatial cross-correlation of optical probes signals

As seen above, single optical probes provide bubble sizes along the probe direction, the latter being usually aligned with the main flow direction. For the distorted bubbles considered in this work, this information is insufficient as one requires also an estimate

of the bubble size in a direction normal to the main flow. Therefore, a new technique has been implemented to access this information. The basis of the proposed method is to correlate the signals of two mono-fiber optical probes placed parallel side by side, at a given distance from each other. This correlation should be sensitive to the bubble size along the direction defined by the two probes tips. In practice, since the mono-fiber optical probes will be vertically aligned and will thus give access to the vertical dimension of the bubbles only, the direction defined by the two tips has been set to horizontal in order to measure the horizontal dimension of the bubbles.

In this section it will be detailed how to deduce the horizontal diameter from the correlations of the signals of the probes as a function of the bubble shape. The nature of this measurement will also be discussed to understand what kind of averaging is performed by the correlation method. Afterwards the feasibility of this method and notably the impact of the bubble concentration on the measured correlation will be studied.

Principle

The normalized cross-correlation is a function that quantifies the similarity of two binary signals by analyzing both signals simultaneously:

$$CC = \frac{\int_{t=0}^{t_{exp}} Signal_{\,A}(t) \times Signal_{\,B}(t)dt}{\int_{t=0}^{t_{exp}} Signal_{\,A}(t)dt} \qquad (3.\ 22)$$

Here $Signal_{\,A}$ and $Signal_{\,B}$ represent the raw signals coming from two different probes at the same elevation in the column at a radial distance (d) and t_{exp} represents the time of registration. The cross-correlation value is maximal if both probes are at the same point in space (distance between probes (d) of 0 mm), since the signals will be identical. In a single bubble-probe interaction, as the distance between the probes increases, the cross-correlation of the probe signals will decrease. The cross-correlation will be zero when the distance between probes becomes larger than the bubble horizontal diameter due to the fact that the same bubble cannot be detected by both probes at the same time. Hence, some information related to the horizontal bubble size can be extracted from the shape of the cross-correlation curve as a function of probes distances.

Some preliminary experiments were carried out in the center of the Phi 150 column and at h/D=2, where the cross-correlation was measured for several probe distances from 0 mm up to 12 mm, as can be seen in Figure 3.14.

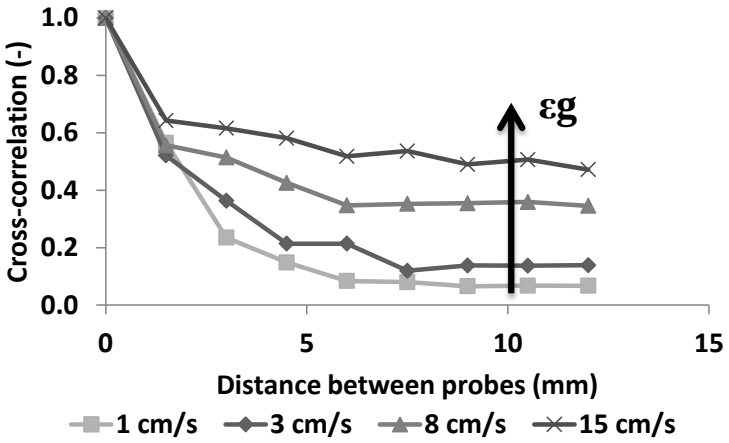

Figure 3.14 – Evolution of the experimental cross-correlation with the distance between the probes for several superficial gas velocities.

The results show that, as expected, the cross-correlation decreases with the distance between the probes. However, the cross-correlation is never zero even when the distances between probes reaches 12 mm, a value much larger than the largest bubble horizontal diameter. In fact, at large distances, the cross-correlation increases with the gas hold-up (εg). This is to be related with the simultaneous detection of two bubbles that increases the cross-correlation. A notable feature of the results of Fig.3.15 is that, up to a distance about 1.5 mm, all the curves have a similar behavior, which seems to indicate that this is the zone that should be explored in order to obtain some information about the horizontal diameter.

Therefore, in order to fully understand the variation of the cross-correlation with the distance between probes, the bubble shape and its orientation, two different approaches were developed: first an analytic approach based on a rectilinear motion of the bubbles and afterwards a numerical approach without any hypothesis on the bubbles movement.

Analytical 2D approach

Let us consider an idealized bubbly flow of spherical shaped bubbles rising along a vertical axis of the column. All the bubbles have the same radius (R) and rising velocity. Moreover, the probability of detect a bubble center in a given point is uniform in all flow volume. If two optical probes (noted Probe A and Probe B in Figure 3.15) are placed parallel side by side, at a given distance (d) from each other along the abscissa axis. Consequently, a rising bubble (represented by a circle in Figure 3.15) will intersect the abscissa axis on the point x and generate a detected chord (C) on each probe that can be determined by Eq. (3.6), considering Ecc=1 since the bubble is spherical.

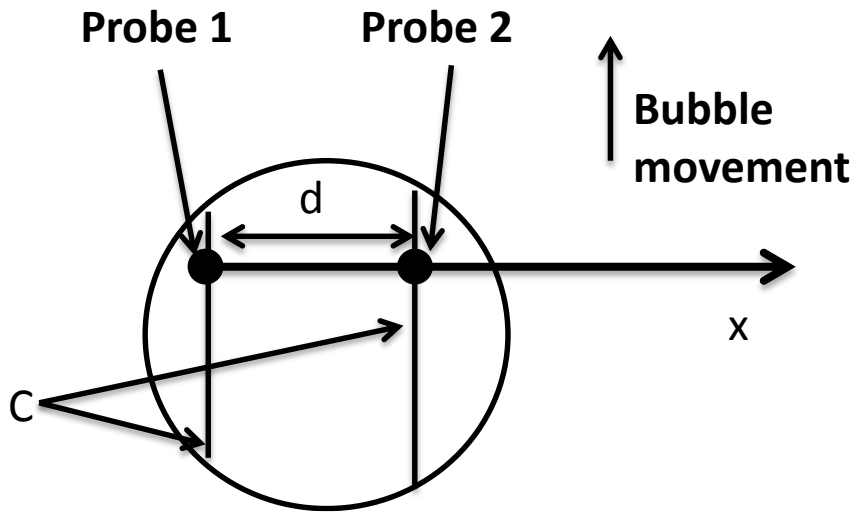

Figure 3.15 – Schematic view of the analytic 2D approach.

Therefore, it is possible to define two events such as:

1 - There is a bubble in the Probe 1

2 - There is a bubble in the Probe 2

The cross-correlation can thus be considered as the conditional probability of A knowing that B have occur:

$$CC = P(2|1) = \frac{P(1 \cap 2)}{P(2)} \qquad (3.\ 23)$$

P(A) can be determined by the definition of the pierced chord (C_1) and the probably of a bubble passing through the point x (P(x)). Hence, the abscises that can generate a detection of the chord by the Probe 1 are comprise between –R and R, so:

$$P(1) = \int_{-R}^{+R} C_1 P(x)dx = \pi R^2 P(x) \tag{3. 24}$$

$P(1 \cap 2)$ represents the probability that a bubble touches both probes at the same time. In such case, the chord generated on the Probe 2 (C_2) can be determined by

$$C_2 = 2\sqrt{D^2 - (x-d)^2} \tag{3. 25}$$

Since we are interest in the bubble positions where the both probes detect the bubble, the contribution of each bubble to $P(1 \cap 2)$ is equal to the min(C_1, C_2): if $x > {}^{d}/_{2}$ the smallest chord is C_1, otherwise if $x < {}^{d}/_{2}$ the smallest chord is C_2. Therefore $P(1 \cap 2)$ can be defined as:

$$P(1 \cap 2) = \int_{R-d}^{d/2} C_2 P(x)dx + \int_{d/2}^{R} C_1 P(x)dx \tag{3. 26}$$

Since both integrals are symmetric to the distance d/2 of the bubble center and equal in value Eq. (3.26) becomes:

$$\begin{aligned} P(1 \cap 2) &= 2\int_{d/2}^{R} C_1 P(x)dx \\ &= 4P(x)\left[\frac{1}{2}x\sqrt{R^2 - x^2} + \frac{R^2}{2}\arcsin\left(\frac{d}{2R}\right)\right]_{\frac{d}{2}}^{R} \\ &= 2P(x)\left[\frac{\pi R^2}{2} - \frac{d}{2}\sqrt{R^2 - \frac{d^2}{4}} - R^2\arcsin\left(\frac{d}{2R}\right)\right] \end{aligned} \tag{3. 27}$$

Replacing Eq.(3.27) and Eq.(3.24) in Eq.(3.23):

$$CC = P(2|1) = 1 - \frac{1}{\pi}\frac{d}{R}\sqrt{1 - \left(\frac{d}{2R}\right)} - \frac{2}{\pi}\arcsin\left(\frac{d}{2R}\right) \tag{3. 28}$$

The Eq. (3.28) was plotted in Figure 3.16 (black line), the results show that for $d > 2R$ the cross-correlation is zero, as expeted.

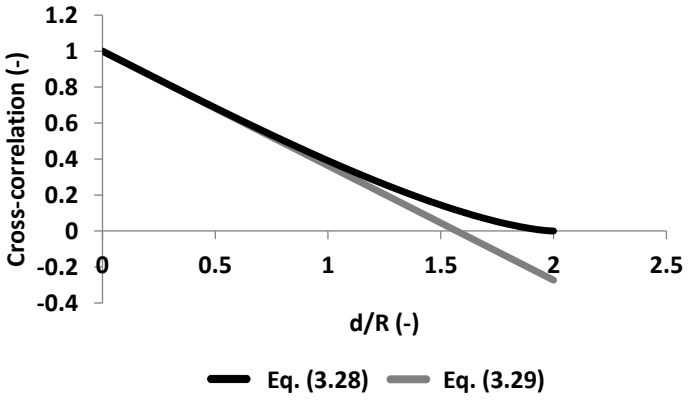

Figure 3.16 – Graphic representation of Eq. (3.28) and Eq. (3.29).

Since in vicinity of $x = 0$ one can develop the function $\arcsin(x)$ as $\arcsin(x) = x + \frac{x^3}{6}$, in the vicinity of $\frac{d}{R} = 0$ Eq. (3.28) can be rewritten as:

$$CC = P(2|1) = 1 - \frac{2}{\pi}\frac{d}{R} \qquad (3.\ 29)$$

So, there is a linear relation between CC and $\frac{d}{R}$.that was also plotted in Figure 3.16 (grey line). Moreover, results show that Eq. (3.29) predicts correctly the exact solution (deviation of 7%).

The previous result was obtained from a 2D approach and for spherical shaped bubbles. Therefore, a more realistic solution should be obtained in a 3D approach and considering ellipsoidal bubbles (oblates).

Analytical 3D approach

Let us consider an idealized bubbly flow of oblate shaped bubbles, with a horizontal radius Rh and a vertical diameter $Rv = EccRh$, where all the bubbles have the same eccentricity. Likewise the 2D approach one should consider that all the bubbles have a vertical motion and the probability of detect a bubble (P(x,y)) is uniform in all the considered volume. Therefore, the pierced chord can be determined by the bubble Dh and distance from the probe as shown in Eq. (3.6). A schematic view of the 3D approach is presented in Figure 3.17.

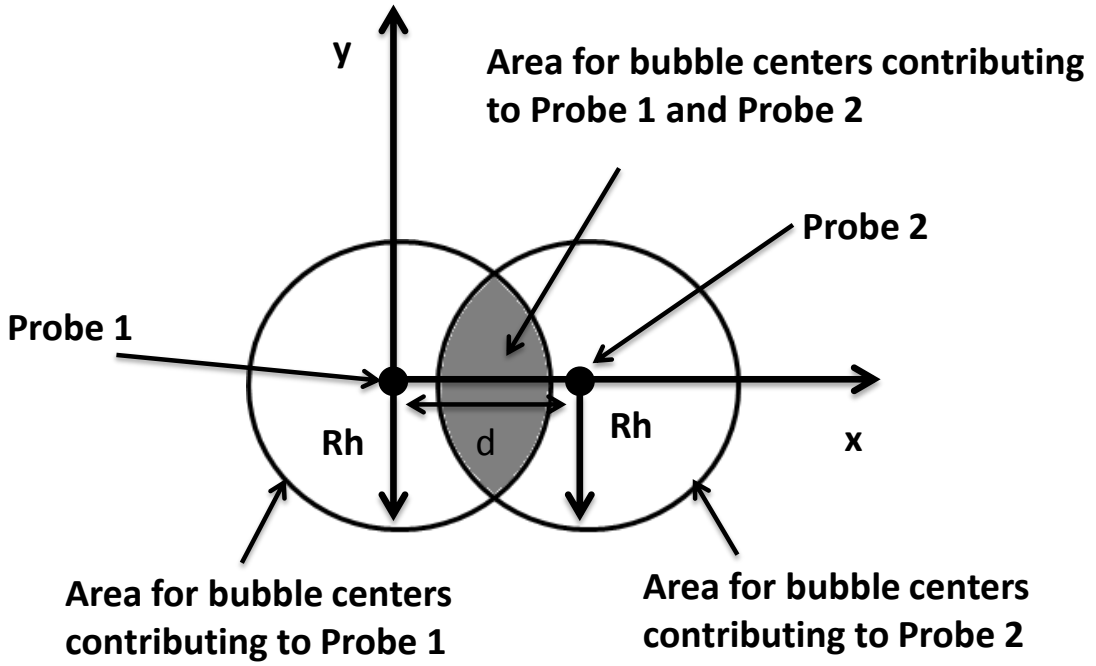

Figure 3.17 - Schematic view of the analytic 3D approach.

The Eq. (3.23) is still valid for a 3D approach, however P(1) is now determined by:

$$P(1) = \int_{|r|<R^2} C_1 P(x,y) ds = \frac{4}{3}\pi Ecc Rh^3 P(x,y) \qquad (3.\ 30)$$

The bubbles contributing to $P(1 \cap 2)$, in a horizontal plan have their center in the grey area of Figure 3.17, so :

$$P(1 \cap 2) = \int_{grey\ area} C_1 P(x,y) ds \qquad (3.\ 31)$$

Since there is a symmetry to d/2, and also a symmetry to the axis of abscesses Eq. (3.31) can be redefined as:

$$P(1 \cap 2) = 4 \int_{\frac{d}{2}}^{R} dx \int_{0}^{Ymax} dy C_1 P(x,y) \qquad (3.\ 32)$$

Since $Y_{max}^2 + x^2 = Rh^2$, Eq. (3.32) becomes:

$$
\begin{aligned}
P(1 \cap 2) &= 4 \int_{\frac{d}{2}}^{R} dx \int_{0}^{Ymax} dy\, C_1 P(x,y) \\
&= 4P(x,y) \int_{\frac{d}{2}}^{R} dx \int_{0}^{Ymax} dy 2Ecc\sqrt{Rh^2 - [x^2+y^2]} \\
&= 8EccP(x,y) \int_{\frac{d}{2}}^{R} dx \int_{0}^{Ymax} dy\sqrt{Ymax^2 - y^2} \\
&= 8EccP(x,y) \int_{\frac{d}{2}}^{R} dx \left[\frac{y}{2}\sqrt{Ymax^2 - y^2}\right. \\
&\left. + \frac{Ymax^2}{2} \arcsin\left(\frac{y}{Ymax}\right)\right]_0^{Ymax} \\
&= 8EccP(x,y) \int_{\frac{d}{2}}^{R} dx \left[\frac{\pi}{2}\frac{Ymax}{2}\right] \\
&= 2\pi EccP(x,y) \int_{\frac{d}{2}}^{R} dx\, (Rh^2 - x^2) \\
&= 2\pi EccP(x,y) R^3 \left[\frac{2}{3} - \frac{d}{2Rh} + \frac{1}{3}\left(\frac{d}{2R}\right)^3\right]
\end{aligned}
\tag{3. 33}
$$

Replacing Eq. (3.33) and Eq. (3.30) in Eq. (3.23):

$$
CC = P(2|1) = 1 - \frac{3}{4}\frac{d}{R} + \frac{1}{16}\left(\frac{d}{R}\right)^3 \tag{3. 34}
$$

Eq. (3.34) have been plotted in Figure 3.18 (black line), the results show that, as already seen for the 2D approach, the cross-correlation becomes zero for d=2R. Additionally, a linear regression was fitted to the curve (grey line), with a slope of 0.75. So it is possible to conclude that for small values of d/Rh, there is a linear evolution of the cross-correlation with the distance between the probes.

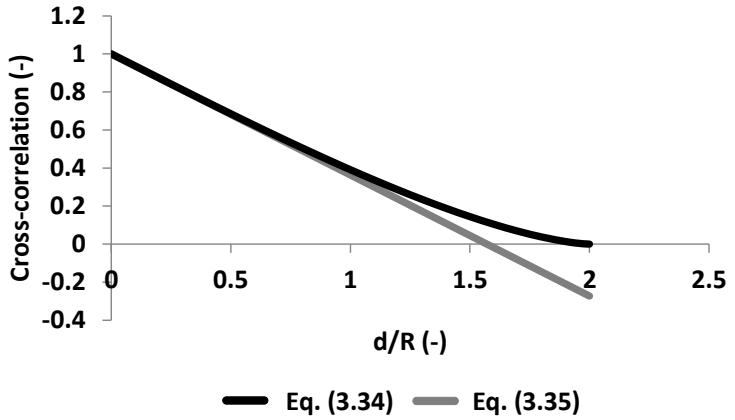

Figure 3.18 – Graphic representation of the Eq. (3.34) and Eq. (3.35).

In the idealized flow considered, both in the 2D and 3D approach, the bubbles had all the same size. However, in real flows there is a distribution of bubble sizes and shapes. Therefore, the previous result can be improved by taking in account a bubble size distribution, yet with a fixed eccentricity.

Analytical 3D polydispersed approach

In order to consider a polydispersed bubble population in the calculus of $P(2|1)$, one should start by integrate P(1) in the system bubble size distribution:

$$\begin{aligned} P(1, polydispersed) &= \int P(Rh)dRh \int_{|r|<R^2} C_1 P(x,y)ds \\ &= \int \frac{4}{3}\pi Ecc Rh^3 P(x,y)P(R)\,dRh \\ &= \frac{4}{3}\pi Ecc P(x,y) < Rh^3 > \end{aligned} \tag{3. 35}$$

In a likely manner, $P(1 \cap 2)$ should also to be integrated over the bubble size distribution:

$$P(1 \cap 2, polydispersed) = \int P(Rh)\,dRhRh^3 \left[\frac{2}{3} - \frac{d}{2Rh} + \frac{1}{3}\left(\frac{d}{2R}\right)^3\right] \tag{3. 36}$$

Thus, $P(2|1, polydispersed)$can be determined by:

$$P(2|1, polydispersed) = 1 - \frac{3}{4}\frac{d < Rh^2 >}{< Rh^3 >} + \frac{1}{16}\frac{d^3}{< Rh^3 >} \tag{3. 37}$$

The results show that the CC is a complex function of different distribution moments, namely Rh_{32} and $<Rh^3>$ as can be seen in Eq. (3.37). Nevertheless, if one considers only the vicinity of $d/Rh = 0$, is possible to say that the CC has a linear evolution with the d/R with a slope of 0.75. Indeed, since this result takes in to account the <Rh> over the entire population, it is only valid if the smallest bubble has $h \geq d/2$, otherwise the average values will be truncated. Nevertheless, this is a major result since it allows to deduce a bubble size from an experimentally measured CC value. However, this result is limited to cases where the bubbles have a rectilinear path, which may be a strong assumption in a flow with unsteady 3D structures. Indeed, such structures are to be expected in our experiments. So, a numerical approach without any assumptions on

the bubble path, and that allows to take in consideration wobbling bubbles will now be presented.

Numerical approach

In order to develop a numerical approach of the cross-correlation, let us start by considering a spherical shaped bubble. A sphere is the simpler bubble geometry, due to its axial and rotational symmetries, meaning that bubble rotation has no impact on cross-correlation calculation. Consequently, a bubble was discretized through a spherical shape with radius R, centered at (x_b, y_b, z_b). For this first computation, the bubble remains fixed in space and probes are moving over space. The first probe position (x_1, y_1, z_1) is always located inside the bubble. The second probe is set at a fixed distance $(x_1, y_1 + d, z_1)$, as can be seen Figure 3.19.

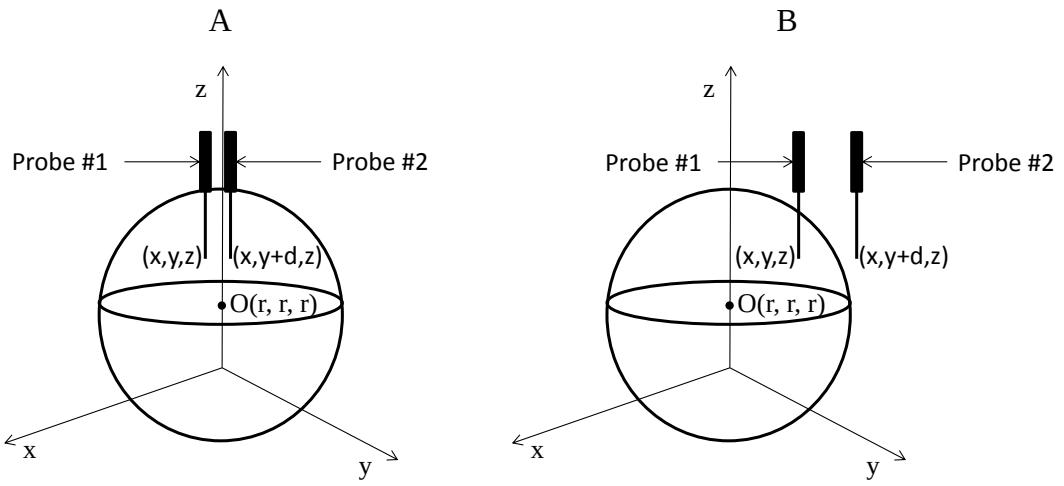

Figure 3.19 – Schematic representation of the model: A) both probes inside the bubble; B) only one probe inside the bubble.

For each position of the first probe, it is verified if both probes are inside the bubble (Figure 3.20 A and B). Such conditions correspond to the following equation:

$$f(x1, y1, z1, d) = \begin{cases} 1, & (x_1 - x_b)^2 + \left((y_1 + d) - y_b\right)^2 + (z_1 - z_b)^2 \leq R^2 \\ 0, & (x_1 - x_b)^2 + \left((y_1 + d) - y_b\right)^2 + (z_1 - z_b)^2 > R^2 \end{cases} \quad (3.\ 38)$$

Then the cross-correlation can be calculated by integrating the above equation over the bubble volume:

$$CC = \iiint f(x1, y1, z1, d)\partial x \partial y \partial z \qquad (3.\ 39)$$

In order to solve Eq. (3.39), the bubble was discretized through 3D geometrical shape and within its volume a mesh was designed. The first probe was positioned in all of the nodes of the mesh, the second probe was set at a fixed horizontal distance and Eq. (3.38) was solved for each position. This procedure was repeated for several distances between probes, from 0 mm up to a distance larger than the bubble horizontal diameter, allowing the description of the effect caused by the distance between probes on the cross-correlation for single bubble-probe interactions. The results showed, as expected, that the slopes of the calculated curves depend on the bubble diameter, as presented in Figure 3.20 A. Additionally, if the distances between probes are normalized by the bubble horizontal diameter, all the simulations collapse on a master curve, as can be seen in Figure 3.20 B. Thus, if one measures the correlation coefficient for a given (known) distance between two probes, then the bubble horizontal diameter can be deduced using that master curve.

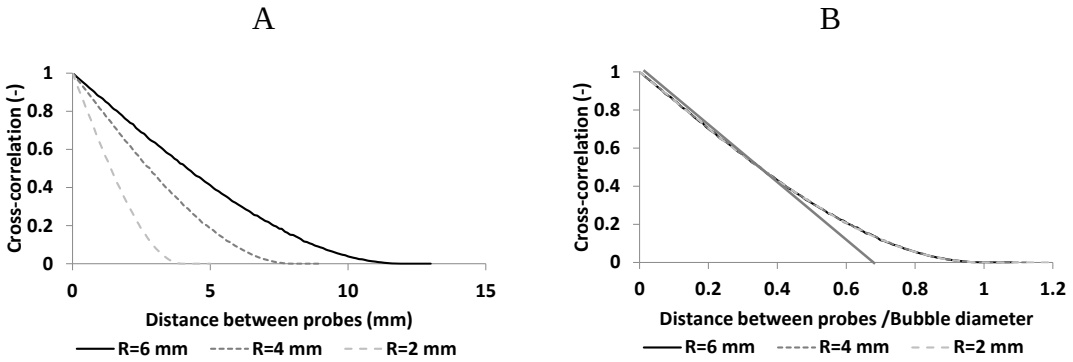

Figure 3.20 – Cross-correlations for spherical bubbles of various size : A) evolution with the distance between the probes; B) evolution with the ratio" distance between the probes/bubble diameter" (model).

In the limit of a vanishing distance, the master curve is nearly linear. In order to retrieve the information on the bubble horizontal diameter, it is thus easier to focus on that initial linear slope. Another advantage is to avoid the perturbations induced by neighbor bubbles as shown on experimental correlations (Figure 3.20). A linear regression of the initial slope of the curve provides:

$$\mathrm{Dh} = -\mathrm{A}\frac{d}{(CC(d) - 1)} \qquad (3.\ 40)$$

where A=1.472. From Eq. (3.40) it is thus possible to calculate the horizontal dimension Dh for spherical bubbles knowing d and measuring CC(d). It should be notice the good

agreement with the result of the analytical approach, which also determined the slope of the cross-correlation curve to be 1.5 (Eq. 3.34).

Alternately, the extrapolation of the slope intersects the abscissa at d/D ≈ 0,7, which indicates that Dh ≈1,6 d at the intersection: this provides the range of measurable sizes with this technique.

The effect of eccentricity and θ angle on the cross-correlation

In order to develop a method capable of measuring the bubble size in the heterogeneous regime, it is necessary to understand how the bubble shape can affect the cross-correlation. In our experimental conditions, the bubble size population will be polydispersed in size and, according to Clift et al. (1978) in tap water/air systems, bubbles larger than 1 mm have an ellipsoidal shape. The distortion of the bubble shape can be described by the eccentricity (Eq. (3.3)), and results from the impact of gravity on the bubbles (Clift et al., 1978). An ellipsoidal bubble can have up to three diameters with different lengths and, consequently, several shapes can be considered. In this work only two different ellipsoidal shapes were considered, namely oblate and prolate shapes, as shown in Figure 3.21.

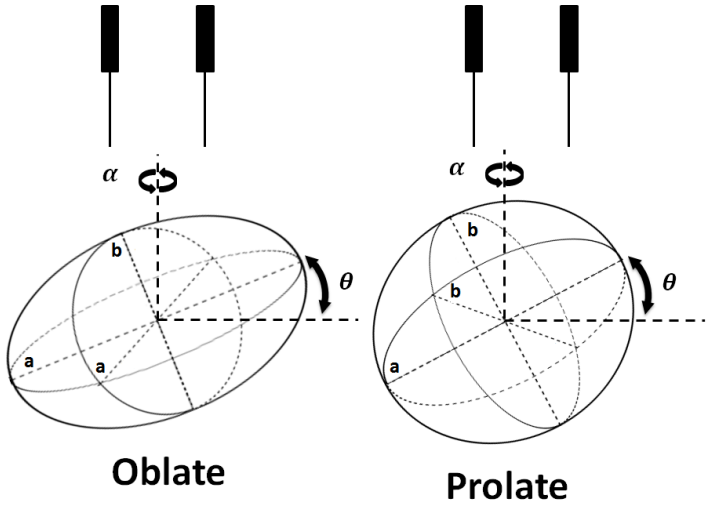

Figure 3.21 - A) Two different configurations of an ellipsoid shaped bubble.

The prolate shaped bubble is an ellipsoid with one large diameter (axis a) along a close to the horizontal direction and two small diameters (axis b) of the same length,

presenting symmetry relatively to the horizontal axis. An oblate ellipsoid has two large diameters (axis a) and a small diameter (axis b) close to the vertical direction, presenting symmetry relatively to the vertical axis, as can be seen in Figure 3.21. The oblate shaped bubble was the first configuration to be studied. Contrarily to a spherical bubble, that is symmetrical relatively to all of its Cartesian axis, the oblate one is only symmetrical with respect to its horizontal axis. To take this fact into consideration in the theoretical approach, the cross-correlation was calculated for an oblate shaped bubble that can be randomly inclined by an angle θ (with respect to an horizontal plane) evolving in a range of +/-30 degrees (Figure 3.21). This range in θ angle was also proposed by Xue et al. (2003) in the development of the four-point optical probe. To correctly reproduce the bubble-probe interactions it was necessary to consider that the bubble can randomly rotate from 0° up to 360° around the b axis (angle α). Up to this point, both probes were set in space at the same height, but in order to simulate this both rotations the second probe is now located at:

$$x_2 = x_1 + d\cos\alpha\sin\theta \quad (3.\ 41)$$

$$y_2 = y_1 + d\sin\alpha\sin\theta \quad (3.\ 42)$$

$$z_2 = z_1 + d\cos\theta \quad (3.\ 43)$$

Where (x_1, y_1, z_1) and (x_2, y_2, z_2) represent, respectively, the first and second probe positions and d represents the distance between probes. Figure 3.22 presents the results from the calculation of the cross-correlation for an oblate shaped bubble with a horizontal diameter of 4 mm, for eccentricities of 1, 0.7 and 0.5.

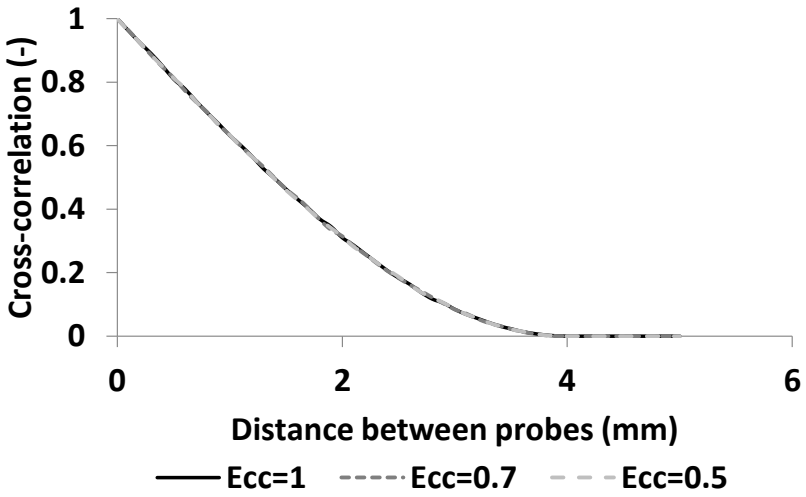

Figure 3.22 - Variation of the cross-correlation with the distance between probes for an oblate shaped bubble of various eccentricities (Dh=4mm, $\theta \in [-30°, 30°]$). (model).

The results showed that, in the considered range of θ angles, the eccentricity has no significant impact on the cross-correlation curves. Since an oblate with an eccentricity of 1 is a sphere, the determination of the horizontal diameter Dh of an oblate shaped bubble can also be achieved using Eq. (3.40).

Another possible configuration for a deformed bubble is a prolate ellipsoid, as schemed in Figure 3.21. In this configuration, the eccentricity impacts the vertical diameter and one of the horizontal diameters, axis b in Figure 3.21. As in the oblate bubble analysis, the angles θ and α were considered to be random between +/- 30 degrees and 0 to 360 degrees, respectively. Recurring to the theoretical approach, the effect of eccentricity was studied through the calculation of cross-correlation curves for a fixed bubble horizontal diameter (4mm), as can be seen in Figure 3.23. In this study, the eccentricity was varied from 0.5 up to 1, a range consistent with the measurements performed in our flow conditions with the endoscopic imaging method (further detailed on this section). The results show that the eccentricity increases the initial slope of the cross-correlation curves, meaning that the previously methodology used to find the bubble horizontal diameter cannot be applied to prolate bubbles. Moreover, it was found that at iso-eccentricity, the curves of the cross-correlation overlap when represented as a function of the ratio 'probe distance/bubble horizontal diameter' (d/Dh). It is possible to conclude that the effect of the bubble horizontal diameter on the cross-correlation curves that was described for the oblate shaped is also present in the case of prolate shaped bubbles. Moreover, there is a second effect caused by the eccentricity that also impacts the cross-correlation curves regardless of the bubble horizontal diameter.

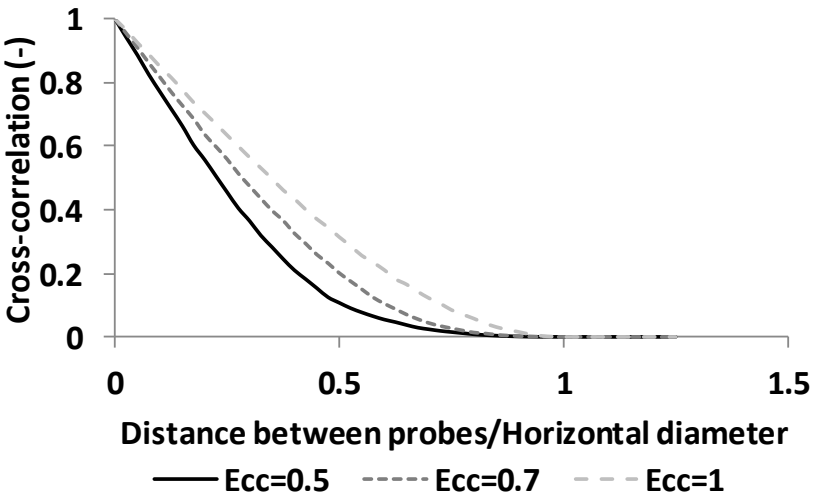

Figure 3.23 – Evolution of the cross-correlation with the ratio 'distance between probes/Horizontal diameter' for prolate shaped bubbles of various eccentricities (model).

In order to extract the information about the bubble horizontal diameter, a study was performed to quantify the impact of eccentricity on the initial slope of the cross-correlation curves. In order to do so, the ratio between the initial slope of a prolate shaped bubble cross-correlation curve and the one of a spherical bubble cross-correlation curve (Ecc=1) was calculated for several eccentricities. This ratio can be calculated by the following fit.

$$\frac{Initial\ slope\ (Ecc)}{Initial\ slope\ of\ a\ sphere} = 0.9933 Ecc^{-0.494} \qquad (3.\ 44)$$

Substituting the previous equation on Eq. (3.40), the A factor yields:

$$\mathrm{A} = 1.426 \mathrm{Ecc}^{-0.494} \qquad (3.\ 45)$$

This result shows that when the bubble eccentricity is known, one can calculate the horizontal diameter of prolate shaped bubbles using the cross-correlation. The sensitivity of the coefficient to eccentricity is significant (Figure 3.24) with deviations up to 40% when comparing the case of a sphere with a prolate shaped bubble with an eccentricity of 0.5.

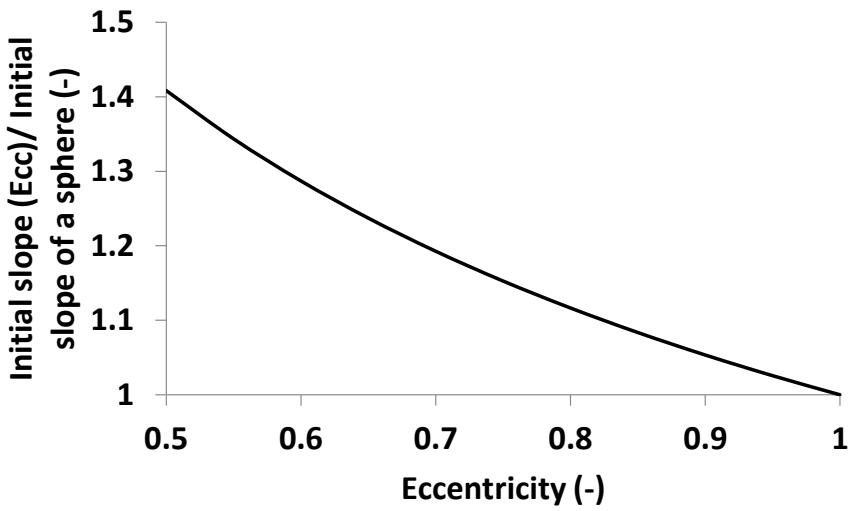

Figure 3.24 – Evolution of the ratio "Initial slope (Ecc)/Initial slope of a sphere" with the eccentricity for prolate shaped bubbles.

Up to this point, the spatial cross-correlation method has proven its ability to measure the bubble size along a horizontal plane. Moreover, in the case of spherical or oblate shape the both diameters on the horizontal plan have the same dimension. Therefore, this dimension can be directly obtained from the experimental cross-correlation and the distance between the probes used in the experiment (Eq. (3.40)). Hence, it has been proved that the eccentricity did not impact these measurements.

On the contrary, in the case of a prolate shaped bubble, there are two different dimensions in a horizontal plan (axis a and b in Figure 3.21). Moreover, the measurement is sensitive to the eccentricity, as shown in Eq. (3.45). In this case, in order to obtain the horizontal size it is necessary to know the bubble eccentricity, which has to be obtained through another measuring method (e.g. endoscopic imaging).

Up to this point three different bubble shapes have been considered in ideal flow conditions (1D, single bubble). In actual flows, deviations from such ideal situations are expected notably due to bubble orientation, distributions in size and in shape, 3D motion, finite void fraction, etc... As a first step, eccentricity and orientation distributions are taken into account. For that, the experimental conditions encountered in the studied bubble columns are the starting point. Thus, to infer the shape of the bubbles on the flow, the endoscope was inserted on the column along its axis. In that manner, contrarily to what has been described in section 3.2, the eccentricity measured will be the ratio between the two horizontal diameters of the bubble. For that reason, that quantity will be referred

to as the horizontal eccentricity. The experiments were carried out on the Phi 400 column, in the center of the column at h/D=3.75 and at superficial gas velocities between 3 cm/s and 16 cm/s. The horizontal eccentricity distribution for all the tested superficial gas velocities is presented in Figure 3.25.

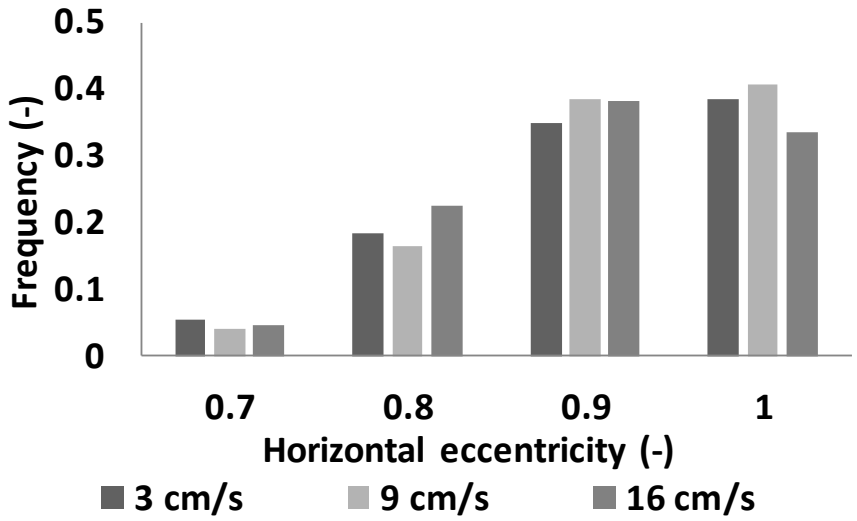

Figure 3.25 – Distribution of the bubble horizontal eccentricity, measured by the endoscopic imaging method. (measurements in the column Phi 400, column center at h/D=3.75)

Further superficial gas velocities were not tested due to insufficient illumination in such experimental conditions. The results show that the majority of the measured bubbles have an horizontal eccentricity higher than 0.8 (~80%) and that there is no significant effect of the superficial gas velocity. Moreover, no bubbles present horizontal eccentricities less than 0.7. Since the prolate shaped bubbles have identical vertical and horizontal eccentricities and since , as will be further shown, the average vertical eccentricity is 0.7, it will be considered that the bubbles present in our flows have an oblate shape.

So far in the cross-correlation calculus the eccentricity has been considered as constant, regardless of the bubble size and the flow regime. However, in a real flow there is a distribution of eccentricities that can evolve with experimental conditions. In order to study the variation of the bubble eccentricity, experiments were conducted in the Phi 400 column, in the column center at h/D=3.75, at superficial gas velocities from 3 cm/s up to 35 cm/s. The PDFs of the eccentricity measured during these experiments are presented in Figure 3.26.

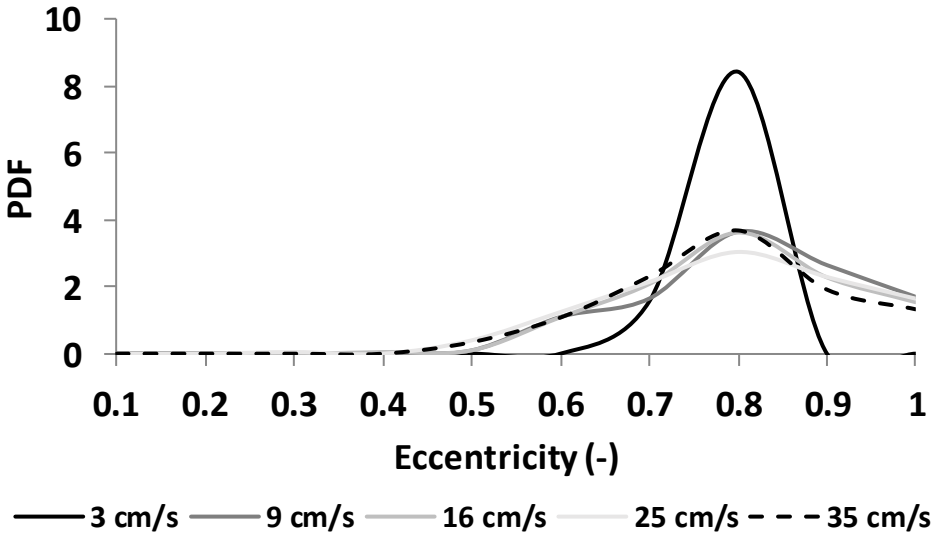

Figure 3.26 – PDF of the bubble vertical eccentricity, measured by the endoscopic imaging method. (measurements in the column Phi 400, column center at h/D=3.75)

The results show, as previously referred, that there are bubbles with different eccentricities. Moreover, at 3 cm/s the eccentricity presents a narrow distribution, between 0.6 and 0.9. Higher superficial gas velocities displayed wider distributions, between 0.5 and 1, and no significant effect of the superficial gas velocity was found for values higher than 9 cm/s. The arithmetical mean and the standard deviation of the presented distributions are depicted in Figure 3.30

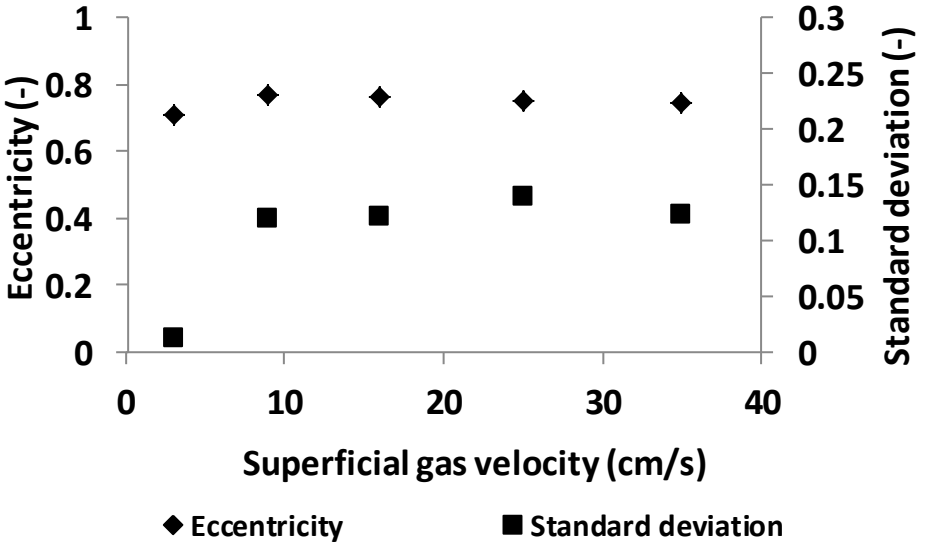

Figure 3.27 – Evolution of the mean vertical eccentricity and of the standard deviation of the vertical eccentricity distribution with the superficial gas velocity, measured by the endoscopic imaging method. (measurements in the column Phi 400, column center at h/D=3.75)

The results indicate that the averaged vertical eccentricity is constant around 0.7 for the all tested superficial gas velocities. Moreover, at 3 cm/s the eccentricity distribution presents a low standard deviation (≈ 0.01) while at higher superficial gas velocities the standard deviation remains constant, close to 0.1. Therefore, in the cross-correlation calculus it will be considered that the eccentricity distribution does not change with the superficial gas velocity.

It is also important to investigate the variation of the eccentricity distribution with the bubble size. Since there is no significant variation of the eccentricity distribution with the superficial gas velocity, the variation of the eccentricity with the bubble size has been performed only for Vsg16 cm/s. Figure 3.30 presents the PDF of the eccentricity for different bubble horizontal diameters.

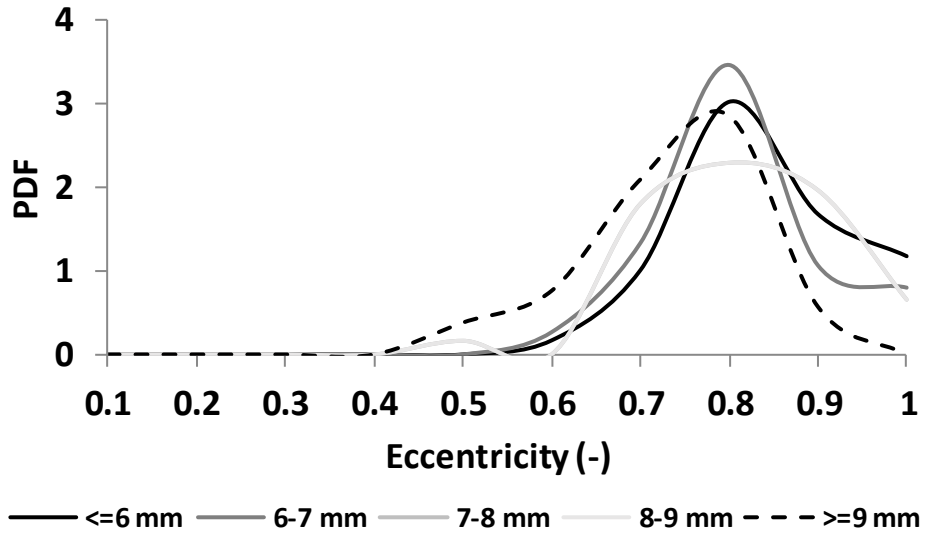

Figure 3.28 - PDF of the bubble horizontal eccentricity for different bubble sizes, measured by the endoscopic imaging method. (measurements in the column Phi 400, column center at h/D=3.75, superficial gas velocity 16 cm/s)

The results demonstrate that the PDF of the eccentricity for the different bubble size classes are similar, so it is possible to assume that the eccentricity distribution is nearly constant over the whole range of horizontal diameters detected in the flow. Consequently, a unique eccentricity distribution will be accounted for the calculus of the cross-correlation.

The angle θ (Figure 3.21), that was previously considered as random between ±30°, was also measured by endoscopic imaging. Since there are bubbles with different eccentricities on the flow, and since eccentricity may have a coupled effect with the angle θ, the distribution of the angle θ (absolute values) is presented in Figure 3.29 for different eccentricities.

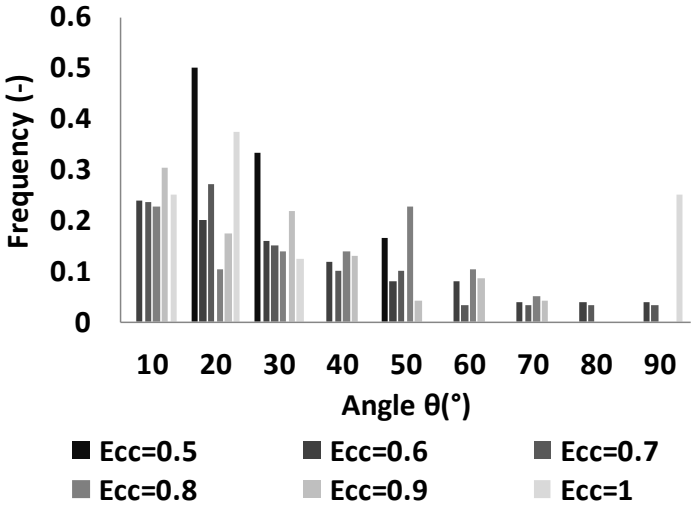

Figure 3.29 – Distribution of angles θ for different bubble eccentricities, measured by the endoscopic imaging method. (measurements in the column Phi 400, column center at h/D=3.75, superficial gas velocity 16 cm/s)

By analyzing Figure 3.29, it is possible to conclude that the θ angle distribution is not random and that it is wider than it was previously considered. Moreover, it is possible to observe that there is no significant correlation between the eccentricity and the θ angle distribution. Therefore, it will be considered that the angle distribution is constant for all the eccentricities present on the flow (from 0.5 up to 1).

Taking into account the above mentioned results of the endoscopic imaging measurements, a new approach of theoretical calculus of the cross-correlation was developed. The theoretical cross-correlation was computed for a bubble population of oblate bubbles with the same distribution of eccentricity (Figure 3.25, superficial gas velocity= 16 cm/s) and θ angle (Figure 3.29) detected on the endoscopic measurements (eccentricity range: 0.5-1; θ angle range: -90 - +90). For each iteration, the bubble eccentricity and θ angle were randomly chosen from their respective distributions and the probes were then set in space using Eqs. (2.25), (2.26) and (2.27). This process was repeated enough times for each probe distance to ensure convergence of the cross-

correlation. Then, this process was repeated for different distances between probes. Figure 3.30 shows the evolution of the cross-correlation as a function of the ratio 'probe distance/bubble horizontal diameter' for both methods. The 1st method corresponds to the approach where the eccentricity was fixed and the bubble inclination (angle θ) was randomly set between ±30°. The 2nd method uses the approach where bubble eccentricity and inclination obey the probability distributions detected by endoscopic imaging.

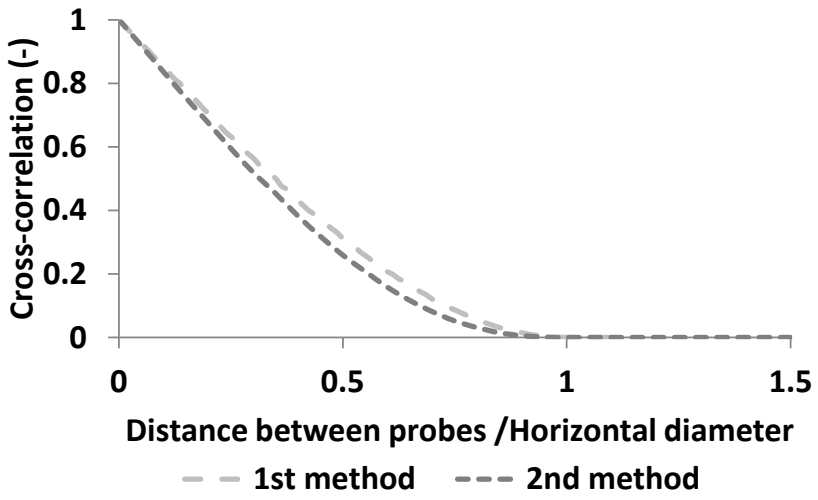

Figure 3.30 – The effect of considering the distribution of eccentricity and range of inclinations θ on the cross-correlation evolution with the ratio 'distance between probes/Horizontal diameter'. (model).

The results show that, with a broader angle distribution and with an eccentricity distribution, the cross-correlation coefficient, for a given probe distance, decreases. After adjusting the linear regression to the new results, the A factor takes now the value 1.598 instead of 1.472.

Regardless of the bubble shape considered, the expression to find the bubble diameter recurring to the cross-correlation value and the probe distance always follows the formalism $\mathrm{Dh} = -\mathrm{A}\frac{d}{(CC(d)-1)}$. Therefore, the impact of the bubble shape, inclinations θ angle and eccentricity on the obtained diameter can be evaluated by the variation of the variable A, as shown in Table 3.11.

Concluding, for spherical bubbles, eccentricity and inclinations are irrelevant and lead to a factor A=1.472 in the equation 3.24 that provides the bubble size. In a first approach for oblate shaped bubbles, the θ angle was considered random between ±30°

with an α angle was also randomly ranging between 0° and 360° (Figure 3.21). Within these ranges, the eccentricity has no impact on the cross-correlation and the factor A remains unchanged. In the case of prolate shaped bubbles, with similar ranges for the angles α and θ angles, the A parameter becomes a function of the bubble eccentricity (c.f. Table 3.11). For sake of comparison, the vertical eccentricity was considered to be 0.7 in agreement with the measured bubbles eccentricities detected in our experiments and presented in Figure 3.27: the resulting factor A becomes 1.7. The second method to calculate the cross-correlation for an oblate shaped bubble takes into account the measured distributions of vertical eccentricities and inclinations with respect to an horizontal plane and the factor A becomes 1.5978. These results show that the largest deviation between the four different approaches is 15.5 %, corroborating thus the resilience of the proposed method.

Table 3.11 – Table of A factors for all bubbles shapes and the deviation of the diameter estimation between a given bubble shape and a spherical bubble

	Sphere	Oblate (1st method) -30< theta <30	Prolate -30< theta <30	Oblate (2nd method) experimental Ecc (Figure 3.25) and θ angle distributions (Figure 3.28)
A	+1.472	+1.472	$1.426Ecc^{-0.494}$ 1.7 at Ecc=0.7	+1.5978
Deviation from the sphere case	-	0%	15.5%	8.54%

.

The void fraction effect

The theoretical approaches previously proposed considered only single bubble interactions with the probes. However, in the experiments, the local void fraction can be as large as 40%, and such conditions may alter the response of the measuring device. When comparing the simulated correlation coefficients (Figure 3.22) with those measured

in actual flows (Figure 3.14), it becomes clear that the measured correlation coefficients never decrease to zero but they reach a plateau that increases with the void fraction. Clearly, that portion of the curve is not exploitable for size measurements. The question is whether the first portion of the curve can still be used for accessing the horizontal bubble size.

To test the effect of the void fraction, a first simulation was carried out in which bubbles of the same size were randomly located in a control volume. In order to simplify the calculus, the bubbles were considered as spheres (Figure 3.31 A, B and C). The random bubble placement procedure imposes that the bubbles should not be intercepted neither by the control volume frontiers nor intercept themselves. The cross-correlation was calculated for configurations with ε_g up to 23 %. In addition, different spatial arrangements were tested in order to check whether or not the results depend on the spatial organization of the bubbles. The same cross-correlation curve was obtained (Figure 3.32), showing that the bubble positioning has no effect.

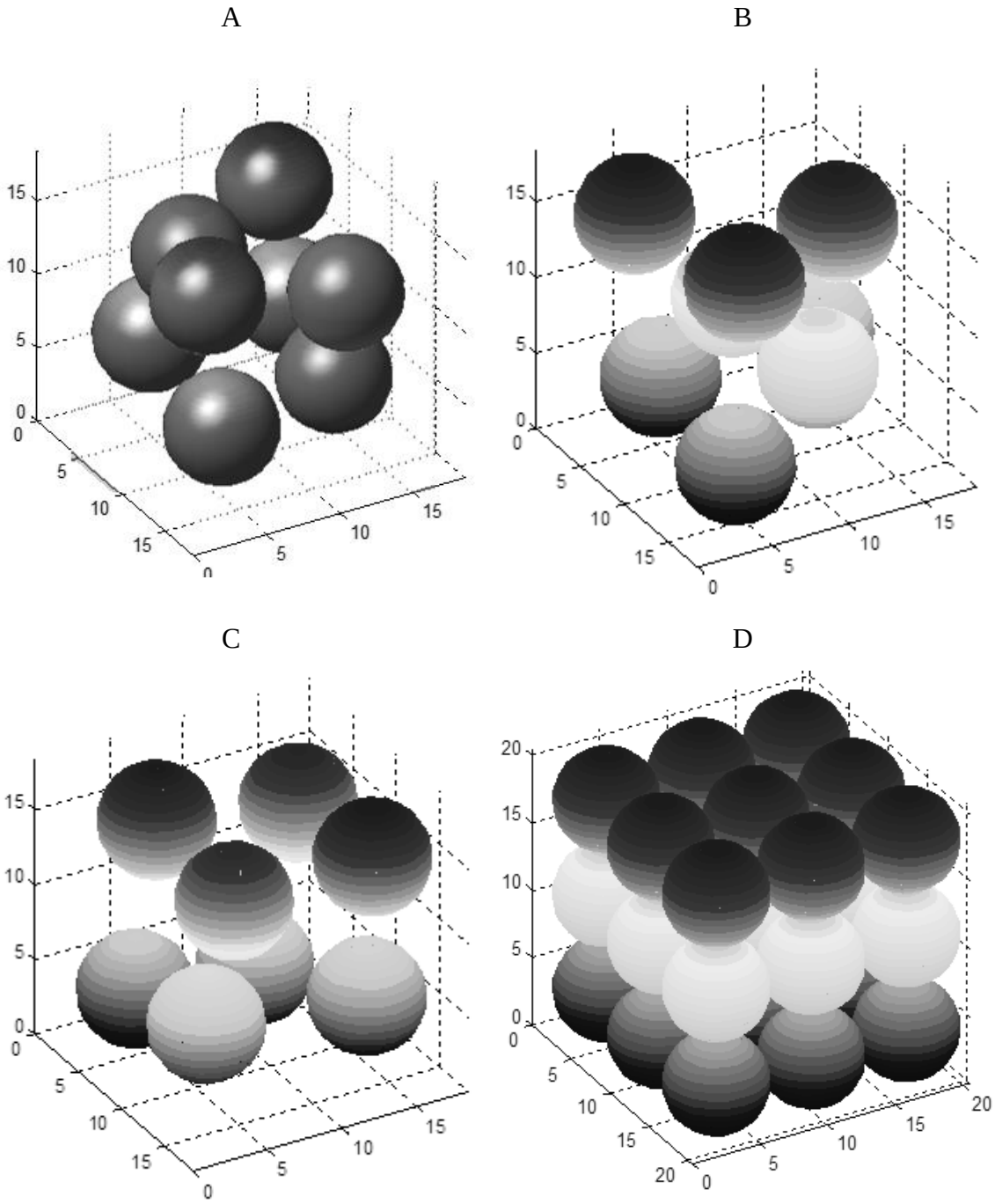

Figure 3.31 – Different 3D arrangements of spherical bubbles: A,B,C) Random placement (void fraction = 23%; D) Manual placement (void fraction = 41%) (model).

A second attempt was made where bubbles were manually set in space in order to decrease the computation time and therefore to simulate higher void fractions (namely 41 %). The selected arrangement is shown in Figure 3.31 D and the resulting cross-correlation curve is presented in Figure 3.32.

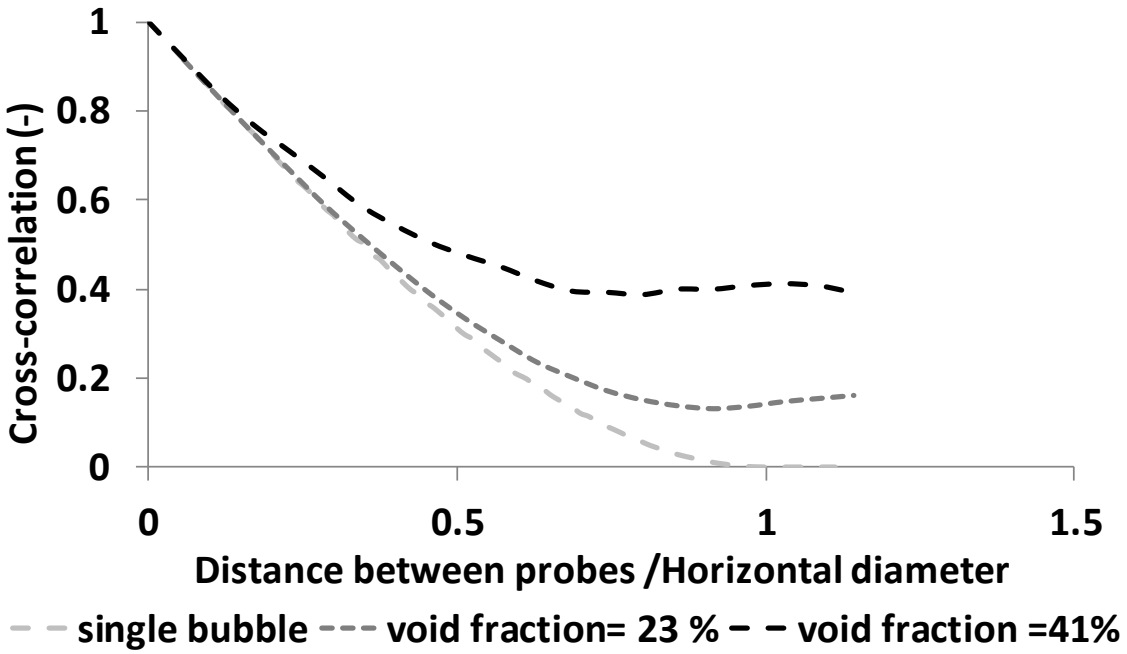

Figure 3.32 - Evolution of the cross-correlation with the ratio 'probe distance/bubble horizontal diameter' for spherical shaped bubbles at different void fractions. (model).

Clearly, the void fraction distorts the correlation coefficient as the probability that the two probes hit different bubbles increases. Yet the curve remains robust for short distances between probes: this trend is indeed expected since the probability to detect two different bubbles on each probe decreases when the probes are close enough to each other. Consequently, the prediction from the single bubble approach remains exploitable for short distances between probes. Therefore, to study the error committed using the single bubble assumption, the relative error of the estimation of the horizontal diameter was calculated as a function of the bubble horizontal diameter, for a probe distance of 0.8 mm, in Figure 3.33.

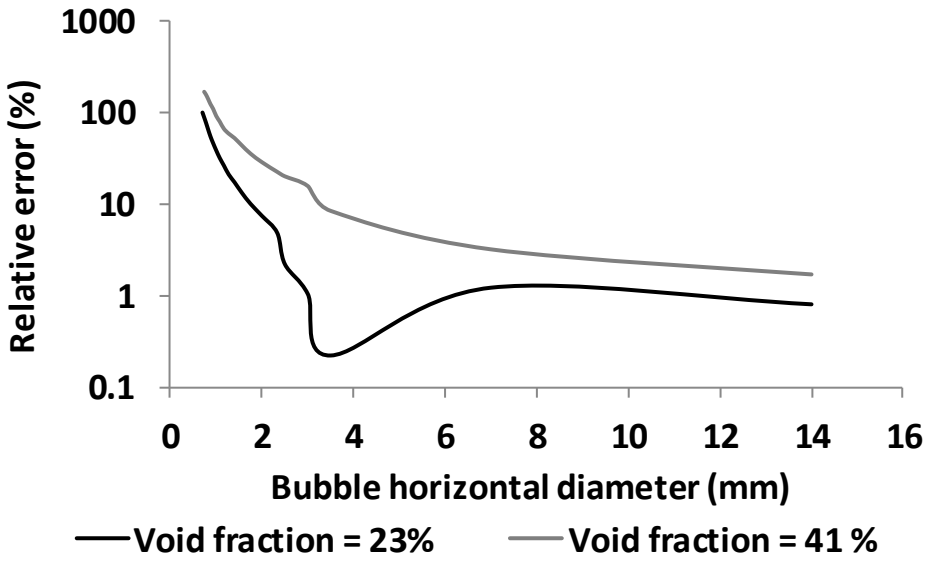

Figure 3.33 – Relative error of resulting of the single bubble approach as a function of bubble horizontal diameter for spherical shaped bubbles at different void fractions. (model , distance between probes = 0.8 mm).

Quantitatively, Figure 3.33 shows that in order to have an error on the bubble diameter estimation below 10%, the bubble horizontal diameter should be larger than 3.5 mm for a void fraction of 41%, and superior than 1.4 mm for a void fraction of 23%. Therefore, if one sets the probe distance to, say, 0.8 mm, the method based on the single bubble approach can correctly measure bubbles with a horizontal diameter above 3.5 mm at a void fraction 41%, and above 1.4 mm at a void fraction of 23%.

These results show the necessity to adapt the distance between probes as a function of the bubble size distribution present in the flow, in order to ensure an acceptable measurement error. In the present work, according to the endoscopic imaging results which will be discussed in chapter 4, at a void fraction around 20% the smallest bubble detected has a 2 mm horizontal diameter. Moreover, at 40% of void fraction the smallest horizontal diameter detected by the endoscopic measurement was 4 mm. Additionally, the local gas hold-up was never higher than 50%. In that view, it is possible to conclude that the chosen distance between the probes (0.8 mm) was sufficient to perform measurements with an error less than 10 % for all the flow conditions consider in this work.

Averaging type

So far, the cross-correlation technique was analyzed considering only monodispersed size distributions. In actual flow conditions, bubbles are polydispersed in size and in shape (or eccentricity). Thus, the measured cross-correlation will result from the contributions of bubbles of different sizes, each population being weighted by its respective contribution to the void fraction. As this technique only allows to determine a single characteristic dimension, the question is whether that dimension is significant when considering a polydispersion of bubbles. In other words, it is important to identify what type of averaging is made by the cross-correlation technique.

To answer this question, the response of a polydispersed population was modeled. N classes of bubbles are considered, each class being associated with an horizontal diameter Dh_i, a vertical diameter Dv_i and a void fraction ε_{gi}. In that vision, it is possible to define a normalized cross-correlation value CC as the ratio between the cross-correlation for a given probe distance and the cross-correlation value measured with both probes in the same point in space. In the case of a single bubble class, CC (i) can be written as:

$$CC(i) = \frac{\int_{t=0}^{T_{exp}} Signal_A(i,t) \times Signal_B(i,t)\partial t}{\varepsilon_{gi}} \tag{3. 46}$$

In case of several size classes present in the flow, the total normalized cross-correlation CC results from the sum of all bubble pulses, seen by both probes at the same time, and can be described as:

$$CC = \frac{\int_{t=0}^{T_{exp}} Signal_A(t) \times Signal_B(t)\partial t}{\varepsilon_g} \tag{3. 47}$$

where each signal can be decomposed as the sum of bubble pulses for each bubble class i, namely:

$$Signal_A(t) \times Signal_B(t) = \sum_i Signal_A(i,t) \times \sum_j Signal_B(j,t) \tag{3. 48}$$

Under the assumption that only one bubble can be detected by both probes at the same time (meaning that the effect of void fraction will not be modeled here):

$$\text{if } i \neq j \qquad Signal_A(i,t) \times Signal_B(j,t) = 0 \tag{3. 49}$$

Eq. (3.48) can be rewritten as

$$Signal_A(t) \times Signal_B(t) = \sum_i Signal_A(i,t) \times Signal_B(i,t) \quad (3.50)$$

By replacing Eq. (3.50) in Eq. (3.47):

$$CC = \frac{\int_{t=0}^{T_{exp}} [\sum_i Signal_A(i,t) \times Signal_B(i,t)] \partial t}{\varepsilon_g} = \frac{\sum_i \left[\int_{t=0}^{T_{exp}} Signal_A(i,t) \times Signal_B(i,t) \partial t\right]}{\varepsilon_g} = \frac{\sum_0^n \varepsilon_{gi} CC(i)}{\varepsilon_g} \quad (3.51)$$

Finally, if Eq. (2.22) is applied to an oblate bubble population with several bubble classes i:

$$\mathrm{CC} = \frac{\sum_1^n \left[1 - \mathrm{A}\frac{d}{D_{hi}}\right] {Dh_i}^2 Dv_i}{\sum_1^n {Dh_i}^2 Dv_i} = \frac{\sum_1^n \left[1 - \mathrm{A}\frac{d}{D_{hi}}\right] Dh_i^3 Ecc_i}{\sum_1^n Dh_i^3 Ecc_i} = \frac{\sum_1^n \left[1 - \mathrm{A}\frac{d}{Dh_i}\right] Dh_i^3}{\sum_1^n Dh_i^3} = \frac{\sum_1^n D_{hi}^3 - \sum_1^n \left[\mathrm{Ad}\frac{Dh_i^3}{Dh_i}\right]}{\sum_1^n Dh_i^3} = 1 - A\mathrm{d}\frac{\sum_1^n Dh_i^2}{\sum_1^n {Dh_i}^3} \quad (3.52)$$

The equivalent diameter is equal to $\frac{\sum_0^n D_{hi}^3}{\sum_0^n {D_{hi}}^2}$ so the mean horizontal diameter obtained from the cross-correlation corresponds to the Sauter average (Dh_{32}) of the horizontal dimension of bubbles using the size distribution present in the system. The same conclusion was obtained in the derivation of the model for spherical bubbles, and the demonstration hereinabove show that that conclusion also holds for distorted bubbles.

Uncertainty determination

Four different sources can contribute to the uncertainty on the bubble diameter measurement using the cross-correlation technique:

- the uncertainty on the distance between optical fibers,
- the reproducibility in the measurement of the cross-correlation,
- the uncertainty in the determination of the slope using a linear regression,

- the deviation from an ideal response due to finite void fraction.

As previously mentioned, the experimental data used for the horizontal diameter determination was obtained using two optical probes at the same elevation on the column, with a distance between probes of 0.8 mm. The distance between the fibers was measured by the society A2 Photonic Sensors recurring to a microscope with an error of +/- 6 µm. This uncertainty in the probe distance alters the diameter estimation only by 0.075%, therefore it will be disregarded.

To evaluate the uncertainty on the experimental determination of the cross-correlation value, the measurements were repeated several times in the same conditions, with the same probes. The results show a variation of 0.44 % on the cross correlation value that affects the diameter estimation by ±2.5 %.

The variation of the cross-correlation with the ratio of the distance between the probes and the bubble horizontal diameter is not linear, making the linear regression an approximation. As it will be presented in chapter 4, the horizontal diameter of the bubbles found in the flow varies from 2 mm up to 14 mm, causing the ratio 'probe distance/bubble horizontal diameter' to vary from 0.06 up to 0.4. Consequently, the slope resulting from the linear regression calculation can vary ±2 %, depending on the interval in which it is calculated (from 0 to 0.06 or from 0 to 0.4). If this difference is transposed to the diameter prediction, a ±6% variation can be found.

The error caused by the simultaneous detection of two bubbles is a function of the void fraction and the ratio 'distance between the probes/bubble horizontal diameter', as can be seen in Figure 3.32. Therefore, it is not possible to estimate a global value for this error, becoming necessary to do it for every operational condition. Moreover, this error can only overestimate the bubble horizontal diameter measurement.

Therefore, the overall uncertainty on the Dh_{32} measurement using the cross-correlation technique will be considered to be ±6%, a value corresponding to the maximum of all sources of uncertainties. If one considers all uncertainties as cumulative, i.e., that all factors bias the measurements in the same way, then the uncertainty reaches ±10.5%, a value still acceptable.

The above considerations assume perfect, non-intrusive optical probes. In practice, the finite size of optical probes can induce bubble shape/trajectory distortions during bubble-probe interactions (Vejrazka et al., 2010) which may contribute to the measurement uncertainty. As previously discussed (section 3.3), most of the considered flow conditions are quite favorable for an optimal probe response. Thus, simulations of

bubble-probe interactions were not attempted. Instead, comparisons with measurements performed using alternative techniques were used to test the reliability of the cross-correlation technique. In addition, deviations from ideal unidirectional flows were also tested.

Spatial cross-correlation measurements

The cross-correlations were measured using two optical probes at the same height in the column, side by side, at a given horizontal distance from each other. Each measurement was performed during the detection of 10000 bubbles, to assure the convergence of the cross-correlation value, as shown in Figure 3.34.

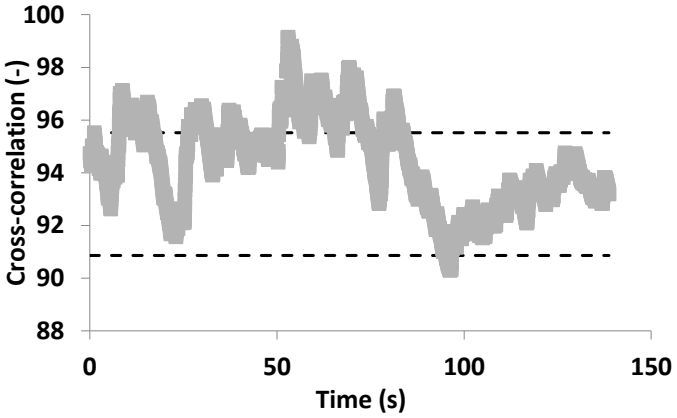

Figure 3.34 – Convergence of the cross-correlation value as function of time for an experiment in the Phi 400 column, at 35 cm/s in the column center (experimental, dashed lines ±2.5 %)

The experiments carried out to measure bubble horizontal diameter were made with a straight bi-probe composed by two independent 1C mono-fiber optical probes. The fibers had the same length and were radially spaced by 0.8 mm. For the experiments with no distance between the probes only one 1C mono-fiber optical probe was used and its signal was auto-correlated.

A resume of the bubble size measuring methods and their capabilities is presented in Table 3.12.

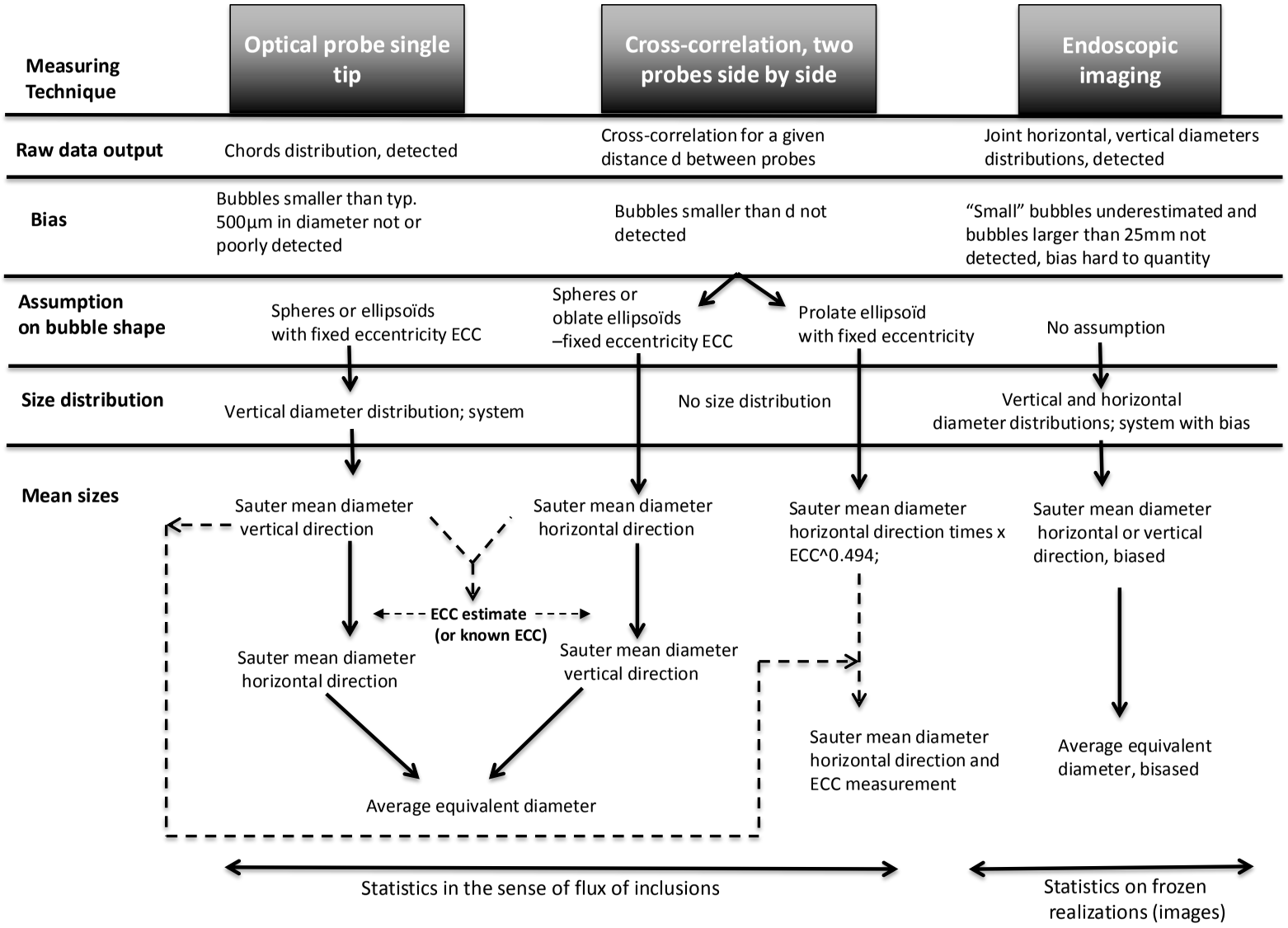

Table 3.12 – Resume of measuring methods and measured variables.

3.5 Validation of local measuring methods

In this section the performances of the above detailed measuring methods will be studied. At first, the Pavlov tube measurements will be compared to the results of other authors obtained in similar conditions. Afterwards, the results of the 1C mono-fiber optical will also be accessed, both the typical measurement capabilities and the new Dh_{32} measurement method. To do so, results obtained in experimental set-ups described in chapter 2 will be compared with results from other authors and with the results of the endoscopic imaging measurements.

Pavlov tube

In order to validate the measurements of the liquid velocity performed with the Pavlov tubes, the results will be compared with measurements from other authors. As presented in Chapter 1, liquid velocity measurements on large bubble columns at high void fractions are scarce in the literature. The available data on the axial liquid velocity are plotted in Figure 3.35.

Degaleesan et al (1990, 2001) have performed measurements with a CARPT system and Forret et al. (2003) have measured liquid velocities with Pavlov tube. A resume of the experimental conditions used by these authors is presented in Table 3.13.

Table 3.13 – Resume of experimental conditions of the literature data on liquid velocity.

Authors	Column diameter (m)	Superficial gas velocity (cm/s)	Global gas hold-up (%)	Measurement h/D	Typical uncertainty (%)	Time resolution (Hz)
Degaleesan et al., 1990	0.3	10.5	-	Averaged between 0.1<h/D<2	-	33
Degaleesan et al., 2001	0.44	9.6	19	Averaged between 0.75<h/D<4	-	33
Forret et al, 2006	0.4	12	19	h/D=3	±10	50

In Figure 3.35 are also plotted the data obtained from the Pavlov tubes with the two sets of pressure sensors, namely one with frequency bandwidth of 8 Hz (referred to as Pavlov @ 8Hz) and one with a frequency bandwidth of 100 Hz (referred to as Pavlov @ 100 Hz). The data were obtained in the Phi 400 column at h/D of 3.75 and for a gas superficial velocity of 9.5 cm/s.

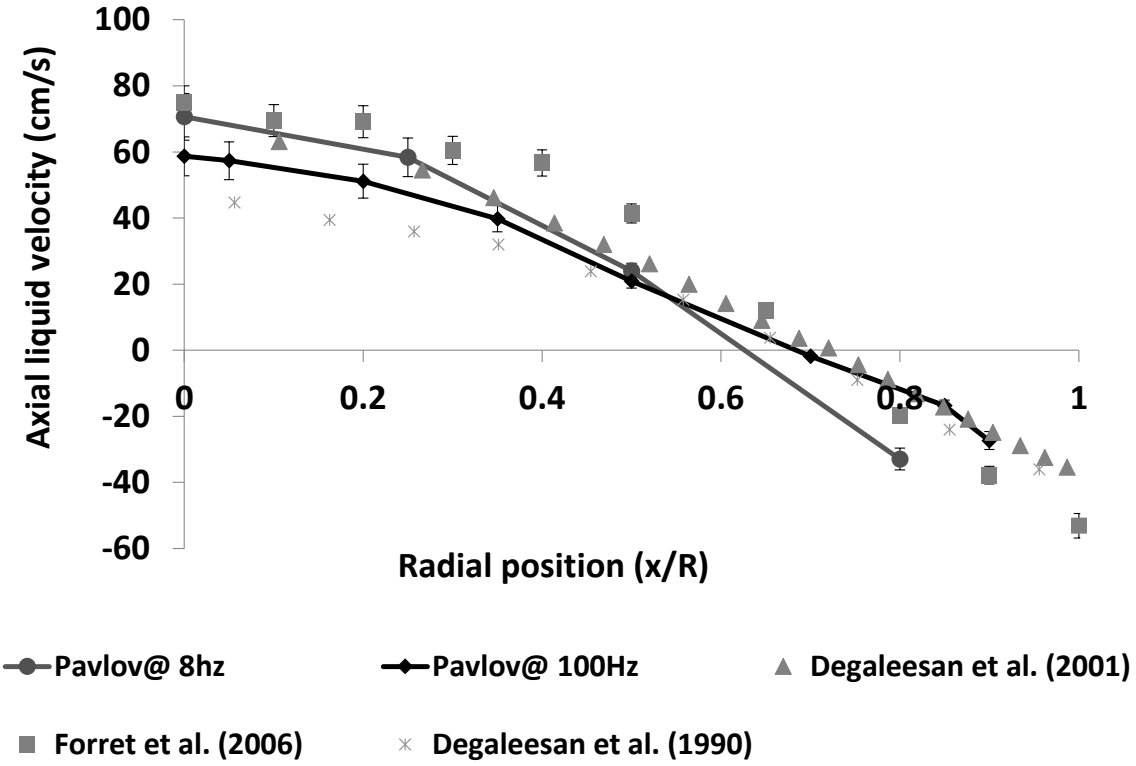

Figure 3.35 – Evolution of the axial liquid velocity with the radial position. (Vertical bars represent the ±10 % measurement error of the Pavlov tube)

Globally the results are all in good agreement all along the column radius. The profiles from the 8 Hz and the 100 Hz Pavlov tubes present the same shape and provide similar values as those found by Degaleesan et al. (2001). The radial profile of Devanathan et al. (1990) has a shape similar to the above mentioned profiles, but with a significantly lower axial liquid velocity in the centre of the column. The liquid velocity in the column centre can be estimated by the correlation Eq (1.3) as a function of the column size and the superficial gas velocity. The measured and predicted liquid velocities in the centre of the column, for all the data series presented in Figure 3.35, are compared in Table 3.14.

Table 3.14 – Measured and predicted values of the axial liquid velocity in the center of the column (ul(0)).

Authors	ul(0) (cm/s)	Eq (1.3) (cm/s)	Difference between measured and estimated values (%)
Degaleesan et al., (1990)	50	59	-14 .8%
Degaleesan et al., (2001)	63	61	3.6 %
Forret et al, (2006)	75	69	8.9%
Pavlov @ 8 hz	70	60	17%
Pavlov @ 100 hz	58	60	-3%

The results show that the measurements of Degaleesan et al., (1990) are considerably lower than the predicted velocity (~15%) , possibly because of the small diameter of their column. Moreover, the higher velocities measured by the Pavlov tube with a frequency bandwidth of 8 Hz are explained by an overestimation of the liquid velocity (+17%): oddly such deviations are observed with the sensor which has the best resolution (typically 0.01 m/s). The results of Forret et al, (2006), Degaleesan et al., (2001) and the Pavlov @ 100 Hz present an agreement between the measurements and the predicted values within a ±10% interval. Let us recall that the resolution of the Pavlov @ 100 Hz is rather poor, typically about 0.1 m/s. So it is possible to conclude that the two Pavlov tubes can correctly measure the mean axial liquid velocity in the Phi 400 bubble column. None of the previously mentioned authors have reported any profile of the radial liquid velocity, so it is impossible to test the response of Pavlov tube in the radial direction.

As referred to in section 3.1, by applying the Reynolds averaging definition it is possible to evaluate the liquid axial velocity fluctuations u’ (where u’ denotes here the root-mean-square of velocity fluctuations) and the turbulence kinetic energy along the axial direction (u'^2). In Figure 3.36 are provides the radial profiles of liquid turbulent kinetic energy reported in literature as well as our measurements performed in the same experimental conditions as detailed in Figure 3.35.

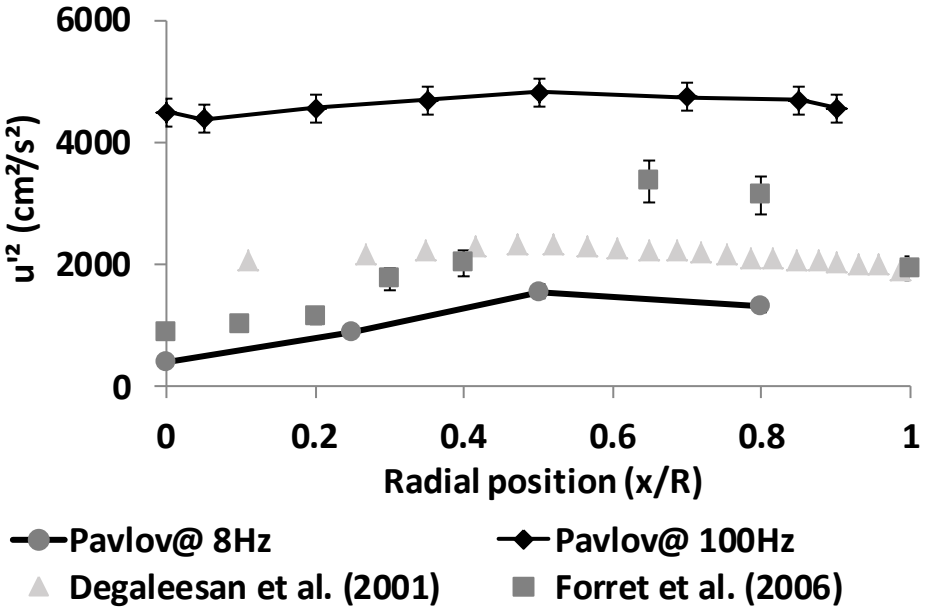

Figure 3.36 – Evolution of the axial liquid turbulent kinetic energy (u'^2) with the radial dimensionless position. (Vertical bars represent the ±20 % measurement error of the Pavlov tube)

Contrary to the mean axial liquid velocity, the available experimental results on the liquid turbulent kinetic energy are in a poor agreement. The Pavlov results present almost flat profiles but with quite different intensities: the 100 Hz Pavlov presents velocity fluctuations four times higher than the 8 Hz Pavlov. The Pavlov @ 100 Hz used for each velocity component two different pressure sensors. Thus, the discrepancy on the results presented in Figure 3.36, can result from a cumulative effect of the uncertainty of each pressure sensor. Moreover, the results from Degaleesan et al. (2001) also present a rather flat profile along the column radius, with values close to the measurements performed with the 8 Hz Pavlov tube. Forret et al. (2006) have reported a profile that peaks around x/R=0.7, the location where the mean axial liquid velocity changes its direction. If one set aside the 100 Hz Pavlov tube, all profiles present similar magnitudes of axial turbulent kinetic energy. Similar are found when comparing the radial liquid turbulence kinetic energy (v'^2) as shown in Figure 3.37.

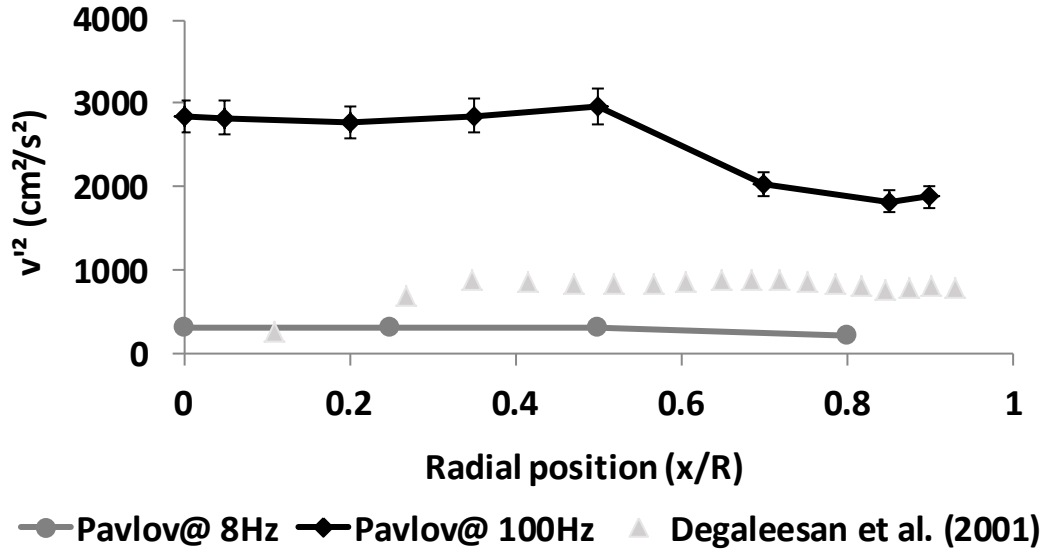

Figure 3.37 – Evolution of radial liquid turbulent kinetic energy (v'^2) with the radial dimensionless position. (Vertical bars represent the ±20 % measurement error of the Pavlov tube)

Since the Pavlov tube is able to measure simultaneously the axial and radial velocity components, the Reynolds stress tensor (u'v') can be computed. The comparison between the results obtained with the two Pavlov tubes configurations and the results from literature are presented in Figure 3.38. Menzel et al. (1990) have measured the liquid velocity in a 0.6 m diameter column using a hot-film anemometry method.

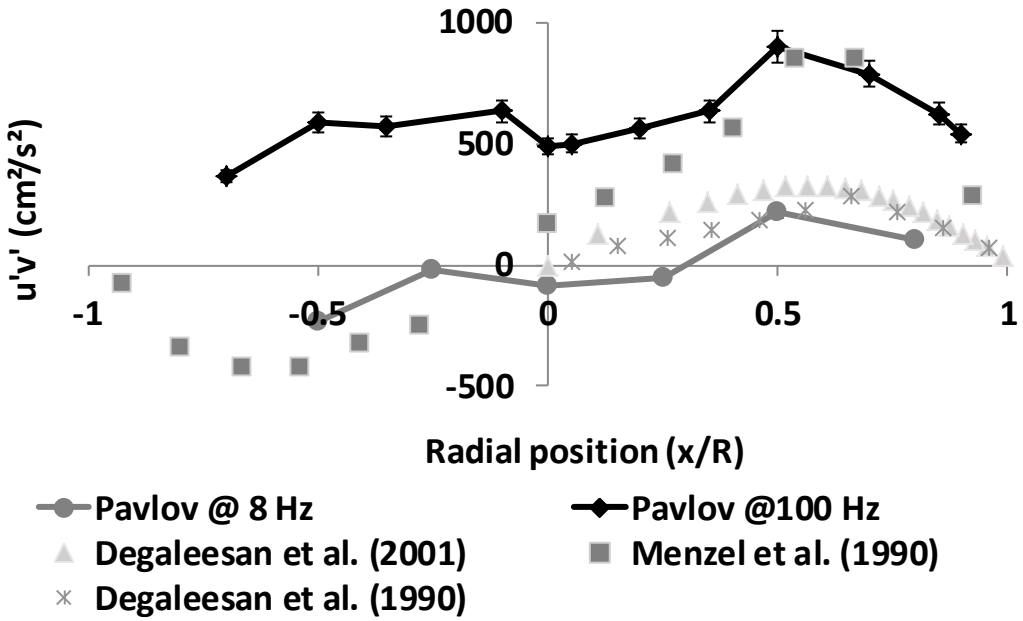

Figure 3.38 – Evolution of the Reynolds stress tensor (u'v') with the radial dimensionless position. (Vertical bars represent the ±20 % measurement error of the Pavlov tube)

The results show that the 8 Hz Pavlov profile presents the same trend than those of Degaleesan et al. (2001) and of Devanathan et al. (1990), but with smaller values of the Reynolds stress tensor. As already noted in Figure 3.36, the 100 Hz Pavlov profile is flat and with a much higher magnitude than the 8 Hz Pavlov. The results form Menzel et al. (1990) present higher values of Reynolds stress tensor, as expected, since they were obtained in a larger column. However, the difference seems too large to be only explained by the scale-up effect alone. An explanation for this difference could be that the 8 Hz Pavlov and the 33 Hz CARPT measurement system are filtering some velocities fluctuations. The 100 Hz Pavlov always gives much higher values of velocity fluctuations than the other methods, even higher than the results of Menzel et al. (1990) that were acquired in a larger bubble column.

Concluding, the time average axial liquid velocities measured from the Pavlov tubes were validated by comparison with similar results from different authors: within ±15%, the magnitudes are in agreement with previous findings. The Pavlov tubes are also able to measure the velocity fluctuations, but large differences were observed between the two systems. In the 8 Hz configuration, the measurements always provide lower values compared with those obtained by other authors, a trend that may be related with the low time resolution of the pressure sensor. Contrarily, the 100 Hz configuration always present higher velocity fluctuations. Both sensors will be exploited for the analysis of the flow behaviour in Chap.4.

Optical probes

In this section, the performance of the 1C mono-fibre optical probe in the experimental conditions described in chapter 2 will be detailed. As previously discussed, these probes were mainly validated in somewhat favourable conditions, namely quasi unidirectional flows. Since this work aims at measuring bubble dynamics in large bubble columns (up to 3 m diameter) and in high gas hold up (up to 30%) it is necessary to verify their performance in heterogeneous and strongly agitated flows. In the following, the measurement capability of the optical probes in terms of gas hold-up, vertical bubble size and bubble velocity will be checked. Afterwards, the new method developed in section 3.4 to access to the Dh_{32} will be tested.

Another factor that can impact the performance of the optical probes is the fouling formation on the probe tip. Since the experiments were carried in large bubble columns it is impossible to use distilled or permutated water. Consequently, deposits can be formed on the probe sensible tip, which can alter the de-wetting process and block the passage of the light beam through the probe tip. Normally, this phenomenon is accompanied with an attenuation of the gas signal voltage and can lead to underestimation of the bubble velocity. Such conditions were detected during the experiments, and since it is an irreversible process the experiments were repeated with a different probe.

Void fraction measurements

Accurate measurements with optical probes require the correct detection of all bubbles crossing the probe tip position. With the discussion on the modified Weber number M in section 3.3, we have already seen that the mean flow conditions considered here are favorable in the sense that trajectory deviations or shape distortions are minimized. Yet, various flow features depart from this ideal view. First, strong velocity fluctuations are present in most flow conditions (see Chap.4) with a magnitude often comparable to the mean velocity. Therefore, some bubble-probe interactions arise with low (and even nearly zero) approaching velocities. In such cases, the M parameter decreases by an order of magnitude, resulting in trajectory modifications, velocity deceleration and thus distorted detections. Even more, velocity fluctuations can lead to flow reversal anywhere along a column radius, and how optical probes detect bubbles arriving from its rear is a situation poorly documented. Finally, the mean flow itself is reversed in regions near the wall. All these features lead to quite challenging conditions for optical probes. Although a systematic investigation of the impact of the bubble trajectory on the probe response could have been feasible on a dedicated test bench, it was decided to directly analyze the probe response in our flow conditions.

As a first step, the bubble detection efficiency was first checked by considering the void fraction measurements. Indeed, the probe provides local gas hold-up, and after integration over a cross-section, one obtains the surfacic gas fraction. The surfacic gas fraction should be equal to the volumic gas fraction (equivalently the global gas hold-up) provided that the flow is quasi fully-developed and stationary. The global gas hold-up $\bar{\varepsilon_g}$ was measured by the bed expansion method and thus it concerns the entire volume of the

column. Therefore, the fully developed assumption is clearly not fulfilled. Despite this shortcoming, the comparison has been attempted. The measurements were performed all over the cross-section with a probe vertical position and pointing downwards.

For the integration, since the gas hold-up was not measured close to the column wall, it was considered that the gas hold-up is zero on the column walls and that it varies linearly between the last measured point(at x/R=0.8) and the wall. Assuming there is no variation of the void fraction along the height of the column, the surfacic void fraction is compared to the global gas hold-up measured. For the integration, we considered the radial profiles have been collected at h/D= 3.75.

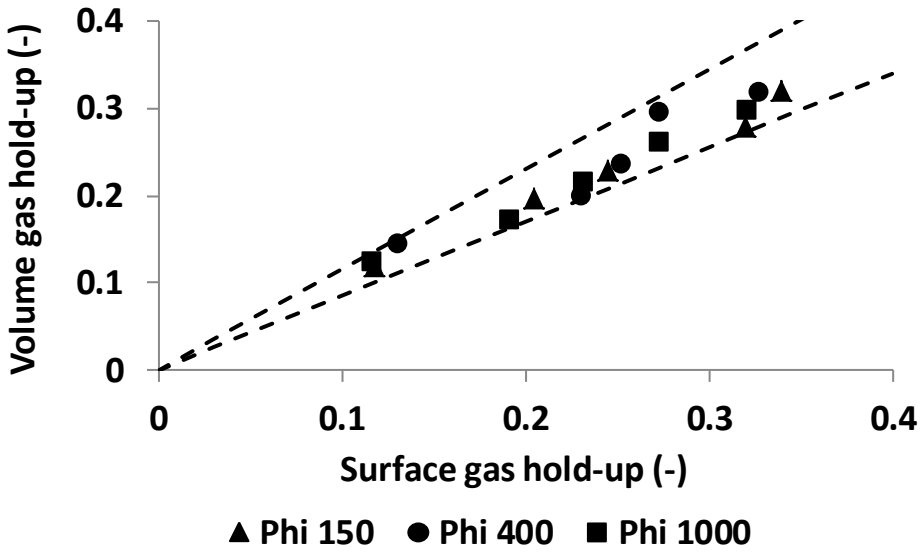

Figure 3.39 – Comparison between the volumic gas hold-up and the surfacic gas hold-up deduced from the optical probes measurements. (Dashed lines ±15 %)

As can be seen in Figure 3.39, the volumic and surfacic results present a deviation under ± 15 % superficial gas velocities ranging from 3 cm/s up to 35 cm/s in the three columns. One should bear in mind that the measurement of the volume gas hold-up was performed by the measurement of the height expansion, with a typical relative uncertainty of ± 10 %. Therefore it is possible to affirm that both measurements are in good agreement.

In conclusion, the void fraction measurements by the 1C mono-fiber optical probe were validated in dense and 3D flows as the ones found in bubble columns up to 1 m of diameter and at gas hold-up values up to nearly 40%. This good result is not too surprising as void fraction measurements with single optical probes are known to be insensitive to

the probe orientation with respect to the main flow at least up to 90° angles (Barrau et al., 1999; Zun et al.,(1995)). Yet, let us recall that in the present conditions, such angles can be much higher than 90° and even reach 180° when the flow is reversed.

The impact of these challenging flow conditions is expected to be much more drastic when considering more refined variables such as the interface velocity, grounded on the de-wetting dynamics, and the bubble size distributions, related with the gas residence time of the probe tip inside bubbles. As a first step, let us first analyze the optical probe signals and some of their characteristics.

Optical probes signal in heterogeneous flows

The raw signals happen to be quite similar to those observed in less complex bubbly flows, notably with very similar bubble signatures expect for the "double bubbles" that will be discussed later.

As a first indication of the correct probe functioning, let us consider the percentage of bubbles of type T1 that corresponds to bubbles signatures with a fully de-wetted probe (see section 3.2): that percentage gives an information on the quality of the measurements. In unidirectional flows and for millimeter size bubbles, this parameter is typically about 90%. The evolution of the percentage of T1 bubbles along the column radius in the Phi 400 for a superficial gas velocity of 16 cm/s is plotted in Figure 3.40 A. Figure 3.40 B presents the evolution of the percentage of T1 bubbles with the superficial gas velocity, for the Phi 150, 400 and 1000 column at center of the column.

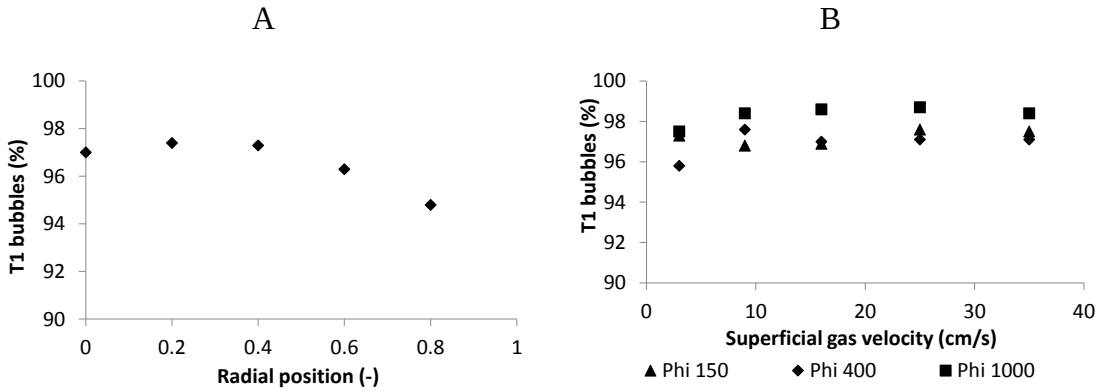

Figure 3.40 - A) Evolution of the % of T1 bubbles in the measurements along the column radius in the Phi 400 column at 16 cm/s at h/D=2.5. B) Evolution of the % of T1 bubbles in the measurements with the superficial gas velocity in the column center at h/D=2.5.

The results depicted in Figure 3.40 B show that, whatever the superficial gas velocity the percentage of T1 bubbles in our measurements were always of the same order of magnitude as in the unidirectional experiments of the literature. Figure 3.40 A shows that the percentage of T1 bubbles slightly decreases along the column radius, however it remains quite large. These trends are to be expected owing to the somewhat large size of bubbles considered here. Indeed, T1 signatures corresponds to signals that reach the upper gas level: here bubble sizes are about a few millimeters while the probe sensing length is a few tens of micrometers so that complete probe de-wetting is highly probable. Since a bubble velocity is evaluated whenever the ratio of the residence time over the rising time is exceeds a few units (Barrau et al., 1999), all T1 signatures will provide a velocity in the present flow condition. Consequently, and contrary to situations involving smaller bubbles (say below 2-3mm), there is no selection criteria on the range of impact angles (the impact angle is defined between the probe axis and the local normal vector to the interface) and the transformation rise time–velocity is therefore unduly applied for some signatures (this is notably so for bubbles trajectories normal to the probe axis). Thus, the % of T1 bubbles is not a meaningful criterion to ascertain the reliability of velocity measurements in the present flow conditions.

To further analyze of the signals delivered by the 1C mono-fiber optical probe, the rising time and gas residence time PDFs have been examined. Examples of such PDFs are presented in Figure 3.41: these data were collected in the center of the Phi 400 column at h/D=2.5 and for a superficial gas velocities of 3 cm/s and 35 cm/s.

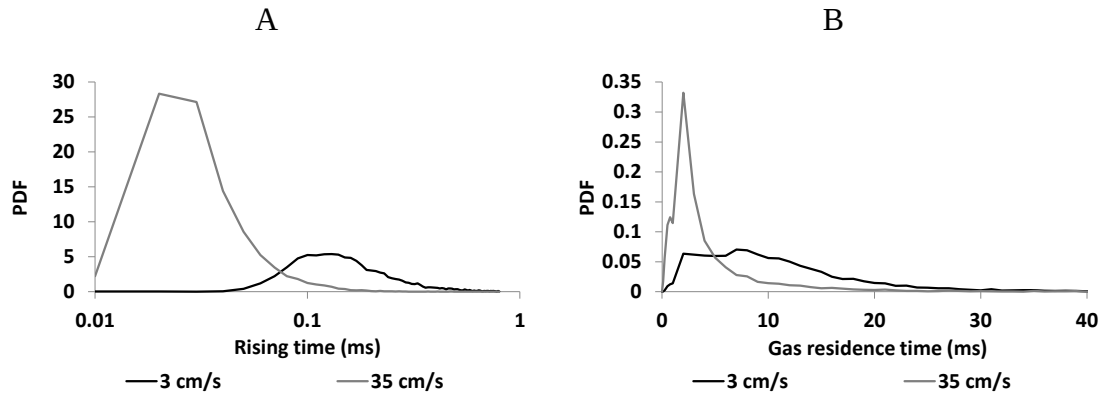

Figure 3.41 - A) PDF of rising times B) PDF of gas residence times (measurements in the Phi 400 column, at the column center and h/D=2.5)

Figure 3.41 A presents the PDFs of the rising times at superficial gas velocities of 3 cm/s and 35 cm/s. These distributions are similar to what is commonly observed in bubbly flows. Let us recall that the rising time corresponds to the time required to de-wet the sensible tip of the probe. As previously referred to, the bubble velocity along the probe axis is given by the ratio between the sensing length of the probe and the rising time of each bubble. Therefore, and as expected, the PDF measured at v_{sg}=35 cm/s is centered on lower values than the one measured at 3 cm/s, since the bubbles are rising faster at 35 cm/s.

Figure 3.41 B presents the PDFs of the gas residence times at superficial gas velocities of 3 cm/s and 35 cm/s. Again, these distributions have the same shape as those commonly gathered in bubbly flows when using conical probes (see also the discussion on the PDF shape in Vejrazka et al. 2010). The gas residence time represents the time that the sensible tip of the probe passed inside each bubble, and the pierced chord can be computed by the product of the bubble velocity and the gas residence time of each bubble The distribution for v_{sg}=3 cm/s is centered on a higher gas residence than the one for v_{sg}=35 cm/s: this is consistent with the change in velocity since the bubble sizes are nearly the same according to endoscopic measurements (see Figure 3.48).

Some special bubble signatures have been detected in the raw signal. The anomaly illustrated Figure 3.42 corresponds to a pair of bubbles separated by a thin liquid bridge. When the distance between the two bubbles is smaller than the probe sensitive length, the probe tip is not completely wet and the signal voltage does not drop down to the *liquid level*. As a consequence, the signal post-treatment considers that there is only one bubble those velocity is that of the first one and with a *gas residence time* corresponding to the sum of both contributions.

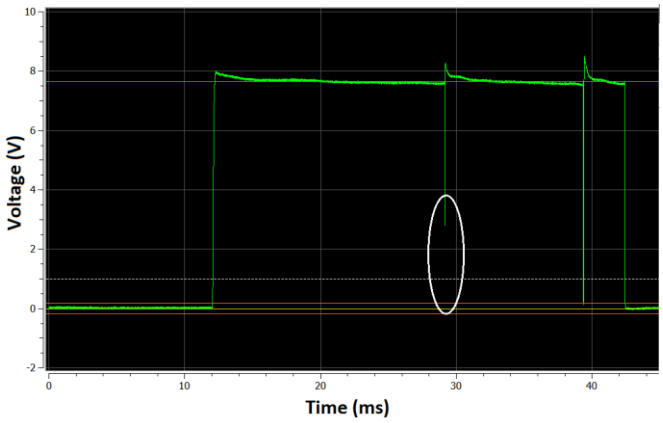

Figure 3.42 – Signal anomaly: two bubbles detected as one.

The occurrence of this phenomenon increases with the gas hold-up, since the distance between bubbles is reduced and the presence of unsteady 3D structures on the flow can lead to the formation of bubble swarms. The impact of this anomaly on the flow was studied for superficial gas velocity of 35 cm/s in the Phi 1000 column center. The probability of detecting a bubble pair happens to be quite small, less than 0.2% of the total number of bubbles detected, and that holds at all superficial velocities (see Table 3.15). In addition, the "double bubble" events have been manually processed to extract the true chord for each bubble. Thereafter, the mean chord has been evaluated accounting for the presence of two bubbles and it has been compared with the value given by the post-processing. As seen from Table 3.15, the maximum difference is less than 2.5%. Thus, the occurrence of bubble pairs has no significant impact on the measurements, and we did not implement any criteria in the signal processing to detect such events.

Table 3.15 – Occurrence of "double bubbles" and their impact on the mean chord.

Superficial gas velocity (cm/s)	9	16	25	35
% fraction of double bubbles detected	0.09	0.11	0.19	0.15
C_{10} (mm) original post-treatment	2.93	3.64	3.82	4.44
C_{10} (mm) with the treatment of double bubbles	2.90	3.60	3.73	4.35

All the above analysis indicates that, even in presence of high gas hold-up and unsteady 3D structures, the optical probes are still capable of correctly detecting the bubbles and in particular, there is no odd behavior of the raw signals nor of the characteristic times statistics.

As already pointed out, a key issue in our flow conditions is the impact of the probe direction with respect to the main flow. Before discussing this, it is important to evaluate how often the flow reverses its direction. This has been quantified by the fraction of time during which the liquid is descending, deduced from the instant velocity measured by the Pavlov tube. The results for the columns Phi 400 and Phi 1000 at h/D= 3.75 are presented in Figure 3.43 A, B and C, respectively.

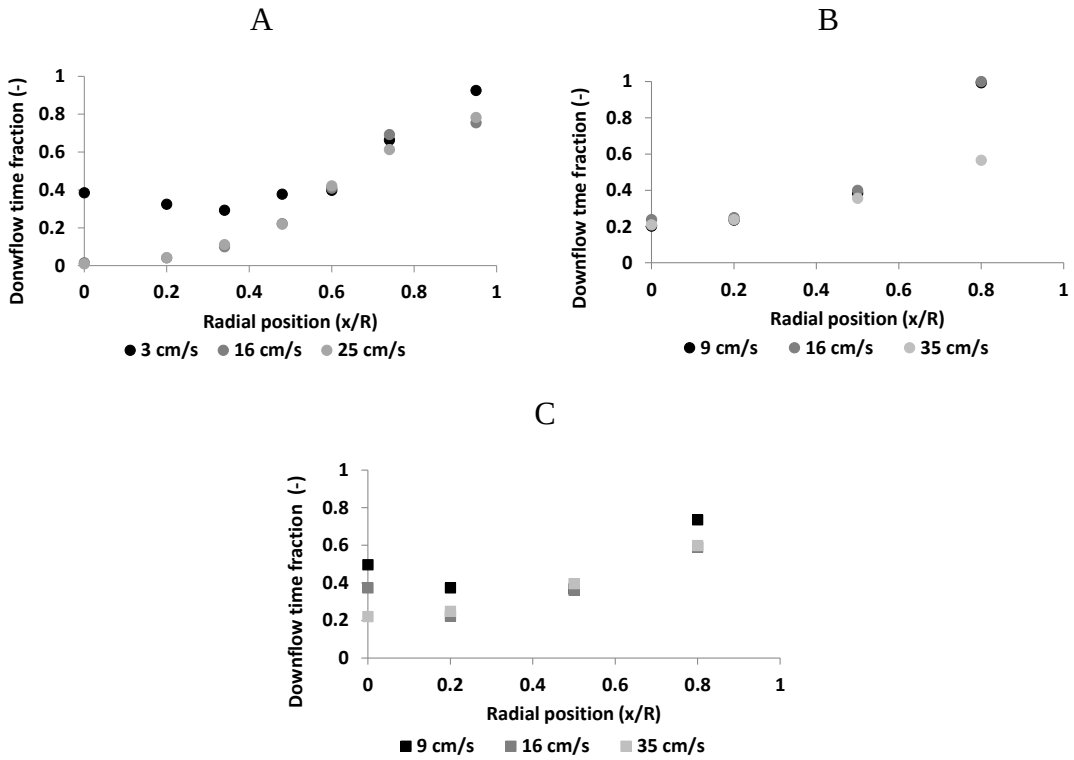

Figure 3.43 – Evolution of the fraction of time with a downward directed velocity along the column radius at h/D=2.5: A) Phi 400 (Pavlov @ 8Hz) B) Phi 400 (Pavlov @ 100Hz) C) Phi 1000 (Pavlov @ 100Hz, h/D=3.75).

Some quantitative differences arise depending on what pressure sensor has been connected to the Pavlov, but clear trends appear. First, and whatever the superficial gas velocity and the column size, the time fraction monotonically increases along the column radius. This is due both to fluctuations than can lead to absolute negative velocities and, at larger distance from the axis, to the downward directed mean liquid motion. Note that a fraction of 50% corresponds roughly to $x/R \approx 0.7$, which is indeed the location of the mean flow reversal: that indicates that the above measurements are consistent. In the central region, the occurrence of a downward liquid velocity remains significant, including on the column axis with typical value between 20 and 40% at low vsg (see Figure 3.43). Note that for v_{sg}=9cm/s and higher, the two pressure sensors provide quite different results near the axis. On the axis, one found 1% according to the 8 Hz sensor, to be compared with 20% for the 100Hz sensor. Owing to the resolution, the results gathered with the 8Hz sensor may be more reliable, so that no absolute negative velocity arise on the axis at v_{sg}=9cm/s and above (see also the velocity pdf in Figure 4.45 Chap.4). At v_{sg}=3cm/s, the magnitude of the negative velocities are up to 20-30cm/s (see Figure 4.45 Chap.4): this is sufficient to entrain a fraction of the bubbles population downward. Also,

and whatever v_{sg}, the occurrence of downward directed velocity is already significant ($\geq$10%) at x/R$\approx$0.2. Thus, when analyzing quantities integrated over a cross-section, one should bear in mind that downward directed motions are always present and will affect the probe response. This was notably the case for the void fraction: it that case, the consequences of the change in flow direction on the measurement uncertainty were limited.

Let us now use the above features to investigate the sensitivity to the probe orientation. To investigate the effect of the bubble trajectory with respect to the probe, measurements were performed in the same flow conditions and for different orientations of the probe with respect to the mean flow. Hereafter, an angle of 0° corresponds to a probe pointing downward. These tests have been only achieved at low v_{sg} (namely 3cm/s) in the center of the Phi 400. As seen above, in these conditions, the liquid velocity is directed downward roughly 40% of the time. Although it is probable that the same figure measured on bubble velocities would have been lower, it is likely that downward directed bubble motion was present as well.

Figure 3.44 presents the effect of the angle on the measured variables. The local gas hold up and the bubble detection frequency are given Figure 3.44 A.

A

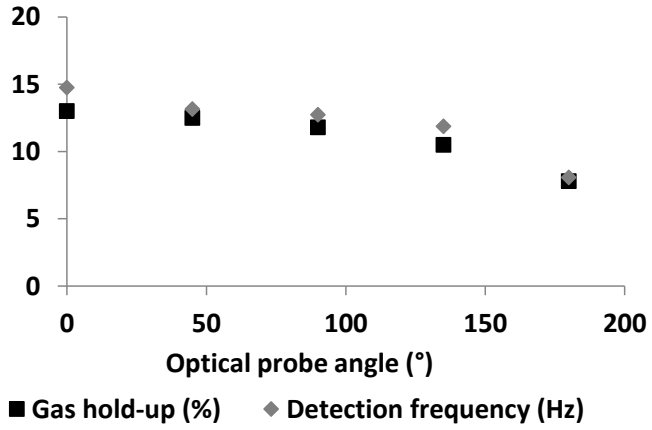

B

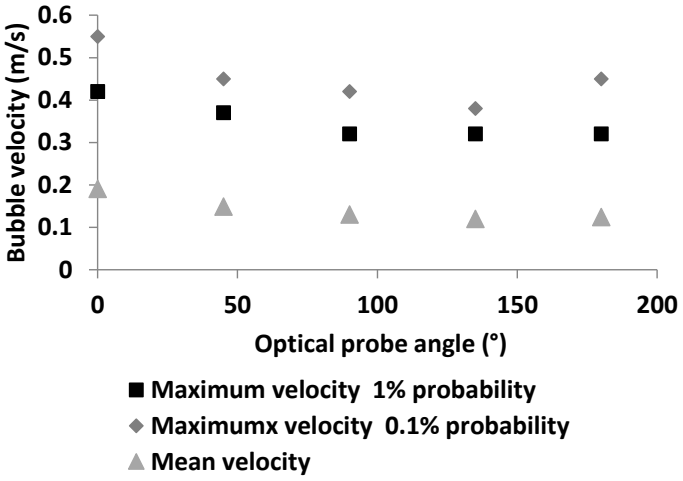

C

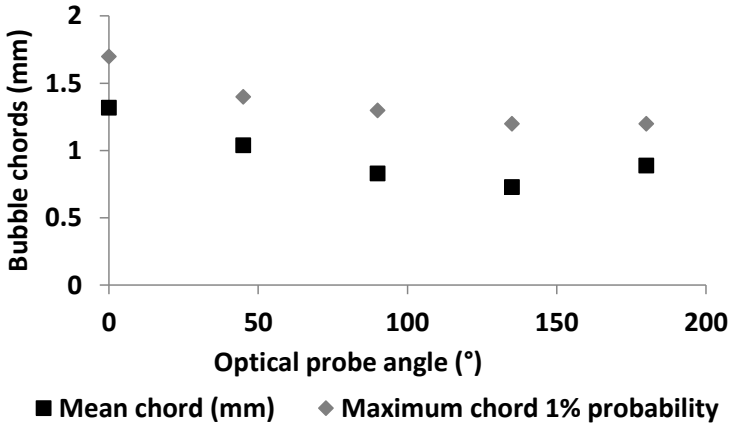

Figure 3.44 – Incidence of the probe orientation with respect to the flow (0° = vertical probe pointing downward) on key quantities: A) Local gas hold-up and bubble detection frequency; B) bubble velocity; C) Bubble chords (Measurements obtained in the Phi 400 column at h/D=2.5 and x/R=0)

The first striking result is that whatever the orientation between 0° and 180°, the probe detects a significant number of bubbles. The detected void fraction and the bubble detection frequency drop by 40% between 0° and 180° when compared with the value at 0°. As flow reversal is present at most 40% of the time and with moderate downward velocities (0.3 cm/s at most) that can hardly entrain the largest bubbles, it is clear that bubbles coming from the rear and hitting the probe tip are also perceived by the probe.

Detected velocities (mean and maximum values) monotonously decrease with the angle (Figure 3.44 B). The decrease is steep between 0 and 45°, and less marked thereafter. The difference between 0° and 180° corresponds to a 30-35% drop in the detected velocity. Similar trends are observed on the mean chord and on maximum chords: again, the drop between 0° and 180° is in the range 35-40% (Figure 3.44 C). As a majority of bubbles are selected for velocity measurement (the decrease of the proportion of T1 bubble with the angle - from 95 to 90% - is negligible), it is clear that the impact conditions (in terms of probe axis with respect to the normal to the interface) are strongly varying. Hence, the rise-time velocity relationship established for close to normal impacts is unduly applied to a larger proportion of hits as the angle increases. The decrease in the velocity is also to be expected as normal impacts provide the shortest de-wetting times, i.e. the largest velocity measurements. For the chord, there is an additional effect due to the lateral motion of bubbles since, for oblique trajectories, the chords detected become closer to the horizontal diameter instead of the vertical dimension of bubbles.

When examining the local gas flux (Figure 3.45), the sensitivity to the probe orientation is even more pronounced with a drop by a factor nearly 60% from 0° to 180° compared to the value at 0°. That corresponds to a ratio of 2.5 between extreme values. Such magnitudes are not surprising as the gas flux gathers information relative to the number of bubbles, velocities and chords.

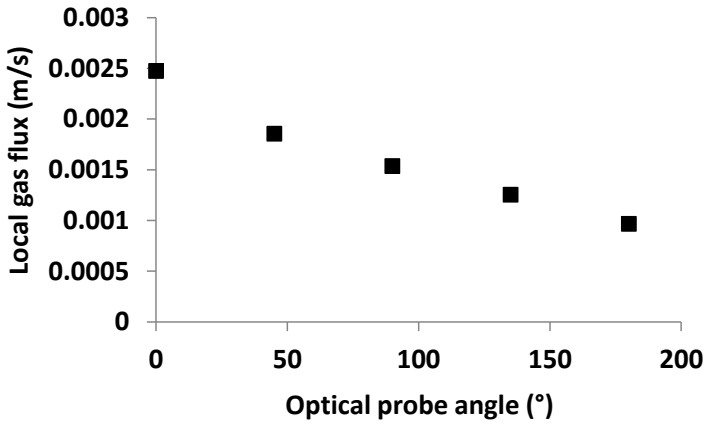

Figure 3.45 - Incidence of the probe orientation with respect to the flow (0° = vertical probe pointing downward) on the local gas flux (Measurements obtained in the Phi 400 column at h/D=2.5 and x/R=0)

The above information are not sufficient to provide a complete understanding of the probe response in such complex flows. In particular, it would have been interesting to repeat the above tests in others flow conditions, such as at higher v_{sg} or in the region of mean downward motion. They nevertheless underline some of the difficulties in the interpretation of the measurements. Let us now evaluate the reliability of the bubble velocity as measured with optical probes in such flow conditions.

Bubble velocity measurements

Inside the bubble columns, we had no possibility to compare the bubble velocity measured with the optical probe with an alternate technique. Indeed, the 1C mono-fiber optical probe is the only method, among those used in this work, which that can measure the bubble velocity. Besides, the comparison of the bubble velocity measurements with the results from others authors can be challenging because the experimental conditions were not the same and the techniques were different. Thus, to roughly evaluate the quality of bubble velocity measurements, we considered the largest velocities detected in each phase and assume that they should be strongly correlated. In a "smooth" bubbly flow, they should be the same but this is no longer true for example if strong in-homogeneities (such as void fraction gradients) are present in the flow.

With the optical probe, the highest interface velocities are expected for bubbles moving vertically upward (shortest de-wetting time): such events also correspond to

optimal detection conditions for optical probes. The liquid velocity was extracted from Pavlov tube data: let us recall that this information is collected over a region of significant extent (≈15mm see Chap. 2). Arbitrarily, the averaging was performed over the 10% highest values. The averages of the 10% highest bubble velocities measured in the Phi 400 column, in the center of the column and at h/D=2.5 for superficial gas velocities ranging from 3 cm/s up to 35 cm/s, are presented in Figure 3.46. The averages of the 10% highest liquid velocities (measured with the Pavlov@8Hz) at the same location in the Phi 400 column for superficial gas velocities of 9 cm/s, 16 cm/s and 35 cm/s are also reported in Figure 3.46. For sake of comparison, and as optical probes are unable to detect the sign of the velocity, the liquid velocities are essentially upward in these selected conditions.

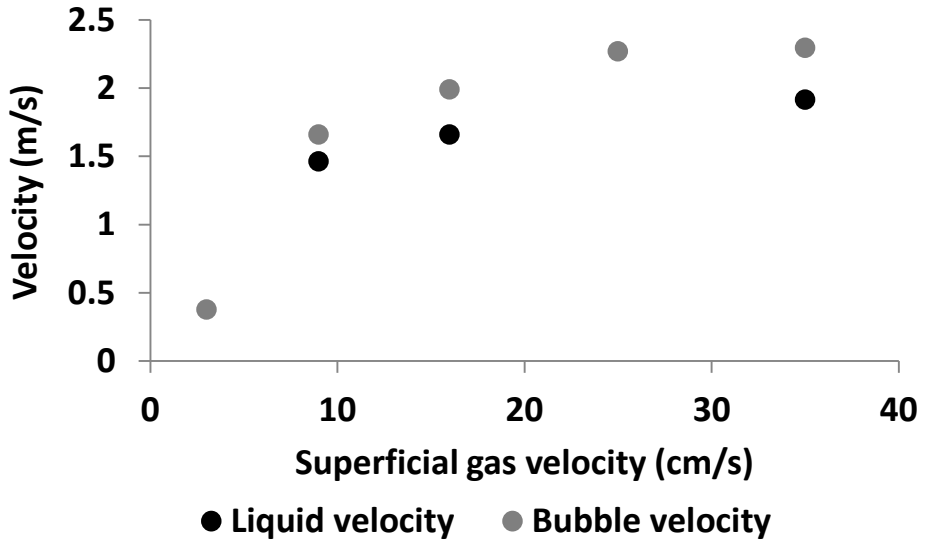

Figure 3.46 – Comparison between the averaged velocity of the 10 % higher velocities detected for the liquid and bubbles. (Measurements performed in the Phi 400 column, at the column center at h/D=2.5. Liquid velocity measured by the Pavlov tube and bubble velocity measured by the optical probes)

The results show that both phasic velocities have comparable magnitudes and exhibit the same trend with the superficial gas velocity. The bubble velocity is slightly higher than that of the liquid. In this view, it is possible to conclude that the bubble velocity seems to be correctly measured when the flow has an ascending unidirectional movement. The same exercise was made in the Phi 1000 column, with data collected in the column center and at h/D= 3.75: in these conditions, the fraction of downward directed motion is higher than in the Phi 400 (Figure 3.43). The corresponding data are presented Figure 3.47.

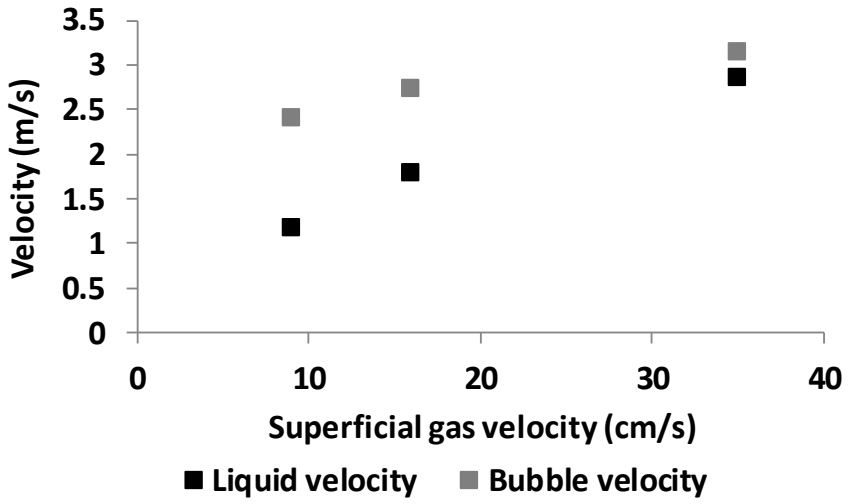

Figure 3.47 – Comparison between the averaged velocity of the 10 % higher velocities detected for the liquid and bubbles. (Measurements performed in the Phi 100 column, at the column center at h/D=3.75. Liquid velocity measured by the Pavlov tube and bubble velocity measured by the optical probes)

As seen in Figure 3.46 and in Figure 3.47, the liquid and bubble velocity present the same evolution with the superficial gas velocity. Yet, the difference between the two velocities in the Phi 1000 column is larger than in the Phi 400 column. In view of Figure 3.47, one may think that the bubble velocity is overestimated, but no evidences were found that could explain a possible overestimation of the measured gas velocity. Globally, the above results are encouraging that but the reliability of bubble velocity measurements cannot be quantified.

Bubble size measurements in the vertical direction

In this section the bubble size measurements of the 1C mono-fiber optical probe will be validated by comparison with the measurements from the endoscopic imaging method. Again, all the data have been collected with a probe pointing downward.

As referred to in section 3.3, the Sauter mean vertical diameter of the bubbles can be calculated from the mean bubble chord, through Eq. (3.16), of an oblate shaped bubble population. In this calculus, unidirectional movement of the bubbles and a constant

eccentricity over the entire bubble population were assumed (the value of the eccentricity is not required).

The endoscope imaging method measures vertical and horizontal diameters for each detected bubble, as described in section 3.2. Therefore, it is possible to calculate the Sauter mean vertical diameter (Dv_{32}) from each measurement series. Note that the optical probe detects continuously the flow passing through the probe (average in time) and the endoscope detects some bubbles inside a control volume (volume average). To obtain comparable averaged quantities, one needs to transform the detected distribution into the size distribution in the system, as seen in section 3.3. Providing that we consider average with respect to the actual size distribution in the system, the various mean diameters are indeed equivalent and can de compared on a solid basis. Let us also bear in mind that the endoscopic method underestimates the weight of the smaller bubbles, but the resulting bias is hard to evaluate.

The Dv_{32} measured by the two methods in the Phi 400 column at a h/D=2.5 and in the column center for superficial gas velocities from 3 cm/s up to 35 cm/s are plotted in Figure 3.48.

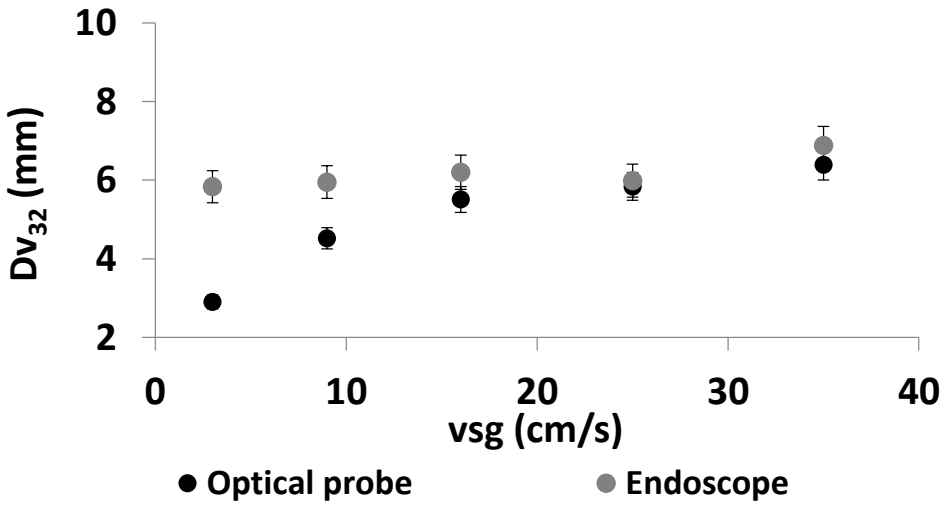

Figure 3.48 – Evolution of the Sauter mean vertical diameter with the superficial gas velocity. (Measurements performed no the Phi 400 column at h/D=3.75 and at center of the column)

The endoscopic imaging results present a constant value Dv_{32} of around of 6 mm for all the tested superficial gas velocity range. For the optical probe, the Dv_{32} increases with the superficial gas velocity between 3 cm/s and about 15 cm/s. As a consequence, the results at 3 cm/s and 9 cm/s present a considerable deviation: the difference between

the two techniques reaches 3mm as vsg=3cm/s. Yet, at superficial gas velocities above about 15cm/s, a good agreement is found between the two methods, with an averaged difference of 1.1 mm.

Similar studies were performed in the axis of the columns. In the Phi 150 column and at a h/D=2.5, the endoscope imaging experiments were only made for superficial gas velocities in the range of 2 cm/s to 13 cm/s while the 1C mono-fiber optical probe measurements were performed between 3 cm/s and 35 cm/s (Figure 3.49).
Measurements were also achieved in the Phi 1000 column at h/D=3.75 and for superficial gas velocities from 3 cm/s up to 35 cm/s (Figure 3.50).

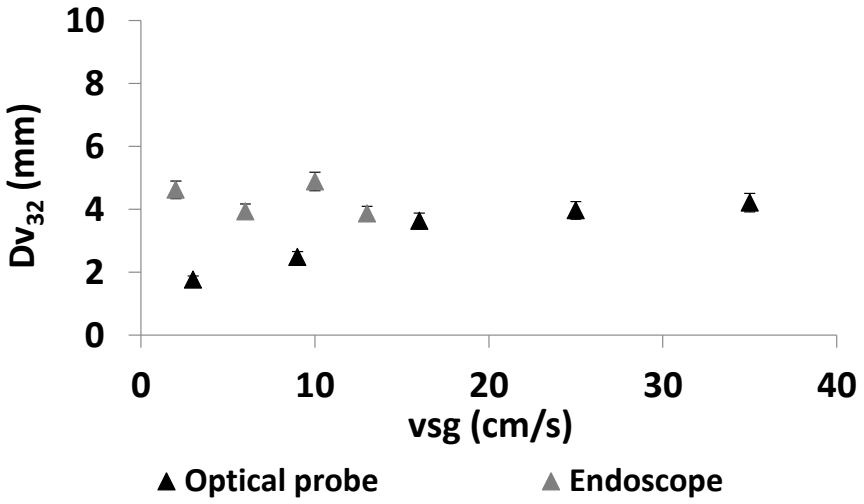

Figure 3.49 – Evolution of the Sauter mean vertical diameter with the superficial gas velocity. (Measurements performed in the Phi 150 column at h/D=2.5, and at center of the column)

The Sauter mean vertical diameter was also measured in the Phi 1000 column by the 1C mono-fiber optical probe and the endoscopic imaging method. The measurements were performed in the center of the column at a h/D=3.75 for superficial gas velocity range from 3 cm/s up to 35 cm/s, as shown in Figure 3.50.

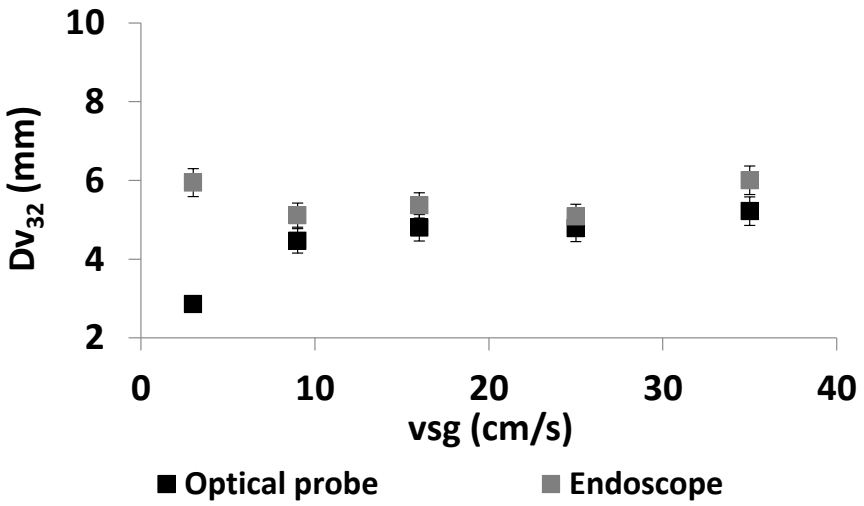

Figure 3.50 – Evolution of the Sauter mean vertical diameter with the superficial gas velocity. (Measurements performed no the Phi 1000 column at h/D=3.75 and at center of the column)

In both cases (in Figure 3.49 and Figure 3.50), the evolutions of the Sauter mean vertical diameter with vsg present a trend similar as the one of Figure 3.48. The endoscope imaging measurements present a constant bubble size along the tested range of superficial gas velocity while the bubble size measured with a 1C mono-fiber optical probe increases with the superficial gas velocity up to $v_{sg} \approx 10$ cm/s or 15 cm/s. As a consequence, significant deviations (≈2 to 3mm) arise between the measurements for the lowest superficial gas velocities. These disagreements disappear at larger velocities, with a mean difference between the two techniques of 1.07 mm in the Phi 1000 column. An estimation of the mean difference could not be performed in the Phi 150 column since the endoscopic and optical probe measurements were carried out at different superficial gas velocities. Globally, the results show that the measurements agreement holds at v_{sg} above 10-15cm/s and for all column diameters.

The evolution of the Sauter mean vertical diameter as measured by the two techniques was also investigated along the column radius in the Phi 400 column and at a superficial gas velocity of 16 cm/s.

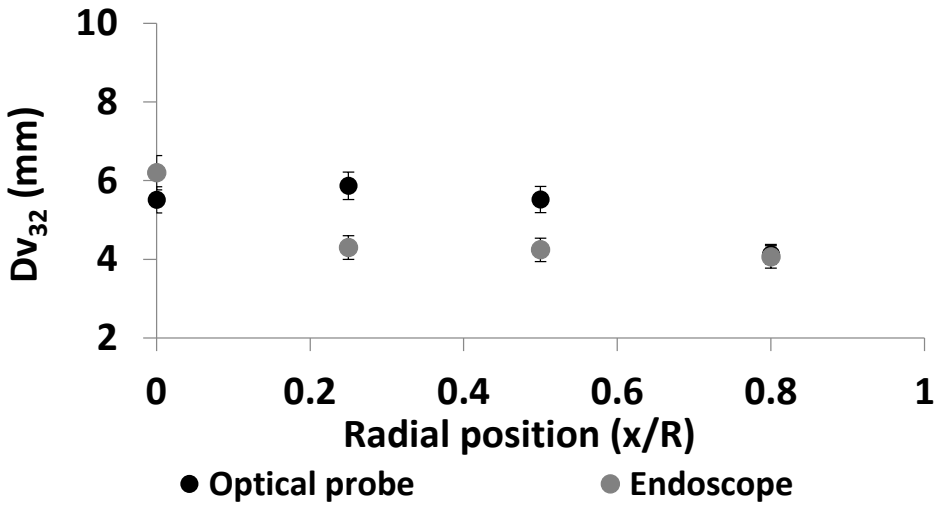

Figure 3.51 – Evolution of the Sauter mean vertical diameter along the column radius. (Measurements performed no the Phi 400 column at h/D=2.5 at a superficial gas velocity of 16cm/s)

The endoscope results show a decrease of the bubble vertical diameter between the column center and the position x/R=0.25, and for larger distances to the axis, the bubble size remains constant. The optical probe results display a parabolic profile with the vertical diameter of the bubbles monotonously decreasing along the column radius. A good agreement is found between the measurements on the column center and also close to the wall at x/R=0.8. For intermediate positions, the endoscope detects a Dv_{32} smaller than the one measured with optical probe (deviation up to 2 mm). Nevertheless, the average difference between measurements is 1.6 mm.

Concluding, 1C mono-fiber optical probe and endoscopic size measurements are in good agreement on the column axis and for all columns for v_{sg} above 10-15cm/s. Significant deviations are found at low superficial gas velocities. One possible explanation for these deviations may be an overestimation of the bubble diameter as measured by the endoscope. Indeed, smaller bubbles hidden behind larger ones are not counted and may be thus underestimated. A priori such a bias should be independent of the velocity. A second explanation arises from the response for the optical probe: indeed, at low v_{sg}, the velocity fluctuations are significant compared with the mean leading to weak impact velocities on the probe and therefore to strong perturbations of the bubble trajectory and velocity. This effect disappears as v_{sg} increases since the probability to apparition of weak or zero absolute velocities drops to zero above about 10cm/s as shown by the liquid velocity distributions (see Figure 4.45 in Chap.4).

The agreement between the two techniques is somewhat degraded when moving along the column radius: this phenomenon is possibly related with the presence of 3D unsteady structures that lead to downward directed velocities: indeed, the fraction of the later drastically increases with the distance to the axis (Figure 3.43) and that induces a bias in the response of the optical probe as discussed in the previous section. Oddly, one should therefore expect the largest deviations to occur in the mean flow recirculation region: instead the agreement between the two techniques is better at x/R=0.8 than for intermediate radial positions.

Aside the mean size discussed above, we also compared the chord distributions given by the optical probe with those deduced from the size distributions measured with the endoscope using the transformation given by Eq. (3.20). For the reconstruction, we considered the distribution of horizontal diameters and we assumed a constant eccentricity, equal to 0.7. Note that we are considering here the statistics on chords along the vertical direction. The comparisons are shown Figure 3.52 for data collected on the axis of the Phi 400 column at h/D= 2.5 and for v_{sg}= 3 cm/s, 16 cm/s and 35cm/s.

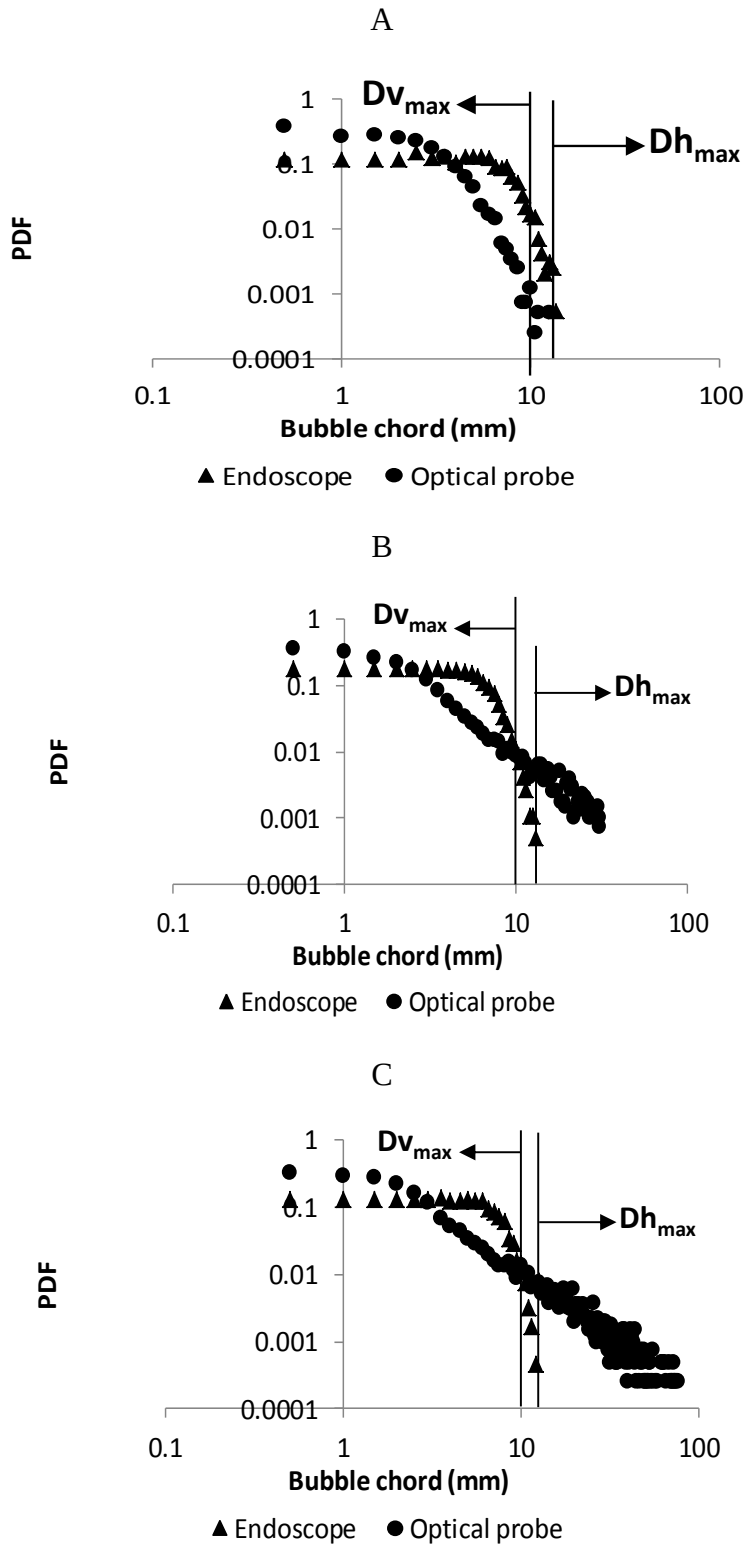

Figure 3.52 – Comparison of chord distributions measured with the optical probe and reconstructed from the endoscope data for the superficial gas velocities of: A) 3 cm/s B) 16 cm/s C) 35 cm/s. (Measurements performed in the center of the Phi 400 column at h/D=2.5) The vertical

lines correspond to the maximum vertical and horizontal diameter detected with the imaging technique

As for the Sauter mean diameters discussed above, the mean chords are similar except at the lowest superficial gas velocity (Table 3.16). Oddly, the chord distributions arising from the two techniques are quite different. In all cases, small chords are underestimated by the endoscope, most probably as a result of the underestimation of the smallest bubbles present in the flow. The most striking feature is the extent of the chord distributions as seen by the optical probe that exceeds the maximum vertical dimensions detected with the endoscope. At 3cm/s, the difference is moderate, but it becomes huge for v_{sg}=16 and 35 cm/s. Even more, the chords detected are larger than the maximum horizontal diameter observed in image analysis. Owing to velocity fluctuations, the probe may indeed combine vertical as well as horizontal dimensions of the bubbles in its statistics. Clearly, this is not the only difficulty here as the above results indicate that incorrect chords are detected even though the associated probability is low. It is highly likely that such defects originate from incorrect bubble velocity measurements since, as already indicated, the discrimination on the impact angle is inefficient in these flow conditions. In support to that, the chord PDF constructed with the mean liquid velocity and with the gas residence times detected by the optical probe never exhibit such overestimated sizes.

Therefore, in such complex bubbly flows, the chord distribution should be considered with care even though the mean chord is significant. In particular, the maximum chord detected should not be used as an estimate of the maximum bubble size.

Table 3.16 – Comparison of different moments of the bubble size distribution, obtained by the endoscope and optical probe.

	v_{sg} (cm/s):	3	16	35
Optical probe	C_{10} SO	2,16	3,78	4,29
Endoscope	Dh_{32} endo	8,57	8,57	9,71
	C_{10} from Dh	4,00	4,00	4,53
	Dv_{32} endo	5,80	6,19	6,90
	C_{10} from Dv	3,87	4,13	4,60
	Max Dh	13.4	16.8	16.8
	Max Dv	10	10.3	10.8

Bubble flux measurements

As mono-fiber optical probes can measure the local gas flux by way of Eq. (3.5), it is thus possible to evaluate the global gas flux in the column by integration over the cross-section. Examples of radial profiles of the local gas flux measured in the Phi 400 column are presented Figure 3.54. In the column Phi 150, the measurements were acquired up to a dimensionless radial distance of x/R= 0.75, that corresponds to 56 % of the column cross-section area. In the Phi 400 and Phi 1000 columns, the measurements were made up to x/R=0.8, that corresponds to 65% of the cross-section area. Consequently, to quantify the impact of the gas flux in this outer zone of the column, two extreme scenarios were considered. The first scenario assumes that the gas flux remains constant between the last measurement point and the wall (Figure 3.53 A), while the second scenario assumes that the gas flux is zero (Figure 3.53 B).

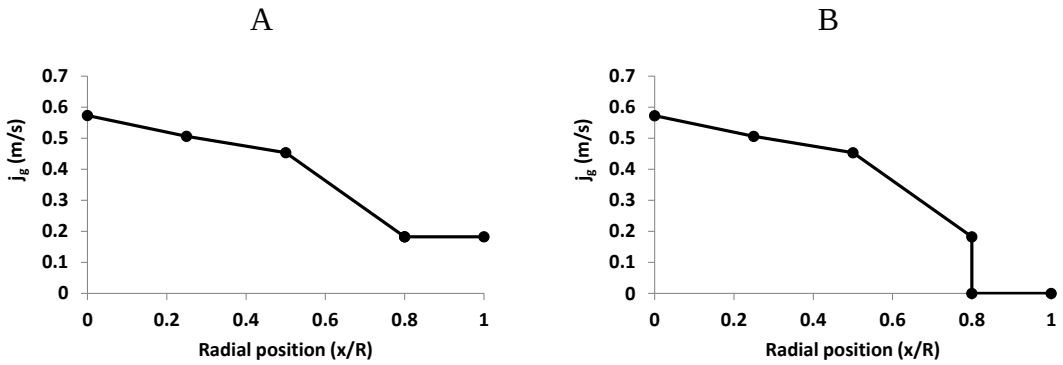

Figure 3.53 – Schematic representation the extrapolation scenari of measured local gas flux for the integration: A) 1st scenario; B) 2nd scenario.

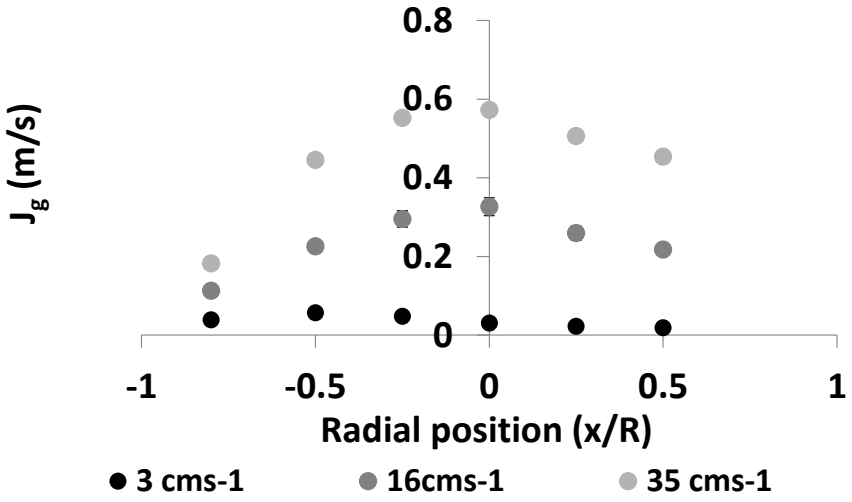

Figure 3.54 – Evolution of the local gas flux measured by the optical probe along the column radius. (Measurements performed in the Phi 400 column at h/D=2.5)

Performing the integration on such basis, a superficial gas velocity can be calculated by dividing the integrated local gas flux by the total cross-section area of the column, as shown in the following expression.

$$vsg_{up}^{1C} = \frac{\oint 2\pi r j_g \partial r}{\oint 2\pi r \partial r} \qquad (3.\ 53)$$

Additionally, in the Phi 400 column the local gas flux was measured in both sides of the column, however only one side was used for the integration.

Figure 3.55 presents the comparison between the superficial gas velocity calculated by Eq. (3.53) and the superficial gas velocity deduced from global gas flow rate measurements, for the columns Phi 150, 400 and 1000. First of all, the differences between the two scenarios are weak. Besides deviations are significant for the Phi 150

column (relative error from 20% to 60%) and the Phi 400 column (relative error from 10% to 50%), while the agreement is quite good (maximum relative error ≈ 15%) for the Phi 1000 column except at the lowest superficial velocity, namely 3 cm/s.

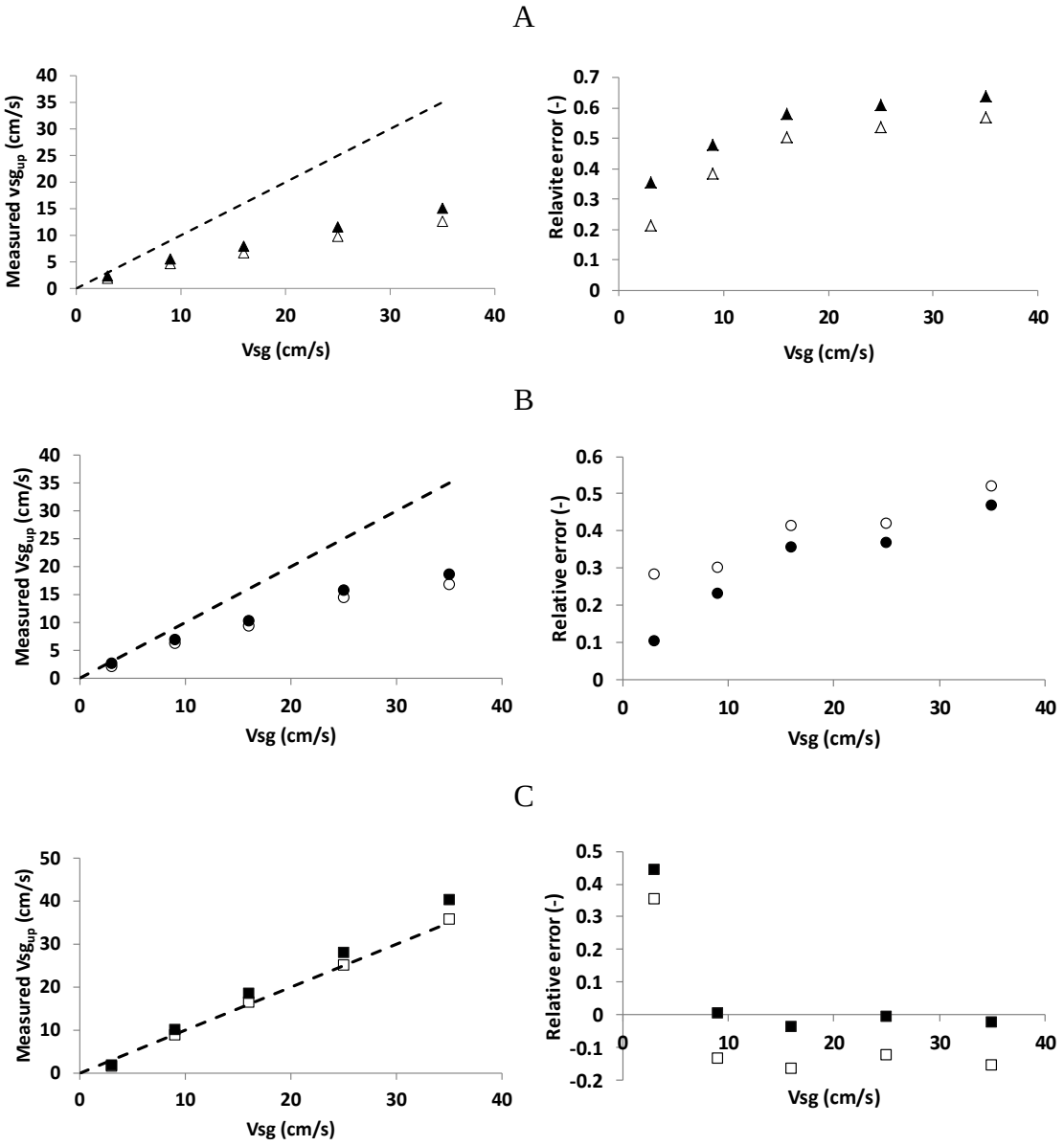

Figure 3.55 – Comparison of vsg as estimated from local measurement with the experimental vsg (1st scenario -filled symbols, 2nd scenario – empty symbols): A) Phi 150; B) Phi 400; C) Phi 1000 (dashed line represents the bisector). Left parity plot, right relative uncertainty

These results deserve a number of comments. First, the optical probe is unable to detect the sign of the velocity, so that, with the probe pointing downward, the local flux is always positive, in the upward direction (Figure 3.43). Therefore, the bubbles dragged down by the liquid, and especially in the outer zone of the column (x/R>0.7) are not

properly accounted for. Instead, they contribute to the upward flux. Beside the central region, i.e. $0<x/R<0.7$, and the outer region where the mean recirculation occurs, i.e. $0.7<x/R<1$, have the same areas: the contribution of the recirculation zone is thus significant (even if the void fraction decreases with the distance to the axis). For these reasons, one should have expected a strong overestimation of vsg computed from local data. However, as seen in Figure 3.55, the integrated flux is always underestimated compared with the injected gas flux, except in the Phi 1000 column where the overestimation is at most 15%.

Among possible reasons for these defects, we have already seen that incorrect measurements of the gas velocity do occur and that they lead to excessive chord sizes. Similarly for the flux, such events bring extra spurious contributions but in an unknown proportion. Second, the flux collects information all along a column radius. For most radial positions, the flow is reversed for a fraction of the time (Figure 3.43), so that the probe is sometimes functioning in bad conditions. As seen in Figure 3.45, the probe orientation can affect the local flux by a factor 2 or more. Moreover, as the fraction of time occupied by downward motions evolves radially, the information seen by the probe is a combination of the actual upward and downward fluxes weighted by the probe sensitivity to its orientation with the mean flow: the outcome on the global flux is hard to predict. Note that, for lack of time, we didn't attempt to vary the probe position to investigate the consequences on the flux.

In addition to the above considerations on the probe response, the observed deviations on the flux strongly increase with v_{sg} in the Phi 150 and Phi 400 columns, while they almost disappear in the Phi 1000 column although the conditions in terms of mean and fluctuating velocities are not much different from those arising in the Phi 400 (see Chap.4). Such trends are difficult to explain.

Thus, the above comparison between integrated and global fluxes is not much informative with respect to the probe capability. Clearly, the outer region leads to strong errors, and we will attempt to exploit the flux in the center of the column in Chapter 4.

Bubble size measurements in the horizontal direction with the cross-correlation method

In order to test the size measured performed with the spatial cross-correlation method (c.f. section 3.4), the results will be compared with the measurements from the endoscope and also with those achieved with the 1C mono-fiber optical probe. The cross-correlation was measured using a distance between probes equal to 0.8 mm: the two probes were pointing downward with their tips aligned at the same elevation. For the cross-correlation technique, the bubble Sauter mean horizontal diameter Dh_{32} was calculated using Eq. (3.39). Two different bubble shapes were considered:

- An oblate shaped bubble population with a bubble orientation and eccentricity distributions existing in the flow, which corresponds to a A factor of 1.5978, as detailed in section 3.4.
- A prolate shaped bubble population with a constant eccentricity (0.7) and a random θ angle in the range of ±30°, that corresponds to a A factor of 1.7.

The horizontal diameter distributions, measured by the endoscopic imaging, were treated to obtain a Sauter average. The above data were also compared with Dh_{32} measurements performed with the 1C mono-fiber optical probe using Eq. (3.16) and considering a constant eccentricity of 0.7.

The tests were performed in the Phi 400 column, at h/D = 2.5, and for superficial gas velocities ranging from 3 cm/s up to 35 cm/s. The resulting data collected on the axis are presented in Figure 3.56, while data collected along a radius are given in Figure 3.57.

Concerning the cross-correlation technique, the Dh_{32} evaluated assuming prolate shaped bubbles, shown in Figure 3.56 and in Figure 3.57, are close within 0.5 mm from the Dh_{32} predictions for oblate bubbles, proving that the eventual error originated by an incorrect choice of the bubble shape has a small impact on the final measurement. This was an expected result since the A factor used in each case varies only from 1.6 to 1.7.

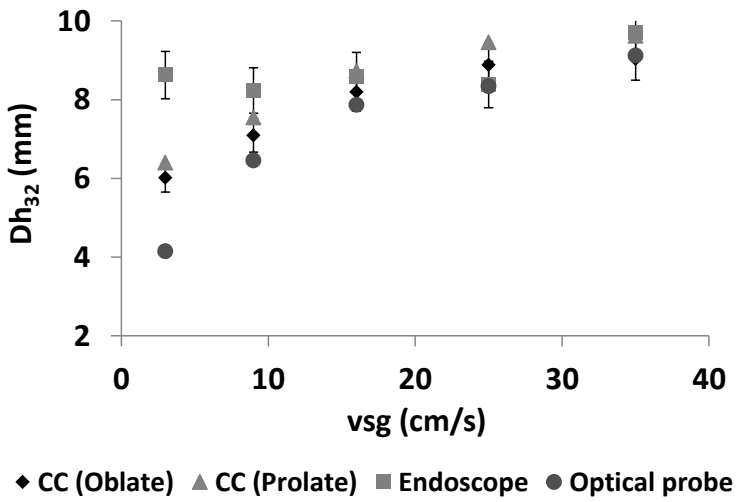

Figure 3.56 – Evolution of the Dh32 measured by cross-correlation, endoscopic imaging and optical probes with the superficial gas velocity (Phi 400, h/D=2.5, x/R=0)

Let us now compared the three techniques. Through the analysis of Figure 3.56, that represents the evolution of the Dh_{32} measured on the column axis (at h/D=2.5) with the gas superficial velocity, it is possible to conclude that all three techniques provide very similar results (within ±1 mm) at large superficial gas velocities, say above 15cm/s. The differences increase at lower v_{sg}: they are less than 2mm at v_{sg}=9 cm/s but reach 2.5mm (for the cross-correlation technique) or 4 mm (for the single probe) at v_{sg}=3 cm/s.

Similar measurements were also performed along the column radius in the Phi 400 column for the superficial gas velocity of 16 cm/s, as presented in Figure 3.57.

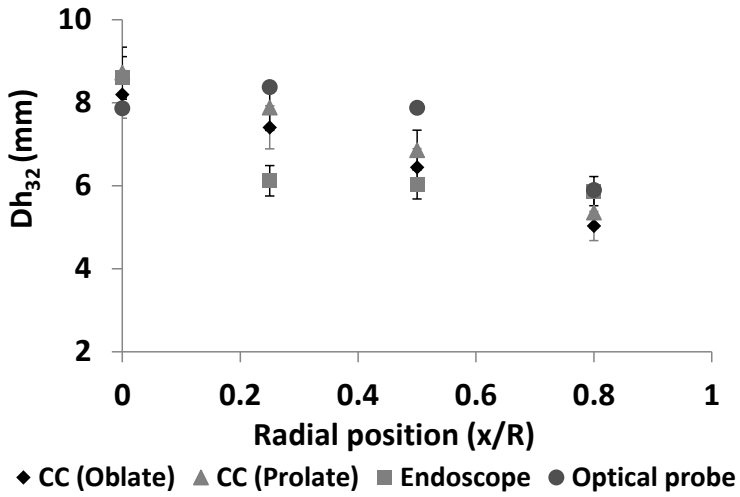

Figure 3.57 – Evolution of the Dh32 measured by cross-correlation, endoscopic imaging and optical probes along the column radius (Phi 400, h/D=2.5,vsg=16cm/s)

For the measurements performed along the column radius in the Phi 400 column at a superficial gas velocity of 16 cm/s, and presented in Figure 3.57, there is again a good agreement between the three methods in the column center. However, the agreement between the results degrades along the column radius. Indeed, the endoscope measurements present a steep decrease of the D_{h32} between the column center and the position x/R=0.2, and a constant bubble size for further positions. For the cross-correlation and the single probe techniques, the bubble size smoothly decreases when moving from the axis to the wall. At intermediate positions, the difference with the endoscope data is comprised between 1.5mm (for the cross-correlation technique) and 2mm (for the single probe), while at x/R=0.8, all three techniques are in good agreement. Globally, the deviation between the cross-correlation and the single probe techniques is 0.9 mm in average and at most 1.5mm. Between the cross-correlation and the endoscopic measurements, the maximum difference amount for 1.3 mm is 0.6mm in average.

Thus, bubble size measurements with the cross-correlation technique have been validated at several superficial gas velocities: moderate differences of the order of 1mm were found with the other two techniques, at least for v_{sg} above about 10 cm/s.

3.6 Detection of flow structures of intermediate scale

In this section, we will briefly introduce a few different approaches aimed at testing the existence, and at quantifying, somewhat coherent flow structures. Indeed, we

do suspect, as can be seen by the observation of the flow along the walls or of the top of the columns (Figure 3.58), the existence inside the flow of meso-scale structures with a dimension intermediate between the bubble size et the column dimension. Both time and space have been considered on both liquid and gas phases.

A

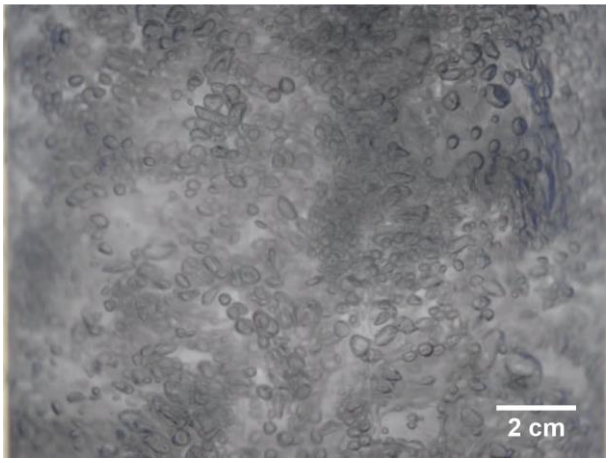

B

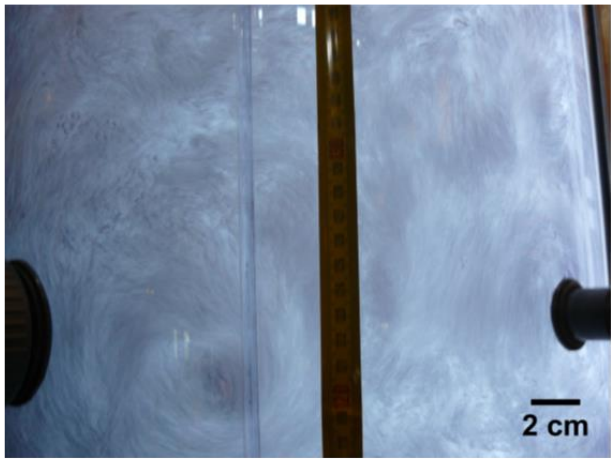

C

Figure 3.58 – Images of the flow in the columns: A) Phi 150 (v_{sg}=15 cm/s); B) Phi 400 C) Phi 3000 (v_{sg}=13 cm/s, top view)

Liquid phase

Analysis in time

The primary outcome of Pavlov tube is instantaneous liquid velocity as a function of time (with some bandwidth limitations). So, it is possible to perform an FFT analysis of the velocity to identify liquid flow time-scales, and their possible evolution along radial position and with the column size, or the superficial gas velocity. The results of this data treatment will be presented in chapter 4.

Analysis in space

Another possibility to measure the coherent structures on the liquid flow is to use two different Pavlov tubes, oriented in the same direction, at the same elevation in the column. Therefore, in likely manner as was done for the cross-correlation of the optical probes signals, the signals of both Pavlov tubes can be cross-correlated for different spatial distances. The outcome of this approach will be an averaged structure size in the direction of the distance between the Pavlov tubes. Due to time limitation and technical difficulties, this approach was not tested: it is presented as a perspective and a possible manner to extend measurement capabilities of the Pavlov tube.

Gas phase

Analysis in time

Using an optical probe, one can access to the temporal evolution of the local void fraction. To do so, it is necessary to compute a moving average over a window of a selected duration, by estimating the ratio of the sum of *gas residence times* over the window duration. Therefore, in a similar manner as was described for the liquid velocity, a continuous void fraction signal can be extracted and an FFT analysis of the signal can be performed.

However, it is necessary to properly define the time scale over which the void fraction will be averaged, which is the most significant step of the process. If this step is too small, it will only be possible to detect the frequency at which the bubbles arrive on the probe tip. In the opposite, an average over a too large time step will smooth out any void fraction evolution and no characteristic frequencies will be detected. Thus, the determination of this time step was achieved by computing the auto-correlation in time

of a single optical probe signal. This exercise showed that there is a time step from which the optical probe signal is not auto-correlated, which was then used in the moving average calculation. The results of FFT analysis of such a "continuous" void fraction signal will be presented in the chapter 4.

Analysis in space

The existence of bubble swarms in the column was investigated recurring to the cross-correlation. The experimental results of the cross-correlation at large distances showed that the cross-correlation does not decrease under the value of the local gas hold-up (c.f. Figure 3.14). Moreover, the local gas hold-up value is the minimum value for the cross-correlation at large distances (provided the flow is not too in-homogeneous). Thus, some useful information can be obtained in the zone bounded by the distance between the probes that ensures single bubble detection, and the distance at which the curves converge to the local gas hold-up.

Therefore, it is possible to define two events such as:

A – There is a bubble in the probe A

B – There is a bubble in the probe B.

Using the fact that the probability of each occurrence of the event A and B is $P(A) = \varepsilon g(A)$ and $P(B) = \varepsilon g(B)$, it is possible to define the cross-correlation as the probability of A knowing B ($P(A|B)$), so:

$$CC = P(A|B) = \frac{P(A \cap B)}{P(B)} \tag{3. 54}$$

If A and B are de-correlated then they are independent events and therefore:

$$P(A \cap B) = P(A) \times P(B) \tag{3. 55}$$

So is possible to rewrite Eq. (3.52)

$$P(A|B) = \frac{P(A)P(B)}{P(B)} = P(A) = \varepsilon_g(A) \tag{3. 56}$$

Consequently, it is possible to affirm that if the cross-correlation is higher than the local gas hold-up, the signals are correlated. Thus, elevated levels of the correlation between the optical probes signals for distances higher than the bubbles horizontal dimension can be related to the presence of bubbles swarms, or higher concentration zones, in the flow.

The experiments that aimed to measure the bubble clusters in the column, followed the previously stated procedure for the cross-correlation measurements. However, the operation was repeated for several distances between probes ranging from 0.8 mm up to 90 mm. Three different configurations of optical probes were used in this study. The measurements with a probe distance of 0.8 mm were performed with a straight bi-probe. The measurements with a probe distance of 1 mm were performed with a bended bi-probe. At last, the measurements with a probe distance equal or higher than 1.5 mm were performed with two independent 1C mono optical probes. The results will be presented in chap.4.

Note that an alternate technique based on resistance tomography and providing an image of the void fraction spatial distribution over a certain area was also envisioned but it was not tested due to lack of time.

In this chapter we have presented the measuring methods that will be used in the acquisition of our experimental database. A resume of all methods and their measuring capacities was presented in Table 3.17. The performance of those methods, under the experimental conditions envisaged in this work, have been studied. Despite some shortcomings, namely some errors on the bubble velocity detection, due to the presence of flow reversal and unsteady 3D structures on the flow, the results are encouraging. A major result was the development of a new method to measure the bubble horizontal diameter (Dh_{32}), which showed to be adapted to perform bubble size measurements even in challenging conditions to perform optical probe measurements. Additionally, this method present an extension of the measurement capabilities of the optical probes, which could only measure the vertical dimension of bubbles.

Table 3.17 – Resume of measuring methods and measured variables.

	Pavlov	Endoscope	Optical probes	Cross-correlation
Liquid velocity	Instantaneous axial and radial velocity and velocity fluctuations.			
Local gas hold-up			Time averaged	
Bubble velocity			Product density f(1)(Chord, Velocity) for each detected bubble The chord distribution can be used to compute the diameter distribution or the Sauter mean horizontal diameter under some assumptions	
Bubble size		Detection of the horizontal and vertical diameter for each detected bubble.		Measurements of the Mean Sauter horizontal diameter

4 Local hydrodynamics in bubble columns

In chapter 1 the local hydrodynamic variables of interest such as gas hold-up, bubble size and velocity, liquid velocity, were identified through a detailed analysis of the literature and of existing modeling attempts. Afterwards, the range of experimental conditions to be considered was defined in chapter 2: the investigations concern bubble columns with a diameter ranging from 0.15 m up to 3 m and for superficial gas velocities from 3 cm/s up to 35 cm/s. Moreover, the ideal injection configuration was studied in order to ensure an homogeneous gas injection in all the columns, both in terms of bubble size and flux. Due to technical constraints it was not possible to install the same gas distributor in all the columns. However, the final configuration and the generated bubble population for the columns Phi 150, Phi 400 and Phi 1000 were also discussed in chapter 2: the new injectors were able to generate a relatively homogenous conditions over the entire columns cross-section. Additionally, the mean bubble size is relatively similar for all the columns, with a small evolution of the generated bubble size with the superficial gas velocity. The only exception concerns the Phi 1000 column at v_{sg} of 3 cm/s, where bubbles neatly larger than in the other columns are formed. These conclusions hold for superficial gas velocities in the range between 3 cm/s and 25 cm/s.

In chapter 3, the measurement methods chosen to measure the identified variables were detailed and validated by comparison, either with reference methods or with data collected from the literature.

In this chapter, the flow dynamics is analyzed. First, we address the question of coalescence. Then, the measurements of local hydrodynamic variables are detailed and their significance in terms of flow organization is discussed. Finally, the first attempts to identify meso-scale flow structures are presented and their characteristics are discussed.

4.1 Bubble coalescence

With respect to data interpretation and also in order to provide refined data bases for testing simulations, it is important to characterize the actual bubble size in the experiments in addition to the data already provided at injection (see Chap.2). In particular, the existence of bubble coalescence in the flow needs to be checked. Indeed,

coalescence can affect the bubble size evolution in the columns and, therefore, it can also impact other variables (e.g. local gas hold-up, bubble velocity, liquid velocity, etc…). To test the presence of coalescence (or breakup), examining the evolution of mean sizes alone can be misleading as the latter can be driven by dispersion and/or by size segregation in addition to coalescence and/or break-up. A more adapted quantity is the number of density flux per size classes, but again a comparison of the evolution of local values along a vertical axis does not account for lateral exchanges. As lateral fluxes are not available, the only option left would be to consider fluxes per size class integrated over a cross section. Yet, owing to the complexity of the flow structure in bubble columns (in particular to flow reversal and lateral size segregation which are detailed later in this chapter) and the limitations of the measuring techniques, such integrated variables will be poorly significant. Thus, with respect to coalescence, we decided to examine if there is any significant evolution of the maximum bubble size along the axis of the columns in addition to mean values Dv32. To do so, we considered the bubble chord distributions obtained from 1C mono-fiber optical probe at different h/D ratios at iso-v_{sg}. Another possibility was to study the evolution of the Dh_{32}, measured by the cross-correlation method. However, the analysis of the mean diameter alone is no sufficient.

Let us first analyze the Sauter mean diameter, deduced from C_{10} from the detected T1 bubbles in the center of the columns Phi 150, Phi 400 and Phi 1000 at several h/D presented in Table 2.5. As mentioned in section 3.3, the rate of T1 bubble always elevated (typically ≥90%) and stable for all the tested conditions. Therefore the T2 bubble have a negligible impact on the determination of the C_{10}. Owing to that, we chosen to only take in account the T1 bubbles in the comparison of the bubble size along the column axis. For sake of simplicity, the measurements obtained at an elevation of 15 cm above the gas distributor in all columns are noted as "h/D≤1". The determination of a typically uncertainty of those measurements may be a challenging task, since the error might be a function of the v_{sg} and the axial position (see section 3.3).

Table 4.18 – Dv_{32} deduced from optical probe measurements for several columns, superficial gas velocities and h/D ratios at x/R=0.

	3 cms-1			16 cms-1			25 cms-1		
	h/D≤1	h/D=2.5	h/D=3.75	h/D≤1	h/D=2.5	h/D=3.75	h/D≤1	h/D=2.5	h/D=3.75
Phi 150	2.7	1.8	-	3.3	3.6	-	3.15	3.9	-
Phi 400	2.55	2.85	2.4	4.2	5.55	4.35	4.65	5.85	4.95
Phi 1000	3.15	2.85	3.45	4.5	4.8	4.65	4.65	4.8	5.7

The results show that, in the Phi 150, the Dv_{32} does not evolve more than 0.9 mm from h/D=1 up to h/D=2.5, whatever the superficial gas velocity. In Phi 400 column, the Dv_{32} was also stable along a vertical at v_{sg}=3 cm/s while it, experienced an increase of Dv_{32} of approximately 1.3 mm for v_{sg}=16 cm/s and 25 cm/s. In the case of the column Phi 1000, the Dv_{32} was quite constant along the column axis for v_{sg}=3 and 16 cm/s, and it experienced a moderate (≈0.9mm) increase at 25 cm/s. Note that the increase is not monotonous with the distance downstream injection. Concluding, for a given gas superficial velocity, the Dv_{32} changes along a vertical in all columns, with deviations never exceeding 1.3 mm. This is also the magnitude of the variations observed at injection in Chap.2 when v_{sg} was varied. Within the above mentioned interval, the mean size does not change much neither due to v_{sg} nor due to axial evolution of bubble size within the columns.

Nevertheless, as referred to above, the analysis of mean sizes is not fully conclusive for the detection of coalescence since it is not possible to distinguish the effects of bubble coalescence and of segregation. In order to do so, let us examine the chord pdfs. The chords PDFs obtained in the Phi 150 column at h/D of 1 and 2.5 are plotted in Figure 4.1 A, B and C at superficial gas velocities of 3, 16 and 25 cm/s, respectively.

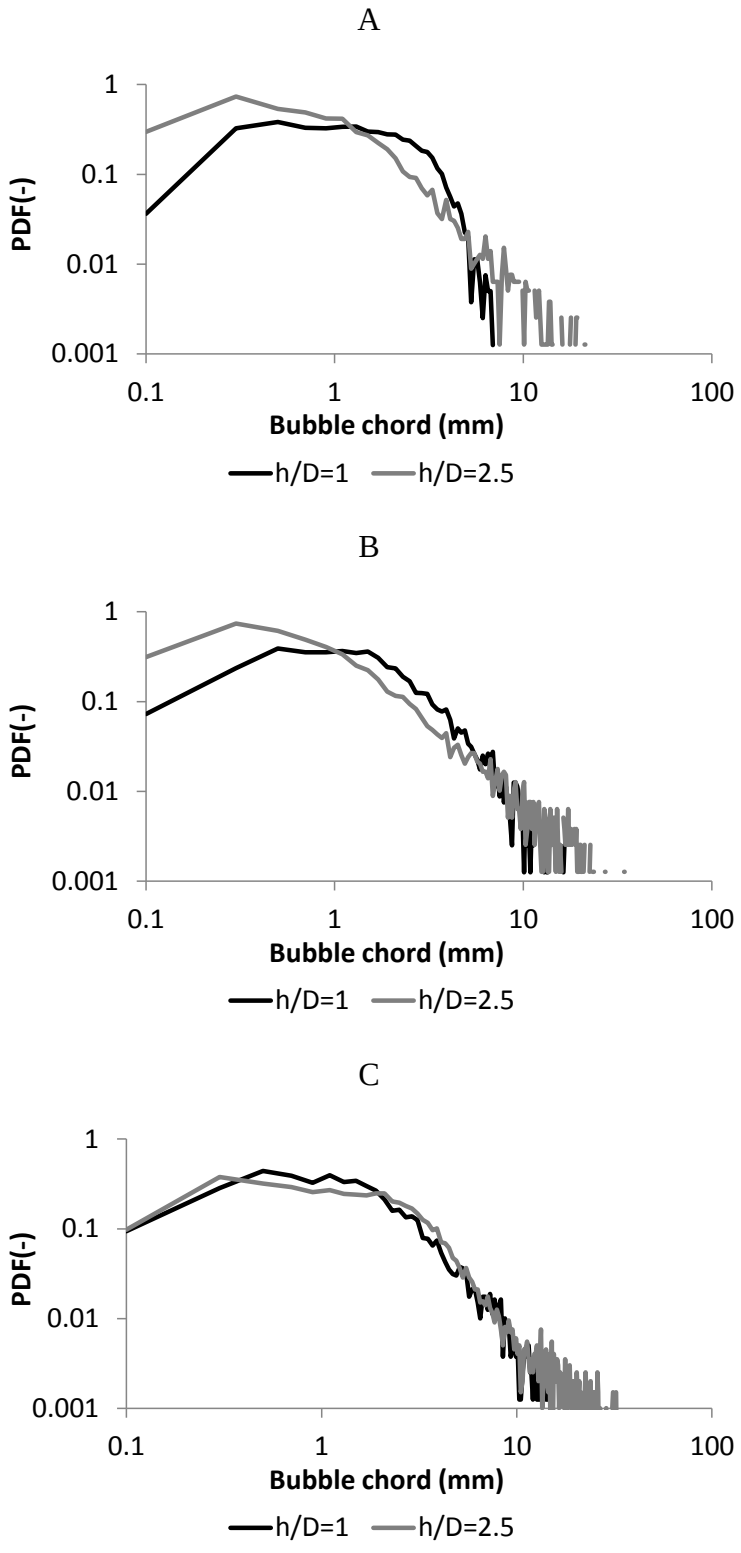

Figure 4.1 – PDFs of the bubble chords measured in the center of the Phi 150 column at h/D=1 and 2 for superficial gas velocities of: A) 3cm/s; B) 16 cm/s; C) 25 cm/s.

Figure 4.1 A shows that at 3 cm/s in the Phi 150 column, the maximum detected chord is roughly 6 mm (for a probability density≥0.01) at both elevations. At h/D=2, some larger

chords were detected, but the probability of detecting chords larger than 6 mm in only 2%. At v_{sg}=16 and 25 cm/s, there is no significant evolution of the maximum detected chord (≈8 mm), at a probability density value of 0.01 see Figure 4.1 B and C). Thus, it is possible to conclude that, in the Phi 150, no evidence of the existence of bubble coalescence was detected.

In the Phi 400 column, the bubble vertical dimension was measured at h/D=0.38, 2.5 and 3.75. The bubble chords PDFs detected in the column center for superficial gas velocities of 3, 16 and 25 cm/s are presented in Figure 4.2 A, B and C, respectively.

A

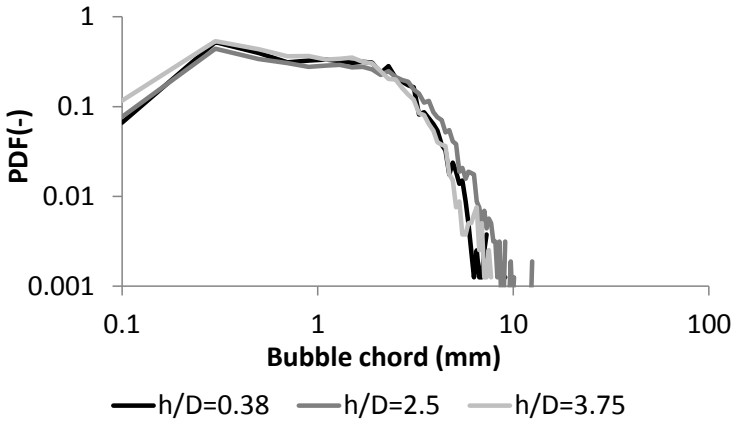

B

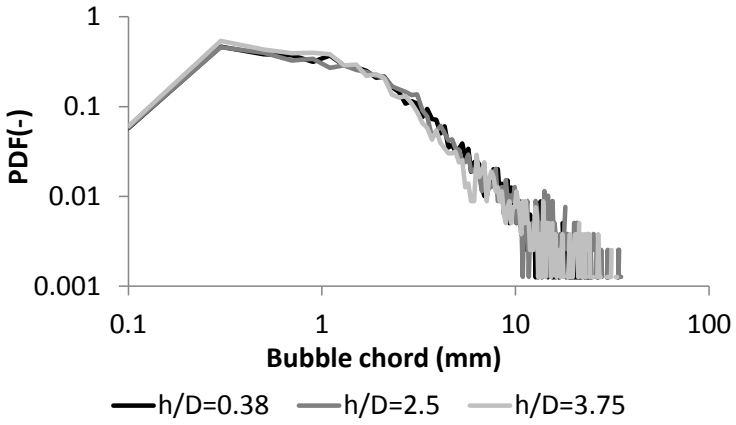

C

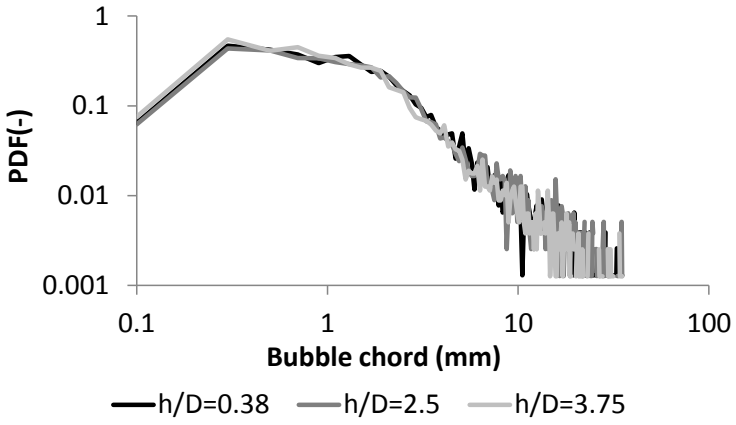

Figure 4.2 – PDFs of the bubble chords measured in the center of the Phi 400 column at h/D ratios of 0.38, 2.5 ad 3.75 for superficial gas velocities of: A) 3cm/s; B) 16 cm/s; C) 25 cm/s

The results show that at 3cm/s in the Phi 400 column the same maximum chord is detected at h/D =0.38, 2.5 and 3.75 (≈5-6.5 mm) for a probability density of 0.01.

However, slightly larger chords (≈10 mm) are detected at h/D=2.5 but again the probability to detect chords larger than 6 mm is only 4%. For superficial gas velocities of 16 cm/s and 25 cm/s, quite similar bubble chords PDFs are obtained at the different axial positions.

The bubble vertical size was measured in the Phi 1000 column at h/D ratios of 0.15, 2.5 and 3.75. The bubble chords PDFs obtained in the center of the column for superficial gas velocities of 3 cm/s, 16 cm/s and 25 cm/s are presented in Figure 4.3 A, B and C, respectively.

A

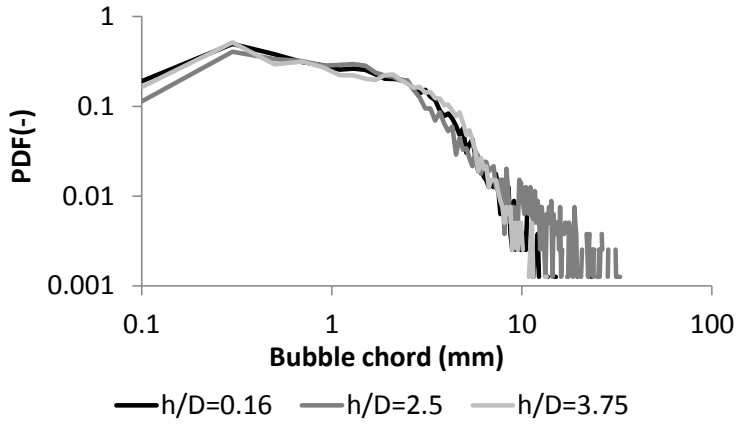

B

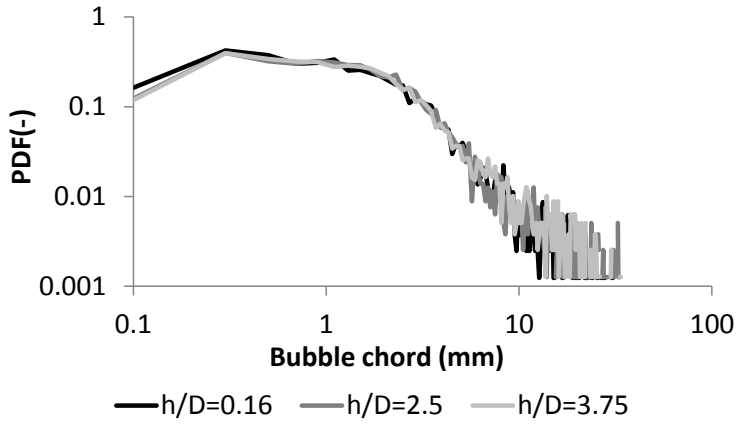

C

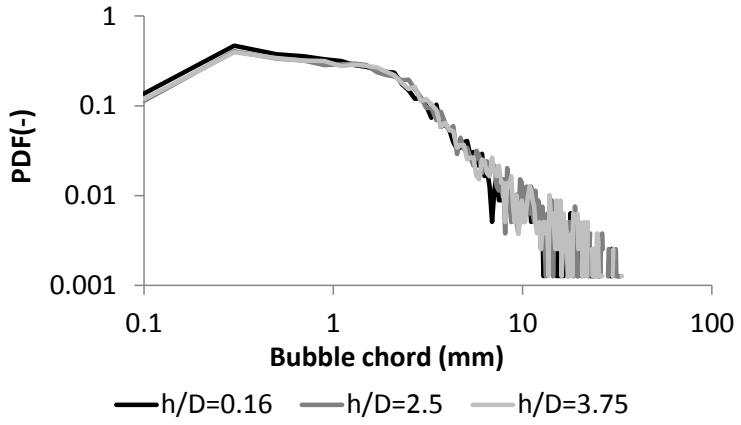

Figure 4.3 – PDFs of the bubble chords measured in the center of the Phi 1000 column at h/D ratios of 0.16, 2.5 ad 3.75 for superficial gas velocities of: A) 3cm/s; B) 16 cm/s; C) 25 cm/s

As noted for the Phi 150 and 400 columns, Figure 4.3 A shows that the same maximum chord (7-8 mm) is detected at all axial positions up to a probability density of 0.01, and some larger chords are detected at h/D=2.5 but they are quite rare events. Moreover,

similar trends are present in the PDFs obtained at superficial gas velocities of 16 cm/s and 25 cm/s with a maximal detected chord ≈8 mm for all the tested elevations.

Concluding, there is no significant bubble coalescence since the analysis of the bubble chord PDFs show that the maximal bubble chord detected was stable along the column axis, for all the tested v_{sg} and in the three columns. As referred to chapter 2, one of the conditions desired for the experiments was to avoid bubble coalescence. Thus, it is possible to conclude that this condition was achieved for all columns and for all flow conditions. As the pdf are only slightly modified, there is also no strong evidence of bubble breakage between the three elevations.

The presence of bubble coalescence was not investigated in the Phi 3000 column since the bubble size measurements were only performed at one elevation in the column.

4.2 Bubble size

Since there is no bubble coalescence, and since the generated bubbles size was found homogeneous in the injection vicinity, in all the columns (see chap. 2 3), the question to be addressed now concerns a possible spatial segregation of bubble size within the columns. Indeed, the study the bubble segregation can be perform using only a mean diameter, so we have chosen the cross-correlation method due to its reliably and simplicity. Since the spatial cross-correlation can only measure the Dh_{32}, it is important to first address the evolution of the bubble eccentricity in order to the fully comprehend the bubble size evolution in the columns.

Bubble eccentricity

The bubble eccentricity was measured recurring to the endoscopic imaging method in the centre of the columns Phi 150, Phi 400 and Phi 1000 at h/D=2.5 for superficial gas velocities ranging from 3 cm/s up to 35 cm/s. The results are presented in Figure 4.4 A. Moreover the bubble eccentricity was also measured along the column radius in the columns Phi 150 (v_{sg}=13 cm/s), Phi 400 and Phi 1000 (v_{sg}=16 cm/s) at h/D=2.5, as shown in Figure 4.4 B.

A

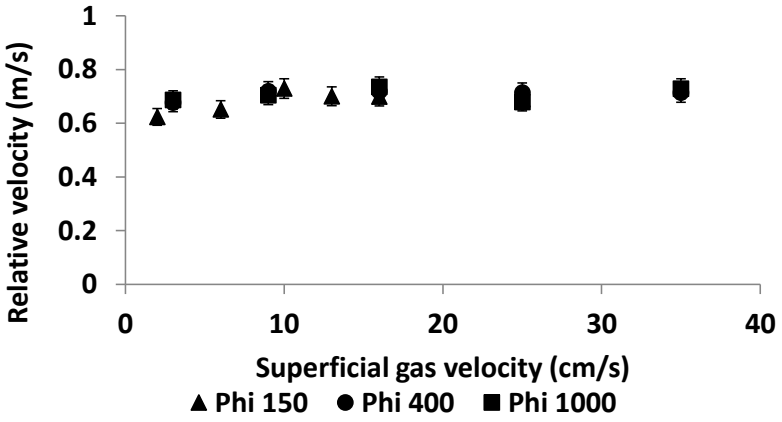

B

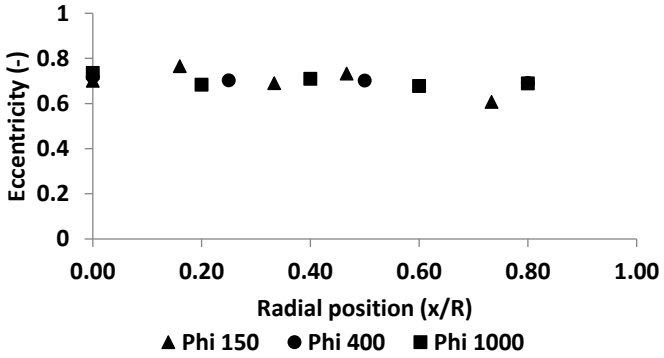

Figure 4.4 – Evolution of the mean eccentricity in the columns Phi 150, Phi 400 and Phi 1000 at h/D=2.5: A) in the column center for superficial gas velocities from 3 cm/s up to 35 cm/s; B) along the column radius (endoscopy).

Figure 4.4 A and B show that the mean bubble eccentricity was quite stable around 0.7 regardless of the superficial gas velocity, the radial position in the column and the column diameter.

Impact of the superficial gas velocity on the lateral size segregation

The bubbles Sauter mean horizontal diameter (Dh_{32}) was measured using the cross-correlation technique along the column radius in the columns Phi 150, Phi 400 and Phi 1000, at h/D=2 for a range of superficial gas velocities from 3 cm/s up to 35 cm/s. In the column Phi 3000, the Dh_{32} was measured in the column centre for superficial gas

velocities from 6 cm/s up to 16 cm/s, and along the column radius for v_{sg}=12 cm/s. The results are presented in Figure 4.5.

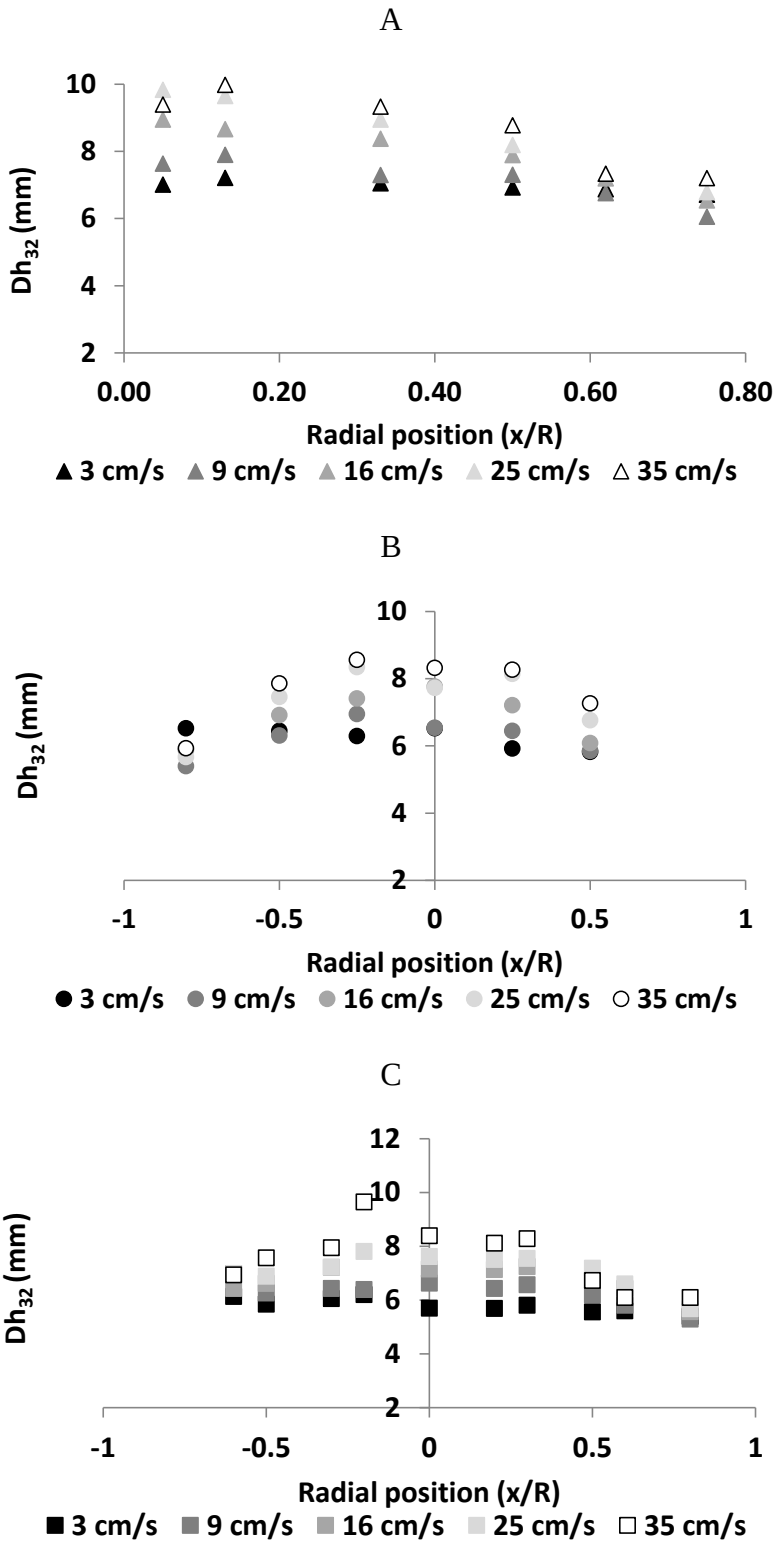

D

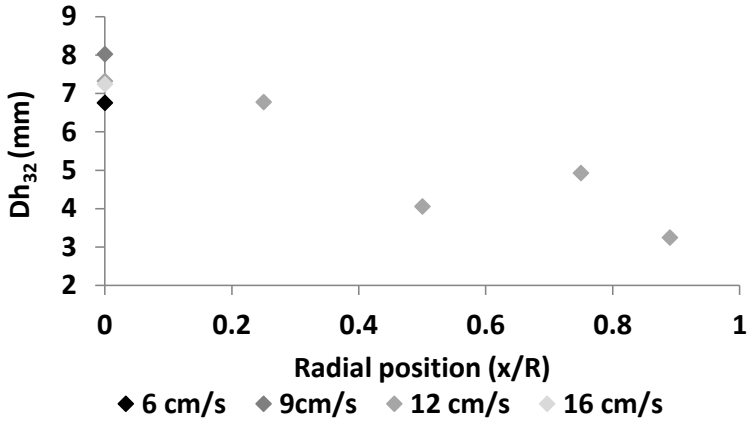

Figure 4.5 – Radial profiles of the bubbles Dh_{32} for several superficial gas velocities in the columns: A) Phi 150 (h/D=2.5); B) Phi 400 (h/D=2.5); c) Phi 1000 (h/D=2.5) D) Phi 3000 (h/D=2.5) (Cross-Correlation)

Figure 4.5 A shows that, in the Phi 150 column at h/D=2 and v_{sg}=3 cm/s, the bubble Dh_{32} is constant (≈ 7 mm) along the column radius. This is an expected result: indeed, the injected bubbles size was also constant, there is no coalescence and at such small v_{sg}, the flow is moderately agitated. When v_{sg} is increased above, say, 9 cm/s, a condition that leads to the generation of liquid recirculations, the Dh_{32} increases up to 9 mm in the column centre. The bubble size did not increase only at the column center, a similar evolution was detected up to x/R=0.5. Contrarily, in the exterior zone of the column (x/R>0.6) the bubble Dh_{32} remain quite constant with the superficial gas velocity. Therefore, the bubble spatial segregation was visible for v_{sg} > 9 cm/s, and increased with the superficial gas velocity, reaching difference on Dh_{32} of 3 mm between the positions x/R=0 and 0.8 for a v_{sg}=35 cm/s.

A similar trend can be seen for the Phi 400 and for the Phi 1000 columns (see Figure 4.5 B and C): the bubble diameter Dh_{32} in the column centre increases from 6 mm to 8 mm when v_{sg} evolves from 3 cm/s up to 35 cm/s. As for the Phi 150 column, the bubble size increases with v_{sg} up to the radial position x/R=0.5. In the outer zone of the column (x/R>0.6) was noted a smaller increase of the Dh_{32}. Concluding, the bubble spatial segregation was noticeable for vsg> 9 cm/s and reach its maximum at v_{sg}=35 cm/s with a difference on the Dh_{32} of ≈2 mm between the positions x/R=0 and 0.8.

In the Phi 3000 column at x/R=0, was registered an evolution similar to the others columns of the bubble Dh_{32} with the v_{sg} from 6 to 16 cm/s, with an increase in bubble size in the column centre from 6 mm up to 8 mm. The analysis of the bubble size evolution

with v_{sg} for other radial position is not possible, since only one radial profile was obtained. Nevertheless, at v_{sg}=12 cm/s the Dh_{32} decreased along the column radius, is a likely manner as in the other columns. However, the bubble spatial segregation was stronger than in the other columns, reaching a Dh_{32} difference of 5 mm between the positions x/R=0 and 0.9.

Concluding, the results show that at v_{sg}=3 cm/s the bubble size was homogeneous (≈6 mm) over the cross-sections of the Phi 150, Phi 400 and Phi 1000 columns. The increase in superficial gas velocity leads to an increase of the Dh_{32} in the column inner zone (x/R≤0.6) for all columns. However in the outer zone (x/R>0.6) the Dh_{32} showed a quite smaller increase with the v_{sg}. Since there is no bubble coalescence/breakup, this evolution of the bubble size can only be due to a lateral size segregation: the larger bubbles are rising in the central part of the column where the liquid phase also has a mainly ascending direction, however the liquid recirculation "drags" the small bubbles to the outer zone of the column. Moreover, the segregation effect seems to be even stronger in the column Phi 3000 where the Dh_{32} decreased down to 2 mm at x/R=0.9 compared with Dh_{32}=8 mm on the axis. Therefore it is important to also investigate the evolution of this segregation phenomenon with the size of the column.

Impact of the bubble column diameter on the lateral size segregation

The horizontal bubble diameter Dh_{32} at x/R=0 and at x/R=0.8 at h/D= 2.5 for the columns Phi 150, Phi 400, Phi 1000 and Phi 3000 are plotted in Figure 4.6.

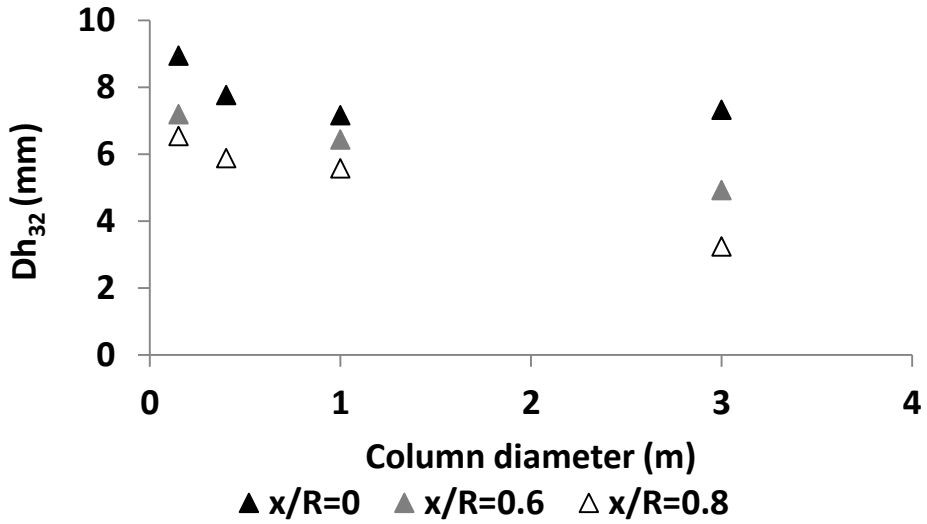

Figure 4.6 – Evolution of the Dh_{32} with the column diameter at h/D=2.5 for the radial positions x/R=0, 0.6 and 0.8. (Measurements obtained at v_{sg}=16 cm/s for the Phi 150, Phi 400 and Phi 1000 and at v_{sg}=13 cm/s for Phi 3000)

The results show that the Dh_{32} in the columns center has decreased between the Phi150 column and the Phi 400, however it was constant (≈ 7mm) for all the other columns. Contrarily, the Dh_{32} at x/R=0.8 and x/R=0.6 have decreased almost linearly with the column diameter, from 6 mm in the Phi 150 column up to 3 mm in the Phi 3000 column. Indeed, the results seem to indicate that the bubble size segregation increase with column diameter. However, this conclusion should be taken with some care, since the bubble injection and coalescence on the column Phi 3000 was not studied. Further confirmation can be achieve by the study of the bubble chords PDFs at iso-v_{sg}, for several radial positions. So, Figure 4.7 A and B present the PDFs of the bubble chords detected in the columns Phi 400 and Phi 1000, respectively, at v_{sg}=16 cm/s.

A

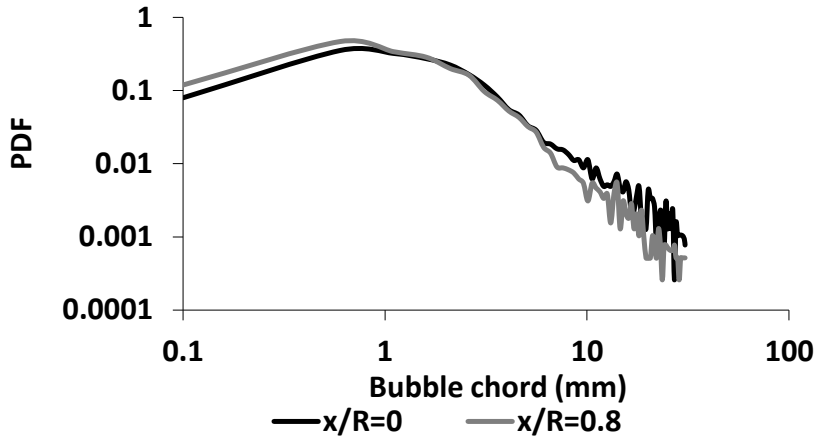

B

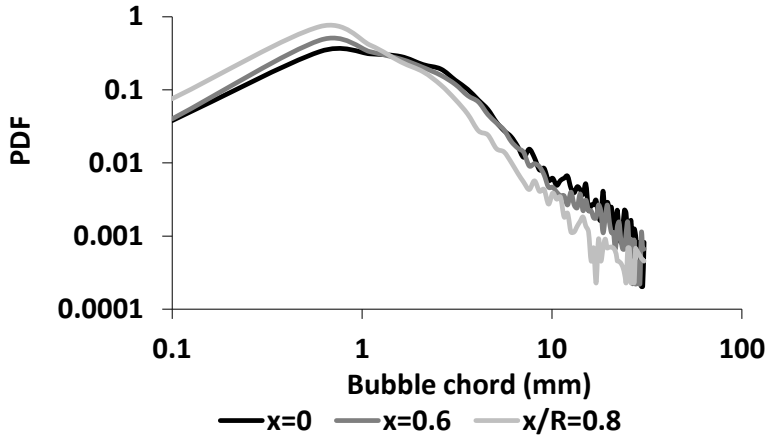

Figure 4.7 – PDFs of the bubble chords at vsg=16 cm/s for several radial positions in the columns: A) Phi 400 B) Phi 1000 (measurements obtained at h/D=2.5)

Analysing Figure 4.7 A is possible to conclude that at x/R=0.8 there is a higher probability of detect bubble chords smaller than 1 mm than at x/R=0. Contrarily, at the larger chords (> 7 mm) the PDF obtained at x/R=0 presents the higher probability of detection, even if the larger detected chord is constant in both positions.

The results obtained in the Phi 1000 column (Figure 4.7 B) show that there is a small difference between the PDF obtained at x/R=0 and 0.5. Nevertheless, the PDF obtained at x/R=0.5 presented higher probabiblities for bubble chords smaller than 1 mm. However, the PDF obtained in at the position x/R=0.8 was quite different from the one obtained in the column center: the probability of detect chords smaller than 1 mm has neatly increased at x/R=0.8, inversely, the probability to detect chords larger than 2 mm was also quite lower.

The analysis of the chords PDFs support the conclusions drawn for the analysis of the mean values: the PDFs at x/R=0.8 have shifted for smaller chords and the difference between the chords PDFs at x/R=0 and x/R=0.8 have increased with the column diameter.

Evolution of the bubble mean size along the column axis

It is also important to study if the bubble segregation phenomena was already established at h/D=2.5 or if it evolves along the column axis. So, the radial profiles of the bubble Dh_{32} in the columns Phi 400 and Phi 1000 for v_{sg}=3 cm/s, 16 cm/s and 35 cm/s at h/D=2.5 and 3.75 are plotted in Figure 4.8 A and B, respectively.

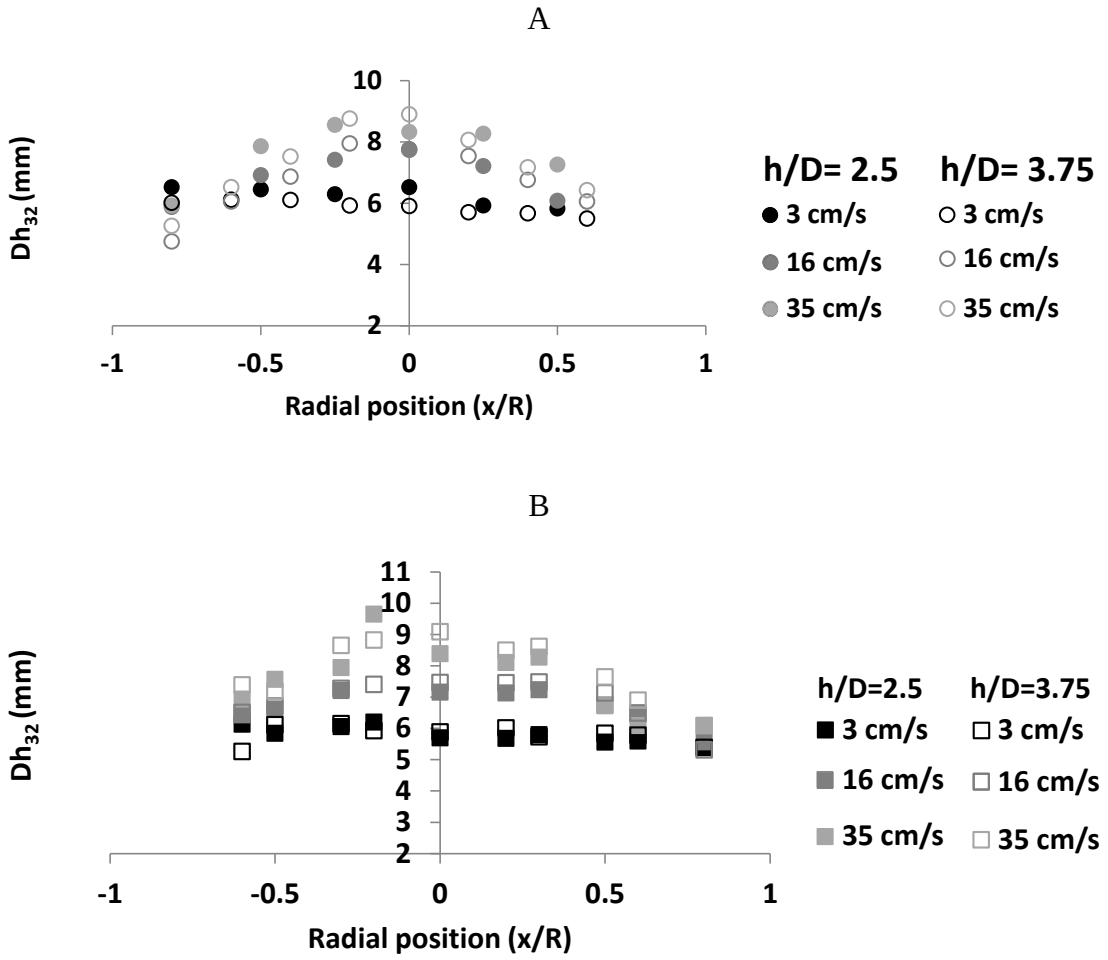

Figure 4.8 – Radial profiles of Dh_{32} at h/D=2.5 and 3.75 for v_{sg} ranging from 3 cm/s up to 35 cm/s in the columns: A) Phi 400; B) Phi 1000.

Figure 4.8 A and B show that quite similar profiles of Dh_{32} were obtained at h/D=2.5 and 3.5, meaning that the spatial segregation of the bubble size was already established at h/D=2.5. Nevertheless, there were some differences on the Dh_{32} values obtained at the two elevations. Further study the evolution of the bubble size on the column axis Table 4.19 and Table 4.20 present the difference of the Dh_{32} measured at h/D=2.5 and 3.75 and at x/R=0 and X/R=0.6 for all the superficial gas velocities for the Phi 400 and Phi 1000 columns, respectively

Table 4.19 – Difference between the Dh_{32} measured at h/D=2.5 and 3.75 in the Phi 400 column.

Units= mm

	Position Radial (x/R)	
Vsg (cm/s)	**0**	**0.6**
3	0.6	0.6
9	-0.5	-0.5
16	-0.2	-0.2
25	-0.4	-0.4
35	-0.4	-0.4

Table 4.20 – Difference between the Dh_{32} measured at h/D=2.5 and 3.75 in the Phi 400 column.

Units= mm

	Position Radial (x/R)	
Vsg (cm/s)	0	0.6
3	-0.2	-0.2
9	-0.2	-0.2
16	-0.3	-0.1
25	-0.5	-0.2
35	-0.7	-0.8

The results presented in Table 4.19 support the conclusion that there is no significant evolution of the Dh_{32} between the h/D=2.5 and 3.75 in the Phi 400 column, since the measurements never differed more than 0.6 mm. The average difference between the measurements, along the radial profile and at iso-v_{sg} was typically 0.7 mm, except for the v_{sg}=3 cm/s where the average difference was 0.3 mm.

The results obtained in the Phi 1000 column presented ever a similar agreement with the maximum difference between both measurements of 0.8 mm, however the average difference along the radial profile of ≈0.3 mm, at iso-v_{sg}.

Concluding, the radial profiles of the Dh_{32} are already established at h/D=2.5, with a maximal difference of the Dh_{32} 0.8 mm. Moreover, in all the columns the bubble Dh_{32} in the column center ranged from typically 6 mm at v_{sg}= 3 cm/s up to 8 mm at v_{sg}= 35 cm/s, as can be seen in Table 4.21. The spatial segregation of bubble size increased with the superficial gas velocity and the column diameter, as can also be seen in Table 4.21.

Table 4.21 – Resume of Dh_{32} measured at x/R=0 and the spatial segregation of the Dh_{32} for all the columns and v_{sg}. Units= mm

		vsg (cm/s)				
		3	**9**	**16**	**25**	**35**
Phi 150	**Dh_{32}(x/R=0)**	7.0	7.6	8.9	9.8	9.4
	Δ Dh_{32}	0.3	1.6	2.4	3.1	2.2
Phi 400	**Dh_{32}(x/R=0)**	6.5	6.5	7.8	7.7	8.3
	Δ Dh_{32}	0.0	1.1	1.9	2.1	2.4
Phi 1000	**Dh_{32}(x/R=0)**	5.7	6.6	7.2	7.6	8.4
	Δ Dh_{32}	0.5	1.5	2.2	2.6	3.0
vsg (cm/s)		**6**	**9**	**12**	**16**	-
Phi 3000	**Dh_{32}(x/R=0)**	6.8	8.0	7.3	7.2	-
	Δ Dh_{32}	-	-	4.0	-	-

4.3 Global gas hold-up

The global gas hold-up can be measured by the difference of the column static height and dynamic height as shown in Eq. (1.1). This method is not very accurate, since it relies on the visual measurement of the bed's free surface height, which can be quite challenging to be determined in agitated flows (relative error: ±10%). However, it is a quick and easy method to apply and it has been commonly used by others authors. The global void fraction was measured in all the columns for a superficial gas velocity range between 2 cm/s and 35 cm/s, except in the Phi 3000 column, where it was measured between 5 cm/s and 15 cm/s. The results are presented in Figure 4.9. Moreover, Forret et al. (2006) have used this method to measure the mean gas hold-up in columns with diameters up to 1 m. Their results for a 0.4 m diameter column, that used a perforated plate with 2 mm inner diameter injectors, are also plotted in Figure 4.9.

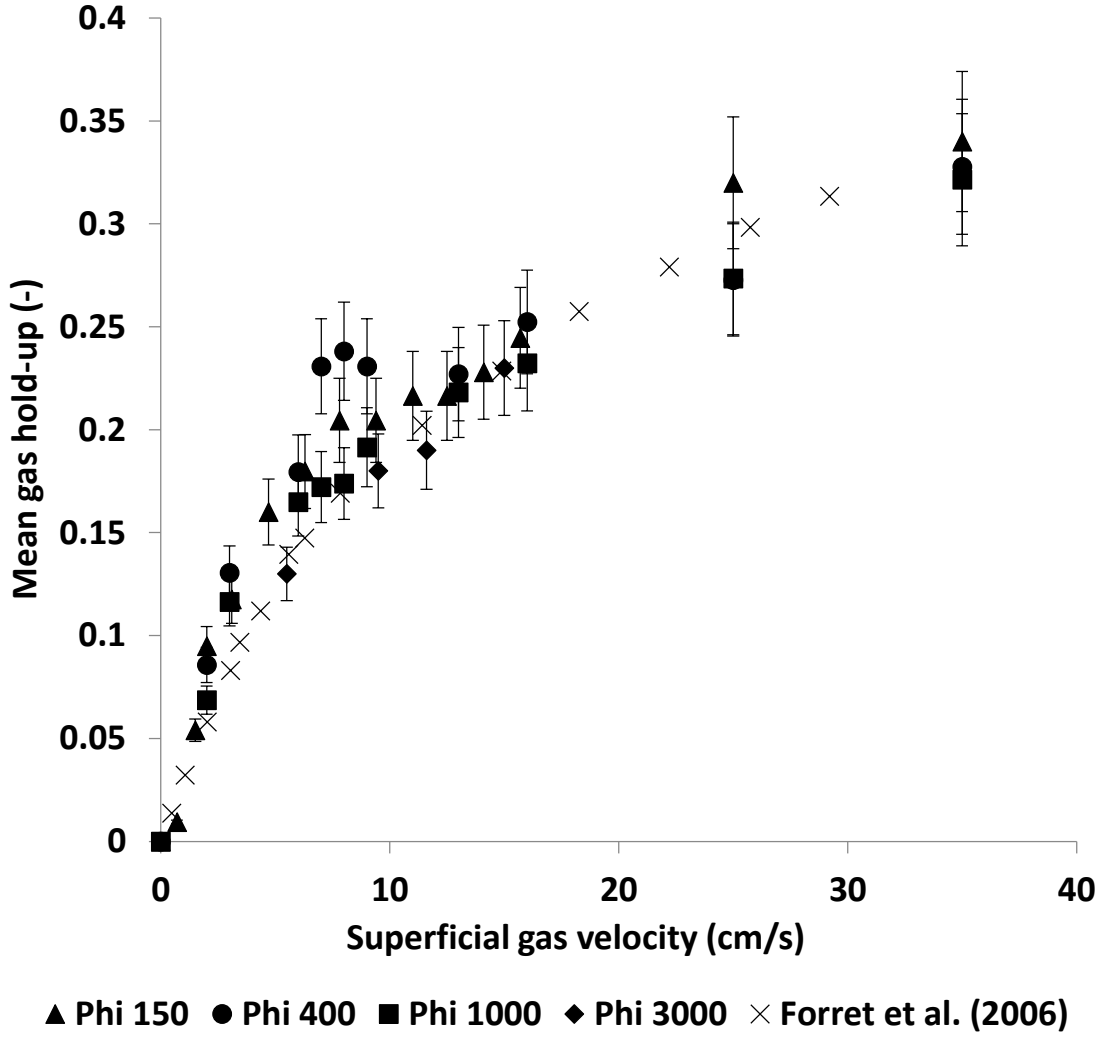

Figure 4.9 – Evolution of the mean gas hold-up with the superficial gas velocity

The results show that, in general, the global gas hold-up has no dependency on the column diameter. That conclusion arises from the good agreement found between the data gathered in columns with a 1:20 scale factor: the mean difference between the measurements in the column Phi 400, Phi 1000 and Phi 3000 relatively to the Phi 150 are 0.017 0.018 and 0.02, respectively. This result is in agreement with the findings of Forret et al. (2006).

In Figure 4.9, the Phi 400 column presents a slightly higher global gas hold-up between the superficial gas velocities of 7 cm/s and 9 cm/s, which could be related with a variation in the bubble size: smaller bubbles rise slowly in the column and consequently can lead to a higher gas hold-up. In order to further understand this phenomena the bubble

chords PDFs for superficial gas velocities of 3 cm/s, 9 cm/s and 16 cm/s at h/D=2.5 obtained in the center of the column are presented in Figure 4.10.

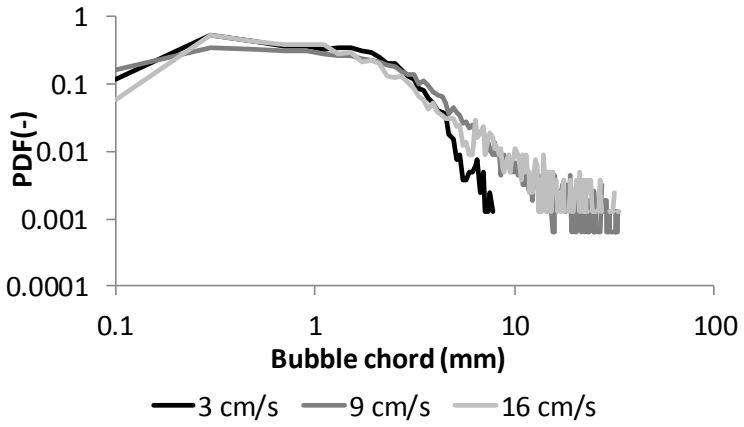

Figure 4.10 – Bubble chords PDFs at superficial gas velocities of 3 cm/s, 9 cm/s and 16 cm/s obtained in the center of the Phi 400 column at h/D=2.5

By analyzing Figure 4.10 it is possible to observe that there is an increase in the maximal detected chords between 3 cm/s and higher superficial gas velocities. However, a similar bubble chord distribution is obtained for v_{sg} of 9 cm/s and 16 cm/s, in both ends of the PDFs. So, no explanation was found to the maximum of the global gas hold-up detected in the Phi 400 column.

Additionally, the results show a good agreement with the data of Forret et al. (2006) in all the range of v_{sg}, except in between vsg= 2 cm/s and 5 cm/s where somewhat higher values were found in our experiments.

The variation of the global gas hold-up can also give us some information on the transition between the homogeneous/heterogeneous regimes. A log-log plot of global gas hold-up as a function of the v_{sg} should present a different slope for the global gas hold-up evolution of in each regime, as shown in Figure 4.11.

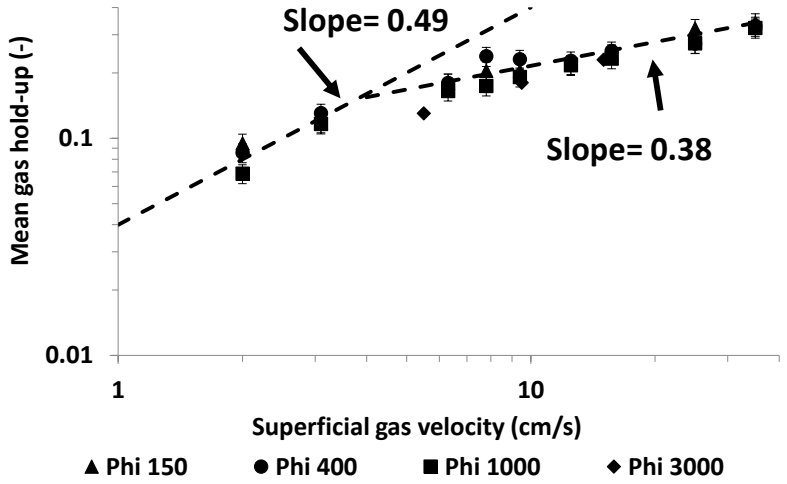

Figure 4.11 – A log-log representation of the global gas hold-up as a function of the superficial gas velocity for all the columns.

Analyzing Figure 4.11 is possible to conclude that the homogeneous regime extends only up to a v_{sg}=3-4 cm/s. At higher superficial gas velocities, the flow is already in the heterogeneous regime. Note also that the global void fraction is nearly linear with v_{sg} when focusing on very low superficial gas velocities (say below 4-5 cm/s): this linearity at low v_{sg} has been often observed (see chap 1) and it is consistent with the model proposed by Ruzcika et al. (2001) in which the liquid backflow takes places everywhere in the spacing between bubbles. This linear region will be not analyzed further owing to the limited number of data.

Table 4.22 presents some correlations from the literature that permit to predict the global gas hold-up as a function of the superficial gas velocity and the physical properties of the gas and liquid phases.

Table 4.22 – Global gas hold-up literature correlations

Correlation	Author
$\overline{\varepsilon g} = 0.505 {v_{sg}}^{0.47} \left(\frac{0.072}{\sigma}\right)^{2/3} \left(\frac{0.001}{\mu_l}\right)^{0.05}$	Hikita and Kikukawa (1974)
$\overline{\varepsilon g} = 0.672 \left(\frac{v_{sg}\mu_l}{\sigma}\right)^{0.578} \left(\frac{{\mu_l}^4 g}{\rho_l \sigma^3}\right)^{-0.131} \left(\frac{\rho_g}{\rho_l}\right)^{0.062} \left(\frac{\mu_g}{\mu_l}\right)^{0.107}$	Hikita et al. (1980)
$\overline{\varepsilon g} = 0.728x' - 0.485x^2 + 0.0975x^3$ $x = v_{sg} \left[\frac{\rho_l^2}{\sigma(\rho_l - \rho_g)g}\right]^{1/4}$	Grover et al. (1986)
$\overline{\varepsilon g} = 296 {v_{sg}}^{0.44} \rho_l^{-0.98} \rho_g^{0.19} \sigma^{-0.16} + 0.009$	Reilly et al. (1986)
$\overline{\varepsilon g} = 129 \left(\frac{\mu_l v_{sg}}{\sigma}\right)^{0.99} \left(\frac{{\mu_l}^4 g}{\rho_l \sigma^3}\right)^{-0.123} \left(\frac{\rho_g}{\rho_l}\right)^{0.187} \left(\frac{\mu_g}{\mu_l}\right)^{0.343} \left(\frac{d_0}{D}\right)^{-0.089}$	Sotelo et al. (1994)

Each of these correlations depend on the superficial gas velocity. Yet, the proposed scaling are quite different, with exponents ranging from 0.44 up to 1. Therefore, to study the dependency of the global gas hold-up with the superficial gas velocity, our experimental data are represented in a log-log plot in Figure 4.12. A power law behavior arises for all columns and over the whole range of v_{sg}. The slopes are close to 0.44±0.05, except for the larger slope (≈0.57) found for the Phi 3000 column that may result from the limited number of data collected and/or because of significant coalescence effects in that column. Putting all the data together, the scaling corresponds to $\langle \varepsilon_g \rangle \propto {v_{sg}}^{0.45}$, and within the resolution of our measurements, there is no effect of the column diameter on the slope. Such a trend is in very good agreement with the correlations proposed by Reilly et al. (1986) or by Hikita and Kikukawa (1974). However, if the lowest superficial gas velocities are discarded, that is for $v_{sg} \geq 5$cm/s, there is still no sensitivity to the column diameter and the behavior with the superficial gas velocity becomes significantly less steep with $\langle \varepsilon_g \rangle \propto {v_{sg}}^{0.35}$.

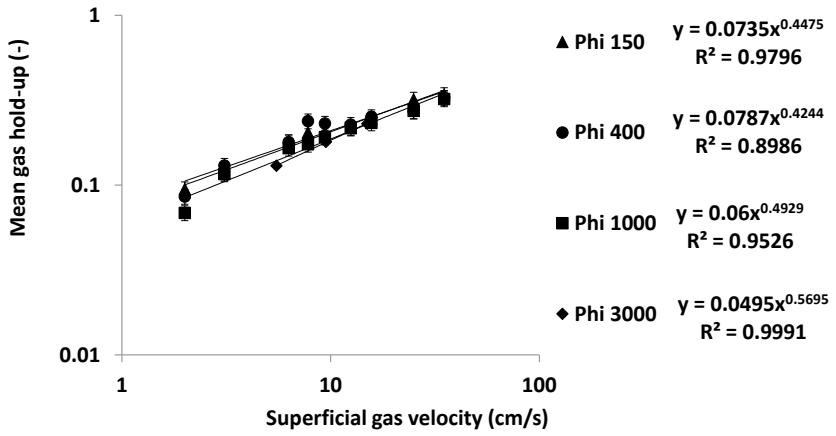

Figure 4.12 – A log-log representation of the global gas hold-up as a function of the superficial gas velocity.

4.4 Local gas hold-up

The radial profiles of gas hold-up that provide some information about the spatial concentration of the gas phase inside the column are detailed in this section. Let us recall that the local gas-hold up is measured using 1C mono-fiber optical probe. For all conditions, the probe was vertical and pointing downwards as seen in Chap.3.

Stabilized flow region

The local gas hold-up profiles were measured at several h/D in the Phi 400 column in order to study their evolution along the column axis. The stabilized flow region, a zone of the flow sufficiently away from the gas distributor and from the free surface to have a quasi-fully developed behaviour, is characterized by an axial invariance of the local gas hold-up profile. Thus, the radial profiles of local hold-up were plotted in Figure 4.13 A, B and C at several h/D ratios (from 0.38 up to 5) for the v_{sg} of 3 cm/s, 16 cm/s and 35cm/s, respectively. There is no profile for v_{sg}=3cm/s at h/D = 5, since the expansion of the bed was not sufficient to perform measurements at such an elevation.

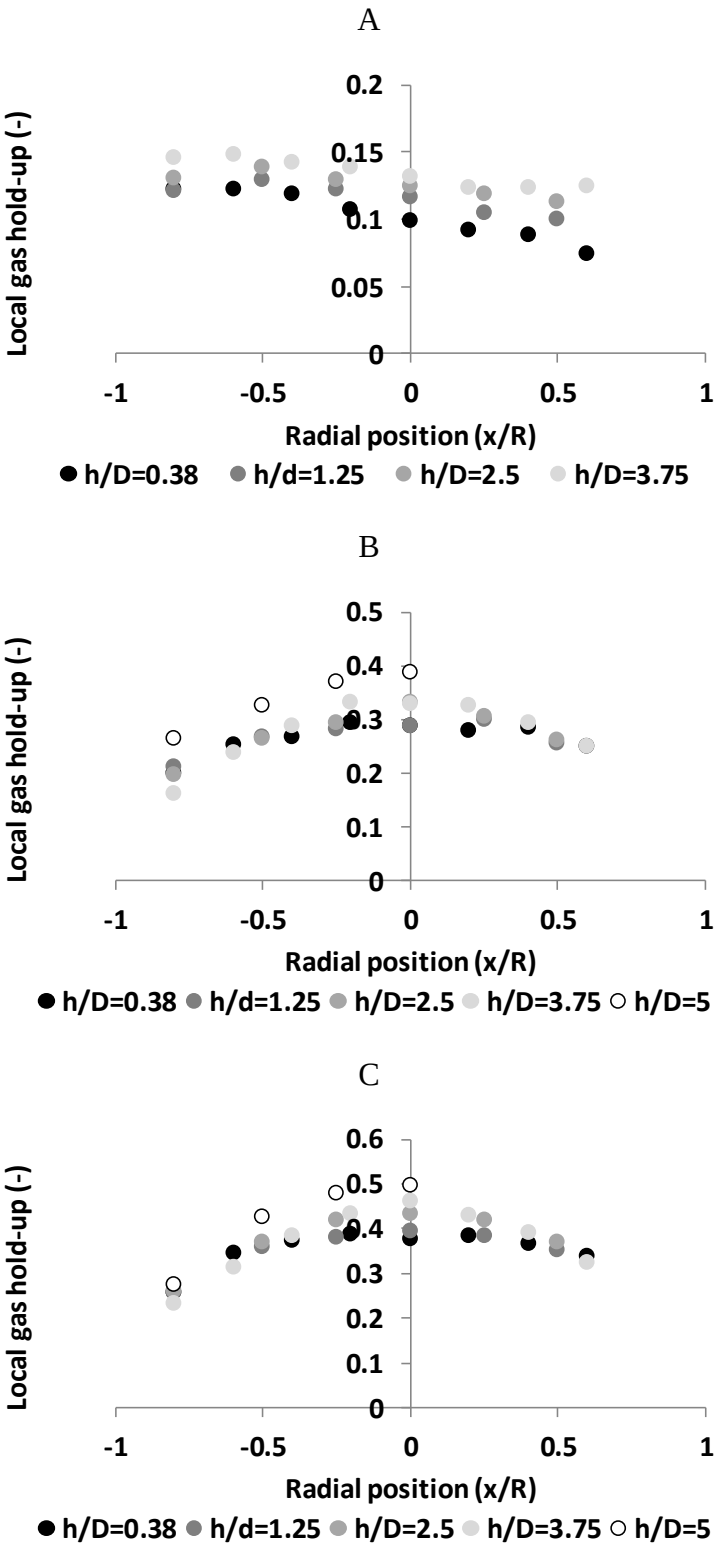

Figure 4.13 – Local gas hold-up radial profiles at several h/D ratios for various superficial gas velocities: A) 3cm/s; B) 16 cm/s; C) 35 cm/s. (Measurements in the Phi 400 column with 1C probe)

At v_{sg} of 3 cm/s, there is an increase of the local gas hold-up from h/d=0.38 up to 2.5. However, the radial profiles obtained at h/D of 2.5 and 3.75 are quite close to each

other. They are also flatter than the ones obtained at lower elevations, namely h/D of 0.38 and 1.25, possibly due to the homogenization of the gas concentration in the column.

By analyzing the measurements obtained at 16 cm/s, it is possible to conclude that there is no significant evolution of the local gas hold-up profiles from h/d=0.38 up to 3.75, except in the center of the column, where slightly lower gas hold-up values were obtained at h/D = 0.32 and 1.25. The measurements performed at h/D = 5 present higher values of the gas hold-up in all the tested radial positions, which could indicate that the measurements were performed too close to the free surface of the column.

Similar conclusions can be drawn for the measurements performed at v_{sg} of 35 cm/s, where no significant evolution is noted for h/D ratios from 0.38 up to 3.75, except in the column center. Once again, the local gas hold-up values measured at h/D of 5 were higher than the ones obtained at lower h/D ratios.

It is impossible to perform the same study on the Phi 150 column since the local gas hold-up was only measured at h/D=1 and 2.5. Nevertheless, the evolution of local gas hold-up profiles will be studied between the two elevations, and both profiles are plotted for superficial gas velocities of 3 cm/s, 9 cm/s and 16 cm/s in Figure 4.14 A.

In a similar order to verify if the established flow region defined for the Phi 400 column is also valid for the column Phi 1000, the local void fraction profiles at h/D=2.5 and 3.75 are presented in Figure 4.14 B.

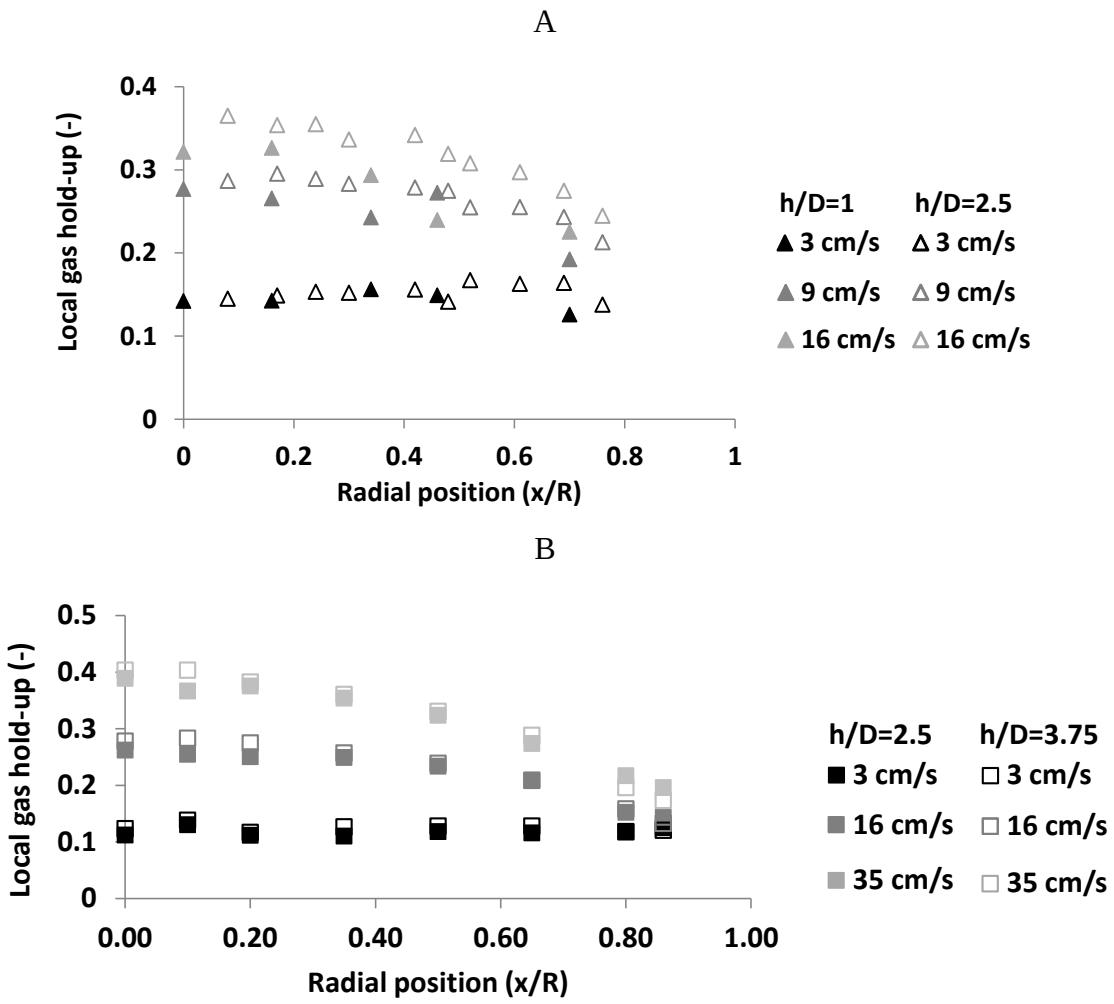

Figure 4.14 – Local gas hold-up radial profiles at several h/D ratios in the columns: A) Phi 150; B) Phi 1000

In the column Phi 150, the results show that at 3 cm/s the radial profile is already established at h/D=1, though at v_{sg}= 9 cm/s and 16 cm/s higher local gas hold-up values are obtained at h/D=2. Since the measurements were not performed at h/D=3.75 it is not possible to verify if the profiles of local gas hold-up changed at higher elevations in the column.

Regarding the column Phi 1000, Figure 4.14 B shows that the radial gas hold-up profiles obtained at h/D=2.5 and 3.75 are overlapping, which is in agreement with the results obtained in the Phi 400 column. In order to analyze these differences in more detail, both in Phi 400 and Phi 1000 columns, the Table 4.23 and Table 4.24 present the

difference found in the εg values between the elevations h/D=2.5 and 3.75 for two radial positions x/R=0 and x/R=0.6.

Table 4.23 – Difference between the εg measured at h/D=2.5 and 3.75 in the Phi 400 column. Units=absolute gas hold-up

		Position Radial (x/R)	
Δ εg	v_{sg} (cm/s)	0	0.6
	3	0.01	0.01
	9	0.01	0.03
	16	0	0.03
	25	0.01	-0.01
	35	0.03	0.02

Table 4.24 – Difference between the εg measured at h/D=2.5 and 3.75 in the Phi 1000 column. Units=absolute gas hold-up

		Position Radial (x/R)	
Δ εg	v_{sg} (cm/s)	0	0.6
	3	0.01	0.01
	9	0.01	0.01
	16	0.02	0
	25	0.02	-0.01
	35	0.01	0.01

In the Phi 400 column, the maximum difference detected between the εg was 0.03, while the average difference in each profile was typically 0.02. In the Phi 1000 column the maximum difference was of 0.02, and the average difference found on each profile was typically 0.01.

Concluding, the results show that the stabilized flow regime zone is located between the h/D ratio of 2.5 and 3.75 in Phi 400 and Phi 1000 columns (for a maximal difference of 0.03). It should be noticed that, in the Phi 150 column it was not possible to verify if the local gas hold-up was constant for h/D>2.5. Additionally, no study of the variation of the local gas hold-up was conducted in the Phi 3000 column. So, it will be considered that in the columns Phi 150 and Phi 3000 the evolution of the local gas hold-up along the column axis is similar to the other columns.

Impact of the superficial gas velocity

The local gas hold-up was measured along the column radius for the Phi 150, 400 and 1000 and 3000 columns at a dimensionless height of h/D=2.5. Figure 4.15 shows the radial profiles of the local gas hold-up scaled by its value measured on the column axis for superficial gas velocities of 9, 16 and 35 cm/s at a dimensionless height of h/D=2.5 for the columns Phi 150, 400 and 1000. In the Phi 3000 the local gas hold-up was measured only at v_{sg}=12 cm/s, and the radial profile is presented in Figure 4.16.

A

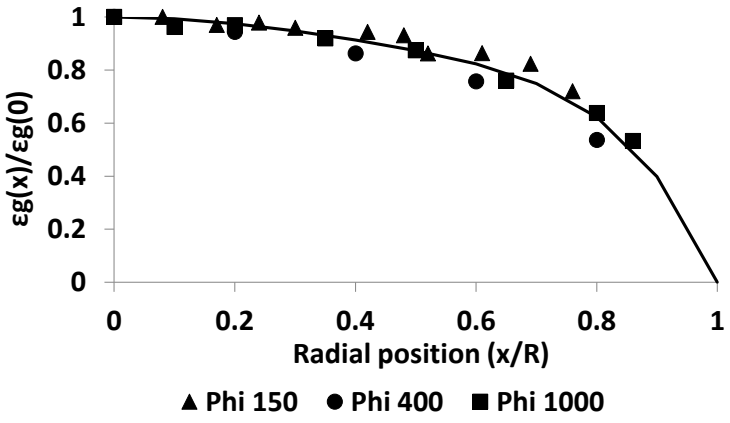

B

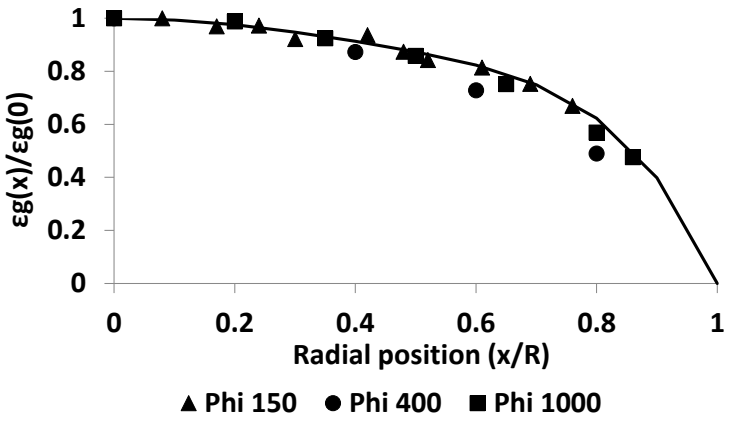

C

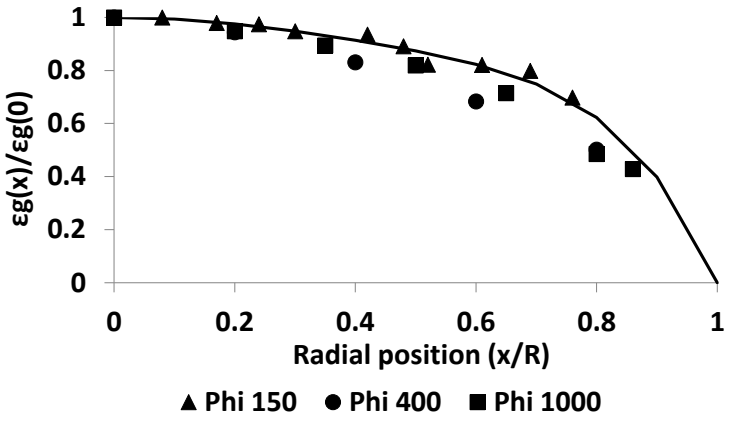

Figure 4.15 – Void fraction radial profiles in the columns Phi 150, Phi 400 and Phi 1000 at h/D=2.5 for superficial gas velocities: A) 9 cm/s; B) 16 cm/s; C) 35 cm/s. (line – Eq (1.1)). The void fraction is scaled by its value measured on the column axis.

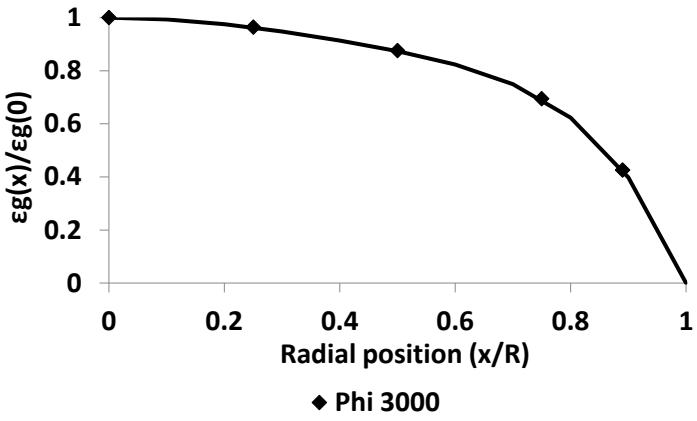

Figure 4.16 - Void fraction radial profile in the column Phi 3000 at h/D=2.5 for v_{sg}=12 cm/s. (line – Eq (1.1)). The void fraction is scaled by its value measured on the column axis.

As can be seen in Figure 4.13 and Figure 4.14, at a superficial gas velocity of 3 cm/s the gas hold-up profiles are flat for all the columns, as expected for the homogeneous regime. At higher superficial gas velocities (9cm/s and above), the profiles have a parabolic-like shape with the maximum gas hold-up in the center of the column, as shown in Figure 4.15 A, B and C. As previously referred to in chapter 1, the column diameter does not have a significant impact on the gas hold-up profiles, as shown by the normalized radial profiles plotted in Figure 4.15 A, B and C. Concluding, it can be stated that the local gas hold-up values are a function of the superficial gas velocity and of the radial position only: they do not depend on the column diameter.

Additionally, the normalized radial gas hold-up profiles can be computed by Eq. (1.1), that is a function of the global gas hold-up ($\bar{\varepsilon_g}$), as previously presented in section 1.2. This correlation was established from experiments carried out in columns with a diameter up to 0.4 m and using optical probes for local gas hold-up measurements. Thus, the calculated profiles are also plotted in Figure 4.15 and Figure 4.16, using the global gas hold-up values reported in Figure 4.9. For this estimate, we considered that the void fraction on the axis can be deduced from the global hold-up using $\varepsilon g(0) = 1.5 \langle \varepsilon g \rangle$ as given by the fit Eq.(1.1) . However, experiments indicate that this ratio is somewhat sensitive to the column diameter: as shown in Figure 4.17, it monotonously decreases from 1.5 in the Phi 150 column down to 1.15 in the Phi 1000 column. In the following, we keep the 1.5 coefficient whenever the fitted void fraction profile is used.

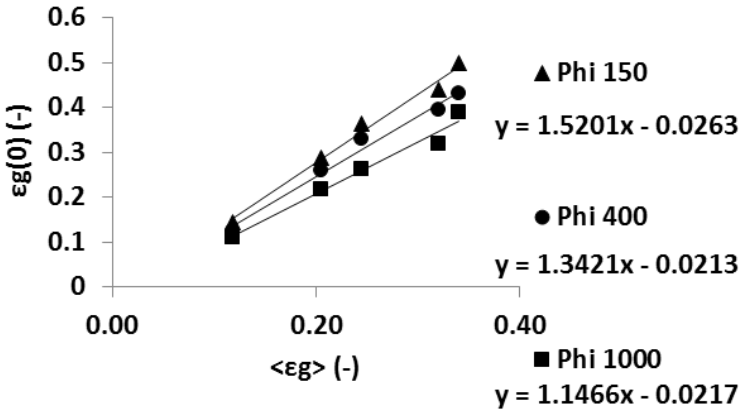

Figure 4.17 - Relationship between the local gas hold-up measured on the axis of the column and the global gas holp-up for three column diameters and for v_{sg} between 3 cm/s and 35 cm/s.

Overall, a good agreement is found between the experimental void fraction values and the predicted ones (Eq. (1.1)) for all the tested positions and for all superficial gas velocities. The case v_{sg}=3 cm/s is here excluded from the discussion since the Eq. (1.1) predicts parabolic shaped profiles and thus it is not adapted for the flat profiles observed in the homogeneous regime. The averaged discrepancies found between the measurements and the values Eq. (1.1) are shown in Table 4.25: these discrepancies have been estimated as the difference between the experimental values and predicted values. The typical deviation is about a few % in void fraction while the largest difference amount for 7% in void.

Table 4.25 – Average differences between the experimental data and the predicted radial profiles of εg (Eq. (1.1)) Units = absolute void fraction

	Phi 150	Phi 400	Phi 1000	Phi 3000
9 cm/s	0.03	0.01	0.01	
12 cm/s	-	-	-	0.001
16 cm/s	0.05	0.06	0.07	
35 cm/s	0.02	0.02	0.05	

Yet, one expects uncertainties in local void fraction measurements at large radial distances for the reasons detailed in Chap.3. Since the measurements are more reliable in the central, upward directed zone, let us analyze the mean void fraction $\langle \varepsilon g_{0-0.7} \rangle$ between x/R=0 and x/R=0.7. Starting from Eq.(1.1) written as $\varepsilon_g(x/R) = \langle \varepsilon_g \rangle \left[a\left(x/R^6 - 1\right) + b\left(x/R^4 - 1\right) + c\left(x/R^2 - 1\right) \right]$, where a=-1.7889, b=1.228 and c=0.939, one has:

$$\langle \varepsilon g_{0-0.7} \rangle = \frac{2\pi R^2 \langle \varepsilon_g \rangle \int_0^{0.7} a\left({}^{x}/_{R}{}^{6} - 1\right) + b\left({}^{x}/_{R}{}^{4} - 1\right) + c\left({}^{x}/_{R}{}^{2} - 1\right) d\,{}^{x}/_{R}}{2\pi \int_0^{0.7R} r dr} \quad (4.1)$$

$$= 1.315 \langle \varepsilon_g \rangle$$

We estimated $\langle \varepsilon g_{0-0.7} \rangle$ using its definition above: the resulting void fraction $\langle \varepsilon g_{0-0.7} \rangle$ happens to evolve also as $vsg^{0.4}$ with minor difference in the exponent depending on the range of vsg considered. All data fall within -11%, +17% of the correlation $\langle \varepsilon g_{0-0.7} \rangle \approx 0.557 v_{sg}^{0.4}$. Again, no clear dependency to the column diameter D can be detected, as seen in Figure 4.18. As these measurements are more reliable in that zone, that gives extra credit to the proposed scaling.

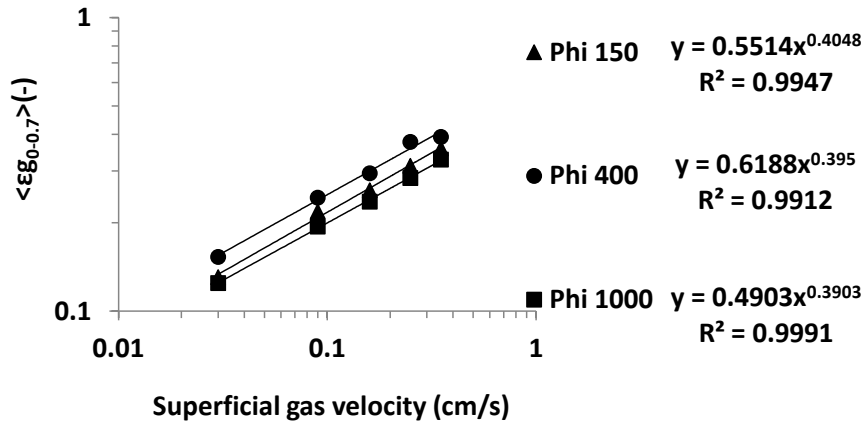

Figure 4.18 – Log-log representation of the $\langle \varepsilon g_{0-0.7} \rangle$ as a function of the superficial gas velocity for the columns Phi 150, Phi 400 and Phi 1000. (Measurements obtained at h/D=2.5)

As detailed in section 4.3, the increase of the global gas hold-up with v_{sg} can be described with a power law with an exponent between 0.45 and 0.35 depending on the range of v_{sg} considered. So, it is interesting to verify if the local gas hold up in the column center (εg(0)) and in the exterior part of the column (εg(0.6)) follow the same scaling. Additionally, in section 4.3 it has been concluded that the global gas hold-up does not depend on the column diameter, that feature should also be verified on the local gas hold-up values. Therefore, Figure 4.19 presents a log-log representation of the variation of εg(0) as a function of the superficial gas velocity for the columns Phi 150, Phi 400 and Phi 1000.

A

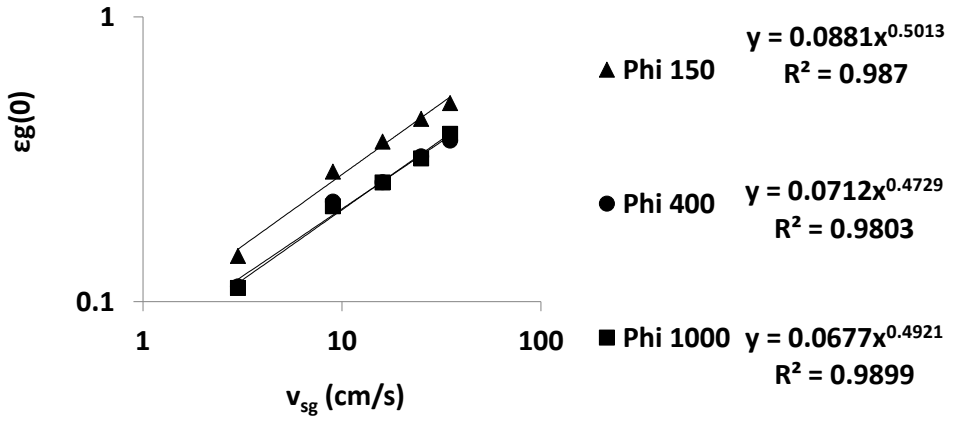

B

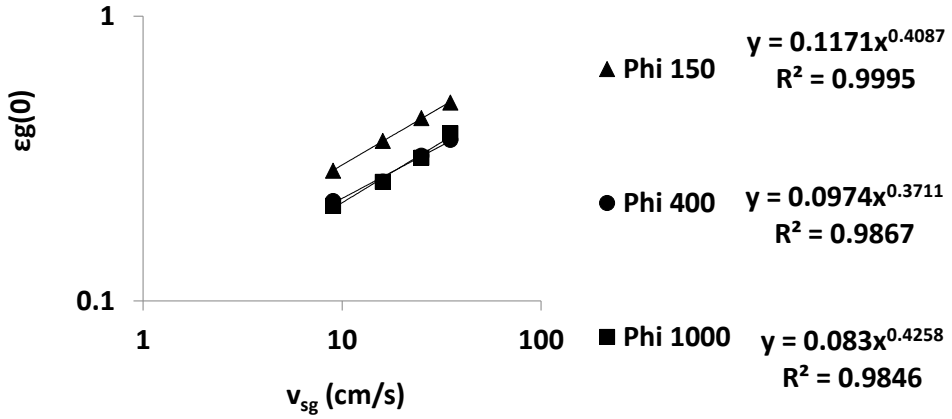

Figure 4.19 – Log-log representation of the local gas hold up at x/R=0 for the columns Phi 150, Phi 400 and Phi 1000 at range of v_{sg} : A)from 3 cm/s up to 35 cm/s; B) from 9 cm/s up to 35 cm/s

Accounting for all available data, εg(0) follows a power law with an exponent ranging between 0.47 and 0.5, similar to what has been seen for the global gas hold-up. Discarding the smallest v_{sg}, i.e. for $v_{sg} \geq$ 5-6cm/s, the data are fitted within ±4% by the expression $\varepsilon g(0) = 0.0982 v_{sg}^{0.4019}$ for all columns, namely Phi 150, 400 and 1000 columns (only one local void fraction data was available for the Phi 3000). That behavior is very close to the one found for the global void fraction with $v_{sg} \geq$ 5-6cm/s, and again, there is no perceivable sensitivity to the column diameter. A similar analysis of the evolution of the local gas hold-up with the superficial gas velocity was performed for the radial position x/R=0.6 for the columns Phi 150, Phi 400 and Phi 1000, as can be seen in Figure 4.20.

A

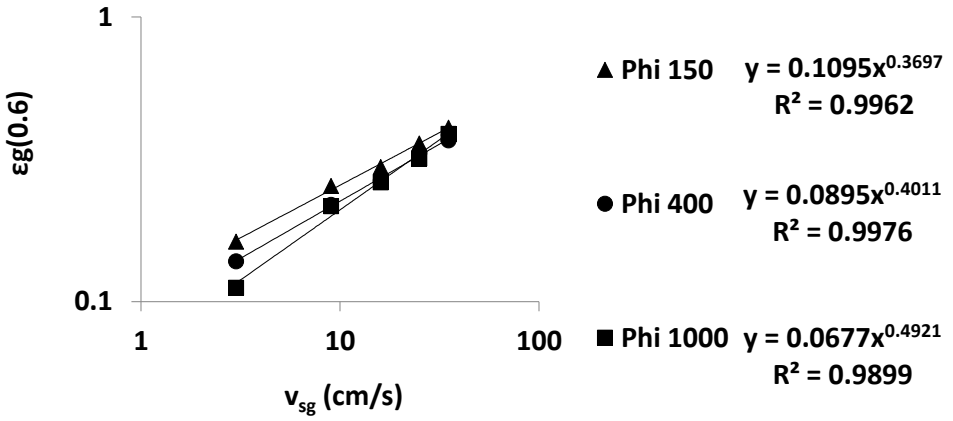

B

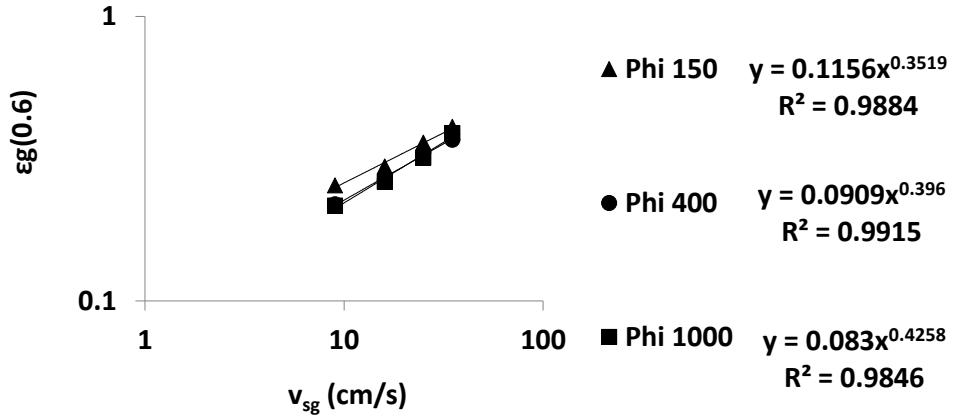

Figure 4.20 - Log-log representation of the local gas hold up at x/R=0.6 for the columns Phi 150, Phi 400 and Phi 1000 at range of v_{sg} : A)from 3 cm/s up to 35 cm/s; B) from 9 cm/s up to 35 cm/s

If all the v_{sg} are taken in to account, the power laws that arises for all the columns have an exponent ranging between 0.37 and 0.5, however if only the v_{sg}>5-6 cm/s are accounted for, the exponent ranges between 0.35 and 0.43. These values are quite close to the exponent found for global gas hold-up and for $\varepsilon g(0)$, and once again no significant effect of the column diameter is detected. The fact that the same scaling holds for local and global gas hold-up arises, and inversely confirms, the similarity of void fraction radial distributions.

In the above section, the evolution of the void fractions either global or local with the control parameters D and v_{sg} has been discussed: clearly these void fractions do not depends on the column diameter. Yet, they increase as vsg^n with an exponent in the range 0.35 - 0.43. In addition, the empirical fit Eq.(1.1) to the void fraction profile has been validated over an enlarged set of conditions and in particular in the largest column

available (Phi 3000). Yet, some uncertainties persist on the precise shape of the void fraction profiles in bubble columns. Indeed, although the global hold-up was recovered within ±15%, uncertainties arise when the flow direction is changing (in Chap.3, we have seen that an improper probe orientation can lead to a 40% underestimation of the void fraction). Thus, one may expect that void fractions at large radial distances and notably for x/R above 0.7 are underestimated. If so, the actual profiles should be steeper near the walls. It would be worthwhile to clarify this question in the future, using an alternate technique based, for example, on a spatially well resolved X or gamma ray tomography.

4.5 Liquid velocity

The liquid velocity was measured using a Pavlov tube with two different sets of pressure sensors, as detailed in section 3.1. The 8 Hz bandwidth pressure sensors were used in the Phi 150 (h/D=2.5), Phi 400 (h/D=2.5 and 3.75) and Phi 3000 (h/D=1.5) where only the axial component of the liquid velocity was measured. The 100 Hz bandwidth pressure sensors were used to perform measurements in the Phi 400 column (h/D=2.5) and in the Phi 1000 column (h/D=3.75).

Stabilized flow region

As previously demonstrated, the bubble Dh_{32} and the local gas hold-up are invariant over the column cross-section the between h/D ratios of 2.5 and 3.75. In order to verify if the mean liquid velocity is also invariant along the column axis, radial profiles of the mean axial liquid velocity were measured at h/D=2.5 and 3.75 in the Phi 400 column, as can be seen in Figure 4.21.

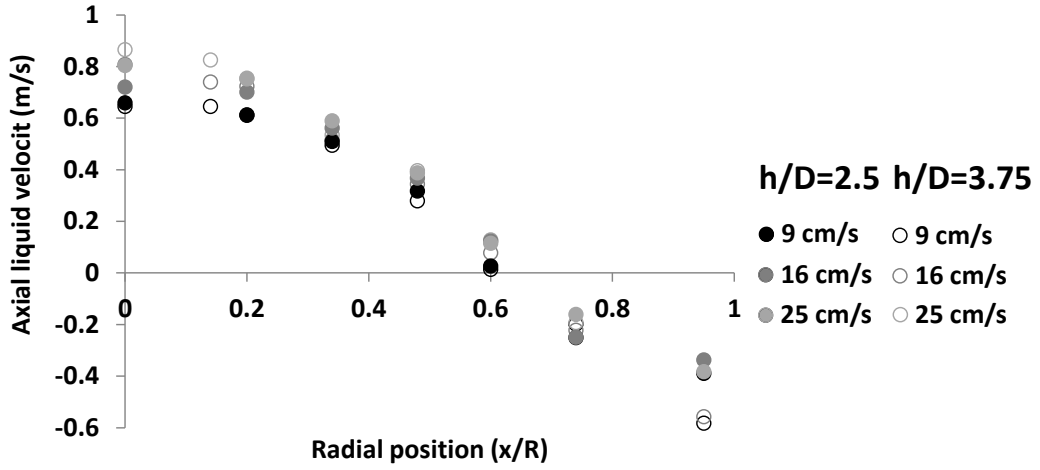

Figure 4.21 – Radial profiles of axial liquid velocity at several superficial gas velocities in the Phi 400 column at h/D ratios of 2.5 and 3.75. (Measurements with 8 Hz bandwidth pressure sensors)

The results show that for superficial gas velocities between 9 cm/s and 25 cm/s, globally there is no significant evolution of the axial liquid velocity radial profiles in the Phi 400 column, between the h/D ratios of 2.5 and 3.75 (coherent with measurement in the Phi 1000 column, Forret, 2006). The differences between the measurements at h/D 2.5 and 3.75 are quantified for the radial positions of x/R=0 and x/R=0.6 in Table 4.26.

Table 4.26 – Differences between the axial liquid velocity at h/D=2.5 and h/D=3.75 for the radial positions x/R=0 and 0.6. Units= Units=m/s

	Radial position (x/r)	
	0	**0.6**
9 cm/s	0.01	0.01
16 cm/s	-0.09	0.05
25 cm/s	-0.06	-0.01

The results show that the maximum difference between the axial liquid velocity in the positions x/R=0 and 0.6 is about 0.09 m/s, while the average difference on the radial profile was typically 0.06 m/s. Therefore, it is possible to conclude that, similarly to the gas hold-up and the bubble Dh_{32}, the mean liquid velocity is also constant between these two elevations in the Phi 400 column.

The liquid velocity on the Phi 150 and Phi 3000 columns was measured only at one elevation, consequently it was not possible to verify if the liquid velocity was also constant between h/D=2.5 and 3.75. Thus, it will be considered that the stabilized flow region detected in the Phi 400 column was also valid for the other columns.

Radial axial liquid velocity profiles

The radial profiles of the mean axial liquid velocity were measured in the Phi 150 (h/D=2.5), Phi 400, Phi 1000 (h/D=3.75) and Phi 3000 (h/D=1.5) for superficial gas velocities from 9 cm/s up to 25 cm/s, as shown in Figure 4.22 A, B, C and D, respectively. All the measurements were performed with the 8 Hz bandwidth pressure sensor, except the ones obtained in the Phi 1000 column.

A

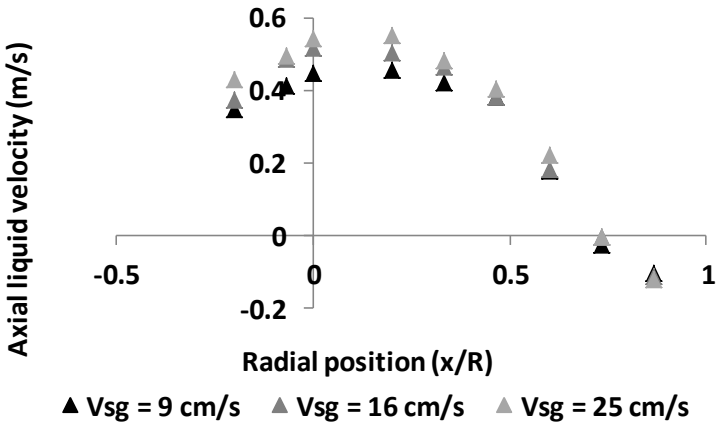

B

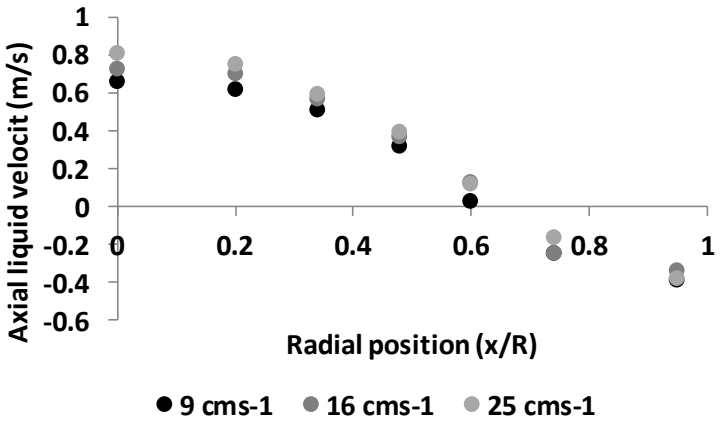

C

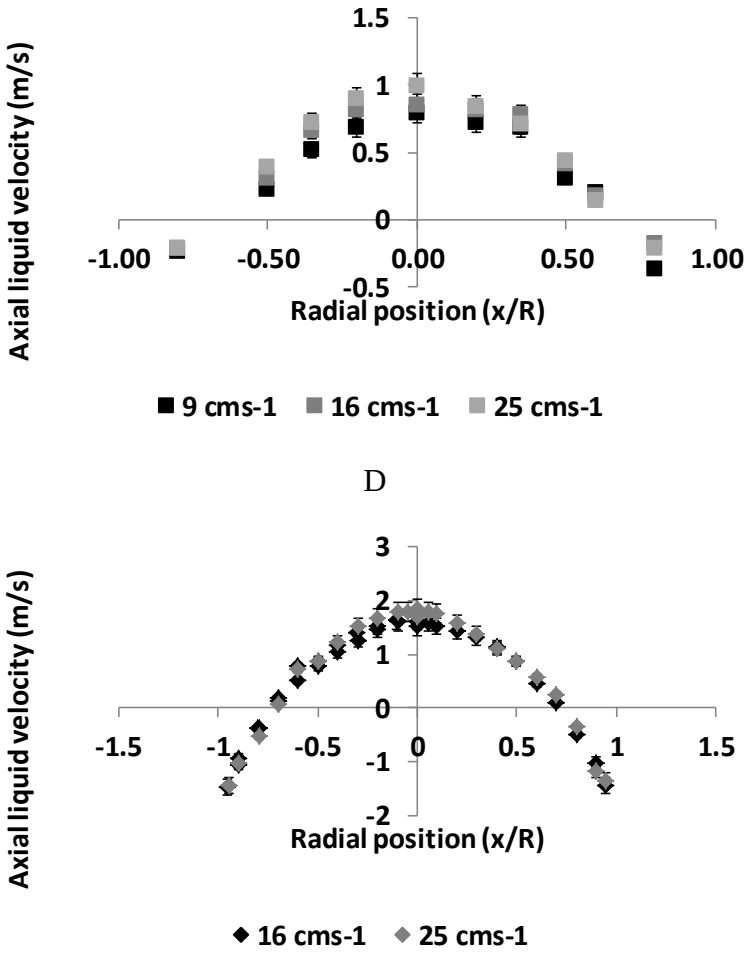

Figure 4.22 – Radial profiles of mean axial liquid velocity at several superficial gas velocities in the columns: A) Phi 150 (h/D=2.5); B) Phi 400 (h/D=2.5); C) Phi 1000 (h/D=3.75); D) Phi 3000 (h/D=1.5).(Phi 150, 400, 1000, 3000 - 8 Hz bandwidth pressure sensors, Phi 1000 – 100 Hz bandwidth pressure sensors)

Figure 4.22 shows that, regardless of the column diameter, the radial profiles present a similar evolution with the superficial gas velocity: there is an increase of the velocity in the center of the column, and all radial profiles show that the direction of the mean axial liquid velocity is inverted at x/R=0.7. Forret et al (2006) have proposed a correlation to determine the radial profiles of the axial liquid velocity as a function of the velocity in column center:

$$ul(x/R) = \frac{ul(0)}{a-c}\left[ae^{(-b(x/R)^2} - c\right] \qquad (4.2)$$

where a=2.976, b=0.943 and c=1.848, and was established based in measurements of the axial liquid velocity with a Pavlov tube in columns with a diameter between 0.15 m and 1 m. The correlation is plotted against the experimental radial profiles of the axial

liquid velocity obtained in the Phi 150, Phi 400, Phi 1000 and Phi 3000 columns for a v_{sg}=16 cm/s in Figure 4.23.

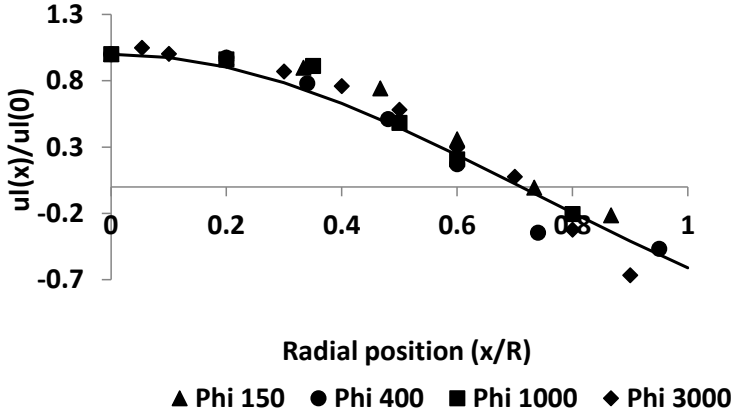

Figure 4.23 – Radial profiles of the mean axial velocity in the columns Phi 150, Phi 400, Phi 1000 and Phi 3000 at vsg=16 cm/s. The mean axial velocity is scaled by its value measured on the column axis. (Line – Eq. (4.1))

Figure 4.23 shows that globally the correlation is in reasonable agreement with the experimental data, additionally shows that the axial liquid radial profiles, normalized by the u(0) present no evolution with the column diameter. The fitting of the correlation with the experimental data is detailed in Table 4.27 for all columns and for v_{sg}= 9 cm/s, 16 cm/s and 35 cm/s.

Table 4.27 – Averaged differences between the experimental and predicted normalized axial liquid velocity profiles.

	Phi 150	Phi 400	Phi 1000	Phi 3000
9 cm/s	0.13	0.10	0.08	-
16 cm/s	0.11	0.08	0.06	0.12
25 cm/s	0.12	0.04	0.03	0.09

First, one should notice that the differences presented in Table 4.27 correspond to a function that varies between 1 and -0.7 (Figure 4.23). Thus, the results show that the Eq. (4.1) has a better agreement with the measurements in the larger columns, namely Phi 1000 and Phi 3000, and at v_{sg}=25 cm/s. Additionally, the maximal differences found, for all the tested $v_{sg,}$ were 0.34, 0.31, 0.27 and 0.44 for the columns Phi 150, Phi 400, Phi 1000 and Phi 3000, respectively. Let us now address the evolution of the axial liquid

velocity in the center of the column with the column diameter and the superficial gas velocity.

Impact of v_{sg} and bubble column diameter on the axial liquid velocity

In order to determine the evolution of the mean axial liquid velocity with the column diameter, a log-log representation of u(0) as a function of the column diameter is plotted Figure 4.24 for superficial gas velocities of 9 cm/s, 16 cm/s and 25 cm/s.

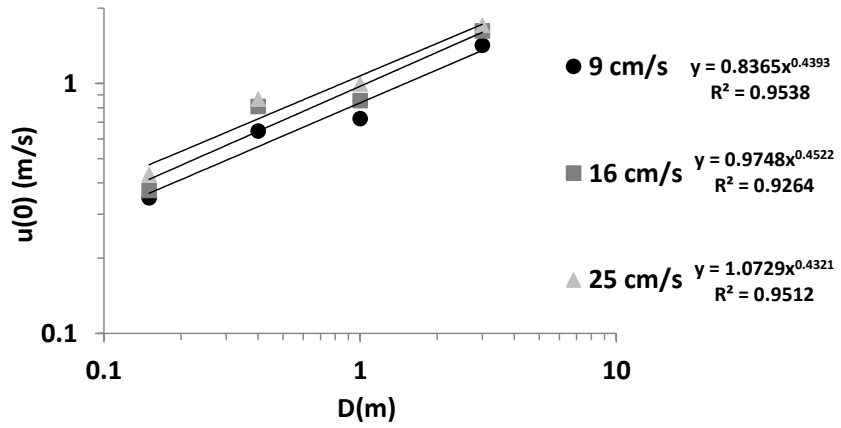

Figure 4.24 – Log-log representation of u(0) as a function of the column diameter, at iso-v_{sg}.

The results show that the variation of u(0) as a function of D for a superficial gas velocity in the range between 9 cm/s to 25 cm/s can be fitted by a power law with an exponent that ranges between 0.44±0.1. The limited variation of the exponent with the superficial gas velocity is a remarkable result. Since the scaling of liquid velocity in the center of the column with the column diameter has been determined as $u(0) \propto D^{0.44}$, one should verify its dependency with the superficial gas velocity. Thus, Figure 4.25 presents a log-log representation of the mean axial liquid velocity in the center of the column $u(0)/D^{0.44}$ as a function of the v_{sg}.

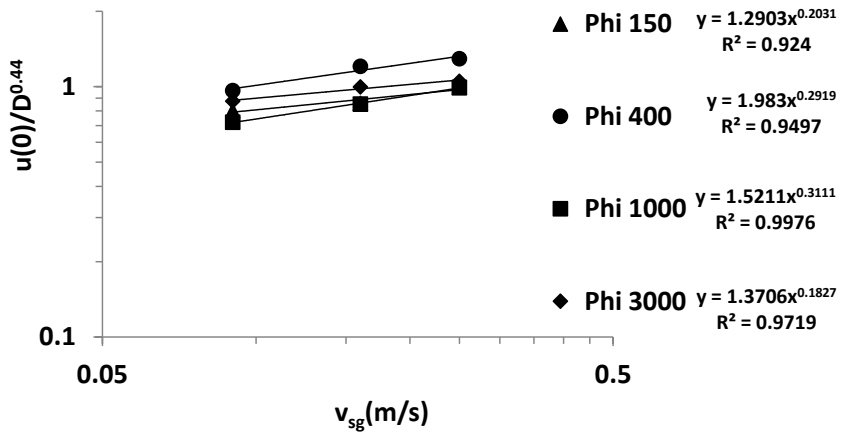

Figure 4.25 – log-log representation the evolution of $u(0)/D^{0.44}$ as a function of the superficial gas velocity for all the columns.

The results show that $u(0)/D^{0.44}$ is somewhat sensitive to v_{sg}, the dependency can also be fitted with a power law with an exponent ranging between 0.18 and 0.31 for a column diameters range from 0.15 m up to 3 m, which is a smaller factor than for the column diameter. We do not perceive any clear trend of that sensitivity with the column diameter. Concluding, the previous analysis showed that the scaling of the experimental axial liquid velocity in the center of the column corresponds to :

$$u(0) = 1.62 \pm 0.3 D^{0.44} v_{sg}^{0.25} \qquad (4.3)$$

Some studies in the literature focus on the correlation of the mean axial liquid velocity in the centre of the column with column diameter, v_{sg} and liquid density and viscosity, as presented in Table 4.28.

Table 4.28 – Correlations of the mean axial liquid velocity in the centre of the column

Correlation	Author
$u(0) = 2.47 vsg^{0.5} D^{0.28}$	Miyauchi and Shyu (1970)
$u(0) = 0.27(gD)^{1/2}\left(\frac{vsg^3\rho_l}{g\mu_l}\right)^{1/8}$	Zehner (1980)
$u(0) = 0.737(vsgD)^{1/3}$	Riquarts (1981)
$u(0) = Q_l + 0.66D^{0.69} + 1.11vsg$	Nottenkamper et al. (1983)

One can notice the strong differences in the correlations proposed in the literature: the exponents of D range from 0.28 to 0.69, and the one for v_{sg} between 1/8 and 1.

Therefore, taking in consideration the range of variation of u(0) with the v_{sg} and D and the correlations presented in Table 4.28, the correlation of Nottenkamper et al. (1983) is the farthest from our experimental results. The correlations of Miyauchi and Shyu (1970) and Riquarts (1981) are the ones with exponents closer to our results. Zehner correlation (1980) presents a good fit for the column diameter, but the impact of the v_{sg} is underestimated. In order to test which correlation better predicts our experimental results, the experimental results of u(0), Eq. (4.3) and the above correlations are plotted in Figure 4.26 A, B and C as a function of the column diameter for the superficial gas velocities of 9 cm/s, 16 cm/s and 25 cm/s, respectively.

A

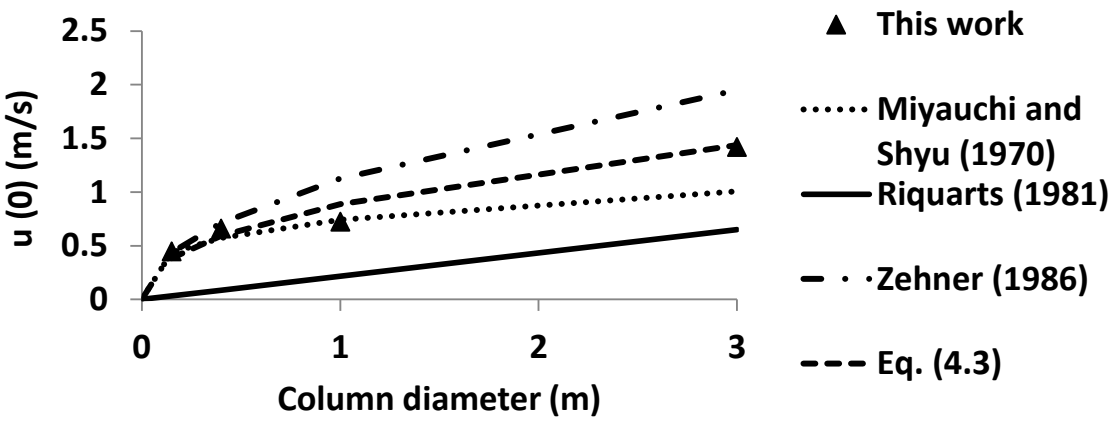

B

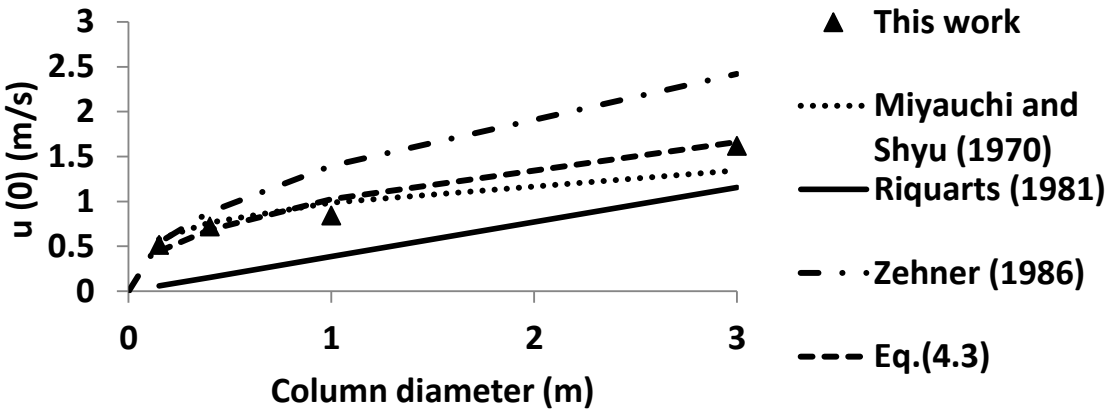

C

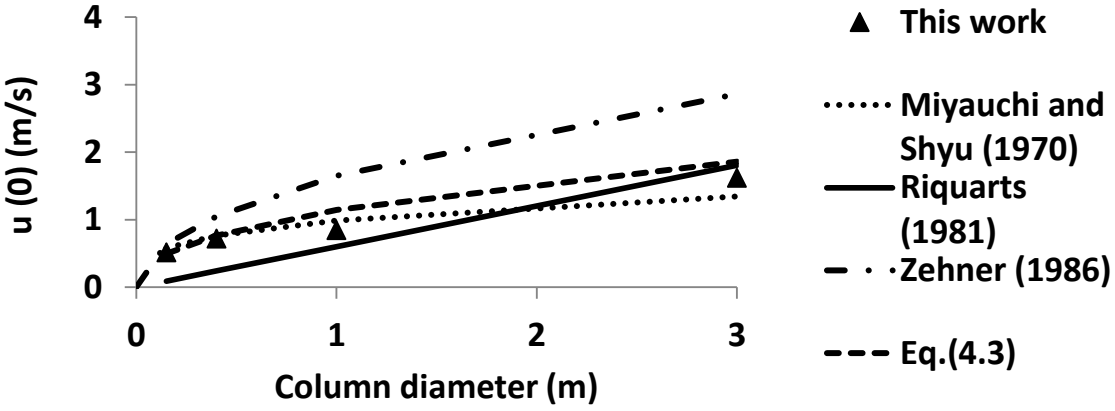

Figure 4.26 – Evolution of u(0) with the column diameter for a v_{sg} of: a) 9 cm/s; B)16 cm/s; C)25 cm/s according to correlations proposed in the literature.

Figure 4.26 shows similar trends regardless of the superficial gas velocities: the correlation of Miyauchi and Shyu (1970) is the one, between the literature correlations, that has the best fit with the experimental results, while the correlation of Riquarts (1981) strongly underestimates the u(0) for all the conditions, except for the column Phi 3000 at

v_{sg}= 25 cm/s. On the contrary the correlation of Zehner (1986) overestimates u(0) for all the columns except for the Phi 150 column. The mean difference between the correlations predictions and the experimental results are presented in Table 4.29.

Table 4.29 – Average difference between experimental values of u(o) and correlations (Figure 4.26). Units= m/s.

	9 cm/s	16 cm/s	25 cm/s
Miyauchi and Shyu (1970)	0.13	0.13	0.19
Riquarts (1981)	0.57	0.49	0.34
Zehner (1986)	0.33	0.39	0.58
Eq (4.3)	0.08	0.08	0.14

As expected, the results presented in Table 4.29 show that the correlation of Miyauchi and Shyu (1970) presents the best fit of our experimental results. Nevertheless, the maximum difference found was 0.4 m/s for the Phi 3000 column at a v_{sg}=9 cm/s. Regarding the remaining correlations the maximum differences found were 0.76 m/s and 1.16 m/s for the correlations of Riquarts and Zehner, respectively. It should be notice that Eq. (4.3) presents somewhat smaller errors than all the others correlations regardless the superficial gas velocity.

As previously referred to, the liquid flow rate descending in the column is equal to the liquid flow rising in the column. Therefore, it is interesting to evaluate if the negative liquid velocity measured at x/R=0.8 has the same evolution with the column diameter as the ascending velocity in the column center. Thus, a log-log representation of -u(0.8) as a function of the column diameter was plotted in Figure 4.27 for the superficial gas velocities of 9 cm/s, 16 cm/s and 25 cm, respectively.

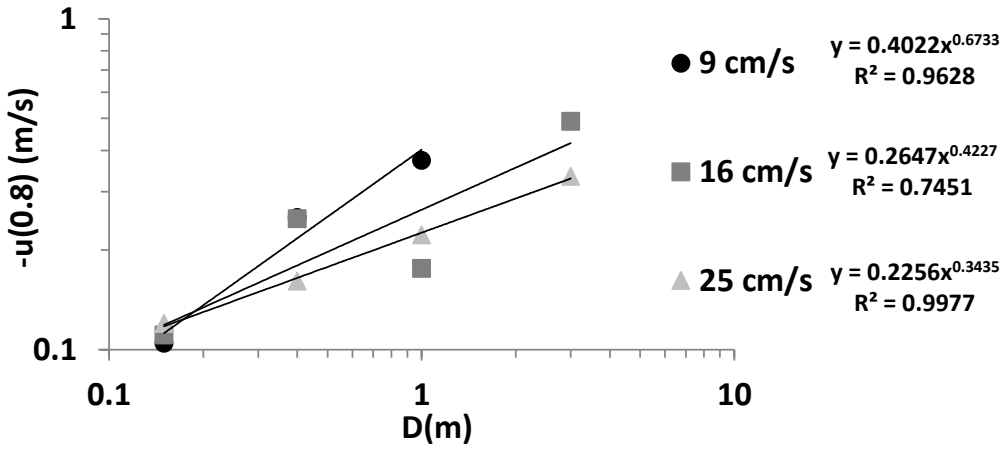

Figure 4.27 – Log-log representation of -u(0.8) as a function of the column diameter, at iso-v_{sg}..

The results show that at x/R=0.8 the power laws fitted to the results of –u(0.8) as a function of D have quite different slopes for the tested v_{sg}, compared with the liquid behavior on the axis shown in Figure 4.24. For the superficial gas velocities of 16 cm/s and 25 cm/s, the mean axial liquid velocity has similar evolution with the column diameter in both tested radial positions (0.34 and 0.42), however a stronger evolution was noted at v_{sg}=9 cm/s.

Concluding, the results showed that the evolution of the liquid velocity in the column center with the column diameter and with v_{sg} corresponds to $u(0) = 1.62D^{0.44}v_{sg}^{0.25}$ for v_{sg} ranging from 9 cm/s up to 25 cm/s in columns with a diameter ranging from 0.15 m up to 3 m. Moreover, the experimental results were compared with correlations reported in the literature: the correlation of Miyauchi and Shyu (1970) presented the best fit with the experimental results in all the tested conditions. However, Eq.(4.3) presented somewhat smaller errors in all the tested conditions Finally, the evolution of the axial mean liquid velocity with the column diameter for the radial positions x/R=0 and x/R=0.8 have been compared: at v_{sg}=3 cm/s -u(0.8) presented a stronger evolution than u (0), however for the v_{sg} of 16 cm/s and 25 cm/s, u has globally a similar evolution with the column diameter.

Net upward liquid flux

The impact of the superficial gas velocity can also be studied regarding the liquid flow rate (Q_l) rising in the core of the column i.e. the region where the mean flow is directed upward. Note that in that region, both velocity and gas hold up measurements are quite reliable In particular, the optical probe is properly oriented with respect to the main flow. Q_L is thus found by solving the following equation between x=0 and 0.7:

$$Q_l = \int_0^r 2\pi r u(x)\big(1 - \epsilon g(x)\big)dr \qquad (4.4)$$

for sake of simplicity, and owing to the conclusion of section 4.4 on the similarity of void fraction profiles, the local void fraction $\epsilon g(x)$ needed in Eq.4.3 has been computed using Eq. (1.1) together with the global void fractions for each column provided in section 4.3. The resulting rising liquid flow rates are presented in Table 4.30.

Table 4.30 – Rising liquid flow rate in the columns for several v_{sg}, m^3/s.

	Phi 150	Phi 400	Phi 1000	Phi 3000
9 cm/s	0.0011	0.0108	0.1035	
16 cm/s	0.0011	0.0109	0.1107	2.0146
25 cm/s	0.0010	0.0149	0.1007	2.0270

The results show that, for a given column diameter, the upward liquid flow rate rising in the column does not significantly evolve with the superficial gas velocity. Since the local liquid velocity increases with v_{sg}, this phenomenon could only be explained by a reduction of the surface available to the liquid, because of the increase of the local gas hold-up with v_{sg} (c.f. section 4.4). However, at iso-v_{sg}, there is a neat increase of the liquid flow rising in the column with the column diameter. The above data plotted versus D, in Figure 4.28 clearly show that the liquid flow rate increases as $D^{2.5}$. All data irrespective of v_{sg} collapse almost perfectly on the same curve, and the liquid flow rate (m3/s) rising in the column can be estimated as a function of the column diameter D (m) by the following fit.

$$Q_l^{up} = 0.123D^{2.5} \qquad (4.5)$$

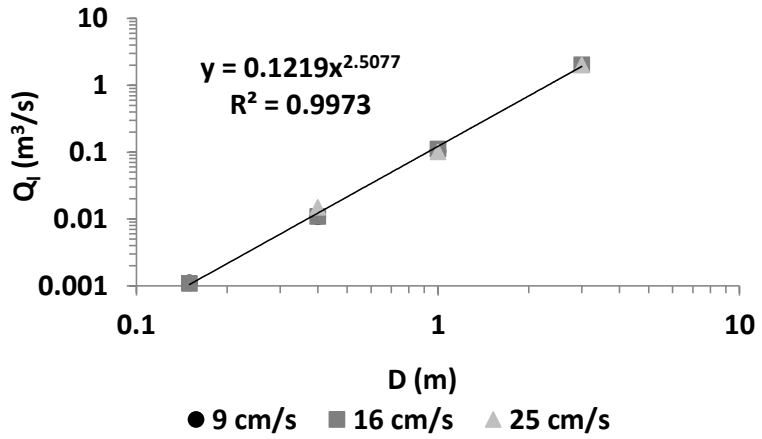

Figure 4.28 – Log-log representation of the liquid flow rate Ql in the ascending region as a function of the column diameter (from Phi 150 to Phi 3000).

Eq.(4.5) provides the magnitude of the liquid entrainment in our bubble columns due to the action of the gas. If the liquid flow rate is divided by the column cross-section, a quantity that represents the superficial liquid velocity in the central ascending part of the flow, the later increases as $D^{0.5}$: one can said that the entrainment "efficiency" increases with the size of the system. Oddly, that efficiency does not depend on vsg, i.e. on the injected gas flow rate. A probable reason for that could be the self-organization of the flow already seen on the fixed boundary of the ascending region at 0.7R and on the similarity of local velocity and void fraction profiles.

The above result can be tentatively put in a non-dimensional form. As a first crude dimensional analysis, one expects four independent non-dimensional parameters to govern the system. Indeed, the involved physical quantities are the injected gas flow rate (or equivalently the superficial gas velocity), the column diameter, the fluids properties (liquid density ρ_l, liquid viscosity ν_l and surface tension σ, the gas density is neglected since the low density ratio gas/liquid is considered to behave as an asymptotic parameter), gravity and bubble size. Note that the liquid static height H0 in the column is discarded since according to Forret (2008), local variables are no longer sensitive to H0 provided that H0>4D, a condition fulfilled in all our experiments. As for a single bubble dynamics in still liquid, Morton and Eötvös parameters characterize the bubble dynamics. A natural velocity scale is $(gD)^{1/2}$ and one can built a Reynolds number on that scale, namely $Re = D\,(gD)^{1/2} / \nu$ (another option can be the ratio of the relative velocity to v_{sg}). The last parameter must be connected with the gas superficial velocity: for such gravity driven flows, it is tentatively taken as a Froude number $vsg/(gD)^{1/2}$.

For the range of bubbles dynamics considered here, the relative velocity does not evolve much with size, and thus the parameters characterizing the bubbles are not expected to play a key role over the experimental range considered. Besides, it has been shown that the upward liquid flow rate does not depend on vsg. Thus, the only dimensionless scaling left is:

$$Q_l^{up} \approx D^2(gD)^{1/2} \tag{4.6}$$

As shown in Figure 4.29, the mean prefactor in Eq.(4.6) is close to 0.0377, and the maximum deviations are -15/+25% for all the conditions considered.

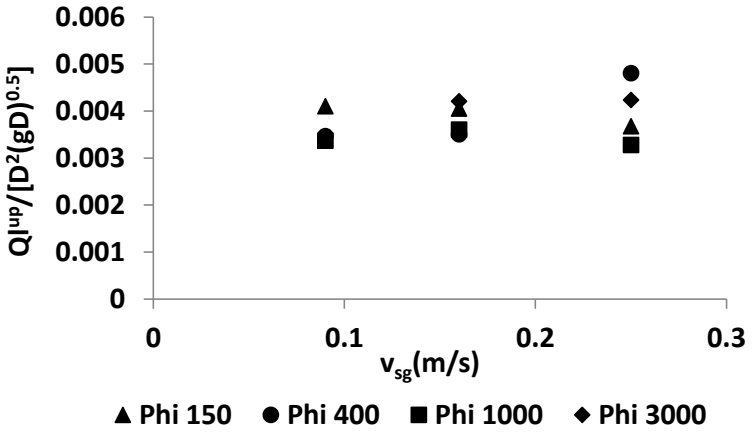

Figure 4.29 - Plot of $Q_{lup}/[D^2(gD)^{0.5}]$ versus the superficial velocity for all flow conditions available with vsg ≥ 9cm/s.

Although part of these deviations may arise from measurement uncertainties (also, we do not correct for the actual ratio εg(0)/<εg> but we took a fixed value =1.5, see section 4.4), there is a possibility that extra parameters, those influence was not neatly detected, may affect the liquid flow rate. In this respect, it is worth testing the consistency of the various scalings discussed above for the void fraction, the liquid velocity and the liquid flow rate. By integrating the fitted profiles of void fraction and liquid velocity between 0 and 0.7R, ones gets from Eq.(4.2):

$$\begin{aligned} Q_l^{up} &= 2\pi R^2 u(0)(0.118 - 0.163\langle \varepsilon g \rangle) \\ &= 0.236\pi R^2 u(0)(1 - 1.1381\langle \varepsilon g \rangle) \end{aligned} \tag{4.7}$$

We closely recover the proper dependency of the liquid flow rate with ($Q_{Lup} \approx D^{2.5}$) as the centerline liquid velocity has been seen to evolve as $u(0) \propto D^{0.44} v_{sg}^{0.25}$. Yet, there is a dependency with vsg present in right hand side of the equation but not on its left hand side. Considering that a correct fit for the global hold-up is $\langle \varepsilon g \rangle \approx$

$0.0812 v_{sg}^{0.395}$, and analyzing the resulting dependency of the r.h.s. with vsg, one find a trend close to $vsg^{0.12}$: thus, even though u(0) and <εg> significantly evolve with vsg, their combination in Eq.(4.6) is almost insensitive to the superficial velocity as expected from the scaling of the liquid flow rate. This slight difference observed arises from uncertainties on measurements, from the limited range in vsg we have explored (a factor less than 10) and also from numerical approximations. Hence, one can conclude that the empirical fits derived for u(0) and for <εg> are consistent with the, more solid, scaling proposed for the liquid flow rate.

Radial velocity component

The mean radial liquid velocity was also measured along the column radius for the Phi 400 (h/D=2.5) and the Phi 1000 (h/D=3.75) columns, using the 100 Hz bandwidth pressure sensors. However, the registered mean radial velocities were smaller than the pressure sensors resolution (0.12 m/s, see section 3.1), consequently the measurements cannot be considered for the analysis.

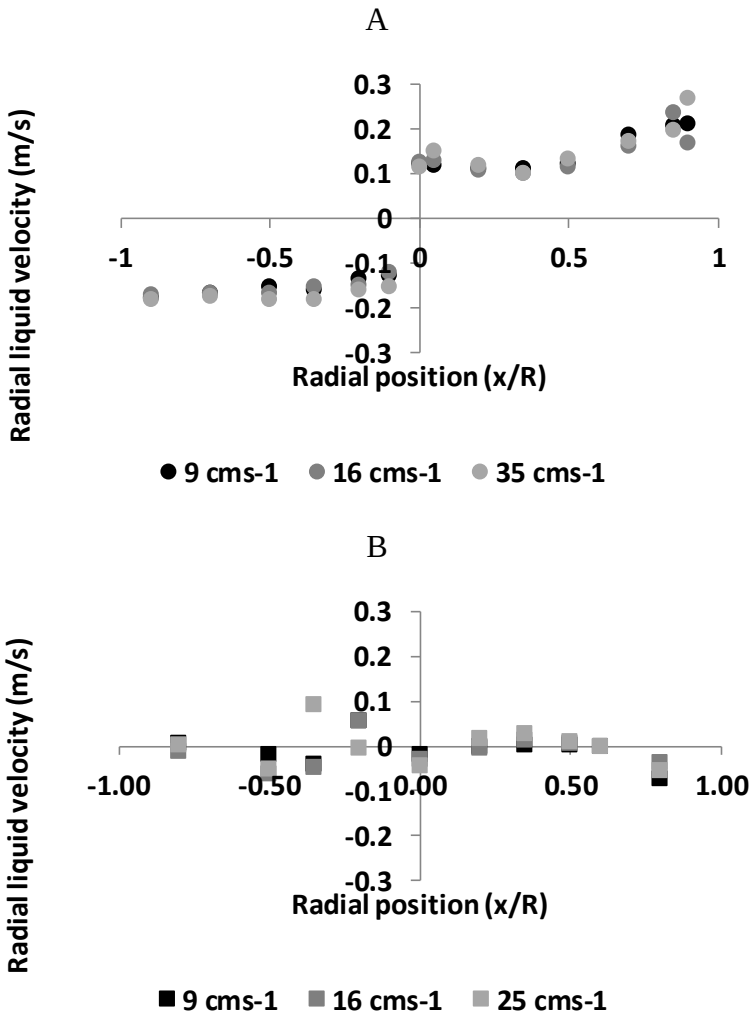

Figure 4.30 – Radial profiles of mean radial liquid velocity at several superficial gas velocities in the columns: A) Phi 400 (h/D=2.5); B) Phi 1000 (h/D=3.75) (measurements performed with the 100 Hz bandwidth pressure sensors)

The results show that, contrary to the axial component, the mean radial liquid velocity does not evolve with the superficial gas velocity. Moreover, the radial profiles are flat except close to the column wall in the Phi 400 column. Additionally, the mean radial velocities in the Phi 400 column are higher than the ones detected in the Phi 1000 column. These results bring credit to the presence of a quasi 1D mean motion in the central portion of the columns.

Concluding, the results show that the liquid recirculation increases with v_{sg} in all the columns. Moreover, the increase in the liquid velocity on the column axis with the superficial gas velocity follows a power law with an exponent ranging typically between 0.2 and 0.3 for v_{sg} from 9 cm/s up to 25 cm/s and D from 0.15m to 3m. Additionally, the uprising liquid flow on the column has been quantified for v_{sg} from 9 cm/s up to 25 cm/s

and over a range of column diameters from 0.15 m up to 3 m, it was found that the liquid flow does not change significantly with v_{sg}, but it increases with the column diameter (c.f. Eq. (4.5)): a scaling as $Q_{Lup} \approx D^2 (gD)^{1/2}$ is tentatively proposed with a prefactor about 0.038.

4.6 Bubble velocity

The bubble velocity is an important parameter in the local hydrodynamics of bubble columns. Consequently, a comprehensive study was carried out in the columns Phi 150, Phi 400 and Phi 1000 for a range of superficial gas velocities from 3 cm/s up to 35 cm/s. These measurements were made with the 1C mono-fiber optical probe, which can measure the bubble velocity component along the probe axis. The presented velocities are the arithmetical mean velocities along the probe axis direction of T1 bubbles. For the reasons discussed in section 3.5 these measurements are poorly reliable. In particular, they do not account for the sign of the velocity. Yet, we attempted to examine these data.

Bubble velocity evolution along the column axis

Up to this point it has been shown that the bubble Dh_{32}, the local gas hold-up and the axial liquid velocity were constant between h/D=2.5 and h/D=3.75. Therefore, it was expected that the bubble velocity remained constant along the column axis. Nevertheless, one should verify the validity of the invariance of the velocity along the column axis assumption. Thus, in Figure 4.31 A and B are presented the radial profiles of the arithmetical averaged bubble velocity on the Phi 400 and Phi 1000 for the h/D ratios of 2.5 and 3.75. No results are presented for the column Phi 150, since it was not possible to perform measurements at h/D=3.75 due to the limited column height (1 m).

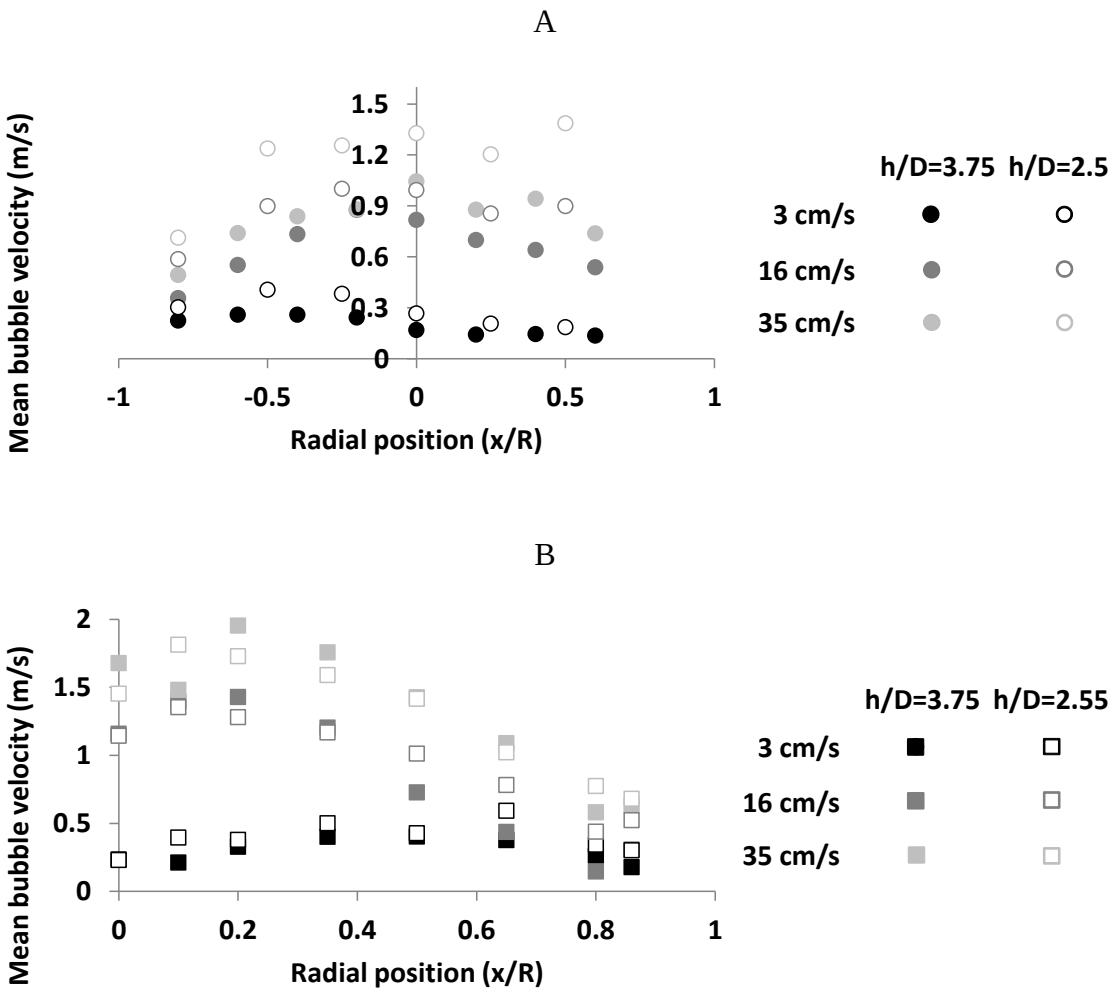

Figure 4.31 – Evolution of the arithmetical average bubble velocity as a function of radial position at h/D=2.5 and 3.75 in the column: A) Phi 400; B) Phi 1000 (1C probe).

Figure 4.31 A shows that in the column Phi 400, at iso-v_{sg}, the mean bubble velocity neatly decreases with the elevation on the column, for all the tested conditions. Since the mean axial liquid velocity is constant between both positions on the column, and the bubble Dh_{32} did no present an evolution between both elevations, the bubble velocity should be also constant. The difference between the mean bubble velocities detected at h/D=2.5 and h/D=3.75 in the Phi 400 column for the superficial gas velocities from 3 cm/s up to 35 cm/s are presented in Table 4.31.

Table 4.31 – Differences between the between the mean bubble velocities detected at h/D=2.5 and at h/D=3.75 in the Phi 400 column. Units= m/s

	Position Radial (x/R)	
Vsg (cm/s)	0	0.5
3	0.15	0.10
9	0.27	0.06
16	0.35	0.18
25	0.40	0.17
35	0.50	0.28

The results show that the difference between the velocities at two elevations increase with the superficial gas velocity for both radial positions, up to a maximum of 0.5 m/s at v_{sg}=35 cm/s in the column axis. Therefore the difference between the measurements found in Figure 4.31 can be related with a degradation of the optical probe, as presented in section 3.5. This degradation is a result of the fouling on the probe tip that can lead to lower bubble velocities measurements. In consequence, these measurements will not be considered in the analysis of the evolution of the bubble velocity along the column axis.

Figure 4.31 B shows that in Phi 1000 column, the measurements performed at h/D=2.5 and 3.75 for all the tested superficial gas velocities presented a good agreement. A more detailed analysis, presented in Table 4.32, gives the difference between the mean bubble velocities detected at h/D=2.5 and at h/D=3.75 in the Phi 1000 column for the superficial gas velocities from 3 cm/s up to 35 cm/s and again for the two radial positions.

Table 4.32 – Differences between the between the mean bubble velocities detected at h/D=2.5 and h/D=3.75 in the Phi 1000 column. Units=m/s

	Position Radial (x/R)	
Vsg (cm/s)	0	0.5
3	0.00	0.22
9	0.02	0.04
16	-0.02	0.34
25	-0.35	0.25
35	-0.23	-0.07

The result shows that contrary to the results of Phi 400 column the difference between the measurements did not evolve linearly with the superficial gas velocity.

Moreover, a very good agreement is found between the measurements in the column centre for vsg<25 cm/s. Still, the maximum difference between the measurements was 0.34 m/s. Concluding, these results together with the local gas hold-up, the bubble size and the liquid velocity measurements show that the flow in the columns was fully established between the elevations of h/D=2.5 and 3.75.

Radial bubble velocity profiles

Likewise the gas hold-up, the bubble velocity was measured in the Phi 150, Phi 400 and Phi 1000 columns at dimensionless height h/D=2.5, along the column radius as can be seen in Figure 4.32 A, B and C, respectively. The measurements obtained in the column Phi 400 at h/D=2.5, were obtained with a probe in normal functioning conditions, contrarily to the data obtained in the same column at h/D=3.75. Hence, they are taken into account in the following analysis.

A

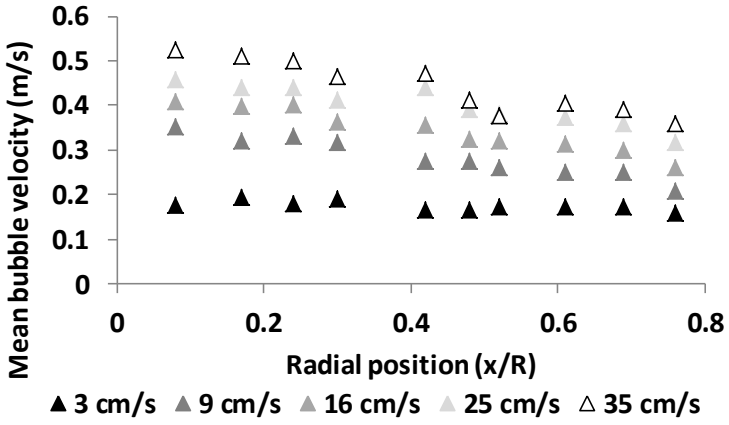

B

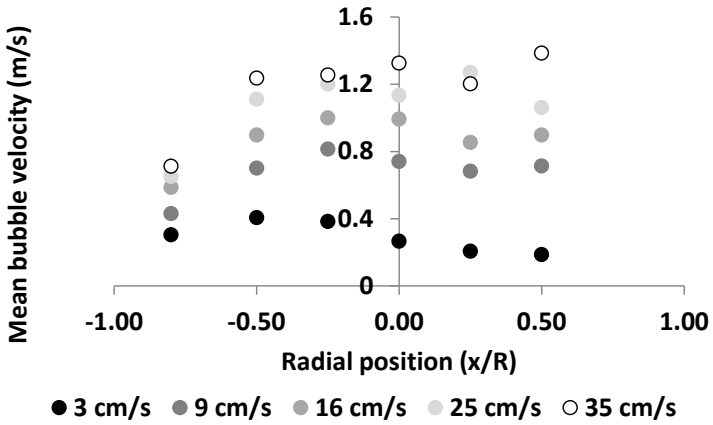

C

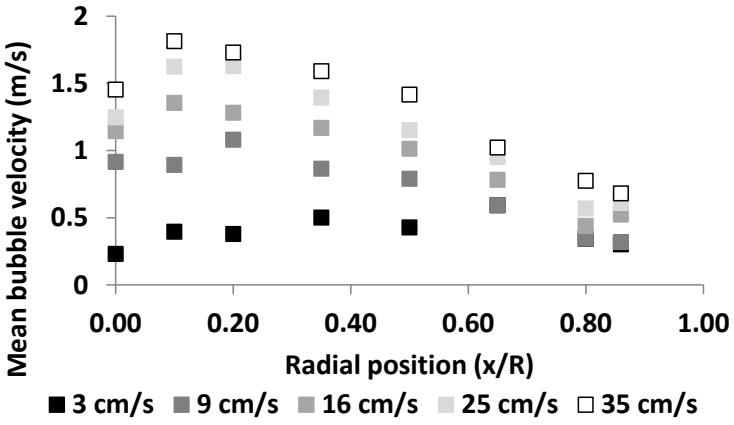

Figure 4.32 – Radial profiles of the axial mean velocity of bubbles at several the superficial gas velocity in: A) Phi 150 (h/D=2.5); B) Phi 400 (h/D=2.5) C) Phi 1000 (h/D=2.5) (1C probe)

In the homogeneous regime (v_{sg}=3 cm/s) a flat profile around 0.2 m/s is observed in all the columns, as expected. At these conditions, the liquid velocity is negligible, so the bubbles velocity is mainly due to the bubble drift velocity.

At higher superficial gas velocities, the profiles present a parabolic-like shape, since there is a larger increase of the bubble velocity in the inner zone of the column than in the outside zone (x/R>0.7). One explanation for this behavior can be the appearance of liquid recirculation in the bubble column. In the column center, the bubbles can be transported by the upward liquid velocity, in the outer zone, they are transported by the downward liquid flux. This phenomenon is verified for all the tested superficial gas velocities in the three columns. However, the Phi 150 column presents more linear velocity profiles along the column radius, as can be seen in Figure 4.32 A. It should be noticed that the bubble velocity was only measured up to the dimensionless radial position x/R=0.75, which could explain the absence of low velocities at the extremities of the radial profile.

Impact of the column diameter and v_{sg} on the bubble velocity

We have seen in section 4.4 that an increase in the column diameter, at iso-v_{sg}, does not affect the gas hold-up profile. However, as referred to in section 4.5, there is an increase in the liquid recirculation within the column. Since the bubble velocity is the sum of the bubble drift velocity and the liquid velocity, it is important to understand how the mean bubbles velocity is impacted by the column size.

The arithmetical mean of bubble vertical velocity in the column centre vb(0) at a h/D=2.5 for the column Phi 150, Phi 400, Phi 1000 for superficial gas velocities ranging between 3 cm/s and 35 cm/s are plotted in Figure 4.33.

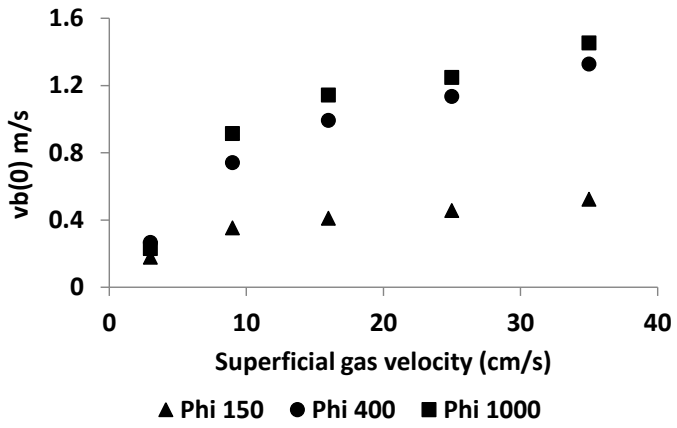

Figure 4.33 – Evolution of the axial mean velocity of bubbles in the column center as a function of the superficial gas velocity for the Phi 150, Phi 400 and Phi 1000 columns at h/D=2.5.

At 3 cm/s the bubble velocity does not present a significant evolution with the column diameter. This is an expected result, since at v_{sg} of 3cm/s the liquid velocity is quite low, the gas injection on the columns was proven to be homogeneous (c.f. section 2.3) and there was not significant evolution on the bubble size along the column axis (cf. section 4.1). However, for superficial gas velocities higher than 3 cm/s, there is a neat increase of the bubble velocity with the column diameter, especially between the column Phi 150 and the column Phi 400.

Moreover, the bubble velocity profiles, at iso-v_{sg}, are more parabolic with the increase of the column diameter, as can be seen in Figure 4.32. This is agreement with the fact that the liquid recirculation rate also increases with the column diameter. As previously referred, the descending flow located at $x/R \geq 0.7$ can slow down and/ or entrain the bubbles on the external part of the column.

Unexpectedly, the results obtained in the Phi 1000 column show that mean bubble velocity maximum is located at x/R=0.2 and not in the center. This observation is valid for all v_{sg} above or equal to 9 cm/s. Since the liquid maximum velocity is located in the column center (c.f. section 4.5) and larger Dh_{32} were also detected in the column center, this phenomenon may be due to the probe sensitivity to lateral bubble motion. Indeed, if the bubble approaches the probe with an angle larger than 30° a significant error can be done in the velocity estimation, as detailed in section 3.5. Therefore, this local increase of the measured velocity v_{sg} can be related with the presence of strong lateral bubble motions that impose a non mono-directional rising path of bubbles. Indeed, and as it will

be seen in section Fig.4.30, the turbulent intensity is minimum along the axis and increases steeply with the radial distance.

Since the evolution of the mean axial liquid velocity with the column diameter followed a power law, it is important to verify if the mean bubble velocity presents the same trend. So, the evolution of bubble velocity in the column center vb(o) as a function of the column diameter D has been plotted in a log-log representation in Figure 4.34, for superficial gas velocities in the range from 3 cm/s to 35 cm/s.

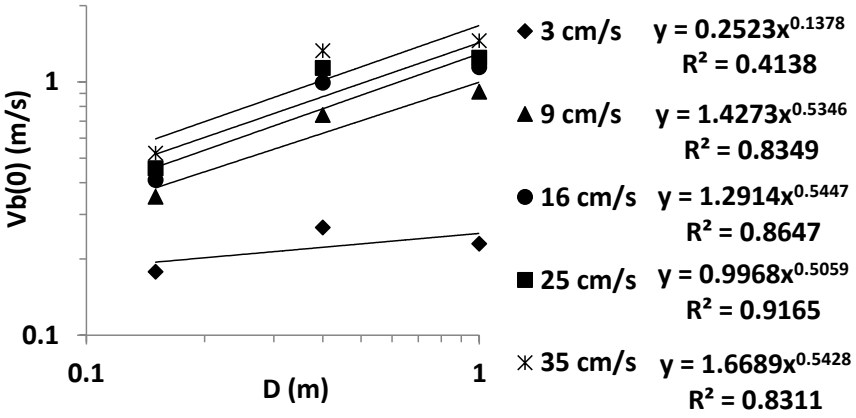

Figure 4.34 – Log-log representation of vb(0) as a function of the column diameter (D) in a range between 0.15 m and 1 m for vsg ranging from 3 cm/s up to 35 cm/s. (Measurements obtained at h/D=2.5)

The results show that, considering all the v_{sg} the evolution of vb(0) with the D follows a power law with an exponent ranging from 0.13 up to 0.54. However, considering only the conditions such that v_{sg}>3-5 cm/s, all the results are fitted with the power law $vb(0) = (1.34 \pm 0.35)D^{0.52\pm0.02}$. The exponent of D found here is slightly higher, but quite close to the one found for the mean axial liquid velocity ($D^{0.44}$). This difference may be due to some quick fluctuations in the flow that are detected by the probe but not by the Pavlov tube due to the low bandwidth (8 Hz) of the pressure sensors. Nevertheless, the agreement between the evolutions of the gas and the liquid velocities with the column diameter show the consistency of the measurements.

Taking into account the evolution of vb(0) with the column diameter, we will analyze now the evolution of the mean bubble velocity in the column center (vb(0)) with the superficial gas velocity. So, a log-log representation of the evolution of the bubble velocity at x/R=0 with the superficial gas velocity for the column Phi 150, Phi 400 and Phi 1000 is plotted in Figure 4.35.

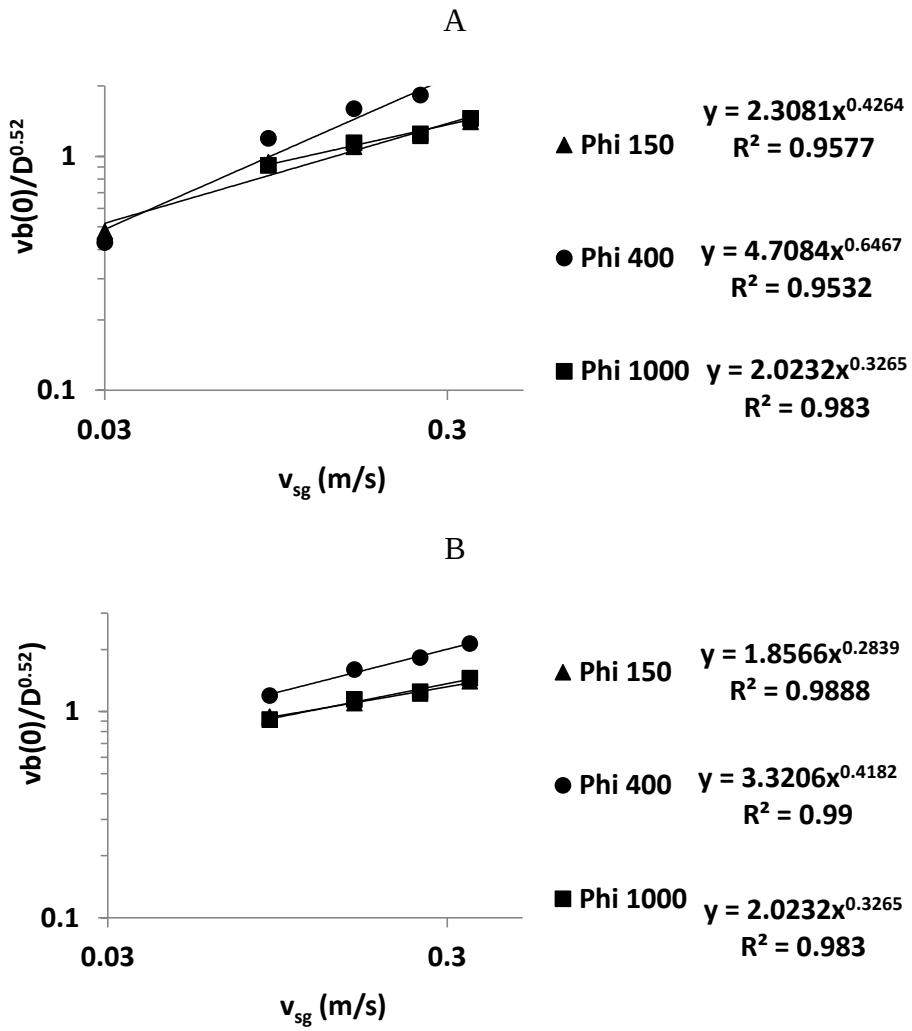

Figure 4.35 - Log-log representation of vb(0)/(1.34D$^{0.52}$) as a function of the superficial gas velocity for the Phi 150, Phi 400, Phi 1000 columns: A) 3 cm/s <v_{sg}< 35 cm/s B) 9 cm/s<v_{sg}<35 cm/s (measurements obtained at h/D=2.5)

Accounting for measurements at all the v_{sg} the quantity vb(0)/D$^{0.52}$ evolves with the superficial gas velocity accordingly to a power law with an exponent ranging from 0.33 up to 0.65. However, if one analyzes the evolution of vb(0)/D$^{0.52}$ for v_{sg}>3-5 cm/s the measurements on the three columns evolve according to $\frac{vb(0)}{D^{0.52}} = (2.59 \pm 0.73) v_{sg}^{0.34\pm0.07}$. Therefore the empirical fit of the vb(0) with the column diameter and the superficial gas velocity, in our experiments, and for v_{sg}>3-5 cm/s writes:

$$vb(0) = 2.59 D^{0.5} v_{sg}^{0.34} \quad (4.8)$$

The fitting obtained by the Eq. (4.4) with our experimental data, is analyzed in the parity plot presented in the Figure 4.36.

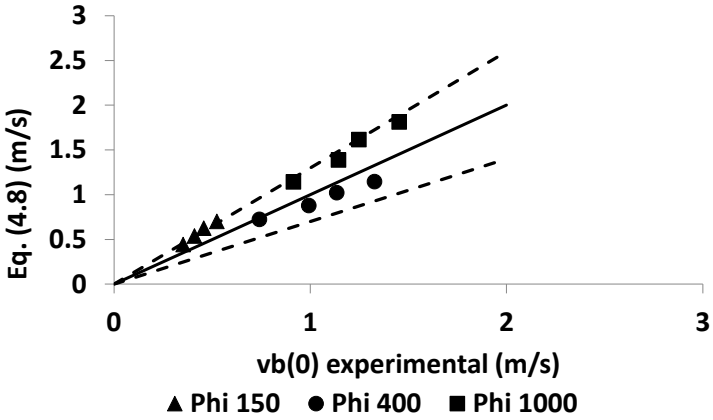

Figure 4.36 – Parity plot between the experimental vb(0) and the predictions of Eq. (4.8). (solid line – bisection line, dashed line- ±30%)

The results show that Eq. (4.8) provides the mean bubble velocity vb(0) in columns with a diameter ranging from 0.15 m up to 1 m and for a vsg ranging from 9 cm/s up to 35 cm/s within a relative error within ±30 %.

Upward gas flux

In section 3.5 the gas flux has been computed by integration over the entire cross-section of the column in order to deduce the superficial gas velocity, and the results presented considerable deviations. Indeed, to deduce the total gas flux one should use the local gas flux measurements obtained in the outer zone of the column (x/R>0.7). However, at larger radial distances above 0.7, the flow has a mean descending direction and, since the optical probe has always been facing downwards, the local gas flux measurements are poorly reliable in the outer zone. So, it is interesting to analyze the evolution of the average upward gas flux in the central zone i.e. for 0<x/R<0.7, with the superficial gas velocity. Therefore upward gas flux was estimated according to:

$$\mathrm{Qg}^{up} = \int_0^{0.7} 2\pi r j_g(x) \partial x \qquad (4.9)$$

where $j_g(x)$ represents the local gas flux. The results are presented in the Figure 4.37 for a v_{sg} ranging between 3 cm/s and 35 cm/s and for the columns Phi 150, Phi 400 and Phi 1000.

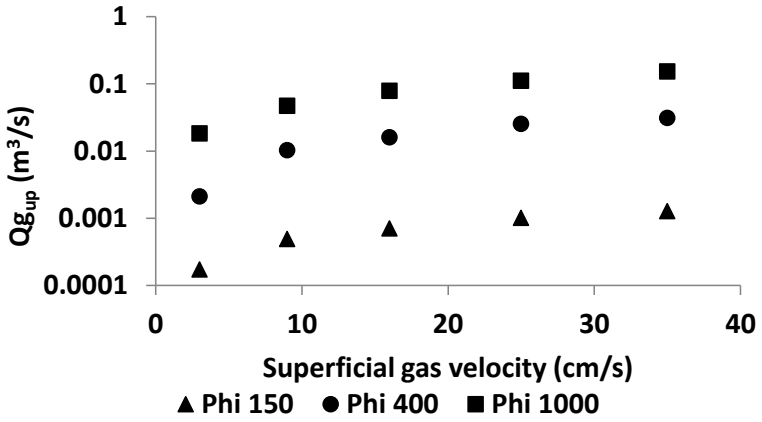

Figure 4.37 – Representation of the upward gas flux (Qg^{up}) with the superficial gas velocity for the columns Phi 150, Phi 400 and Phi 1000 (measurementsd obtained for at h/D=2.5)

The results show that the Qg^{up} increases both with the v_{sg} and with the column diameter (the gas flow rate spans nearly 3 orders of magnitude). Therefore, let us first study the evolution of the Qg^{up} with the column diameter: in Figure 4.38 Qg^{up} is represented as a function of the column diameter for various superficial gas velocities from 3 cm/s up to 35 cm/s.

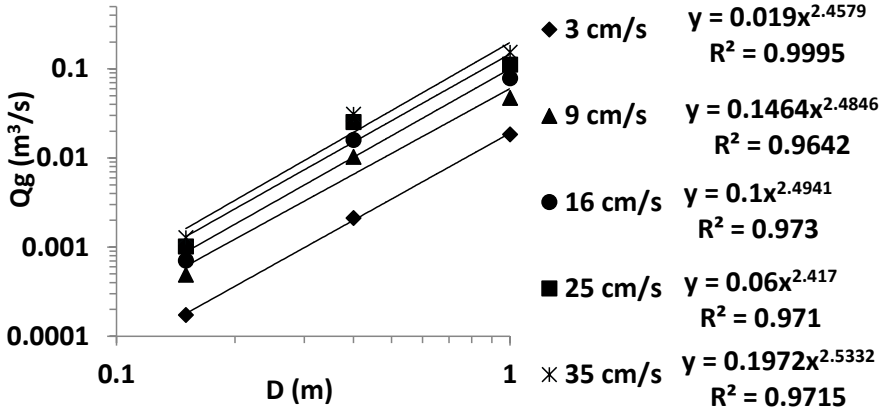

Figure 4.38 – Log-log representation of the evolution of the Qg^{up} as a function of the column diameter for superficial gas velocities from 3 cm/s up to 35 cm/s. (measurements obtained at h/D=2.5)

The results show that if one takes all the v_{sg} into consideration, Qg_{up} evolves with D according to a power law with an exponent ranging from 2.41 up to 2.53. Yet, if only the data such that vsg>3-6 cm/s are taken into considered, all the data are fitted by Qg^{up} =

$(1.25 \pm 0.065)D^{2.47\pm0.06}$. Both trends are in a good agreement with the variation of the net liquid flux ($D^{2.5}$) observed in section 4.5. Since the scaling of the Qg^{up} with the column diameter is known, one can now study the evolution of Qg^{up} with the v_{sg}.

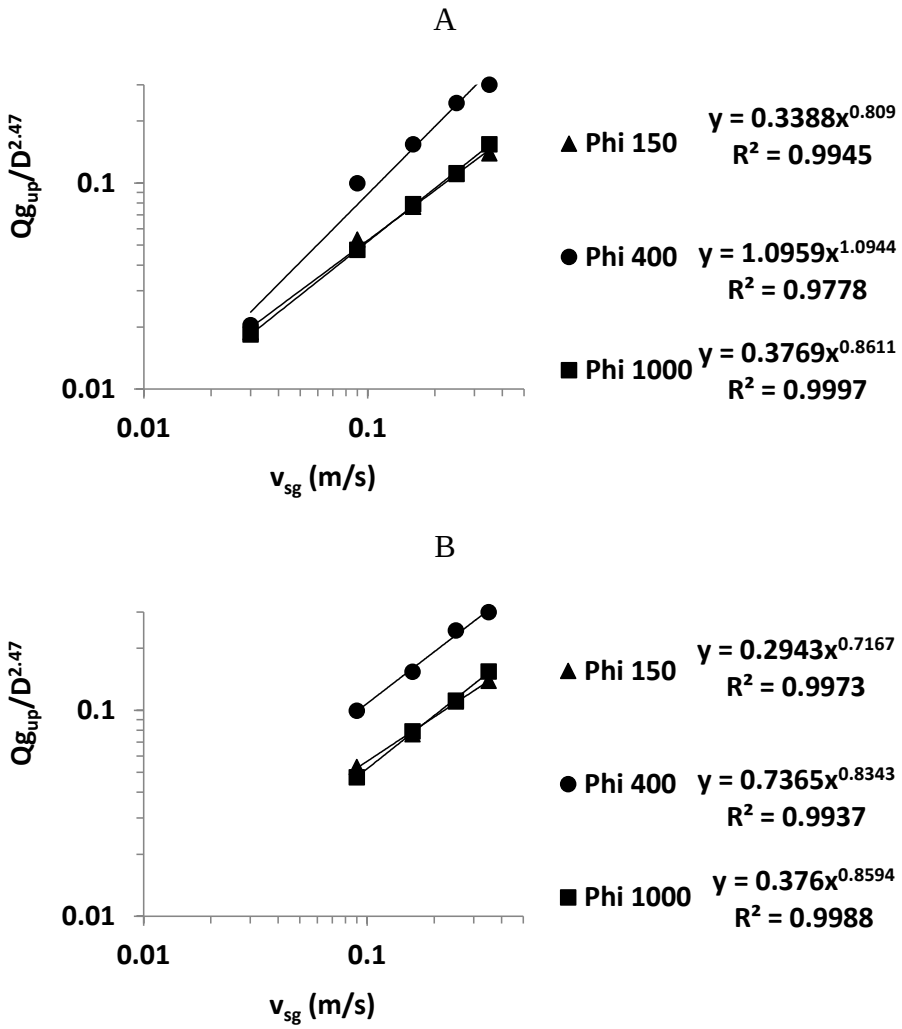

Figure 4.39 - Log-log representation of the evolution of the Qg_{up} as a function of the superficial gas velocities for the columns Phi 150, Phi 400 and Phi 1000 and a range of v_{sg}:A) from 3 cm/s up to 35 cm/s; B) from 9 cm/s up to 35 cm/s. (measurements obtained at hD=2.5)

Considering the entire range of v_{sg}, Qg^{up} evolve with v_{sg} according to a power law with an exponent ranging from 0.8 to 1.09. Restricting the range to vsg>3-5 cm/s, the data are well fitted by $\frac{Qg^{up}}{D^{2.47}} = (0.51 \pm 0.23)v_{sg}^{0.79\pm0.07}$. So, it is possible to conclude that the upward gas flux deduced from our experimental results evolve with respect to the column diameter and the superficial gas velocity according to:

$$Qg^{up} = 0.51D^{2.47}v_{sg}^{0.79} \quad (4.10)$$

As for the liquid phase, the consistency of the fits proposed for the gas flow rate, the gas velocity and the void fraction can be checked since $Qg^{up} \propto D^2 vb\varepsilon g$. Collecting the fits for the bubble velocity and the void fraction is possible to find $Qg^{up} \propto D^{2.5} v_{sg}^{0.7-0.8}$ that is in a good agreement with Eq.(4.10). Thus, the trends are consistent with each over.

If the Qg_{up} is correctly measured it should be larger than the flux of gas injected in the column. However, as can be seen in Figure 4.40 the ratio between the Qg^{up} deduced and the gas flow injected into the column is always inferior to 1, except for the column Phi 1000 at a superficial gas velocity of 3 cm/s. Indeed, even in the zone of the column where the flow is mostly directed upward, the local gas flux measurements are underestimated. However, even if the absolute values are not reliable, we observe convincing trends in the evolutions of $Qg^{up}/Qg_{injected}$ with the column diameter and the superficial gas velocities, namely in agreement with the scaling found for the net upward flux.

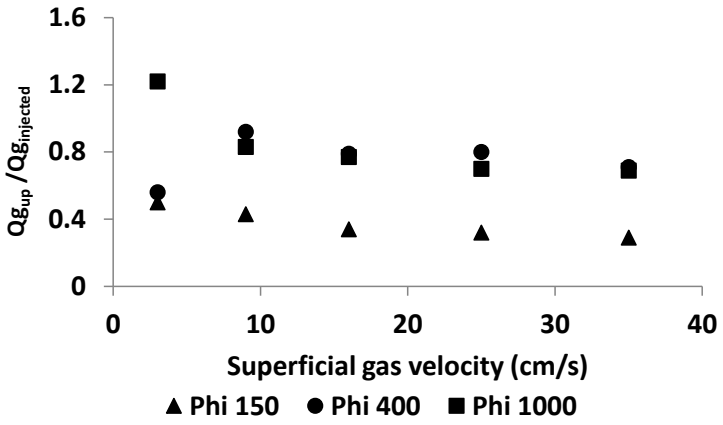

Figure 4.40 – Evolution of the ratio $Qg^{up}/Qg_{injected}$ as a function of the superficial gas velocity for the column Phi 150, Phi 400 and Phi 1000. (measurements obtained at h/D=2.5)

4.7 Velocity fluctuations

Liquid velocity fluctuations

From the axial liquid velocities (u) measurements presented in section 4.5, it is possible to compute the axial liquid velocities fluctuations (u'). As seen in section 4.5,

the radial liquid velocities (u) were not exploitable, the radial liquid velocity fluctuations (v') have not been analysed. Moreover, due to technical problems the liquid velocities fluctuations measured with the 100 Hz bandwidth pressure sensors were not well resolved and cannot be exploited either. In addition, since the measurements obtained in the Phi 1000 column were obtained with only a 100 Hz bandwidth pressure sensors, no data will be presented regarding the Phi 1000 column.

The radial profiles of the root mean square of the axial liquid velocity fluctuations (r.m.s.(u')) on the Phi 150, Phi 400 and Phi 3000 columns are plotted in Figure 4.41 for the superficial gas velocities of 9 cm/s, 16 cm/s and 25 cm/s.

A

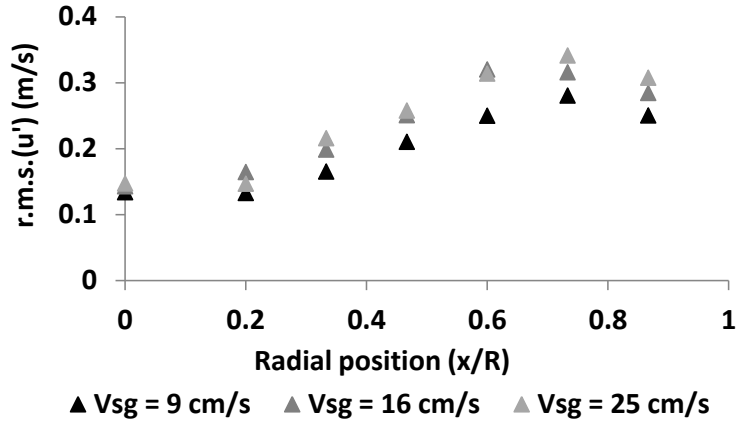

B

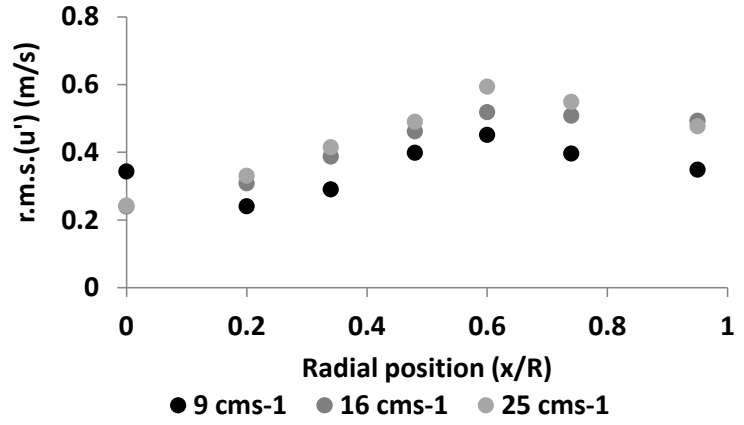

C

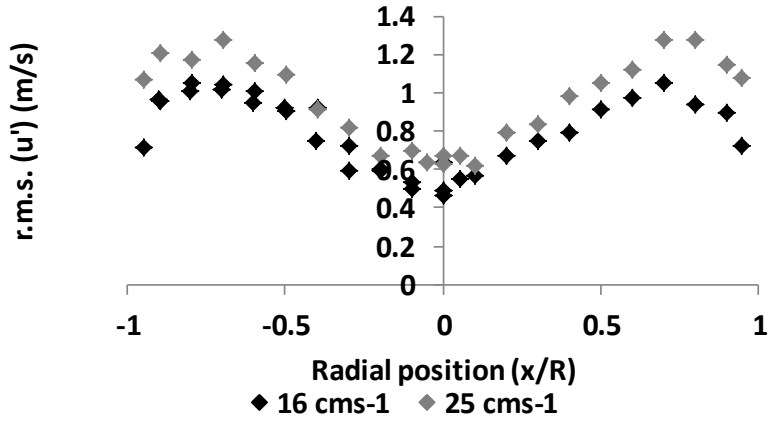

Figure 4.41 – Radial profiles of the axial liquid velocity r.ms (u') for several superficial gas velocities in the columns: A) Phi 150 (h/D=2.5); B) Phi 400 (h/D=2.5) C) Phi 3000 (h/D=1.5) (measurements obtained using the 8Hz bandwidth pressure sensors)

Figure 4.41 shows that, globally the radial profiles have similar shapes regardless of the column diameter: there is a neat increase of the axial r.m.s.(u') along the column

radius up to approximately x/R=0.7, and a decrease for further radial positions. This is an expected result, since x/R=0.7 is the location where the mean axial liquid velocity reverses its direction and where the velocity gradient is maximum. Moreover, at all radial positions in the three columns, the velocities fluctuations generally increase with the superficial gas velocity. Let us now analyse the dependence of u' on the superficial gas velocity and the column diameter.

Impact of the v_{sg} and D on the liquid velocity fluctuations

In order to further investigate the variation of the velocity fluctuations with the v_{sg}, the evolution of the r.m.s.(u'[0.7]) at the radial position x/R=0.7 is plotted versus v_{sg} in Figure 4.42 for the columns Phi 150, Phi 400 and Phi 3000.

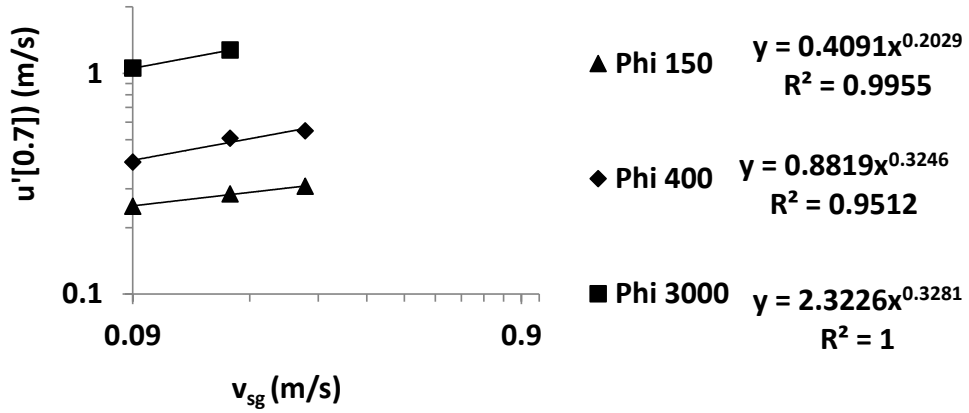

Figure 4.42 – Log-log representation of the evolution of r.m.s.(u') at the radial position x/R=0.7 as a function of the v_{sg} for the columns Phi 150, Phi 400 and Phi 3000. (Measurements obtained at h/D=2.5)

The results show that the liquid r.m.s.(u'[0.7]) experiences similar evolutions with the superficial gas velocity whatever the column diameter. Moreover, compared with the mean axial liquid velocity (Figure 4.25), the liquid velocity fluctuations have an equivalent evolution ($\approx vsg^{0.28}$) with the superficial gas velocity. Let us now analyse the variation of u' with the column diameter.

Figure 4.41 has already shown that the liquid velocity fluctuations also increase with the column diameter. To quantify this evolution, r.m.s.(u') measured at the radial position x/R=0.7 are plotted versus the column diameter as shown in Figure 4.43.

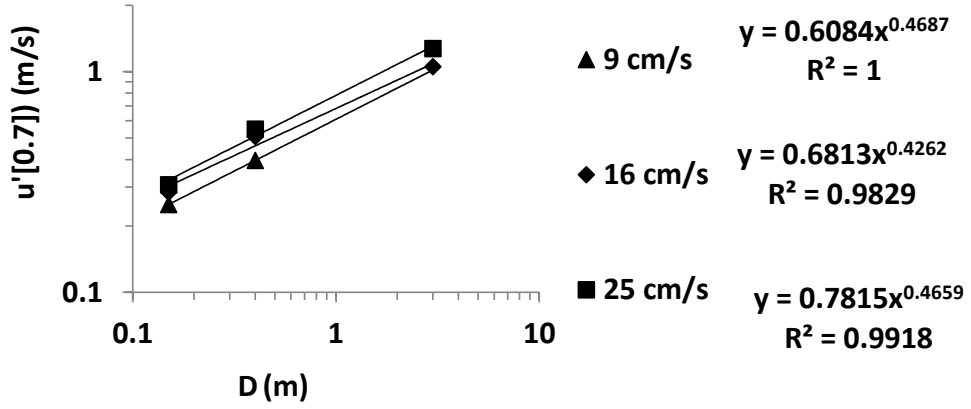

Figure 4.43 – Log-log representation of the evolution of r.m.s.(u') measured at x/R=0.7 as a function of the column diameter for v_{sg}=9 cm/s, 16 cm/s and 25 cm/s. (Measurements obtained at h/D=2.5).

For all tested superficial gas velocities, the r.m.s.(u') exhibit quite similar trends with the column diameter, with a scaling evolving from $D^{0.43}$ to $D^{0.47}$: i.e. the larger the column, the more intense the velocity fluctuations. It can be also pointed out that the velocity fluctuations and the mean velocities have very similar dependencies with the column diameter. Consequently, the turbulence intensity u'/u is expected to be independent (or nearly independent) on the column size. The axial turbulent intensity is quite strong in our flow conditions: on the axis, as shown in Figure 4.44, u'/u is always above 25-30%. Note that the few values above unity in Figure 4.44 correspond to very low vsg for which the pdfs of the absolute liquid velocity extend to both negative and positive values, and are affected by the poor resolution of the sensors in the vicinity of a zero velocity (see Figure 4.45).

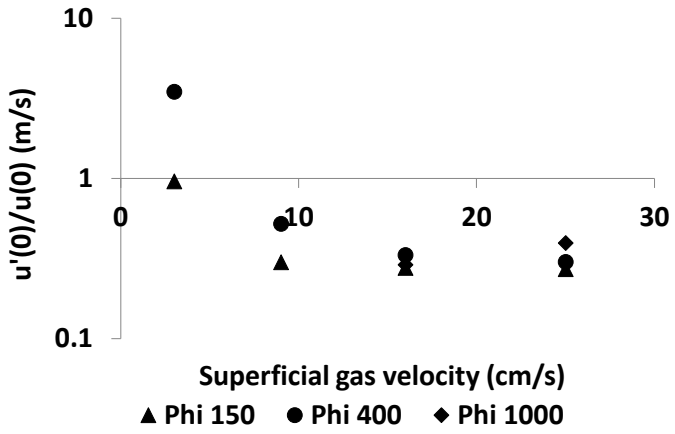

Figure 4.44 – Evolution of the axial turbulent intensity on the column axis versus the gas superficial velocity as measured in the columns Phi 150, Phi400 and Phi 3000.

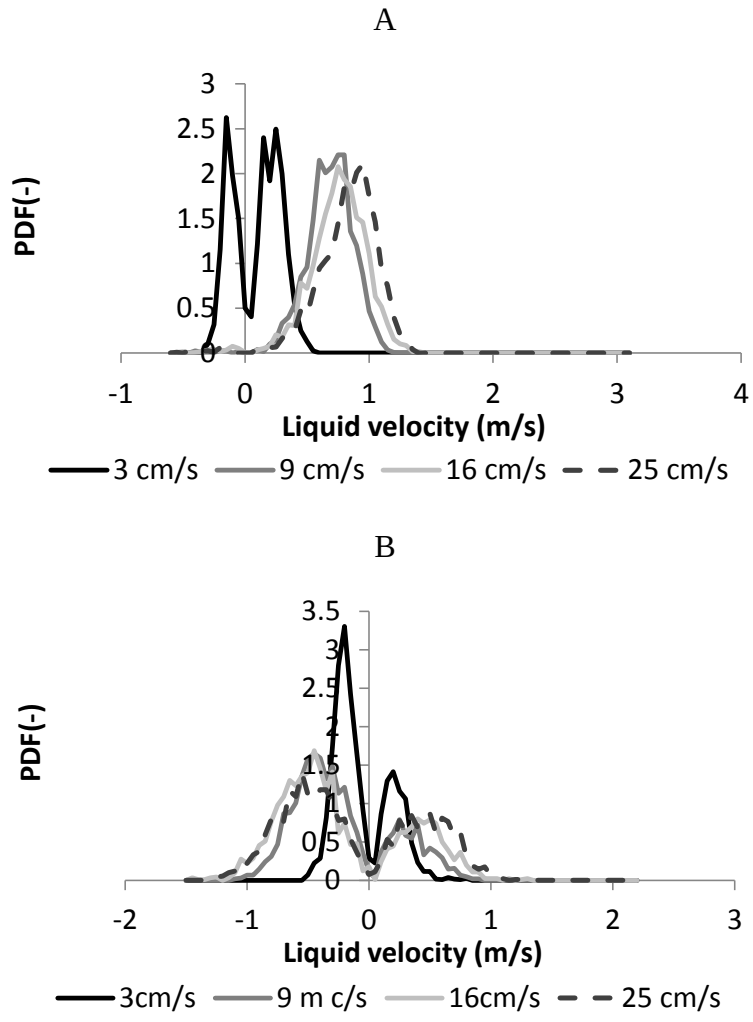

Figure 4.45 – Liquid velocity PDFs for several superficial gas velocities, measured in the column Phi 400 at the radial position: A)x/R=0; x/R=0.8 (measurements obtained with the 8 Hz bandwidth pressure sensor)

Liquid velocity fluctuations are expected to arise from the turbulence generated in the liquid phase, but also from the presence of bubbles. In spatially homogeneous conditions, the contribution of a swarm of bubbles is known to depend on the void fraction, with scalings varying according to the range of particulate Reynolds numbers considered (Biesheuvel & Van Wijngaarden, 1984, Cartellier & Rivière, 2001, Lance & Bataille, 1991, Garnier et al., 2002, Hunt and Eames, 2002; Risso et al., 2008, Cartellier et al., 2009, Riboux et al., 2013 to quote a few). Complex interactions between somewhat homogeneous turbulence and pseudo-turbulence have also been reported (see notably Lance & Bataille, 1991, Spelt and Biesheuvel, 1997, Rensen et al., 2005). In the present flow conditions, and as already evoked, one expects significant void fraction gradients to be present in the flow: such in-homogeneities, connected to convective instabilities, are known to induce strong velocity fluctuations. Thus, as a first tentative, it is worth analyzing the evolution of the liquid velocity fluctuations with the local void fraction.
For that, and to compare with previous results, the r.m.s. of the axial liquid velocity u' is scaled by the relative velocity. Let us first consider the terminal velocity vr0 of an isolated bubble: the ratio u'/vr0 is comprised between 0.5 and 2 as seen in Figure 4.46 (No data are available for the Phi 1000 column because of the low resolution of the Pavlov @ 100Hz sensor).

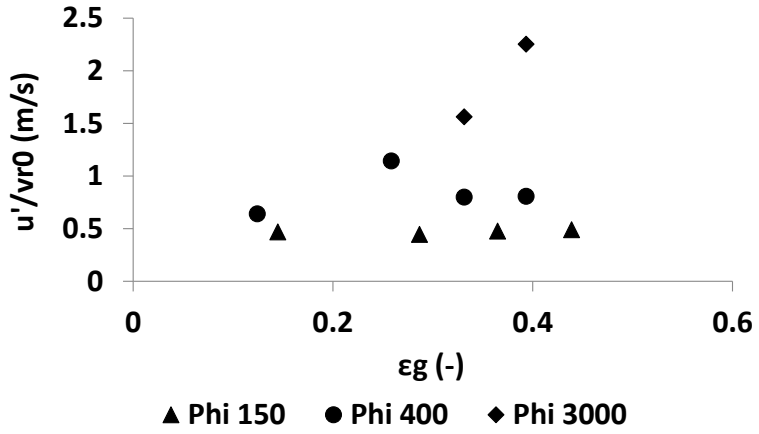

Figure 4.46 - Evolution of the r.m.s. of the axial liquid velocity u' scaled by the relative velocity of an isolated bubble (here ≈ 0.3 m/s) versus the local void fraction at two radial positions in the columns Phi 150, Phi400 and Phi 3000. For this set of data, vsg ranges from 3 to 25cm/s.

The ratio u'/vr0 increases with the local void fraction: such a trend is commonly reported in various bubbly flows. Yet, the magnitude observed here is far off the usual observations: typically, in homogeneous bubble swarms with bubbles at high particulate

number (typically O(1000)), one founds $\left(\frac{u\prime}{vr0}\right)^2 \approx 0.5 - 1\varepsilon g$. Here, $\left(\frac{u\prime}{vr0}\right)^2$ is of the order of 3-10 εg, i.e. much larger than in homogeneous conditions. Such a feature may tentatively be attributed to the presence of large scale meso-structures. If so, it is more appropriate to consider the average relative velocity estimated from measurements as will be presented in section 4.9, to be a better adapted velocity scale. Considering the scenario Q_{Gup}=$Q_{Ginjection}$, that provides the lowest average relative velocity, the ratio u'/vr apparent is plotted in Figure 4.47. The number of flow conditions is here even more limited as some information are lacking to evaluate the apparent relative velocity (see Table 4.33 section 4.9).

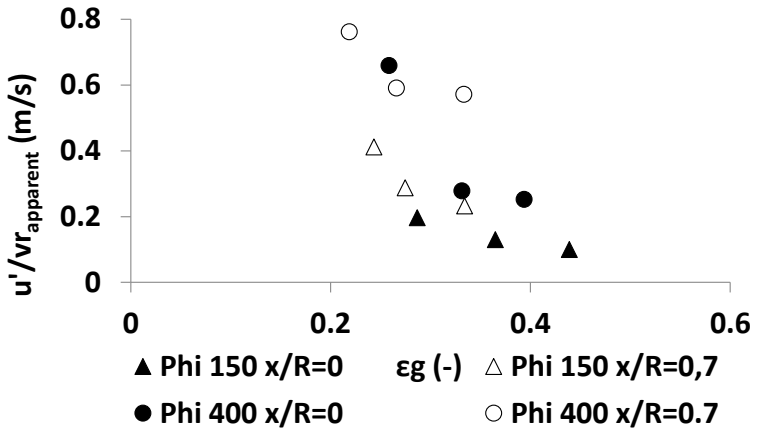

Figure 4.47 – Evolution of the r.m.s. of the axial liquid velocity u' scaled by the estimated average relative velocity (with the scenario QGup=QGinjection, see Table 4.33 section 4.9) versus the local void fraction at two radial positions in the columns Phi 150 and Phi 400. For this set of data, vsg ranges from 9 to 25cm/s

Despite this limited number of data, the magnitude of u'/vr apparent is now comprised between 0.1 and 0.8 which can be considered as encouraging. Oddly, compared to the behavior of u'/vr0, the trend is now reversed as u'/vr decreases with the local void fraction. Although this trend is clearly due to the neat increase of the apparent relative velocity with the void fraction (see Figure 4.55 section 4.9), it may traduce a complex coupling between density gradients, fluctuations and mean transport. Further analysis is clearly required to understand the origin of such fluctuations in dense bubbly columns. As a first step, section 4.10 will bring some pieces of information regarding the characteristics of the meso-scale structures.

The turbulent viscosity is an important parameter in the flow modeling, however it was not accounted for in our studies since it has been detailed studied in the work of Forret (2008) in quite similar experimental conditions.

Gas velocity fluctuations

The bubble velocity fluctuations (vb') can by computed recurring to the bubble velocities (vb) performed by the 1C mono-fiber optical probe, as it was done for the liquid velocities. However, it should be noticed that contrary to liquid velocity measurements, where the velocity is continuously measured at a certain frequency, the bubble velocity measurements are discrete since they arise only when a bubble is detected by the probe. Nevertheless, the lowest bubble detection rate in our experiments was 30 bubbles/s, a value obtained for v_{sg}=9 cm/s and at the farthest radial position: this rate is more than 3 times larger than the rate of liquid velocity measurements (8 Hz).

The bubble velocity fluctuations at v_{sg}= 9 cm/s, 16 cm/s and 25 cm/s obtained at h/D=2.5 in the columns Phi 150, Phi 400 and Phi 1000 are plotted in Figure 4.48 A, B and C, respectively.

A

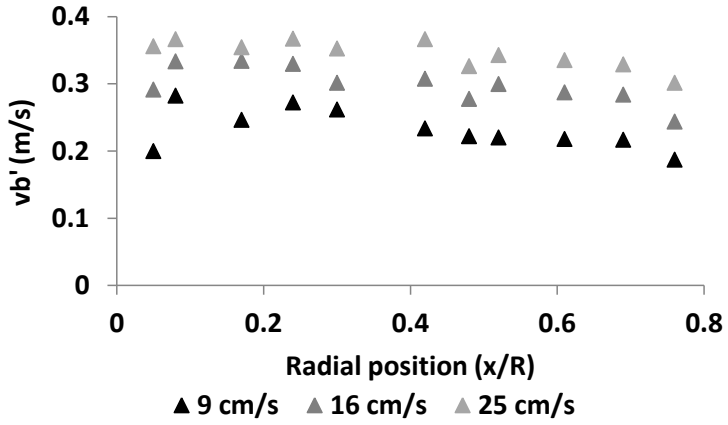

B

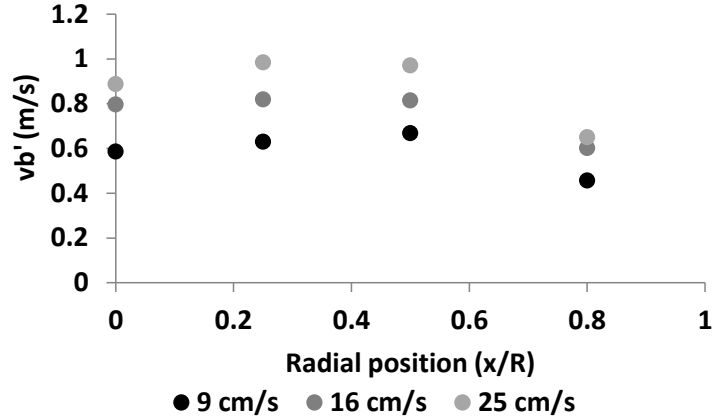

C

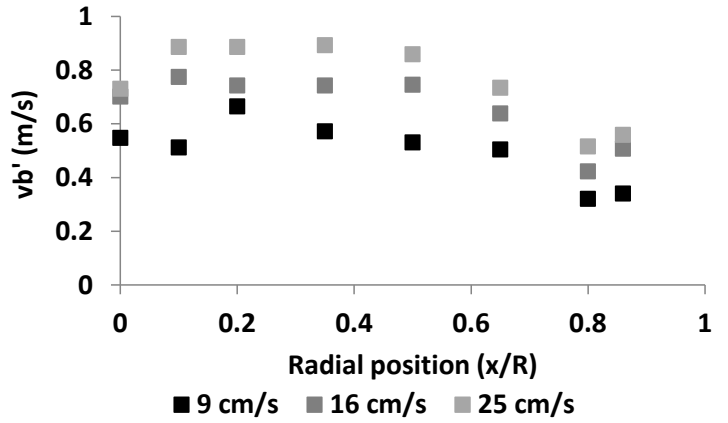

Figure 4.48 – Radial profiles of bubble velocity fluctuations for several v_{sg} in the columns: A) Phi 150, B) Phi 400; C) Phi 1000. (Measurements obtained at h/D=2.5).

Figure 4.48 A, shows that in the Phi 150 column, the radial profiles of vb' are flat at all the tested v_{sg}, contrary to the u' radial profiles that present clear maxima at x/R=0.7. Moreover, for a given v_{sg}, the gas velocity fluctuations are much higher than the liquid velocity fluctuations (Figure 4.41 A). These higher fluctuations can be generated by some bubble swarms rising quickly through the column, and the corresponding liquid velocity fluctuations can be not detected by the Pavlov tube due to the low bandwidth (8 Hz). Therefore, these phenomena can explain the stronger increase of mean bubble velocity with the superficial gas velocity than the liquid velocity.

Regarding the Phi 400 column, the radial profiles experience a slight increase up to the radial position x/R=0.5, while smaller values are detected at x/R=0.8. As for the Phi 150 column measurements, the velocity gas fluctuations are neatly higher than the liquid velocity fluctuations. Similar conclusions can be drawn for the Phi 1000 column, since the radial profiles also pass through a maximum around the radial position x/R=0.5, and increases with the superficial gas velocity.

For all conditions, the gas velocity fluctuations happen to be much higher than the liquid velocity fluctuations. This behavior may be related to flow in-homogeneities, such as dense bubble swarms. This could also be due to measurement difficulties. Indeed, and as seen in Chap.3, incorrect data leading to an overestimation of the bubble velocity are sometimes detected using the single probe: hence, the bubble velocity fluctuations are probably overestimated. On another hand, for the liquid, quick fluctuations in velocity could be filtered by the low bandwidth (8 Hz) of the Pavlov tube. We have some evidence when comparing the frequency spectrum between the 8Hz and the 100Hz sensors. Thus, these defects of the measuring techniques may explain that bubble velocity fluctuations exceed those in the liquid, but a physical origin cannot be set aside.

Although these data may not be fully reliable, it is worth examining how the bubble velocity fluctuations evolve with D and with vsg.

Impact of the v_{sg} and D on the gas velocity fluctuations

Let us start by the analysis of the variation of vb' with v_{sg} Figure 4.49 present the gas velocity fluctuations on the column axis (vb'(0)) as a function of the v_{sg} in a range between 9 cm/s and 25 cm/s for the columns Phi 150, Phi 400 and Phi 1000 .

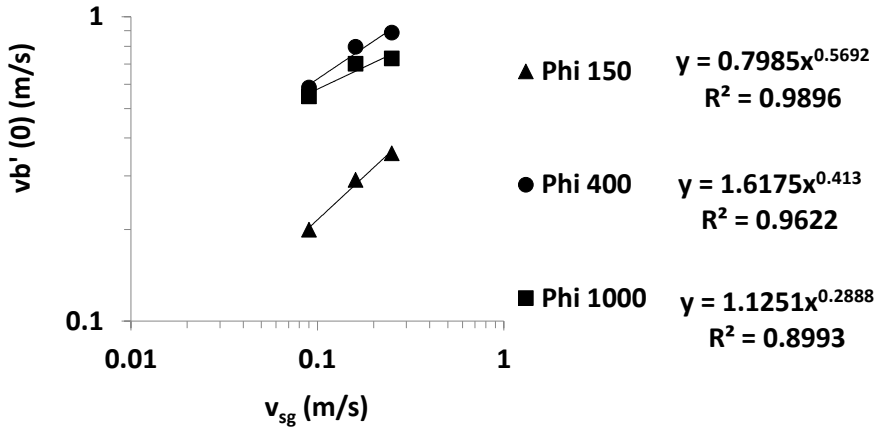

Figure 4.49 – Log-log representation of vb'(0) as a function of the v_{sg} in a range between 9 cm/s and 25 cm/s for the columns Phi 150, Phi 400 and Phi 1000. (Measurements obtained at h/D=2.5)

The results show that the gas velocity fluctuations evolution with the v_{sg} follow the power law $vb' = (1.2 \pm 0.4)v_{sg}^{0.43\pm0.1}$ whatever the column diameter. Therefore, vb' has a somewhat higher dependency of v_{sg} than mean bubble velocity vb, so the gas turbulent intensity (vb'/vb) marginally increase with v_{sg}, at iso-D. The evolution of vb' with the column diameter is presented in Figure 4.50 for the superficial gas velocities of 9 cm/s, 16 cm/s and 25 cm/s.

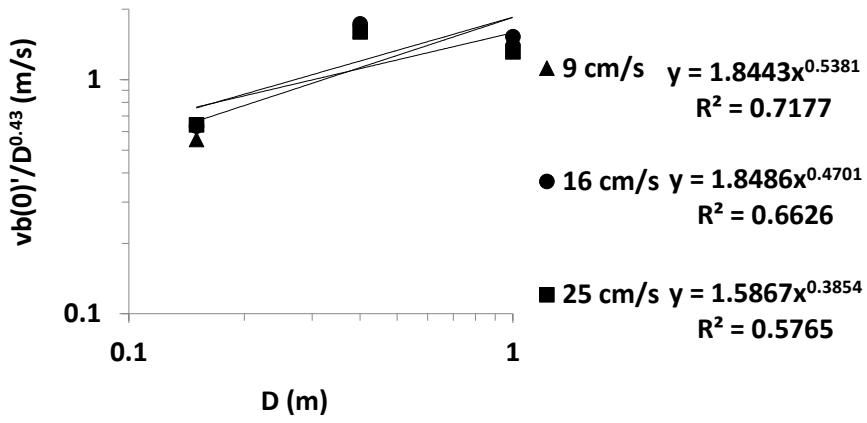

Figure 4.50 - Log-log representation of vb'(0) as a function of the D for a v_{sg} range between 9 cm/s and 25 cm/s. (Measurements obtained at h/D=2.5)

The results show that the dependence of vb'(0) on D is not well fitted by a power law (very few data available here), regardless the superficial gas velocity. Moreover, this dependence show no sensibility to the v_{sg} of all the column diameter studied. However, it is possible to conclude that vb'(0) increases somehow with the column diameter.

4.8 Comparison with Xue et al. data base

Xue et al. (2008) have also measured the mean bubble velocity in a 0.16 m diameter column with an air/water system, using a four point optical probe. The bubble column was equipped with a perforated plate with 163 0.5 mm i.d. injectors, and the measurements were made recurring to a four-point optical probe at h/D=5.1. Xue et al. (2008) have measured the ascending and descending velocity of bubbles along the column diameter, thus the presented mean velocity accounts for both measurements. Figure 4.52 depicts a comparison between the measurements of Xue et al (2008) and the measurements performed in the Phi 150 column.

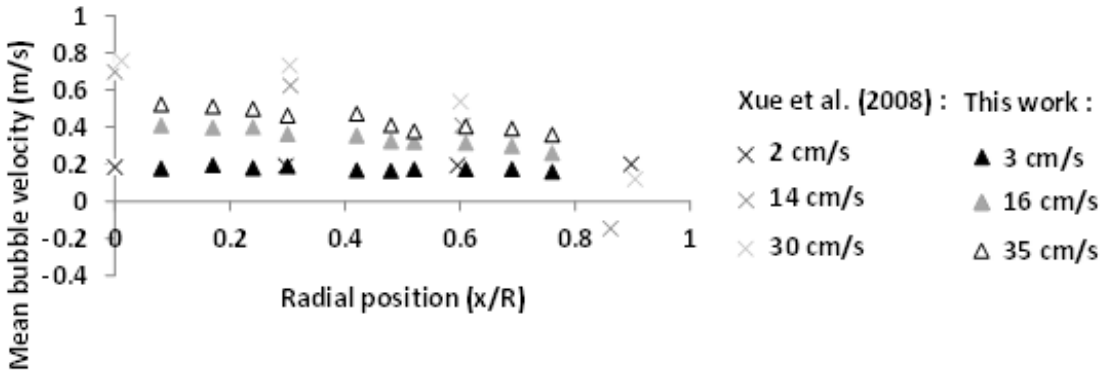

Figure 4.51 – Comparison between bubble size measurements of this work (Phi 150) and Xue et al. (2008).

The results show that for the superficial gas velocity of 3 cm/s there is a very good agreement between both measurements. However, at higher superficial gas velocities the radial profiles of the mean bubble velocity performed by Xue et al. (2008) present a parabolic shape. As a result, at column center Xue et al. (2008) have reported higher velocities, but near to the wall there is a better agreement between both measurements. In

order to understand the difference between the velocity measurements both local gas hold-up profiles can be compared, as done in Figure 4.52.

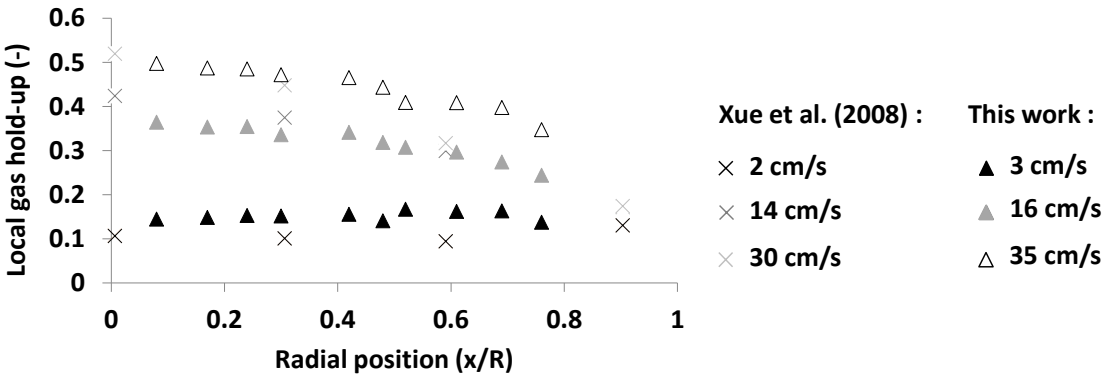

Figure 4.52 - Comparison between local gas gold-up measurements of this work (Phi 150) and Xue et al. (2008).

Figure 4.52 shows that at superficial gas velocity of 3 cm/s a relatively good agreement is found between both measurements, as the two present a flat local gas hold-profile. However, the results of Xue et al.(2008) present somewhat smaller values. At superficial gas velocity of 16 cm/s, a good agreement is found between both measurements along the column radius, except for the column center, where Xue et al. (2008) have reported a slightly higher local gas hold-up. However, at 35 cm/s the Xue et al (2008) measurements present a more parabolic shaped profile, consequently even if similar gas hold-up values were measured in the column center, there was a considerable deviation $x/R \geq 0.3$. Xue et al. (2008) have also reported the C_{10} on the column center and at $x/R=0.9$ as a function of the v_{sg}, therefore a comparison between the C_{10} obtained in our experiments and the reported values are presented in Figure 4.53.

A

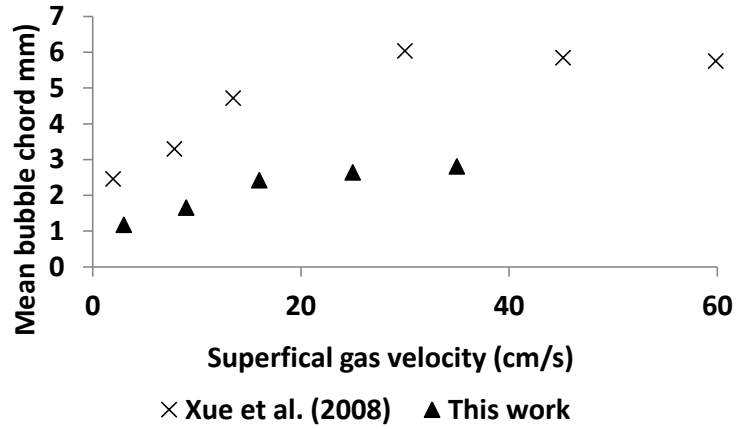

B

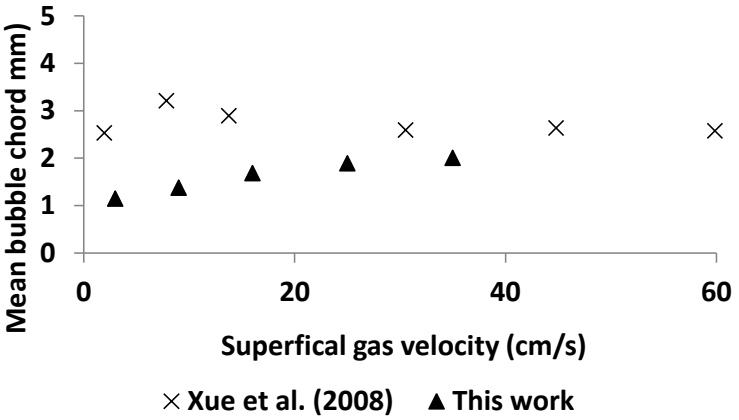

Figure 4.53 - Comparison between mean bubble chord measurements of this work (Phi 150) and Xue et al. (2008) at A) x/R=0 B)x/R= 0.9 for Xue et al. (2008) and x/R=0.8 for this work.

Globally, Figure 4.53 shows that Xue et al. (2008) have reported larger mean bubble chords than the detected ones on our experiments, regardless the v_{sg} or the radial position. However, analyzing the data for v_{sg}=3 cm/s is possible to conclude that in both cases the mean chord was constant for two radial positions and differing only by 1 mm. Explaining the good agreement found in the gas hold-up and velocity radial profiles.

Nevertheless, the results of Xue et al. (2008) present a stronger increase of the mean chord on the column center than in our experiments. Xue (2008) reported existence of bubble coalescence close to the injector, which could explain the difference between the results. Concerning the results obtained at x/R=0.8 and 0.9, the difference between the measurements is quite smaller, typically 1 mm. So, the larger bubbles on the column axis found on the measurements of Xue et al. (2008) can explain the higher bubble velocities in the column axis. Since there was a higher bubble velocity in the column center, the

liquid recirculation was also stronger which explain the more parabolic-like gas hold-up profiles. The spatial bubble size segregation in the experiments of Xue et al. (2008) reached a difference of 4 mm between the C_{10} detected in column axis and at x/R=0.9. In our experiments the difference of the C_{10} was typically < 1 mm: this difference may also be due to the higher liquid recirculation on the Xue et al. (2008) experiments.

Concluding, a good agreement was found between both measurements for a superficial gas velocity of 3 cm/s. However, at higher v_{sg}, Xue et al (2008) detected larger bubbles in the column center that may be linked with the water quality that changed the rate of bubble coalescence/breakage relatively to our experiments, which lead to a higher bubble velocities in inner zone of the column (x/R<0.6). Consequently, one can infer that the liquid recirculation was higher in the experiments of Xue et al. (2008) for superficial gas velocities of 16 and 35 cm/s, which may explain both the higher spatial bubble size segregation and the more parabolic-like gas hold-up profiles in the data of Xue et al. (2008) than in our experiments.

4.9 Relative velocity between phases

One of the initial objectives was to measure the mean relative velocity of the gas phase relative to the liquid phase inside the various columns. This parameter is indeed an essential element in modeling: in particular, it has a direct influence on the gas hold-up.

The relative velocity was to be deduced from independent measurements of each phasic velocities. Yet, and as seen in the previous sections, the magnitude of bubble velocities derived from single probe measurements are not reliable, even though consistent trends with control parameters have been identified (see section 4.6). The relative velocities (vr) along the column radius in the columns Phi 150, Phi 400 and Phi 1000 are plotted in Figure 4.54: huge differences in the outer zone of the column (x/R>0.6) are due to the sign of the velocity, therefore we will only analyse the measured relative velocity in the inner zone of the column.

A

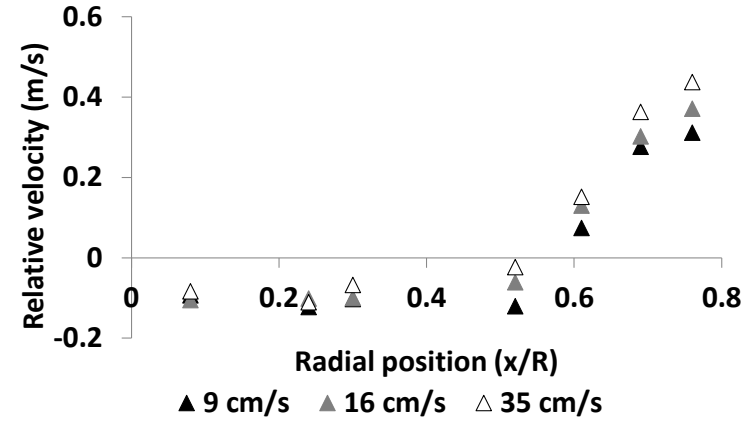

B

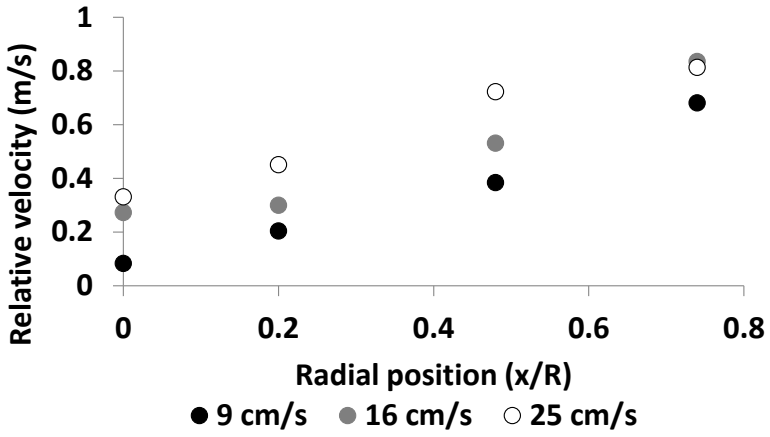

C

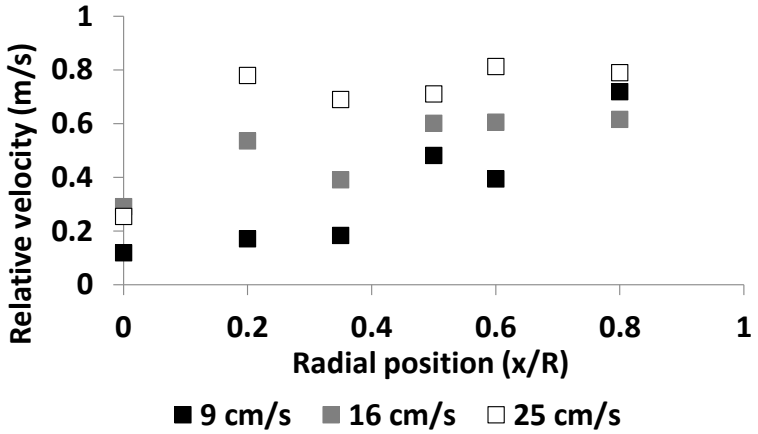

Figure 4.54 – Evolution of the measured relative velocity along the column axis for vsg of 9 cm/s, 16 cm/s, 25 cm/s in the columns: A) Phi 150; B) Phi 400; C)Phi 1000.

Figure 4.54 shows the measure relative velocity could be negative, a drawback that can be linked with the already mentioned bubble velocity underestimation. However, analyzing Figure 4.54 A and B, it is possible to conclude that the relative velocity increase with v_{sg} and with the column diameter. Additionally, vr can reach severe values up to 0.8m/s, namely at x/R=0.2 at v_{sg}=25 cm/s. These values are more than 2.5 times higher than the bubble velocity predicted for a single bubble in a stagnant liquid (c.f. section 2.3).

Another way to evaluate a "mean" relative velocity is to consider the kinematic relationship connecting the gas flow rate fraction β with the void fraction. Such an approach requires a quasi-established 1D flow. This was what we had in mind when we considered the mean variables integrated between 0 and 0.7 R. That region is indeed co-current upward directed two-phase flow, almost 1D as discussed on section 4.5.

Let us briefly recall the origin of the kinematic relationship. Starting with volumic flow rates Q_g and Q_l injected in a tube of cross-section S, the mean phasic velocities $<U_g>$ and $<U_l>$ averaged over the cross-section, are by definition:

$$Q_g = \oint \varepsilon g v b(x) dx = \varepsilon g S \langle U_g \rangle \tag{4.11}$$

$$Q_l = \oint (1-\varepsilon g) u(x) dx = (1-\varepsilon g) S \langle U_l \rangle \tag{4.12}$$

where for the last equalities the local void fraction εg has been assumed to be uniformly distributed over the cross-section. Starting from the relative velocity of the gas phase, namely $U_r = U_G - U_L$ and averaging this relation over the cross-section, one obtains:

$$\langle U_r \rangle = \frac{Q_g}{\varepsilon g S} - \frac{Q_l}{(1-\varepsilon g) S} \tag{4.13}$$

Introducing the gas flow rate fraction β defined as $\frac{Q_G}{(Q_G + Q_L)}$, one has $\frac{Q_G}{Q_L} = \frac{\beta}{(1-\beta)}$, and the above equation can be transformed into:

$$\frac{\langle U_r \rangle}{\langle U_l \rangle} \frac{\varepsilon g}{(1-\varepsilon g)} = \frac{\beta}{(1-\beta)} - \frac{\varepsilon g}{(1-\varepsilon g)} \Leftrightarrow \varepsilon g = \frac{\beta}{\left[1 + (1-\beta)\frac{\langle U_r \rangle}{\langle U_l \rangle}\right]} \tag{4.14}$$

That equation relates the void fraction with the gas flow rate fraction. The slip ratio $\frac{\langle U_r \rangle}{\langle U_l \rangle}$, which is the ratio of the relative velocity to the continuous phase velocity (both averaged over a cross-section), controls the difference between εg and β. When the relative velocity is zero, then $\varepsilon g = \beta$. If the velocity of the dispersed phase exceeds that of the

continuous phase (i.e. $\langle U_r \rangle$ positive), then the dispersed phase is diluted in the flow and εg becomes less than β. The opposite holds if the dispersed phase lags behind the flow (i.e. $\langle U_r \rangle$ negative). Putting into another form, the average slip ratio is given by:

$$\frac{\langle U_r \rangle}{\langle U_l \rangle} = \frac{(\beta - \varepsilon g)}{\varepsilon g (1 - \beta)} \tag{4.15}$$

The above equation provides a way to evaluate the relative velocity $<U_r>$ averaged over a cross-section once εg, β and $\langle U_l \rangle$ are known. Applied to the core region of the bubble column, i.e. for 0< x/R < 0.7, the gas flow rate fraction writes:

$$\beta_{core} = \frac{Q_g{}^{up}}{(Q_g{}^{up} + Q_l{}^{up})} \tag{4.16}$$

We have already evaluated $Q_l{}^{up}$ in section 4.5, and we have determined the average void fraction $\langle \varepsilon g_{0-0.7} \rangle$ in the core zone (Eq. (4.1)). The remaining unknown is $Q_g{}^{up}$ that was evaluated in section 4.6 but it proves to be strongly underestimated. We nevertheless attempted to analyze the kinematic considering two assumptions for the magnitude of $Q_g{}^{up}$. Before that, let us note that for a given liquid flow rate, the gas flow rate fraction increases with the gas flow rate. Besides, for a given void fraction, the slip ratio increases with β. Therefore, the slip ratio is an increasing function of $Q_g{}^{up}$ for values of the given liquid flow rate and of the void fraction. Alternately, the minimum slip ratio is obtained for the minimum gas flow rate. In that perspective, we considered two scenarios:

i) the gas flow rate is given by the measured value (strongly underestimated),

ii) the gas flow rate in the core region equals its minimum that is the total injected gas flow rate in the column.

The predicted slip ratio is given in Table 4.33 for the two scenarios: in all cases, this ratio is above unity, it reaches values up to 2.5 when using measured gas flow rates and up to nearly 10 when considering the injected gas flow rate.

Table 4.33 – Comparison of both scenarios on the calculus of $\langle U_r \rangle$.

		Measured				Obtained with Qg^{up}			Obtained with $Qg^{injected}$		
	D(m)	v_{sg} (cm/s)	Ql^{up} (m^3/s)	Qg^{up} (m^3/s)	$\varepsilon g_{0\text{-}0.7}$ (-)	$\beta^{0.7}$	<Ur>/<Ul>	Ur (m/s)	$\beta^{0.7}$	<Ur>/<Ul>	Ur (m/s)
Phi 150	0.15	3	-	0.00027	0.13	-	-	-	-		-
		9	0.00110	0.00068	0.22	0.38	1.22	0.2	0.59	4.18	0.68
		16	0.00108	0.00097	0.26	0.47	1.57	0.27	0.72	6.49	1.1
		25	0.00098	0.00142	0.31	0.59	2.17	0.36	0.82	8.88	1.47
		35	-	0.00180	0.36	-	-		-		-
Phi 400	0.4	3	-	0.00212	0.15	-	-		-		-
		9	0.01078	0.01035	0.24	0.49	1.98	0.46	0.51	2.26	0.52
		16	0.01088	0.01603	0.30	0.6	2.52	0.63	0.65	3.41	0.86
		25	0.01492	0.02539	0.38	0.63	1.81	0.71	0.68	2.48	0.96
		35	-	0.03114	0.39	-	-	-	-		-
Phi 1000	1	3	-	0.02881	0.12	-	-	-	-		-
		9	0.10349	0.05844	0.19	0.36	1.34	0.45	0.41	1.84	0.61
		16	0.11070	0.09677	0.24	0.47	1.83	0.69	0.53	2.68	1.01
		25	0.10068	0.13835	0.28	0.58	2.46	0.9	0.66	3.91	1.43
		35	-	0.19021	0.33	-	-	-	-	-	-

The results show that the predicted slip ratio when transformed into an average relative velocity, the latter far exceeds the terminal velocity of isolated bubbles (about 0.3 cm/s in our conditions) in most cases. The relative velocity values increases up to nearly 1 m/s at large v_{sg} and/or in large columns when considering the injected gas flow rate. The situation is worse when using the measured gas flow rate, with relative velocities reaching 1.4 m/s. The reality is probably between these two estimates as the gas flow rate in the core region exceeds the injected flow rate due to the recirculation.

Plotted against the mean void fraction in the core (Figure 4.55), the average relative velocity happens to neatly increase with the gas content. It departs significantly from the terminal velocity in still fluid for void fractions above about 20-25%. Note that, although the relative velocity estimates presented above are not very precise, the limited uncertainties on the measured liquid flow rate and void fraction in the central region of the flow as precludes any flaw in the above analysis.

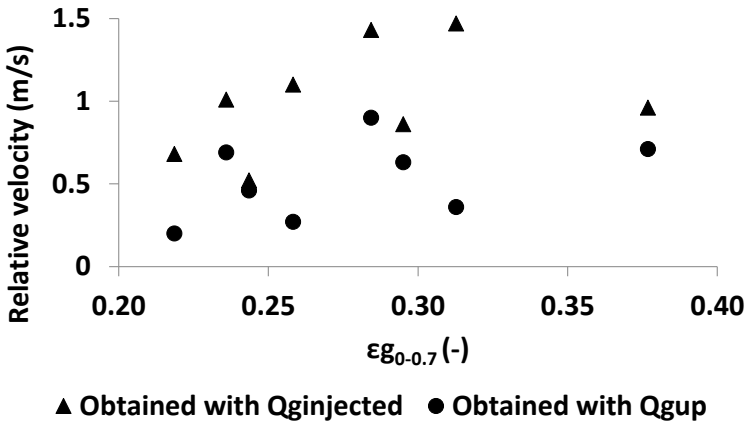

Figure 4.55 – Evolution of the relative velocity with $\varepsilon g_{0\text{-}0.7}$ for the columns Phi 150, Phi 400 and Phi 1000. (Calculated by Eq. (4.16))

The physical origin of such a behavior could be seek on interaction of bubbles with turbulence and/or on collective effects. Pair interactions alone are not likely to explain such relative velocities (Yuan and Prosperetti, 1994; Ruzicka, 2000). Instead, collective behavior involving a significant number of bubbles are to be preferred. One may indeed expect the existence of meso-scale structures associated with significant void fraction gradients such as those detected along the walls (c.f. section 3.6): the latter could be the result of convective instabilities due to differential buoyancy, similar to what is observed in sedimentation (see also Brenner, 1999). In addition, meso-scale turbulent structures interacting with these clusters can lead to significant non trivial interactions between the two-phases. Such effects are well documented (but not fully understood) in turbulent flows laden with much more dense particles (even though the mechanisms cannot be directly transposed to bubbly flows), and it has been shown that particle clustering has a strong impact on the settling velocity (Aliseda et al, 2000; Monchaix et al, 2012; Balanchandar and Eaton, 2010): the latter is significantly speeded up by the turbulent field. In the gravity driven bubbly flows considered here, it is thus possibly that interactions between turbulent structures and bubble clusters are at also play and induce a larger foaming velocities. The section 4.10 will be devoted to some tentatives to identify such meso-scale structures.

A second consequence of the above observations, is that such a behavior has to be accounted for when simulating bubble columns: in chapter 5, a preliminary analysis of the sensitivity of Eulerian two-fluid model prediction to the relative velocity will be proposed.

4.10 Characterization of flow structures

We have seen that the mean relative velocity of the dispersed phase significantly exceeds (up to a factor 2-3) the terminal velocity of isolated bubbles. In addition, the mean relative velocity increases both with vsg and D (see Table 4.33): alternately, the data indicate that the mean relative velocity increases with the average void fraction but that it evolves also with the column size as well. Similarly, velocity fluctuations scaled by the actual relative velocity are changing with the void fraction (see Figure 4.55) but seem to evolve also with the column size, even if the evidence is slim due to the limited number of data available. As already suggested, such behaviours may be related with the existence of bubble swarms or denser regions in the flow, those relative motion with respect to the liquid exceeds the bubble terminal velocity. In order to check the existence of such structures, and possibly to determine their characteristics size and time scales, various data processing options have been envisioned by, due to lack of time, only a few have been quantitatively exploited.

A first option was based on the analysis of images either of the flow along the walls or of oscillations arising of on top of the column. Some illustrations are provided in Figure 4.56. Qualitatively, turbulent structures of large size are easily detected: in the example of Figure 4.56 A, their typical extend is 15-20 cm. In addition, regions of high and low void fraction seem to be present, but they are more difficult to detect (there are more visible on movies) and to quantify. Another clue about the presence of large scale structures arises when observing from the top as shown Figure 4.56 B, but these structures are seen at the free surface and they may not be representative of the interior of the flow.

A

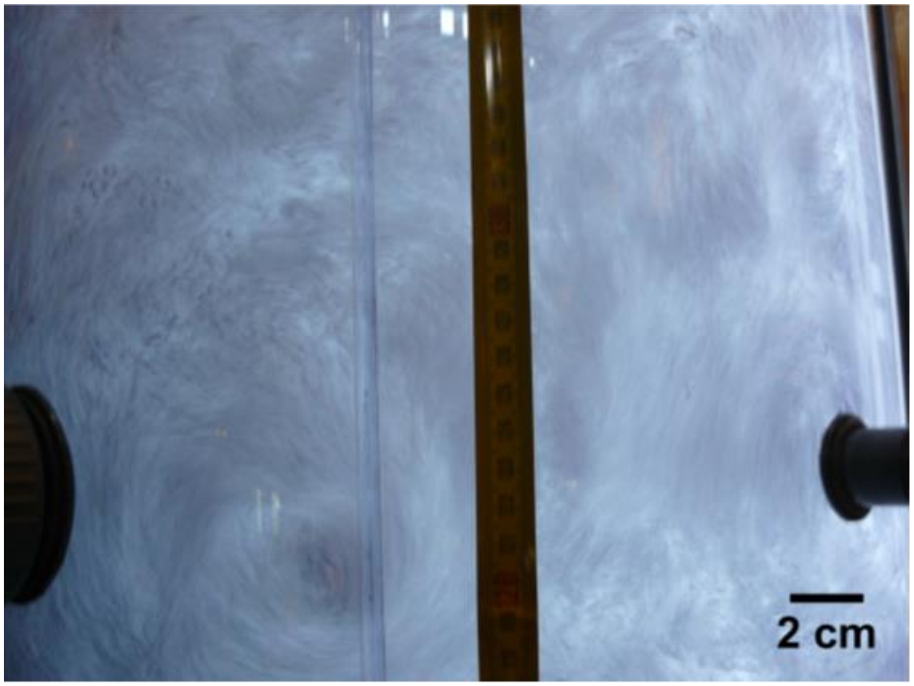

B

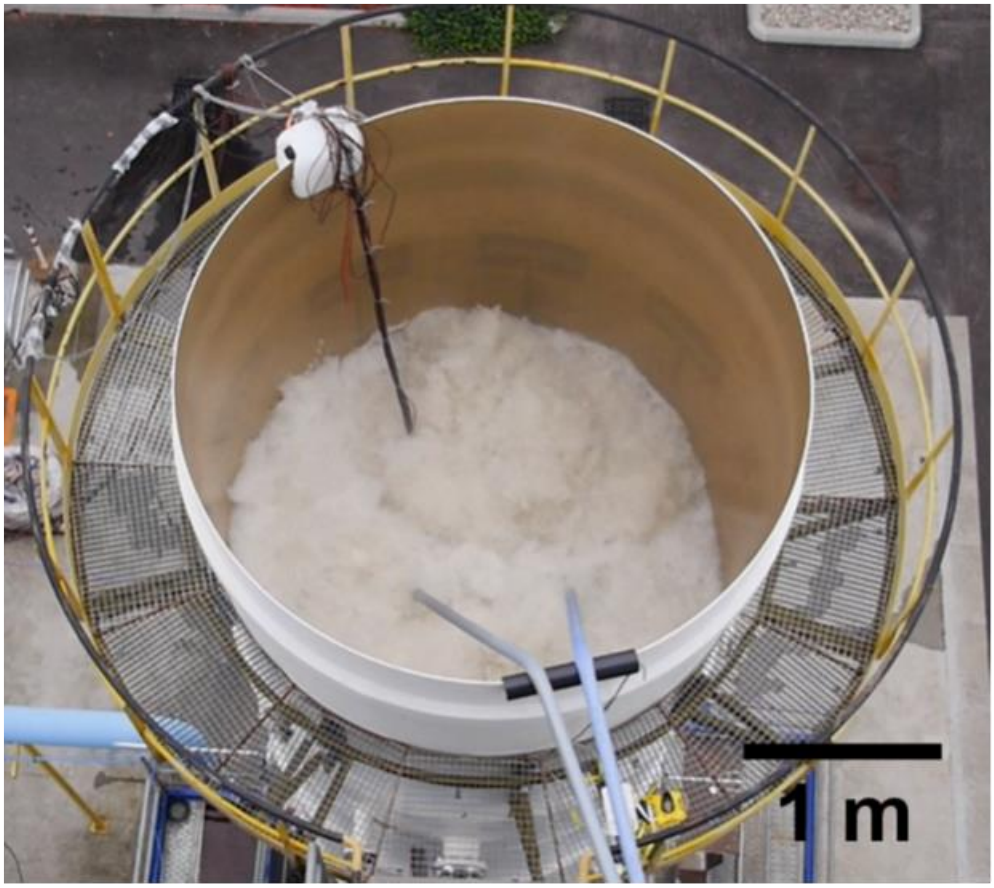

Figure 4.56 - A) Lateral image of the flow near the wall of the Phi 400 (v_{sg}= 25 cm/s, h/D=2.5); B) Top-view of the Phi 3000 (v_{sg} = 16 cm/s)

To extract some information from the interior of the flow, two techniques were used which are presented hereafter.

Characterization of the size of meso-scale structures

As seen in section 3.6, and for a distance between two optical probes larger than the bubbles horizontal diameter, a cross-correlation higher than the local gas hold-up implies that there is a higher probability of detecting a bubble at both locations. Such a behaviour could be the mark of the existence of high void fraction regions in the flow. If so, analysing the variation of the cross-correlation with the distance between probes will give access to some characteristic dimension of these structures.

The spatial cross-correlations were measured for probes distances ranging from 0.8 mm up to 5 mm, 10 mm and 800mm in the Phi 150, Phi 400 and Phi 1000 columns, respectively. Moreover, in all the measurements, both probes were located at the same elevation in the column, symmetrically located with respect to the column axis, in order to ensure the same local gas hold-up on both probes. These measurements were carried out at superficial gas velocities ranging between 3 cm/s and 35 cm/s at h/D=2.5. A typical evolution of such correlations at large distances is exemplified in Figure 4.57.

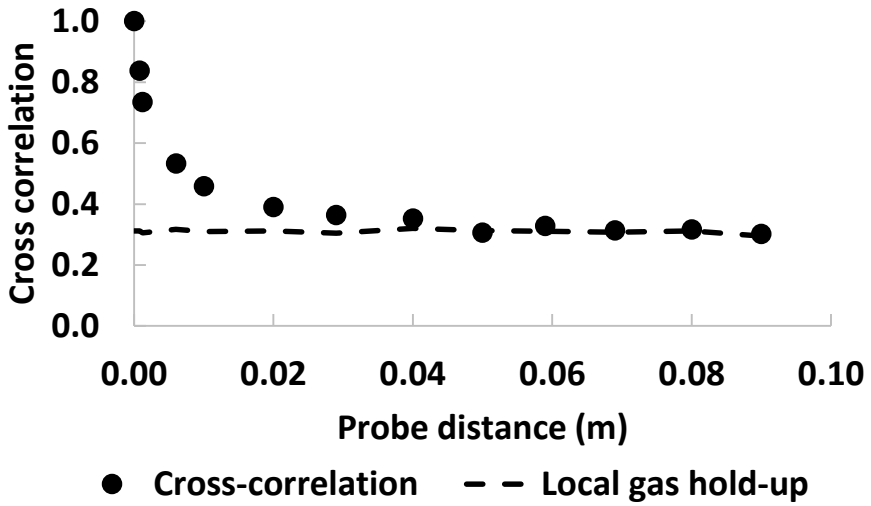

Figure 4.57 – Evolution of the cross-correlation with the distance between the probes. The dash line indicates the local gas hold-up at the probes positions. (Measurements obtained in the column Phi 400, at h/D=2.5 and for vsg=16 cm/s).

Figure 4.58 provides plots of the difference between the cross-correlation value minus the local gas hold-up (CC-εg(x)), for the v_{sg} values of 3 cm/s, 16 cm/s and 25 cm/s, respectively. At large distances that quantity drops to zero as expected.

A

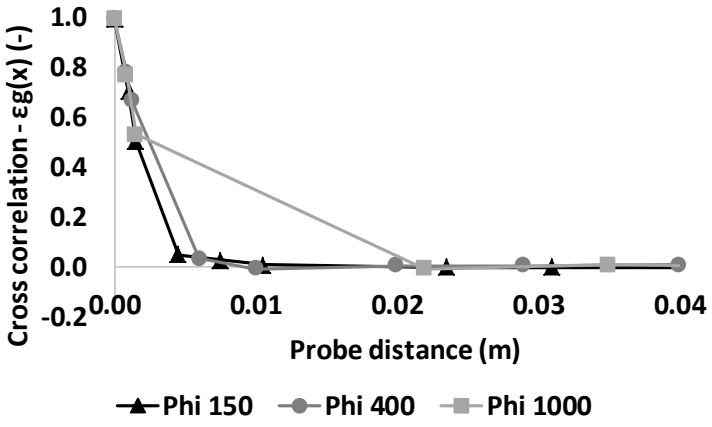

B

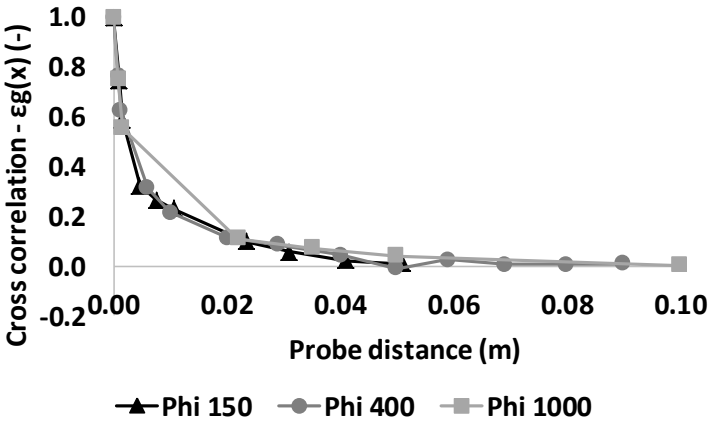

C

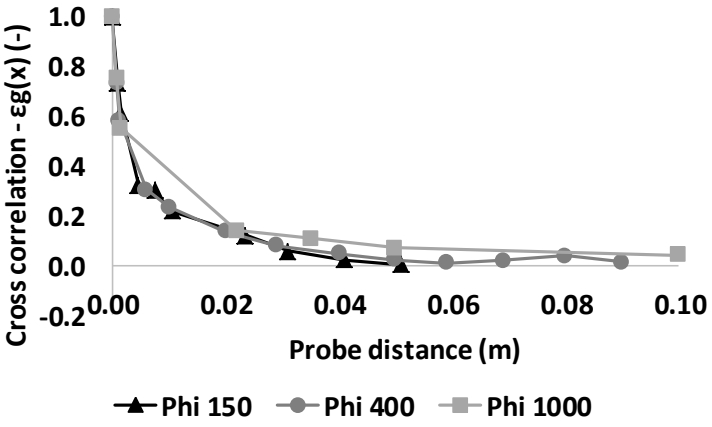

Figure 4.58 – Evolution of the difference (CC-εg(x)) with the probe distance in the columns Phi 150, Phi 400 and Phi 1000 for superficial gas velocities of: A) 3 cm/s; B) 16 cm/s; C) 25 cm/s.

For v_{sg}=3 cm/s, the results show that in the Phi 150 and Phi 400 columns, the quantity CC-εg(x) converges to zero for probe distances close to the typical bubble

horizontal diameter (i. e.6-8 mm). In the Phi 1000, the quantity CC-εg(x) becomes zero at larger distances between probes, but the spatial discretisation was not sufficient since measurements are lacking between 0.0015 and 0.007 mm. So, it is possible to affirm that no evidence was found of the presence of bubble swarms at v_{sg}=3 cm/s.

However, at 16 cm/s and 25 cm/s, the cross-correlation remains higher than the local void fraction for probe distances significantly larger than the typical bubble horizontal diameter. Furthermore, the results of the three columns present a similar trend both at for a given v_{sg} for v_{sg}=16 cm/s or 35 cm/s. So, it seems that the mean size of the bubble swarm is independent on the column diameter. In an attempt to found some characteristic size of these structures, we set an arbitrary criteria at a value of CC-εg(x)=0.1, estimating that at this level the signals remain slightly correlated. Therefore, an approximated size of the structures can be determined by the distance between the probes at which the CC-εg(x) reaches the value of 0.1. The corresponding data, scaled by the average Dh_{32} (6 mm) on the flow, are presented Figure 4.59 versus the superficial velocity.

.

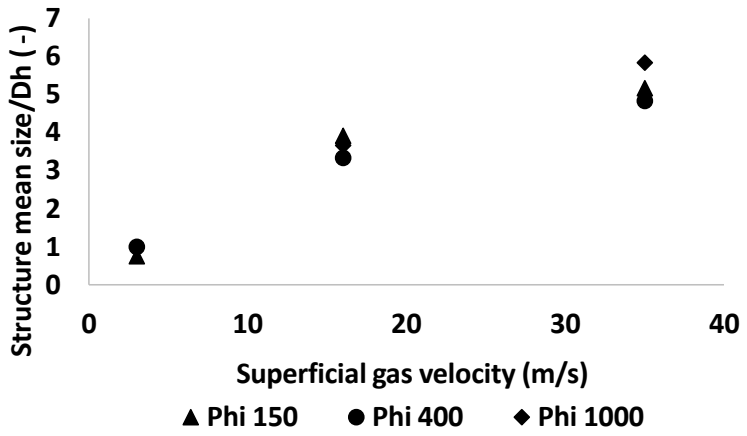

Figure 4.59 – Evolution of the mean structure size scaled by the average Dh on the flow (6 mm) with the superficial gas velocity for the columns Phi 150, Phi 400 and Phi 1000.

Figure 4.59 shows that the mean structure size linearly increases with the superficial gas velocity and that it is almost independently of the column diameter. Moreover, as previously stated, at v_{sg}=3 cm/s the signals are only correlated up to the typically one horizontal diameter of a bubble. For v_{sg}=16 cm/s and 25 cm/s, the size of the structures is approximately 20 mm and 30-35 mm, respectively. That amount for 3-4

to 5-6 bubbles horizontal diameters respectively. This amount seems significantly lower than the magnitudes of the vertical structures detected from images.

Characterization of the structures time scale

We considered the frequency analysis of the continuous Pavlov signals. The Pavlov tube was equipped with an enlarged bandwidth (100 Hz) sensor precisely to ensure a better time resolution. As already indicated, these sensors were not functioning in a differential mode and they prove to be much less reliable than the original 8Hz version. Thus, the spectrum analyses were not exploited (some examples are given in annex 1).

An alternate option consists in exploiting the signals delivered by optical probes. Indeed, bubble swarms or at least denser regions in the flow should be identifiable from the time variation of an "instantaneous" gas hold-up. Since the local gas hold-up, measured by the optical probe is computed by the integration in time of the optical probe signal, it is necessary to define an adapted time interval for the analysis. The result is expected to depend on that time window: the later has to be selected between the residence time of inclusions and the larger duration for which the void fraction converges. Note that an alternative would be to exploit the auto-correlation of a single probe signal by varying time delay as already practiced to identify micro-structures in bubbly flows (Cartellier et al., 1991).

As a preliminary analysis of the optical probe output, an "instantaneous" void fraction has been estimated using averaging over a sliding window of duration ΔT. One second of signal treated that way is shown Figure 4.60. Two durations have been considered, namely ΔT=40ms and ΔT=100ms. In the selected flow conditions, the average residence time of the gas phase on the probe tip was 2.3 ms, the selected time windows correspond thus to about 20 and 100 mean residence time respectively. As expected, the fluctuations are smoothed down when increasing ΔT but they are present at both scales. Moreover, their amplitude is quite large: gas concentrations typically evolve between 0.2 to 0.7, to be compared with the (converged) local void fraction equal to 0.39. This result provides a first indication of the strong concentration gradients existing in the flow. Besides, the typical time scales associated with these fluctuations are about 0.05-0.2 second. For the flow conditions considered, the typical phasic velocities were slightly above 1 m/s: that leads to meso-scale structures of the order of 5-20 cm, a magnitude

similar to the size of vertical structures visually detected near walls. In terms of bubble size, these lengths represent 10 to 40 Sauter mean horizontal diameters. Compared with the spatial cross-correlation technique, the above figures are neatly larger. Even though the correlation technique could damp the fluctuations in concentration, we must point out that we are comparing here a few realisations with a fully converge information so that no definitive conclusion can be draw. A statistical analysis is clearly required to conclude, but these observations seem consistent.

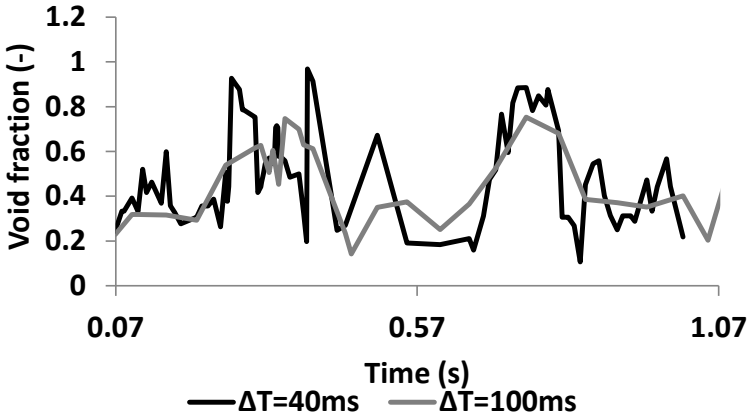

Figure 4.60 - Time history of "instantaneous" void fractions averaged over windows of duration ΔT. (flow conditions: Phi 1000, x/R=0, h/D=2.5, v_{sg}=35cm/s).

We also took advantage of this analysis to evaluate the average bubble velocity within the same time windows. The results are shown Figure 4.61 for ΔT=100ms in the same flow conditions as above. A significant correlation arises since local concentration peaks correspond to maxima in bubble velocity. Clearly, a statistical analysis is required to confirm that point, but the observation is consistent with the existence of collective effects and also with the fact that these structures can have a drastic impact on the rising velocity of bubbles.

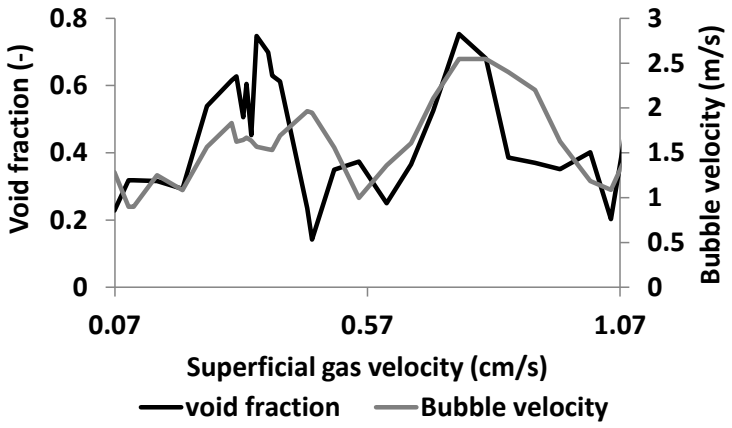

Figure 4.61 - Time history of "instantaneous" void fraction and bubble velocity averaged over a sliding windows of duration ΔT=100ms. (flow conditions: Phi 1000, x/R=0, h/D=2.5, v_{sg}=35cm/s).

Although limited to a single flow condition, the above analysis demonstrates its usefulness for the investigation of these dense bubbly flows. Such an investigation deserves to be pursued in order to confirm the above behaviors in a statistical sense and, if meaningful, in order to quantify how the scales evolve with to flow conditions, how concentrations and velocities are correlated.

Others possibilities to characterize such structures would have been possible but were not exploited due to lack of time. Some quantifications of the fraction of time the flow remains directed upward (or downward) have been discussed in Chap.3: that analysis could have been extended to the determination of the distributions of the waiting times between zero crossings of the Pavlov signal. Spatial correlations of Pavlov signals (technically difficult to implement) have been envisioned but were technically challenging. An electrical tomography technique that maps the void fraction over a certain area has been also considered but preliminary measurements have shown that its response time was far too low. Preliminary attempts have been also made to exploit an ultra-sound Doppler velocimetry that were encouraging.

4.11 Conclusions

In the present chapter, we have analysed various global and local variables measured in different bubble columns, studied their scaling within the column diameter (varied in a 1:20 range) and the superficial gas velocity (varied over a 1:10 range) and we

have exploited the available results to try to better understand the hydrodynamics of these bubbly flows.

First, we have analysed the possible presence of coalescence through a detailed scrutiny of the bubble chords PDFs obtained at different heights in each column. No evidence of bubble coalescence was found in the columns Phi 150, Phi 400 and Phi 1000 for superficial gas velocities comprised between 3 cm/s and 25 cm/s. Additionally, no strong evidence of bubble breakage was detected. Concerning the characteristics of bubbles, the average eccentricity was found to be 0.7 in all conditions. The mean bubble size was determined using the spatial cross-correlation technique developed in Chapter 3. The Sauter mean diameter was found relatively constant whatever the flow conditions, its extreme values ranging between 6mm and 9 mm on the symmetry axis. Information have also been collected on the lateral bubble size segregation: the later amounts to 2-3 mm except in the Phi 3000 column where it reaches 5mm. Therefore, the initial objective of ensuring a quasi constant bubble size in the various columns and over a significant range of gas flow rate was satisfactorily fulfilled.

The axial evolutions of all the main variables, namely bubble size, void fraction and phasic velocities indicate that the zone of quasi fully-developed flow extends at least from h/D= 2.5 to h/D=3.75 (this was not tested in the Phi 3000). The analysis of the flow was then based on local data collected in that zone.

Over the range of conditions considered, the global gas hold-up increased up to 35%. The transition between the homogeneous and heterogeneous regimes was determined to occur for superficial gas velocities about 3-4 cm/s. In the heterogeneous regime, the empirical fit proposed by Schweitzer et al. (2001) for the radial profiles of local gas hold-up normalized by the void fraction on the axis (Eq.(1.1)) was found to be in quite good agreement with experiments: its validity has thus been extended to larger column diameters (i.e. up to 3m). We then investigated the evolution of global and local gas hold-up with the two main parameters that were varied in the present study, namely the column diameter and the superficial gas velocity.

Global and local gas hold-ups were found independent of the column diameter. When all regimes are considered, they increase with the superficial gas velocity according to $\langle \varepsilon g \rangle \propto v_{sg}^{n}$, with an exponent n comprised between 0.40 and 0.45. This is close to the proposals of Hikita and Kikukawa (1974) or of Reilly et al. (1986). Yet, when restricting the conditions to the heterogeneous regime only, the exponent neatly decreases, down to ≈ 0.35.

Similarly, the mean axial liquid velocity scaled by its value on the axis happens to be reasonably well predicted by the empirical fit Eq. (4.2) proposed by Forret el al. (2006), regardless of the column diameter. Besides, the mean liquid velocity on the column axis is found to evolve as $u(0) \approx v_{sg}^{0.5} D^{0.28}$ in partial agreement with the correlation of Miyauchi and Shyu (1970) Note that the exact exponent of D is 0.5. Indeed, we focused on the central portion of the column where the mean flow is directed upward (i.e. -0.7 ≤ x/R ≤ 0.7) and is quasi 1D, the measured mean radial liquid velocity being close to zero. Surprisingly, the corresponding liquid flow rate (Q_l^{up}) only depends on the column diameter and does vary with the superficial gas velocity. In non-dimensional terms $Q_l^{up} \approx D^{0.5}\sqrt{gD}$. That non-trivial result states that the entrainment capacity in a bubble column of a sufficient height compared to its diameter and for large (6-8mm) bubbles, is a function of its size and not of the injected gas flow rate.

Despite serious issues on bubble velocity measurements with optical probes in such flow conditions, meaningful trends were obtained. The mean axial bubble velocity on the symmetry axis consistently evolves as $vb(0) \approx D^{0.5} v_{sg}^{0.34}$. That trend was established for D in the interval [0.15 m, 1 m] and for v_{sg} between 9 cm/s and 35 cm/s. Moreover, the upward gas flux (Qg^{up}) in the core region increases as $Qg^{up} = 0.51 D^{2.47} v_{sg}^{0.79}$: its sensitivity to the column diameter is the same as for the liquid flow rate, but, and as expected, it increases with the gas superficial velocity as well. A comparison with the injected gas flow reveals that the measured gas flow rate Qg^{up} is strongly underestimated. Therefore, convincing trends were extracted for the above variables, but their magnitudes are not available.

The velocity fluctuations in the liquid and gas phases were then considered. Regarding the former, the radial profiles exhibit maxima at the radial position x/R=0.7, the location where the mean liquid velocity reverses its direction. At this location, the sensitivities of the liquid axial velocity fluctuations (u'(0.7)) to D and vsg parameters are found to be very similar to those of the mean liquid velocity . Consequently, the turbulence intensity remains nearly constant, around 25-30% in all conditions. We then tested if the liquid velocity fluctuations are related with the local void fraction, as it happens in pseudo-turbulence. When scaling u' with the terminal velocity of a single bubble, the fluctuations do increase with the local gas hold-up but their magnitude exceeds by far those found in homogeneous systems. Therefore, as convective type instabilities related to concentration gradients are know to led to strong pulsations in

velocities, one anticipates the presence of meso-scale in-homogeneities in the flow. Consequently, we considered the actual relative velocity (vr) estimated in section 4.9 from kinematic considerations as a more appropriate velocity scale: the magnitude of u'/vr is found to be O(1) which is encouraging. Yet, the trend with the void fraction is inverted as u'/vr is now decreasing with εg: this behavior probably arises from the strong and complex coupling between the void fraction and the actual relative velocity in these gravity driven bubbly flows. In addition, let us emphasis that when convective type instabilities are at play, a more appropriate scaling should involve the magnitude of concentration gradients instead of the mean gas content. For the gas phase, the velocity fluctuations are nearly uniform along the column radius, a behavior that may be due to bubble velocity measurements limitations. The gas velocity fluctuations on the column axis were found to evolve as $vb'(0) \approx v_{sg}^{0.43}$, and no clear influence of the column diameter was identified: owing to limitations on the measuring technique, the results relative to the gas phase velocity fluctuations are to be considered with caution.

Our measurements were also compared with Xue et al. (2008) database: a good agreement was found between these two sets of data at $v_{sg=}$3 cm/s. However, at larger vsg, the presence of larger bubbles (by a factor close to 2) and of stronger spatial segregation in Xue et al. experiments lead to differences in the local void fraction measurements up to 0.10. Consequently the liquid velocity measurements could not be compared.

The mean relative velocity was then deduced from a kinematic approach applied to the core region using the measured liquid flow rate and gas hold up combined with realistic guesses for the gas flow rate. That analysis demonstrates that, at large gas concentrations, the mean relative velocity is several times higher (typ. 2-3 times) than the terminal velocity of a single bubble in a stagnant liquid (≈30 cm/s in our conditions). Again, the physical origin of such a behavior could be connected with flow in-homogeneities, either due to collective effects and/or interactions with powerful turbulence structures.

The presence of meso-scale structures is therefore suspected both from the analysis of the turbulence in the liquid and from the estimated magnitude of the relative velocity. Aside examining images of the flow near walls, we attempted to detect and to characterize these in-homogeneities in the interior of the flow. Using the cross-correlation of signals from optical probes separated by a distances larger than a bubble horizontal diameter, regions denser than the average concentration were perceived for $v_{sg} \geq$16 cm/s:

their spatial extension was found to be about 4 to 6 times the averaged bubble diameter Dh_{32}. An alternate analysis of the fluctuations in concentration over time indicates that the void fraction strongly fluctuates, with amplitudes comparable to the mean concentration. Besides, the associated meso-scale structures have a typical length about 10 to 40 Sauter mean horizontal diameters. Although a detailed statistical analysis is required, these first evidences clearly support that meso-scale structures are indeed present in the flow. In addition, they are expected to play a key role on the value of the actual relative velocity of the dispersed phase.

The above features must be accounted for in the flow modeling since, and as shown in section 4.9, predictions grounded on the terminal bubble velocity become erroneous at large void fractions. Therefore, in chapter 5, we attempted to represent these complex dynamics by way of a modified drag law. The analysis is first achieved using a 1D model, and it leads to a drag law correction by way of a swarm factor. A preliminary sensitivity study to the proposed correction implemented in a 3D unsteady simulation based on an Eulerian two-fluid is then presented and discussed.

5 Looking for a relevant drag law for bubble column simulations

Bubble diameter measurements are of first importance to study and model the interaction between gas and liquid in bubble flows. As explained in chapter 1, the bubble diameter plays a key role in the expression of the momentum exchange between phases. Especially concerning the drag force that is proportional to the projected surface of bubbles in the direction of the flow. The drag force is considered as the main force that has to be taken into account for CFD simulations (Laborde-Boutet et al, 2009; Jakobsen et al. 2005).

Bubble diameters have been previously successfully measured in various bubble columns and superficial velocities, so they can be used to calculate relative gas velocities as it will be detailed below. The objective of this chapter is to compare the relevance of existing drag law formulations that are picked up from literature. The chapter is structured as following:

i) Establish the relation between bubble diameter, drag coefficient and relative velocity in bubbly flows.
ii) Compare different drag law formulations for a given criteria of comparison (gas flow rate).
iii) Estimate and discuss the relevance of the selected drag law(s) once implemented in 3D CFD RANS simulations.

This chapter is primarily based on the work of Luca Gemello, Master internship student in 2015 at IFPEN.

5.1 Estimation of the relative velocity inside bubble columns

As complex heterogeneous regimes are involved in bubble columns at high void fraction, i.e. velocity and gas hold-up gradients are present. As consequence, is not possible to simply assume a local equilibrium between drag and Archimedes forces. Therefore complete momentum balance equations have to be solved to estimate the local relative velocity. The following approach is based on different assumptions:

- Only average lengths are solved, Reynolds equations are considered.

- The axial pressure gradient is constant along the radius of the column.
- The flow is invariant in the vertical direction.
- The flow is axisymmetric.

The axial component of the momentum balance on each phase K (K=G or L) is written as below:

$$0 = -\varepsilon_K \frac{dP}{dz} + \varepsilon_K . \rho_K . g - \frac{1}{r} . \frac{d}{dr} (\varepsilon_K . r . \tau_K) + I_K \qquad (5.\ 50)$$

with g=-9.81m/s². Other components of the momentum balance are null. τ_K is the stress tensor of the phase K, and can be modeled with the turbulent viscosity concept :

$$\tau_K = \rho_K . \mu_{t,K} . \frac{dU_K}{dr} \qquad (5.\ 51)$$

$\mu_{t,K}$ is the turbulent viscosity in the phase K. U_K is the mean axial velocity of the phase K. I_K is the exchange term between both phases ($I_G = -I_L$). ε_G is noted ε thereafter. Only the drag is considered in this term. The drag force applied on a single bubble is written as:

$$\vec{F} = -\frac{1}{2} \rho_L \cdot S \cdot C_D \cdot \overrightarrow{V_R} |V_R| \qquad (5.\ 52)$$

where S is the projected area of the bubble in the flow direction. In case of a spherical bubbles of diameter d, $S = \pi d^2/4$. It is easy to link the local gas fraction to the diameter and the number of bubbles per unit of volume n_v (m^{-3}) :

$$n_v = \frac{6\varepsilon}{\pi d^3} \qquad (5.\ 53)$$

As a consequence, the force density (N/m^3) that is involved in the momentum balance axial component is written as following.

$$I_L = n_v \cdot \left\| \vec{F} \right\| = \frac{3\varepsilon C_D}{4d} \rho_L V_R^2 \qquad (5.\ 54)$$

And in case of a bubble size distribution, it is known (and not demonstrated here) that the appropriate bubble diameter is the Sauter Diameter d_{32}. The case of non-spherical bubbles is less known. If oblate bubbles are considered, with an horizontal (d_h) and a vertical (d_v) diameter, the projected surface of bubble is proportional to d_h^2, and the bubble volume is proportional to dh^2dv. As a consequence the equation is replaced by

$$I_L = \frac{6\varepsilon}{\pi d_v {d_h}^2} \cdot \frac{1}{2} \rho_L \cdot \frac{\pi}{4} {d_h}^2 \cdot C_D \cdot |V_R|^2 = \frac{3\varepsilon C_D}{4 d_v} \rho_L V_R^2 \qquad (5.\ 55)$$

So the vertical diameter of bubbles seems to be the pertinent one for the calculation of the drag force. I_L is positive at any point of the column, as only phase averaged velocities are

considered. V_R is the relative velocity (=V_G-V_L). Summing Eq. (5.1) for the gas and liquid phase lead to

$$0 = -\frac{dP}{dz} + (1-\varepsilon).\rho_L.g + \varepsilon.\rho_G.g - \frac{1}{r}.\frac{d}{dr}(\varepsilon.r.\tau_G + (1-\varepsilon).r.\tau_L) \qquad (5.\ 56)$$

A classical assumption (Uyema and Miyauchi, 1979) consists to consider the gas stress tensor as negligible compared to the liquid one. As a consequence:

$$0 = -\frac{dP}{dz} + (1-\varepsilon).\rho_L.g + \varepsilon.\rho_G.g - \frac{1}{r}.\frac{d}{dr}\left((1-\varepsilon).r.\tau_L\right) \qquad (5.\ 57)$$

$(1-\varepsilon).\tau_L$ is noted τ as the « mean flow » stress tensor. Following the calculation of Uyema and Miyauchi (1979), the pressure gradient term can be calculated by integrating the equation 8 between 0 and R. We obtain :

$$\frac{dP}{dz} = \rho_L.g.(1-\bar{\epsilon}) - \frac{2}{R}.\tau_W \qquad (5.\ 58)$$

τ_W is the shear stress at wall. $\bar{\epsilon}$ is the averaged gas hold-up overall the column. The Figure 5.1 represents the mean liquid flow inside a bubble column under heterogeneous regime. Always following cited authors, τ_W is linked to the velocity of liquid at the boundary of the laminar sublayer (δ). By assuming that this velocity is the minimal liquid velocity measurable close to the wall, it is proposed to estimate τ_W by :

$$\tau_W = \rho_L\left(\frac{U_W}{11.63}\right)^2 \text{ at r} = \text{R} \qquad (5.\ 59)$$

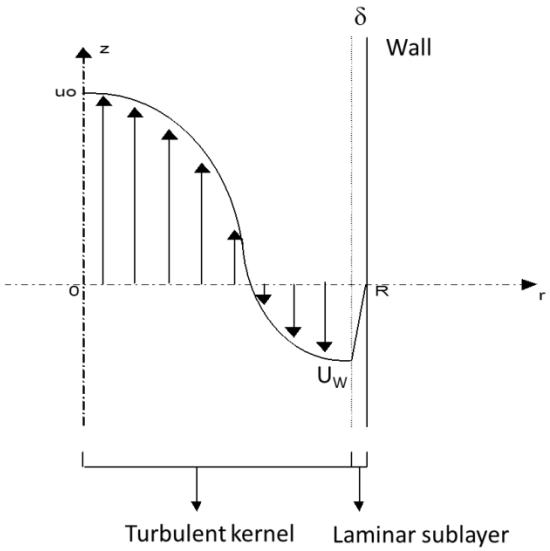

Figure 5.1 - Liquid velocity profile inside a bubble column in the heterogeneous regime.

The Figure 5.1 represents the mean liquid velocity profile in a column and maximum (U_0) and minimum velocity (U_W). Following Forret et al. (2003), in the heterogeneous regime the liquid velocity profile are all similar when normalized by the maximum velocity at the center and expressed as function of the normalized position (x=r/R). A good agreement is obtained with the following fitting function:

$$u(x) = \frac{u_0}{a-c}\left(a.e^{-b.x^2-c}\right) \tag{5. 60}$$

With a=2.976, b=0.943, c=1848. This equation involves that Uw≈-0.6. U_0.and eq.10 can be replaced by

$$\tau_W = \rho_L\left(\frac{U_0}{19.38}\right)^2 \tag{5. 61}$$

And Eq. (5.9) by

$$\frac{dP}{dz} = \rho_L.g.(1-\bar{\epsilon}) - \frac{2}{R}.\rho_L\left(\frac{U_0}{19.38}\right)^2 \tag{5. 62}$$

The Eq.(5.7) can be now replaced by

$$\begin{aligned}&\frac{1}{r}.\frac{d}{dr}\left((1-\varepsilon).r.\tau_L\right)\\&= (\bar{\varepsilon}-\varepsilon).\rho_L.g + \varepsilon.\rho_G.g + \frac{2}{R}.\rho_L\left(\frac{U_0}{19.38}\right)^2\end{aligned} \tag{5. 63}$$

The last two equations are now used in Eq. (5.1) for the liquid phase that lead to

$$0 = \varepsilon.(1-\bar{\varepsilon}).\rho_L.g - \varepsilon.\rho_G.g - \varepsilon\frac{2}{R}.\rho_L\left(\frac{U_0}{19.38}\right)^2 + I_L \tag{5. 64}$$

The momentum exchange term between phases is developed to let appear the drag coefficient and the relative velocity:

$$0 = (1-\bar{\varepsilon}).\rho_L.g - \rho_G.g - \frac{2}{R}.\rho_L\left(\frac{U_0}{19.38}\right)^2 + \frac{3C_D}{4d}\rho_L V_R^2 \tag{5. 65}$$

This equation can be either used in its complete form or can be simplified. The gas density is negligible except for very high pressure applications. The term associated to the shear stress at wall is also very low compared to others, and can be neglected. This lead to the following expression

$$0 = (1-\bar{\varepsilon}).g + \frac{3C_D}{4d}V_R^2 \tag{5. 66}$$

Or

$$V_r = \sqrt{\frac{4(1-\bar{\varepsilon}).(-g).d}{3C_D}} \tag{5. 67}$$

This expression is very easy to use in order to estimate the relative velocity at any radial position in the column. For a given Cd coefficient, the mean gas velocity can thus be calculated only from liquid velocity profile and average gas hold-up. If the drag coefficient depends on the local gas hold-up, measurements can be used. But similar gas hold-up profiles have also been measured in various bubble columns, when normalized by the average gas hold-up (Schweitzer et al., 2001). The following expression can be used for example:

$$\varepsilon(x) = \bar{\varepsilon}.[A(x^6 - 1) + B(x^4 - 1) + C(x^2 - 1)] \qquad (5.\ 68)$$

with A=-1.7989, B=1.228, C=-0.939

Notes

In case of equilibrium between the drag and Archimed forces, the addition of equations Eq.1L multiplied by ε plus Eq.(5.1) for the gas phase multiplied by (1-ε) leads to

$$\mathrm{I_L} + (1 - \varepsilon).\varepsilon.\mathrm{g}.\Delta\rho = 0 \qquad (5.\ 69)$$

or

$$\mathrm{V_r} = -\sqrt{\frac{4(1 - \varepsilon).(-\mathrm{g}).\mathrm{d}}{3\mathrm{C_D}}} \qquad (5.\ 70)$$

This equation is similar to Eq.18 but the local void fraction is involved and not the average over all the column.

The physical meaning of the momentum exchange term may be discussed. A strong assumption is done when the formalism of drag force is used to model the totality of the momentum exchange. As equations are phase averaged and steady state profiles are considered, the drag has to be interpreted as a macroscopic apparent friction force that encompasses very complex small scale interactions between bubbles and the surrounding liquid flow. Gas and liquid velocity fluctuations may interact and contribute to the total momentum exchange between phases, but these interactions, if any, are not considered besides the apparent drag law.

5.2 Identification of relevant drag law formulation

The method

Available experimental data that may be used for validation are:

- Geometry of the columns and operating conditions (including gas flow rate).
- Liquid velocity measurement, especially at the center of the column.
- Gas hold-up measurement, average and local.
- Sauter bubble diameter (vertical/horizontal, eccentricity). Data provided by the cross correlation method are used because they are the only ones available at any bubble column diameter. At any rate, the eccentricity is known and it is constant for all experiments except in the Phi 3000 column.

If only the liquid velocity at the center of the column and the average gas hold-up are available, previously validated correlations Eq.(5.11) and Eq.(5.19) are used to estimate liquid velocity and gas hold-up radial profiles. Ideally, local relative velocity measurements may be used to study the drag law. This would need to measure accurately the gas phase velocity in the bubbly flows. Although the bubble diameters measured by the single probe method are assessed as relevant, the measured velocities have to be considered very carefully as explained in section 3.5. For this reason it has been decided not to use gas velocity measurements but only the injected gas flow rate for drag law validation.

As a consequence the following sequence is followed to estimate the relevance of a given drag law:

For a given operating condition and bubble column, for a given drag law:

a) Calculation / measurement of local gas hold-up and liquid velocity profiles.

b) Estimation of the relative velocity using Eq.18. This is used to estimate the local gas velocity $V_G(r) = V_L(r) + V_R(r)$. This is based on cross correlation measurements of horizontal diameters, and estimation of vertical diameters by using the measured eccentricity (Ecc ≈ 0.7).

c) Integration of the gas flow rate on the column section and calculate the associated superficial gas velocity.

$$V_{sg} = \frac{\int_0^R 2\pi r * \varepsilon_G(r) * V_G(r) dr}{\int_0^R 2\pi r dr} \quad (5.\ 71)$$

d) Compare the calculated v_{sg} to the experimental one.

The vertical bubble Sauter diameter is used, based on the horizontal diameter measurement and the eccentricity. The calculated v_{sg} is interpreted as the v_{sg} that would be coherent with a given choice of drag law. A good agreement between calculated and experimental v_{sg} does not validate the drag law formulation as only average gas velocity are compared, but on the contrary a large difference between v_{sg} excludes the relevance of the considered drag law. Otherwise, it is reasonable to think that a good estimation of v_{sg} signifies that the considered drag law delivers relative velocities that are in the good range of magnitude.

As almost flat bubble diameter profiles have been measured in the different bubble columns, only average bubble diameters are used to estimate the relevance of drag laws. This simplification is also justified by the fact that in case of ellipsoidal bubbles in the range of diameters [6-8mm], the terminal velocity of bubbles is almost constant.

A last assumption is to consider that the average gas hold-up does not depend on the bubble column diameter. This result has been validated by Forret et al (2003), and verified during the present study (see Chap.4, Figure 4.9).

Considered drag laws

As discussed in the chapter 1, various drag laws are available in literature to model the friction between bubbles and surrounding liquid. They are generally validated in a given range of bubble size or shape and interface properties (clean / contaminated interfaces). The terminal velocity of single bubbles is computed for different drag laws in Figure 5.2.

A

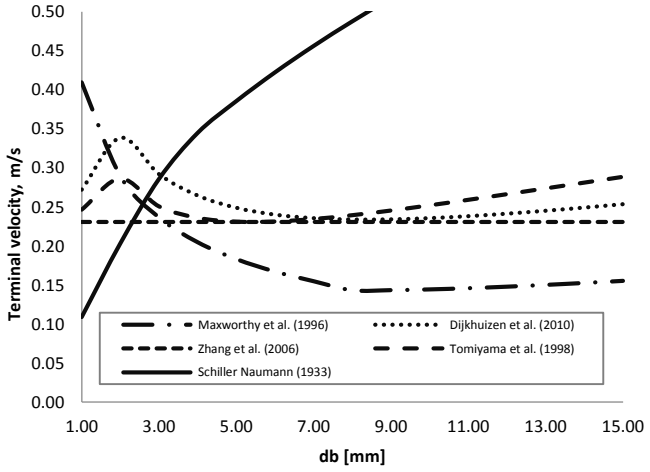

B

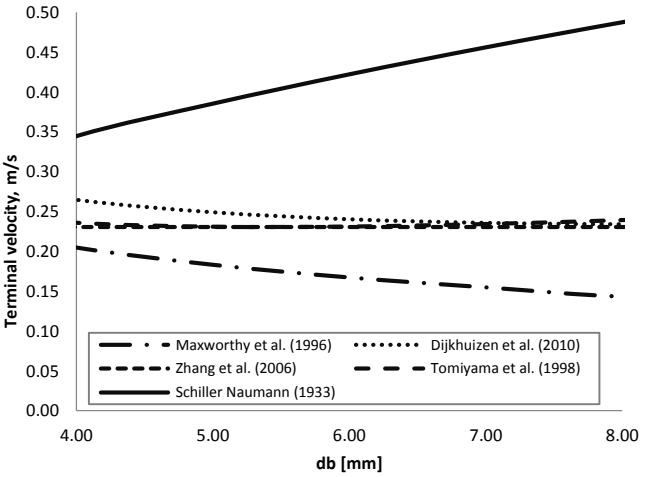

Figure 5.2: Terminal velocity associated to various single bubble drag laws (cd0) (air in water): A) Full range B) focus on [4-8mm] bubbles.

The Schiller & Naumann correlation is usable with spherical bubbles, i.e. small bubbles (< 3mm). Above this value, terminal velocity is overestimated. Recent drag laws of Tomiyama, Dijkhuisen and Zhang produce similar terminal velocities in the range of interest [4-8mm]. The single bubble drag laws are not sufficient to describe the friction between phases when the gas fraction exceed a few percent of hold-up, and swarm factors are used to take into account the collective effect of neighboring bubbles. The swarm factor (h) is thus multiplied to the single bubble drag law (Cd0). Different swarm factors are also reported in Figure 5.3.

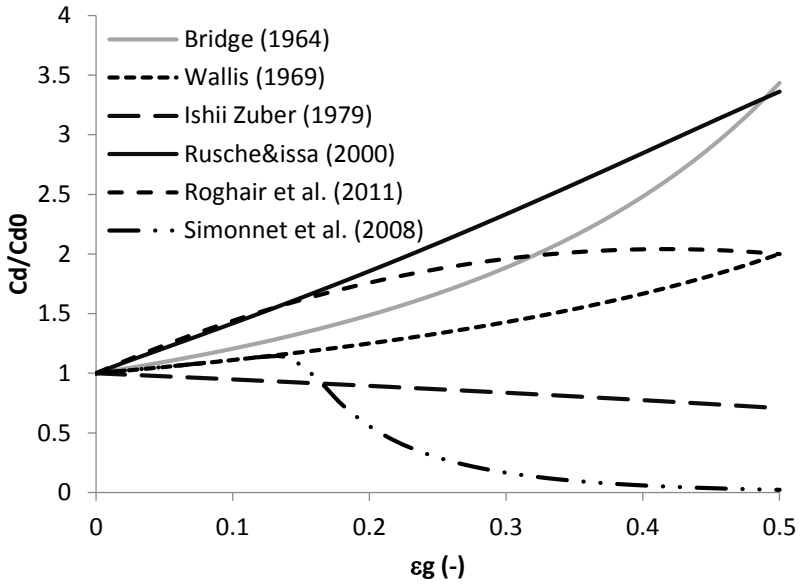

Figure 5.3: Comparison of swarm factors versus the gas hold-up.

Major part of swarm factors proposed in literature increases the drag law with the gas hold-up. The Ishii-Zuber swarm factor slightly decreases the drag laws. The Simmonet drag law is completely different. It is based on direct measurements of relative velocities in a bubble column, regardless the flow regime (homogeneous or heterogeneous). It shows a first classical behavior at low gas hold-up, which is similar to the swarm factor of Wallis. But above 15% of gas fraction, the swarm factor falls down to zero.

Results

Single bubble drag laws are considered in a first step in the Phi 400mm column. Results are presented in term of parity diagram in Figure 5.4. Perfect results would fit with the diagonal of the graph, indicating that calculated v_{sg} are equal to the corresponding experimental v_{sg}. Calculation values are reported in Table 5.1 to easier the reading.

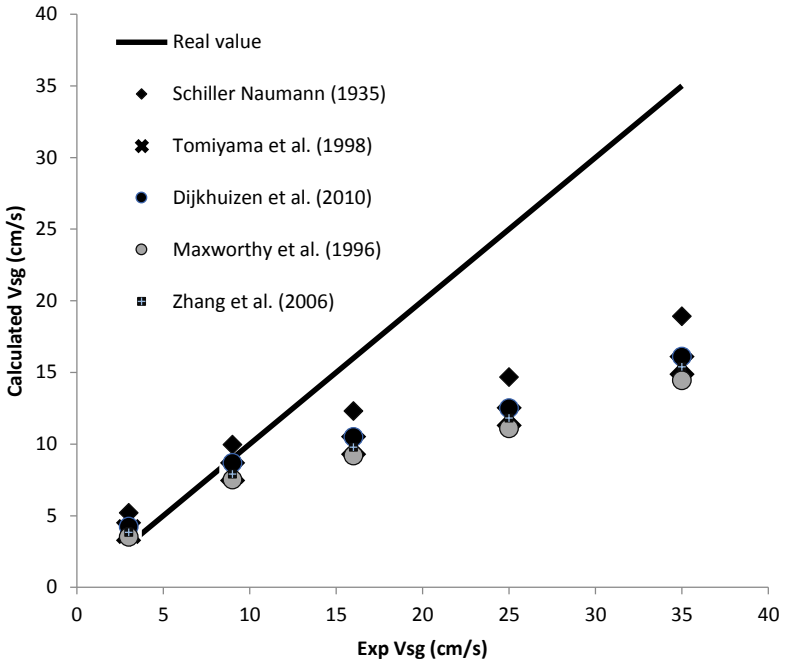

Figure 5.4 : Parity diagram concerning single bubble drag laws

Table 5.1 ***: calculated values of*** v_{sg} ***(column Phi 400mm)***

v_{sg} (cm/s)	3	9	16	25	35
Schiller Naumann (1935)	5.21	9.98	12.32	14.68	18.94
Tomiyama et al. (1998)	3.91	8.08	9.91	11.93	15.49
Dijkhuizen et al. (2010)	4.25	8.71	10.51	12.52	16.11
Maxworthy et al. (1996)	3.54	7.54	9.21	11.11	14.45
Zhang et al. (2006)	3.85	7.92	9.80	11.82	15.40

At low gas flow rate all drag laws have a good agreement with experimental data, except the Schiller and Naumann law that overestimates the gas flow rate. This is due to the overestimation of the relative velocity associated to this law, as it is valid~~ated~~ only for rigid spheres but very famous also for many dispersed two-phase flow simulations. Here, the measured bubble diameters are in the range of [3-7mm], as a consequence bubble velocities are higher than those deduced from other drag laws.

At high gas flow rate every law strongly underestimates the gas velocity. This shows that single bubble drag laws are not usable in dense flows, i.e. at v_{sg} > 10cm/s or εg > 15-20% approximately. Results are similar in other columns and are not detailed.
A very important point has to be noticed at this step of the study. The underestimation of gas velocities at high gas flow rates proves that involved drag coefficients are too high

and lead to too low relative velocities. Only swarm factors able to decrease strongly the drag coefficient at high gas hold-up have to be considered to improve results. This is illustrated in Figure 5.5 below where the Tomiyama (1998) Cd0 drag law is used associated with different swarm factors, always on the Phi 400mm column.

We observe that the swarm factors of Bridge and Wallis does not change significantly the quality of the comparison, whereas the Simonnet swarm factor delivers very good results with an average error on v_{sg} below 10%.

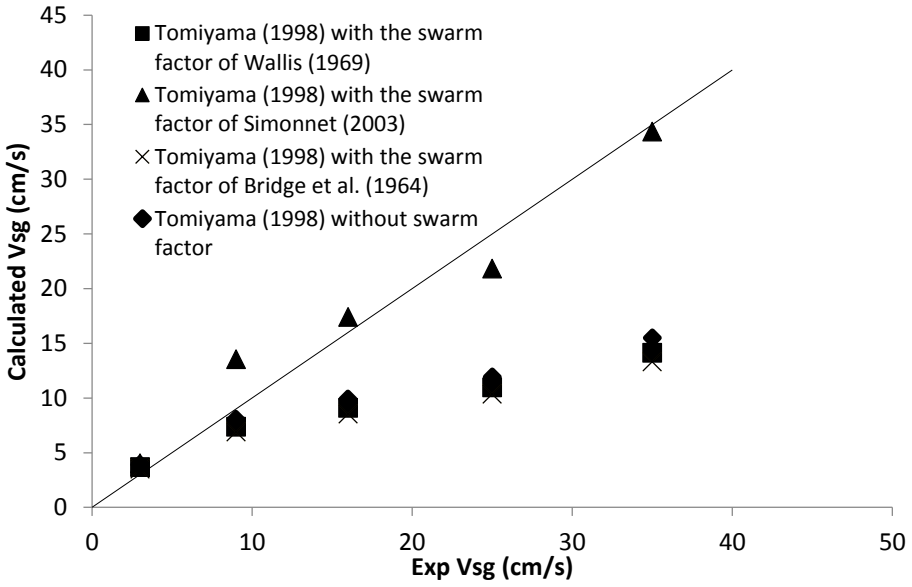

Figure 5.5: Parity diagram on v_{sg} with Cd0 (Tomiyama (1998) with different swarm factors (data from the Phi 400 bubble column)

The same drag law is used with data from other bubble columns (Phi 150 – 400 – 1000 – 3000mm). Results are presented in Figure 5.6. We observe a very good agreement for all the bubble columns, with an average error of 13%.

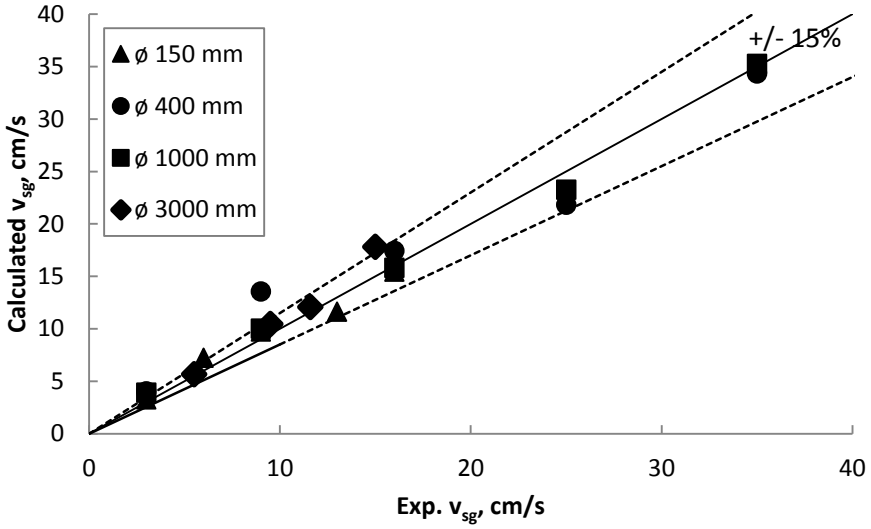

Figure 5.6: Parity diagram on v_{sg} with Cd0 (Tomiyama (1998) plus Swarm factor of Simmonet (2008). Data from the bubble columns (Phi 150 – 400 – 1000- 3000)

Conclusions

Different drag laws have been evaluated in term of ability to simulate the superficial gas velocities operated in the tested bubble columns. Results show that:

- Different laws can be used to model bubbly flows at low gas fraction and involving bubbles of several millimeters, as the law of Tomiyama (1998) but another choice would lead to similar results.
- At high gas fraction (εg>15%) it is necessary to involve a swarm factor that is able to decrease dramatically the drag coefficient compared to single bubble drag. The Simmonet swarm factor is the only identified one that delivers a good agreement between experimental and calculated gas flow rates.

The physical meaning of the adopted swarm factor is not clear and may be investigated in future works. At this step it can be interpreted as an apparent swarm factor that may encompass complex microscale interactions between phases.

The next step consists in the evaluation of the relevance to use the proposed drag law for 3D transient CFD simulations of bubble columns.

5.3 3D CFD Simulations of bubble columns

The objective of this part is to evaluate if the drag law identified by using a very simple (steady-state 1D) model is still appropriate when involved in more realistic CFD simulations wherein hydrodynamics of both phases is simulated and not forced by a profile correlation.

This is done with the help of a commercial CFD software used commonly at IFPEN research center. The objective was also to validate a tool for engineers in order to assist scale-up and design of gas-liquid bubbly reactors. As a consequence, benefits and disadvantages of commercial CFD codes are incurred: it has been possible to perform CFD simulations of bubble columns in a very short time, i.e. several weeks, and to implement successfully the identified drag law, but in the other hand some solving parameters and equations are just chosen by users and have to be used without a total control of them. The global philosophy was also to follow the "rule of thumbs" or state-of-the-art concerning the use of 2-fluid models and to focus on the impact of the drag law modeling. Therefore turbulence modeling is not studied, nor the influence of other forces exerted on the bubbles as lift or added mass.

5.4 CFD implementation

Calculation Domain

CFD simulations are performed using ANSYS Fluent 14.5. The initial studied case is the Phi 400mm column, and other column diameters are then studied by applying homothetic modifications of the established calculation domain and mesh. The column is modeled as a cylinder with an initial height of liquid equal to 4 diameters. In order to ensure that the column can be used with void fraction up to 50%, the total height of the column should be at least twice of the initial height of the liquid; conservatively, it was decided to use a ratio of the total height of the column and the initial height of the liquid amounts to approximately 2.2 (Troshko, 2006). Whereas gas is injected through different

holes at the bottom of the column, the gas sparging device is modeled by a porous surface that generates an homogeneous gas dispersion at the bottom of the column. This simplification is mandatory to keep the computing time coherent with the computing power available at IFPEN, and is very classical in literature (MClure et al., 2015). As experimentally no holes are present below a distance of 1cm from the wall, the gas-inlet zone is modeled as a circular area of diameter 380 mm. The gas volume fraction in the inlet zone is set arbitrary to 0.544. The outlet zone at the top of the column has a backflow volume fraction of gas equal to 1. The Figure 5.7 illustrates the calculation geometry used for CFD simulations.

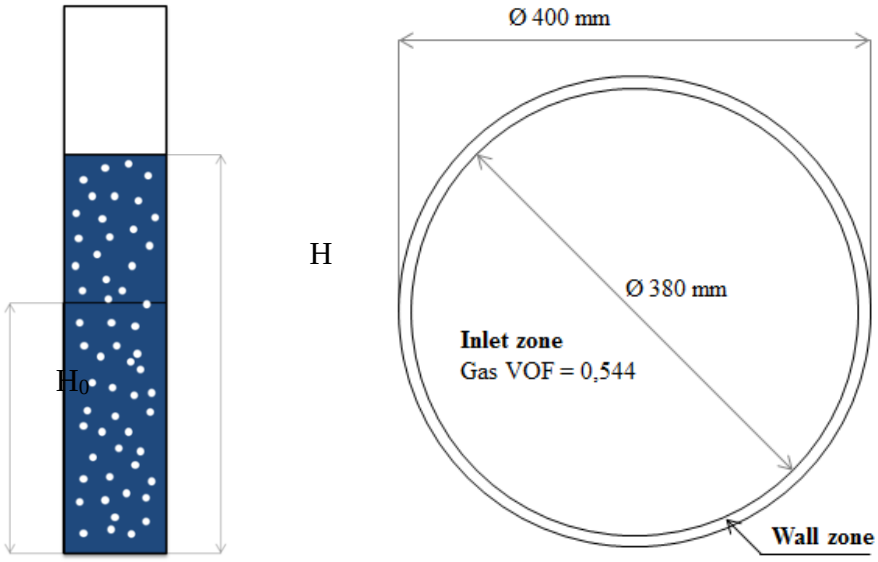

Figure 5.7: ideal axial section and bottom of the column Phi 400 mm

Mesh

The meshes are elaborated with Fluent Gambit 2.4. Using a tetrahedral mesh leads to completely wrong results and the column lost water, i.e. the total amount of water present within the column decreases. Using a homogeneous cooper mesh the results are better. The cooper mesh is a hexahedral mesh where initially an unstructured tetragonal 2D mesh is mapped at the bottom and is extruded along the column. With a cooper mesh of 20 mm for the column Phi 400 mm, the interface between the two phases is not well defined and the results are far from the experimental data. Using a finer cooper mesh of 10 mm (Figure 5.8), the lost amount of water is null and the interphase profile between gas and liquid is

well defined. In all the simulations with the column Phi 400 mm this mesh is used. For the other columns the same number of cells is used, scaling the column Phi 400 mm. The number of cells is approximately 10^6.

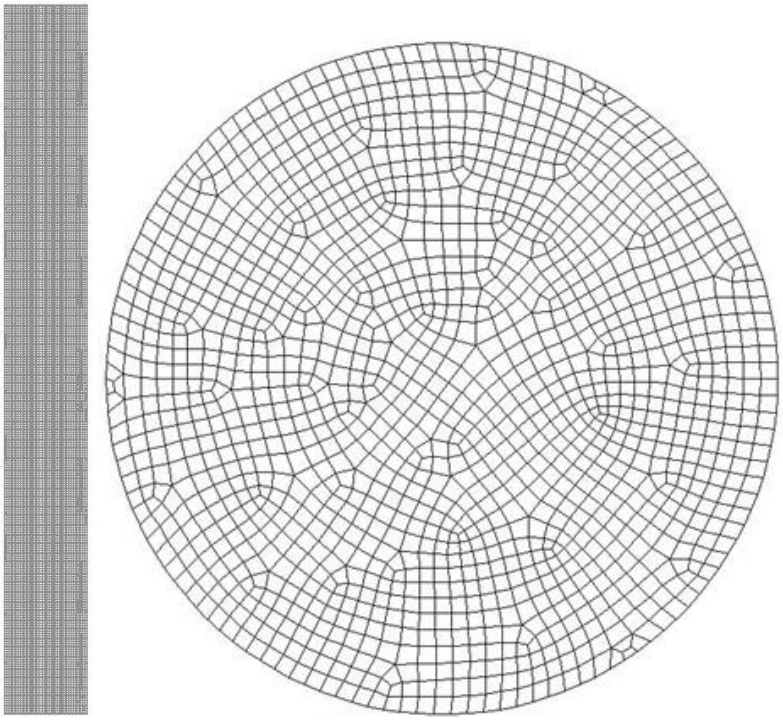

(a) **(b)**

Figure 5.8: Cooper mesh 10 mm, (a) axial and (b) bottom view

Physical modeling and Solver parameters

Studying high gas fraction systems in heterogeneous regime, the simulations must be transient and 3D, since the movements of the bubble is chaotic. Instantaneous properties must be averaged on a sample time. The multiphase Eulerian model is used, with an implicit scheme. The primary phase is liquid water. The secondary and dispersed phase is air, with bubbles having a constant diameter of 6 mm that is the measured mean equivalent diameter under the operating conditions studied. The bubbles of the secondary phase are monodispersed, assuming the same size for all of them. The constant bubble diameter used during simulations is motivated by the fact that using the Tomiyama law for single bubble drag, the effect of bubble diameter appears to have a very small effect on the terminal velocity (see Figure 5.2).

The RNG k-ϵ model is used with the dispersed turbulence model. The RNG k-ϵ model capture better unsteady motions of bubbles caused by the churn turbulent regime. The dispersed turbulence model is suitable since the two phases have a completely different density. Standard wall functions are considered. The lift force is not necessary since it is required only for 2D simulation; in a 3D simulation the effect is really low and it is very more difficult to reach convergence. The virtual mass is not enabled. The QUICK method is used. A courant number of 1 is imposed for simulations. The time step is generally equal to 0.005s.

As the 2 fluid model provide unsteady flows, averaged lengths are calculated by applying averaging processing on a time of simulation of 30s.

5.5 Results

Results in the medium column of Phi 400mm are first discussed. In a second step simulations performed in other columns are presented.

Phi 400 Column

First simulations are performed in the range of v_{sg} [3-25cm/s]. 3 drag laws are compared:

-Schiller & Naumann. This drag law is commonly used to simulate bubbly flows. It is validated for spherical bubbles only.

-Tomiyama (1998). This drag law has been developed to model the drag of deformable bubbles.

-Tomiyama with the Simmonet swarm factor. This drag laws has been previously identified as pertinent to represent the average slip velocity between gas and liquid.

Average gas hold-ups resulting from these 3 series of CFD simulations are reported in Figure 5.9. The Schiller and Naumann drag law provides underestimated gas hold-up at low gas velocity. This is coherent with previous results of Figure 5.4 suggesting also that this drag law generates too high relative velocity. This is linked to the assumption of spherical bubbles that is not verified in our conditions. However, the trend reverses at high gas velocity and CFD simulations overestimated the gas hold-up within the same

drag law. This suggests the necessity to modify the drag law to take into account for the high volume fraction of gas.

Using the Tomiyama drag law leads to similar results but shifted to higher gas fractions. At the lower v_{sg}, the CFD simulation fits well with experiments, but for high v_{sg} the hold-up is always overestimated.

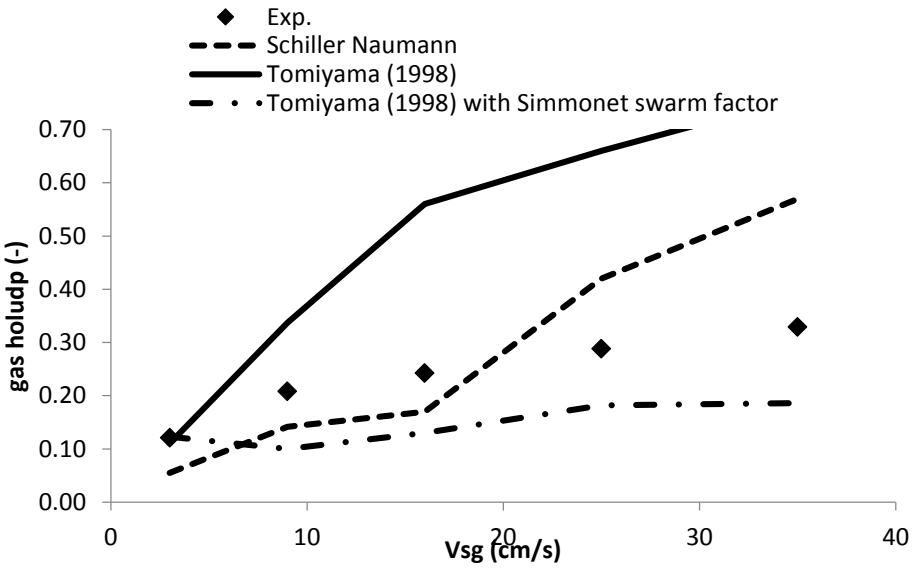

Figure 5.9 - Global gas hold-up comparison in the Phi 400mm column.

The first results provided by the Tomiyama drag law with the Simmonet swarm factor are disappointing except at v_{sg}=3cm/s where the swarm factor plays a negligible role, CFD simulations always underestimate the gas hold-up. This suggests that this drag law provides too high relative velocities.

Fortunately this is easily explained if we take a look at the instantaneous CFD snapshots of gas fraction, as reported in Figure 5.10. We observe that the CFD model generates clusters of bubbles. Big pockets of gas of approximately 20 cm are observed. Close to 100% of gas volume fraction is reached inside the pockets. This is not physical, since coalescence is not simulated and the bubble diameter is a priori imposed by. This behavior is supposed to be linked with the formalism of the drag law, since it has not been observed with other drag laws.

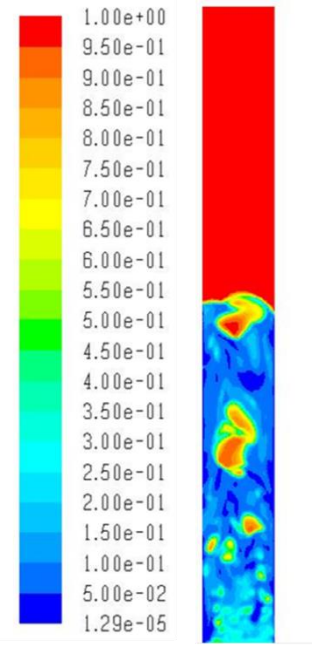

Figure 5.10 - CFD snapshot of gas hold-up at v_{sg}=16cm/s, with Tomiyama drag law with the Simmonet swarm (before correction).

The Simmonet swarm factor tends to zero at high gas fraction, which may modify locally the gas velocity and promote the clustering of gas. If we look at the work of Simmonet et al. (2007) we can notice that the swarm factor is described as valid for bubbles from 5 to 10 mm and for local void fractions less than 30%. Above this limit, the swarm factor is extrapolated outside its range of validation. But at high gas flow rate, the local gas fraction can widely exceed this boundary and move the h factor towards zero. During CFD simulation, the use of this swarm factor may lead to very high gas velocity at high gas fraction.

It is proposed to correct the swarm factor in order to avoid this problem. A simple possibility consists to apply a threshold on the swarm factor in order to limit the decrease of the drag coefficient above a given value of h, as illustrated in Figure 5.11. This modification is empirical and is not based on physical considerations other than the necessity to maintain the drag coefficient at a minimal value. After several tries, it is proposed to retain the value of h_{min} = 0.08 which give satisfactory results. In the same figure is illustrated a snapshot of gas fraction, and gas pockets have disappeared.

As the threshold is applied at high gas fraction (>38%), it has no effect on the average gas flow rate calculation involved in the first part of the chapter. Resulting calculations are identical to those presented in Figure 5.6 (parity diagram on v_{sg}) and are thus not reported here.

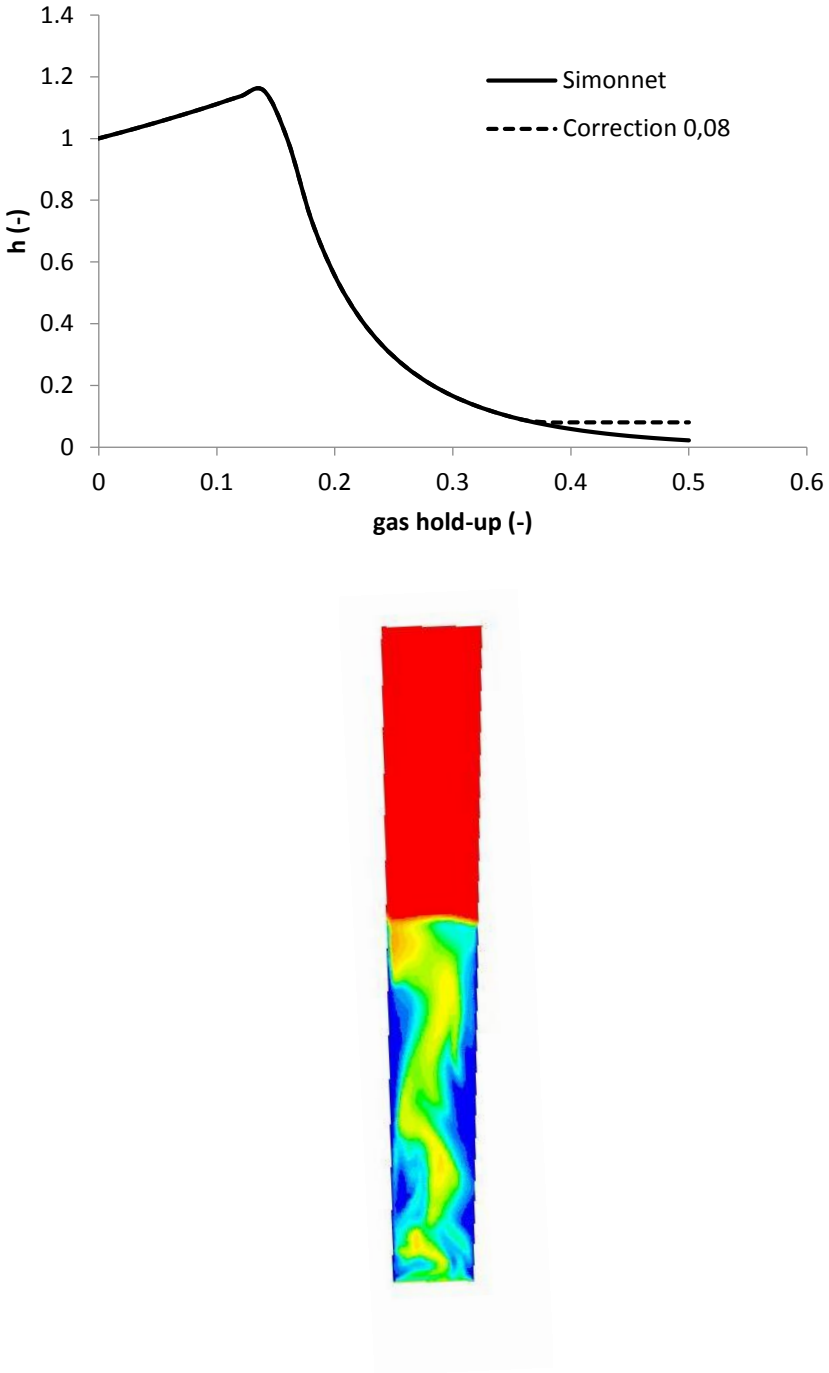

Figure 5.11 - Modification of the Simmonet swarm factor with h_{min}=0.08, and snapshot of CFD simulations at v_{sg}=16cm/s.

CFD simulated radial profiles of gas hold-up and liquid velocity are in acceptable agreement with experimental data, as presented in Figure 5.12 and Figure 5.13 (v_{sg} = 16cm/s). The average errors concerning these variables are below 15%. Concerning the

gas hold-up profiles, the largest deviations are observed close to the walls, where measurements are difficult to be performed. The interpolation of experimental data tends smoothly to zero at the wall, but the real hold-up profile may be sharper.

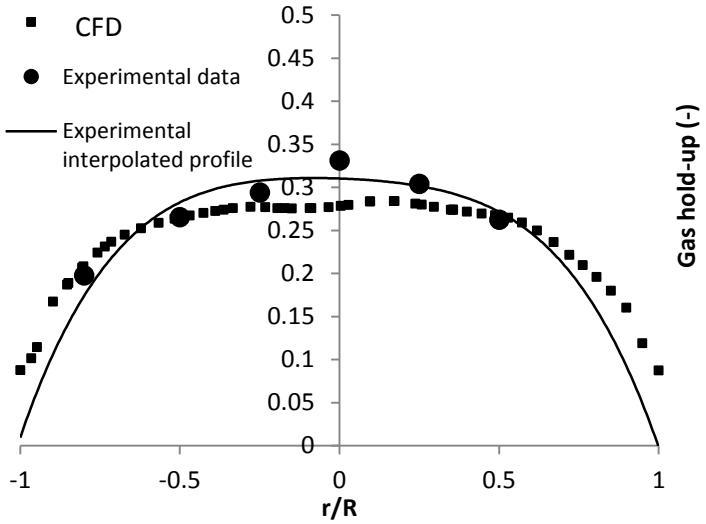

Figure 5.12 : Comparison between experimental hold-up (measurements, interpolated profile) and CFD simulations. Phi 400mm column at v_{sg} = 16cm/s, with the drag law of Tomiyama and the modified Simmonet swarm factor

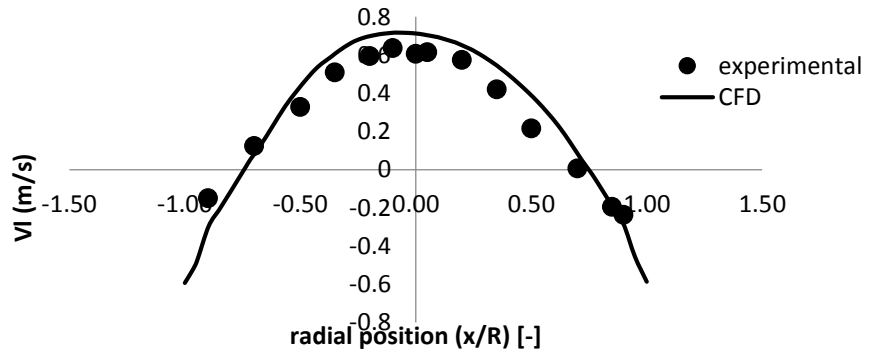

Figure 5.13 : Comparison between experimental liquid velocity profiles and CFD simulations. Phi 400mm column at v_{sg} = 16cm/s, with the drag law of Tomiyama and the modified Simmonet swarm factor.

As good CFD results have been obtained at v_{sg}=16cm/s, the gas velocity is extended to other values in the global range of measurement. The CFD and experimental gas hold-ups are compared in Figure 5.14. A good agreement is found for any gas inlet conditions.

The comparison of the simulated and experimental liquid axial velocities is also satisfactory, excepted at low v_{sg} (< 8cm/s) where the axial velocity is underestimated by CFD (Figure 5.15). These results validate also the turbulent viscosity model (RNG-K-ε) because big bias on this length may lead to deviations on the liquid velocity gradients. Deviations at low gas velocity may also be explained by the turbulent viscosity model, because it is poorly suitable when the flow is not fully turbulent.

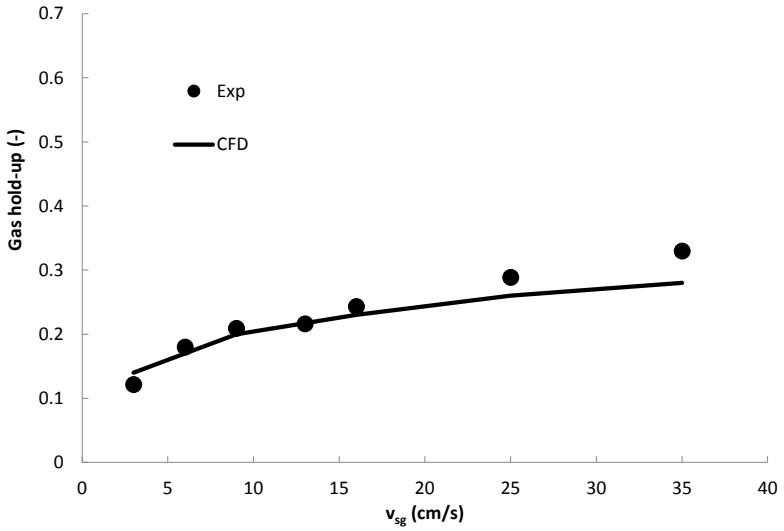

Figure 5.14 : Comparison between experimental global hold-up and CFD simulations (continuous line), with the drag law of Tomiyama and the modified Simmonet swarm factor, Phi 400 column in the range of v_{sg} [3-35 cm/s].

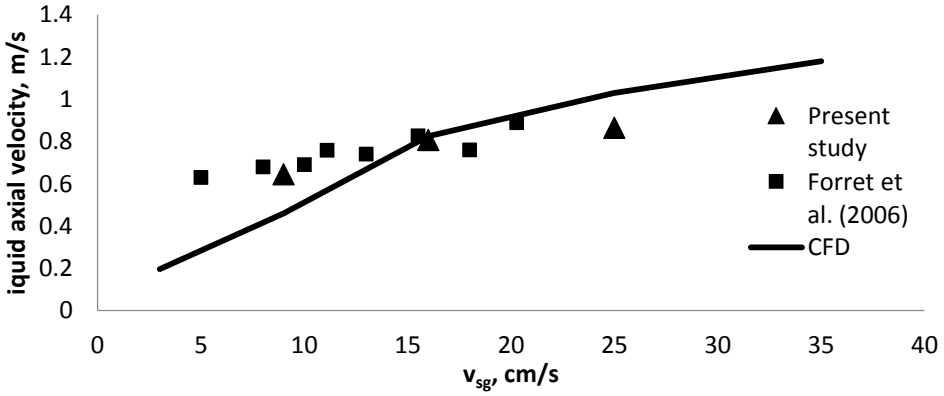

Figure 5.15 : Comparison between experimental liquid axial velocity and CFD simulations (with the drag law of Tomiyama and the modified Simmonet swarm factor, Phi 400 column in the range of v_{sg} [3-35 cm/s].

The comparison between experiments and CFD simulations in the medium column Phi 400mm are very satisfactory when using the identified drag law (Tomiyama plus

modified swarm factor of Simonnet), they are now extended to other bubble columns investigated during the study.

Scale-up considerations

Similar CFD simulations are performed now in the Phi 150, Phi 1000 and Phi 3000mm columns. Results are compared with the experimental data of the present study and with the experimental data of Forret et al. (2003) when available. Gas hold-up and axial liquid velocities are discussed separately.

The Figure 5.16 reports the CFD results concerning the global gas fraction, and compares them to experimental measurements, the latter being supposed to be equal in the different columns (as presented in Figure 4.9). Results show that the agreement between CFD and experiments increases with the column diameter. The gas hold-up is underestimated in the smaller column, but it is well predicted at higher scales. A parity diagram is reported in Figure 5.17. It shows that except for the smallest column, experimental hold-ups are fairly well simulated at any v_{sg}, the error being less than 15%.

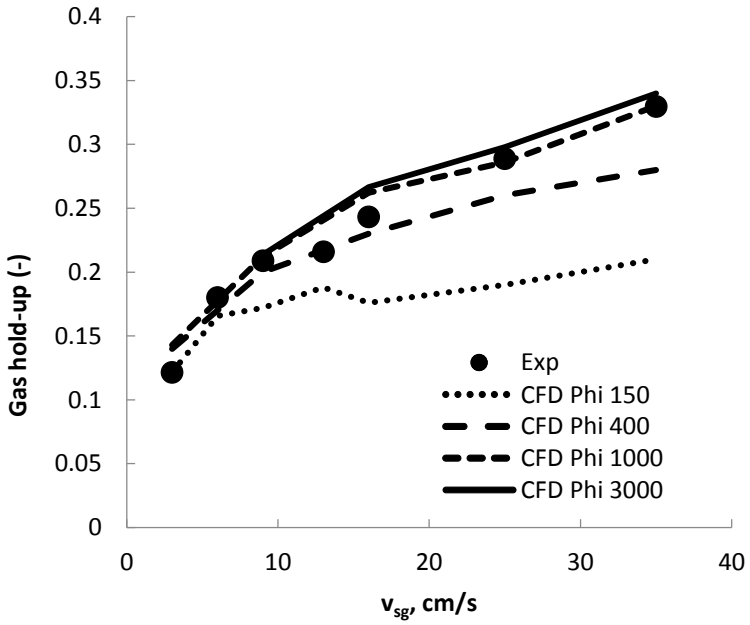

Figure 5.16 : Comparison between experimental hold-up and CFD simulations (lines) with the drag law of Tomiyama and the modified Simmonet swarm factor, Phi 150-400-1000-3000 columns in the range of v_{sg} [3-35 cm/s].

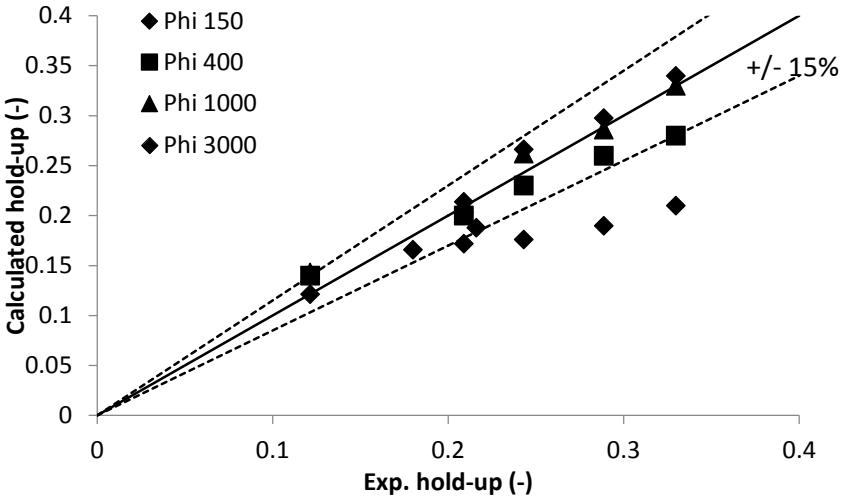

Figure 5.17 : Parity diagram of the comparison between experimental hold-up and CFD simulations, with the drag law of Tomiyama and the modified Simmonet swarm factor, Phi 150-400-1000-3000 columns in the range of v_{sg} [3-35 cm/s].

Besides the gas hold-up, the liquid velocity is another important variable that CFD has to predict quantitatively. As good radial velocity profiles have been calculated in the column 400mm, only liquid axial velocity at the center of the column are presented here. Figure 5.18, Figure 5.19 and Figure 5.20 report the comparison between experimental and calculated axial velocity at Phi 150, Phi 1000 and Phi 3000mm, in the range of v_{sg} [5-35cm/s], and the Figure 5.21 presents the parity diagram of the liquid velocity profiles for every columns. At Phi 150mm, CFD slightly underestimates the axial liquid velocity for a gas velocity above 5 cm/s, but simulations at higher scales are in good agreement with experiments. The mean difference between CFD and experiments at any scale is below 15%.

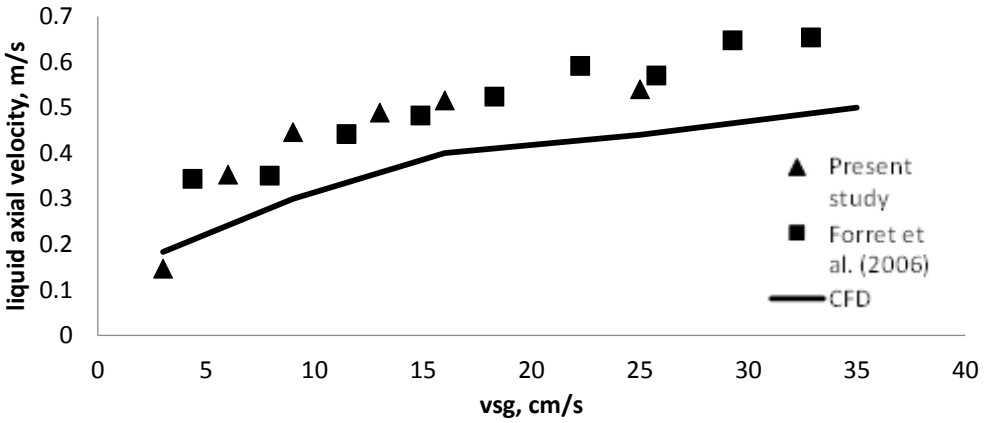

Figure 5.18 : Comparison between experimental liquid axial velocity on the column axis and CFD simulations, with the drag law of Tomiyama and the modified Simmonet swarm factor, Phi 150 column in the range of v_{sg} [3-35 cm/s].

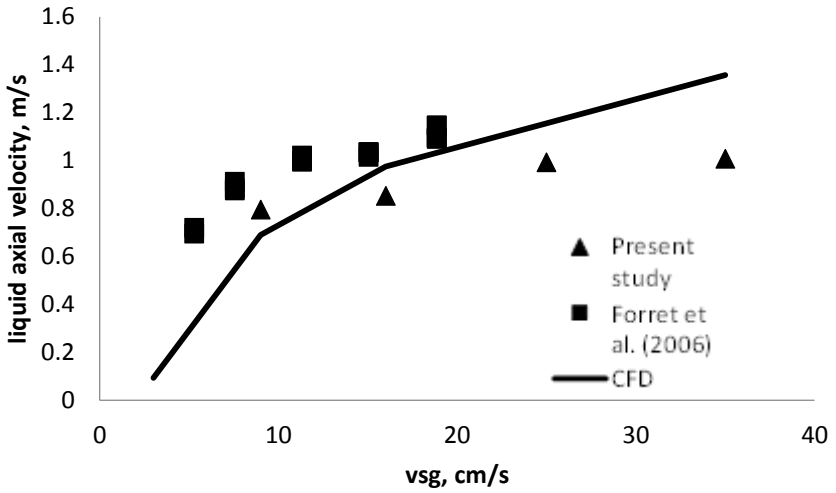

Figure 5.19 : Comparison between experimental liquid axial velocity on the column axis and CFD simulations, with the drag law of Tomiyama and the modified Simmonet swarm factor, Phi 1000 column in the range of v_{sg} [3-35 cm/s].

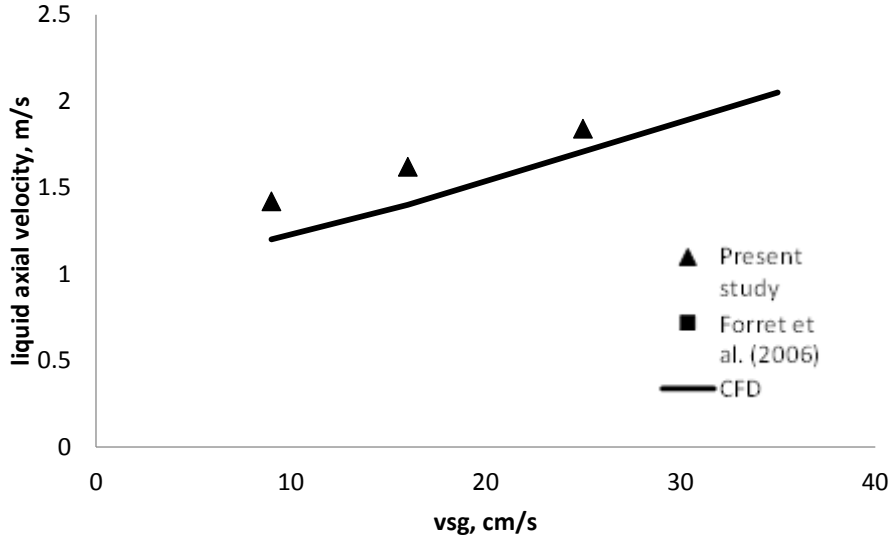

Figure 5.20 : Comparison between experimental liquid axial velocity on the column axis and CFD simulations, with the drag law of Tomiyama and the modified Simmonet swarm factor, Phi 3000 column in the range of v_{sg} [3-35 cm/s].

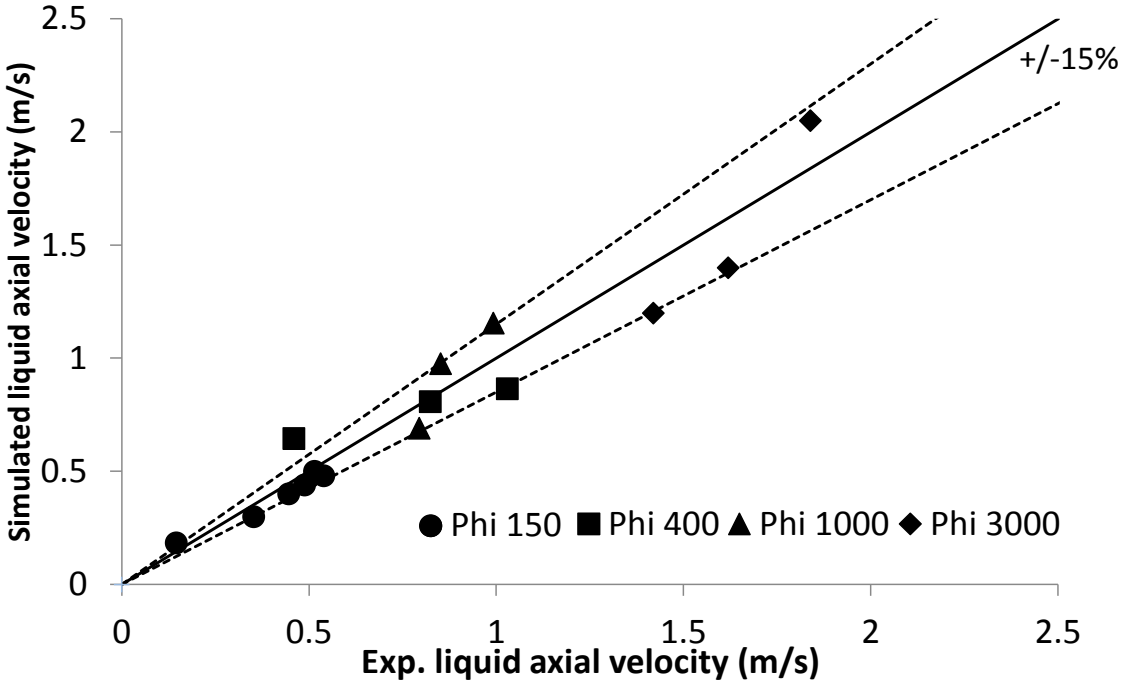

Figure 5.21 : Parity diagram of the comparison between experimental axial velocity on the column axis and CFD simulations, with the drag law of Tomiyama and the modified Simmonet swarm factor, Phi 150-400-1000-3000 columns in the range of v_{sg} [3-35 cm/s].

5.6 Conclusions

The objective of this chapter was to use the experimental bubble diameter measurements to compare the relevance of different drag law formulations. In a first step, gas flow rates generated by different drag laws are calculated and compared to experiments. This calculation is based on the prior knowledge of average liquid velocity, gas hold-up and bubble diameter profiles. At this step, it has been observed that:

- Different single bubble drag laws may be good candidates to simulate dilute flows, and the law of Tomiyama (1998) has been chosen for the following of the study
- It is necessary to account for a swarm factor to represent the drag law at high gas hold-up. The Simmonet (2007) swarm factor has been identified as very relevant with our data.

In a second step, 3D CFD Unsteady RANS simulations have been performed with a commercial software to validate or not the choice of drag law. CFD simulations have been performed in a wide range of column scales and gas flow rates. Comparisons between CFD and experiments show that:

- The swarm factor of Simmonet is not appropriate to simulate bubbly flows at gas fraction above ~40%, because it induces the formation of non-physical gas pockets during simulations.

- We propose to modify the Simmonet swarm factor by applying a threshold h_{min} equal to 0.08 in order to cap the relative velocity during simulations.

- The Tomyiama drag law associated to the modified Simmonet swarm factor appears as a very robust empirical drag law, able to simulate the major part of present data with a very good agreement. The error on the gas hold-up and liquid axial velocity is below 15%.

As this CFD study was conducted on a relatively short time, a perspective of this work would be to study more in detail the effect of the choice of the turbulence model (not studied here). Another important point would be to evaluate the effect of the bubble size on the CFD simulations, because it has not been considered here (as the Tomiyama drag

coefficient is quite insensitive to the bubble diameter in the range [5-8mm]). Slight hold-up modifications may be possible.

Finally, the identified drag law formulation being empirical, it would be very interesting to investigate the drag inside dense bubbly flows, by means of DNS simulations or local fluid measurements, if possible. This may help to understand why the drag coefficient decreases in heterogeneous regime.

Conclusions

Bubble column reactors are widely used in chemical industry to provide large interfacial areas, strong liquid agitation and efficient thermal exchanges. Yet, the complex hydrodynamics of gravity driven bubbly flows, together with the lack of adapted correlations imposes that the scale-up procedures for bubble columns is still a very "empirical" and somewhat uncertain process. CFD simulations could be a possible alternative: for an industrial-like bubble column, involving large column dimensions and high void fractions, the most common approach is based on Eulerian two-phase models. However, these models require closing laws for quantities such as the Reynolds stress sensor or the interphase momentum exchanges, which are not fully established. Consequently, to solve the up-scaling problems, the usual practice is either to recur to semi-empirical correlations validated over a limited range of parameters, and/or to fit some parameters such as the bubble size in order to obtain realistic (but may poorly correct) solutions in simulations.

In that context, the objective of this work was to construct and analyze a database of local hydrodynamics properties that could help improving our understanding of bubbly flows dynamics, that could contribute to identify the relevant scale-up laws, and also that would help developing more adapted closures.

Accordingly, experiments have been undertaken over extended ranges in terms of column diameter (from 0.15 m up to 3 m) and of superficial gas velocities (from 3cm/s to 35 cm/s). In addition, to access the intrinsic dynamics of these systems, very significant efforts have been dedicated to the control of flow conditions. A specific attention has been paid to ensure a fairly constant mean bubble size as well as spatially homogeneous injection over the whole set of flow conditions considered. Quantitatively, the bubble eccentricity remained constant (0.7) in all experimental conditions. The vertical Sauter mean diameter Dh_{32} on the column axis varied between 6 mm and 9 mm, while the radial size segregation amounted to 2-3 mm, except in the Phi 3000 column, where it reaches 5 mm (it has not been possible to change the injector in that column). Even though all experiments were using air and water, coalescence, which is often invoked as the origin of incorrect predictions from averaged models, proves negligible in all conditions, except perhaps in the Phi 3000 column where it was not thoroughly tested.

A battery of measuring techniques has been implement to access various local quantities: void fraction as well as bubble size and axial velocity distributions from conical optical probes, bubble horizontal and vertical diameters from an endoscopic imaging technique, axial and radial liquid velocities from Pavlov tubes. In these drastic flow conditions involving flow reversal and unsteady 3D structures, the conical probe was surprisingly efficient for void fraction and for mean size measurements, while the bubble velocity happened to be strongly underestimated. To measure the bubble horizontal diameter (Dh_{32}), a new method based on the cross-correlation of the signals delivered by closely separated optical probes has been proposed: it proves to be well adapted even in the challenging conditions encountered in bubble columns at large gas fraction. That method also provides an interesting extension of the measurement capabilities of optical probes.

With these sensors, a number of experimental results have been gathered at different heights along the columns. The main outcomes are the following. First, the existence of a quasi fully-established flow region previously identified in the literature was confirmed here in all conditions except in the Phi 3000 where it was not tested: that zone extends at least from h/D= 2.5 to h/D=3.75. Within that region for all columns and for vsg>9 cm/s, the local gas hold-up profiles normalized by the void fraction on the axis happen to be reasonably well fitted by the empirical correlation of Schweitzer et al. (2001) given by Eq.(1.1). Similarly, the liquid velocity profiles scaled by the velocity on the axis are quite close to the empirical fit proposed by Forret et al. (2003) given by Eq.(4.2). Hence, these two proposals have been proved valid over an extended range of column diameters. These results indicate that, when in the heterogeneous regime, the flow are self-similar whatever the column size and the superficial gas velocity. Hence, the sensitivity to these two parameters of the void fraction as well as liquid and gas mean velocities estimated on the symmetry axis has been investigated: clear and consistent trends have been identified. These results brought clarification among the diverse correlations proposed in the literature. Owing to the observed self-similarity, the analysis was then focused on the upward directed inner zone, defined between -0.7R and 0.7R. The upward directed liquid flow rate (Q_l^{up}) in that inner zone was shown to growth as $Q_l^{up} \approx D^2\sqrt{gD}$, indicating that the entrainment capability in our bubble columns of is set by the column diameter only and - surprisingly- not by the gas superficial velocity. Yet, the upward directed gas flow rate increases with D but also with the injected gas

flow rate, as expected. There is thus some global flow organization that forces the solution such that the mean flow reversal occurs at an “universal” radial position 0.7R, and that sets an upward liquid flow rate controlled by the column diameter only: the adjustment is then supported by the change in the gas hold-up. Even though no simple model was proposed to predict this behavior, the above information are believed to be of practical interest for the up-scaling of bubble columns.

Pursuing on the analysis of the core region, the mean relative velocity of the gas phase was deduced from a kinematic approach: as the void fraction increases, the mean relative velocity becomes up to several times higher than the terminal velocity of a single bubble in stagnant liquid. This result was tentatively linked with the existence of concentration gradients, and pieces of experimental evidence were provided in support to that. In addition, phasic velocity fluctuations were also found significant, with a typical turbulent intensity in the liquid close to 25-30% on the column axis. These fluctuations seem to be closely related with the observed mean relative velocity, both in terms of their evolution with the control parameters and in terms of magnitude. Besides, a few measurements indicate that the fluctuations in the bubble velocity are also well correlated with local changes in density. All together, we gather some evidence that convective type instabilities do arise in bubble columns in the heterogeneous regime, that they lead to strong concentration fluctuation at a scale comprised between a few and a few tens of bubble sizes. An analogy with the convective instabilities observed in sedimentation could be pursued provided that information is made available on the magnitude of density gradients with respect to flow conditions. Another open question is how to connect these meso-scale structures with the increase in the mean relative velocity of bubbles: similar questions have been notably addressed in turbulent flows laden with dense particles but the mechanisms are not directly transposable to bubble columns.

Finally, and in order to account for the observed relative velocities, we have proposed to introduce a swarm factor in order to correct the drag law: the proposed factor forces a drastic drag reduction for void fractions above about 15%. A preliminary sensitive study of the modified drag law was performed in 3D URANS simulations: the results are quite encouraging even though it is an indirect way to represent complex underlying mechanisms. This proposal has to be more thoroughly tested in particular in relation with the modeling of turbulence: it provides already useful hints for the simulation of bubble columns.

Various perspectives can be drawn from this work. First, many data remain to be analyzed concerning notably the density fluctuation and their associated time and space characteristics. In addition, conditional statistics would be quite useful to understand the connection between the structures and the mean flow behavior. Extra experiments could be also envisioned to specifically address this question.

On the measuring techniques, using differential pressure sensors with better resolutions and bandwidths for the Pavlov tube would be quite useful to characterize the liquid velocity statistics. It will also be useful to use alternate techniques such as ultrasounds or tomography. One of the weakest aspect is indisputably the poor reliability of local gas velocity measurements.

On modeling, the construction of a dedicated 1D model may provide some clues on the origin of the observed scaling for the entrained liquid flow rate. For simulations, the acquired database deserves to be exploited further including in the framework of EDQNM approaches.

References

Akita, K., & Yoshida, F. (1974). Bubble size, interfacial area, and liquid-phase mass transfer coefficient in bubble columns. *Industrial & Engineering Chemistry Process Design and Development*, *13*(1), 84-91.

Al-Masry, W. A., Ali, E. M., & Aqeel, Y. M. (2005). Determination of bubble characteristics in bubble columns using statistical analysis of acoustic sound measurements. *Chemical Engineering Research and Design*, *83*(10), 1196-1207.

Andreotti, M. (2009). *Ecoulements à bulles : micro-structuration et agitation induite à mombre de Reynolds particulaire modérè* (Doctoral dissertation, University of Grenoble).

Barrau, E., Rivière, N., Poupot, C., & Cartellier, A. (1999). Single and double optical probes in air-water two-phase flows: real time signal processing and sensor performance. *International journal of multiphase flow*, *25*(2), 229-256.

Biesheuvel A. & Van Wijngaarden L., Two-phase flow equations for a dilute dispersion of gas bubbles in liquid, J. Fluid Mech. 148, 301- 318 (1984).

Brahem, R. (2013). Étude de l'effet d'échelle sur les plateaux à clapets de colonnes d'absorption (Doctoral dissertation).

Brenner M.P., Screening mechanisms in sedimentation, Phys Fluids 11 (4) 754-772 (1999).

Cartellier A. & Rivière R., Bubble-induced agitation and microstructure in uniform bubbly flows at small to moderate particle Reynolds numbers. Phys. Fluids 13, 2165 (2001).

Cartellier A., Andreotti M. and Sechet Ph., Induced agitation in homogeneous bubbly flows at moderate particle Reynolds number, Phys. Rev. E. 80, 065301(R) (2009) DOI: 10.1103/PhysRevE.80.065301

Cartellier, A. (1990). Optical probes for local void fraction measurements: characterization of performance. *Review of Scientific Instruments*, *61*(2), 874-886.

Cartellier, A. (1992). Simultaneous void fraction measurement, bubble velocity, and size estimate using a single optical probe in gas–liquid two-phase flows. *Review of Scientific Instruments*, *63*(11), 5442-5453.

Cartellier, A. (1998 C). Measurement of gas phase characteristics using new monofiber optical probes and real-time signal processing. *Nuclear engineering and design*, *184*(2), 393-408.

Cartellier, A. (2001). Optical probes for multiphase flow characterization: Some recent improvements. *Chemical engineering & technology*, *24*(5), 535-538.

Cartellier, A. (2006). Optical probes for multiphase flows. *Encylopedia of Sensors*, vol-7.

Cartellier, A., & Barrau, E. (1998 A). Monofiber optical probes for gas detection and gas velocity measurements: conical probes. *International journal of multiphase flow*, *24*(8), 1265-1294.

Cartellier, A., & Barrau, E. (1998 B). Monofiber optical probes for gas detection and gas velocity measurements: optimised sensing tips. *International journal of multiphase flow*, *24*(8), 1295-1315.

Cartellier, A., Andreotti, M., & Sechet, P. (2009). Induced agitation in homogeneous bubbly flows at moderate particle Reynolds number. Physical review E, 80(6), 065301.

Chaouki, J., Larachi, F., & Dudukovic, M. P. (1997). Noninvasive tomographic and velocimetric monitoring of multiphase flows. *Industrial & engineering chemistry research*, *36*(11), 4476-4503.

Chaumat, H., Billet, A. M., & Delmas, H. (2007 A). Hydrodynamics and mass transfer in bubble column: Influence of liquid phase surface tension. *Chemical Engineering Science*, *62*(24), 7378-7390.

Chaumat, H., Billet-Duquenne, A. M., Augier, F., Mathieu, C., & Delmas, H. (2005). Mass transfer in bubble column for industrial conditions—effects of organic medium, gas and liquid flow rates and column design. *Chemical engineering science*, *60*(22), 5930-5936.

Chaumat, H., Billet-Duquenne, A. M., Augier, F., Mathieu, C., & Delmas, H. (2007 B). On the reliability of an optical fibre probe in bubble column under industrial relevant operating conditions. *Experimental thermal and fluid science*, *31*(6), 495-504.

Chaumat, H., Billet-Duquenne, A. M., Augier, F., Mathieu, C., & Delmas, H. (2005). Application of the double optic probe technique to distorted tumbling bubbles in aqueous or organic liquid. *Chemical engineering science*, *60*(22), 6134-6145.

Chaumat, Hélene, Anne-Marie Billet, and Henri Delmas. "Axial and radial investigation of hydrodynamics in a bubble column; influence of fluids flow rates and sparger type." *International Journal of Chemical Reactor Engineering*4.1 (2006).

Clark, N. N., & Turton, R. (1988). Chord length distributions related to bubble size distributions in multiphase flows. *International Journal of Multiphase Flow*, *14*(4), 413-424.

Clift, R., Grace, J. R., & Weber, M. E. (1978). *Bubbles, drops, and particles*. Courier Corporation.

Colombet, D. (2012) *Modélisation de réacteurs Gaz-Liquide de type colonne à bulles en conditions industrielles* (Doctoral dissertation, Toulouse, INSA).

Colombet, D., Legendre, D., Cockx, A., Guiraud, P., Risso, F., Daniel, C., & Galinat, S. (2011). Experimental study of mass transfer in a dense bubble swarm. *Chemical engineering science*, *66*(14), 3432-3440.

Colombet, D., Legendre, D., Risso, F., Cockx, A., & Guiraud, P. (2015). Dynamics and mass transfer of rising bubbles in a homogenous swarm at large gas volume fraction. *Journal of Fluid Mechanics*, *763*, 254-285.

De Swart, J. W. A., Van Vliet, R. E., & Krishna, R., & Van Baten, J. M. (2001). Scaling up bubble column reactors with the aid of CFD. *Chemical Engineering Research and Design*, *79*(3), 283-309.

De Swart, J. W. A., Van Vliet, R. E., & Krishna,, R. (1996). Size, structure and dynamics of "large" bubbles in a two-dimensional slurry bubble column. *Chemical Engineering Science*, *51*(20), 4619-4629.

Deckwer, W. D. (1992). *Bubble column reactors* (Vol. 200). R. W. Field (Ed.). New York: Wiley.

Degaleesan, S., Dudukovic, M., & Pan, Y. (2001). Experimental study of gas-induced liquid-flow structures in bubble columns. *AIChE journal*, *47*(9), 1913-1931.

Devanathan, N., Moslemian, D., & Dudukovic, M. P. (1990). Flow mapping in bubble columns using CARPT. *Chemical Engineering Science*, *45*(8), 2285-2291.

Ekambara, K., Dhotre, M. T., & Joshi, J. B. (2005). CFD simulations of bubble column reactors: 1D, 2D and 3D approach. Chemical engineering science, 60(23), 6733-6746.

Fan, J. M., & Cui, Z. (2005). Effect of acoustic standing wave in a bubble column. *Industrial & engineering chemistry research*, *44*(17), 7010-7018.

Ferreira, A., Pereira, G., Teixeira, J. A., & Rocha, F. (2012). Statistical tool combined with image analysis to characterize hydrodynamics and mass transfer in a bubble column. *Chemical engineering journal*, *180*, 216-228

Forret, A. (2003) Hydrodynamics scale-up of slurry bubble columns (Doctoral dissertation, Lyon, Université Claude Bernard)

Forret, A., Schweitzer, J. M., Gauthier, T., Krishna, R., & Schweich, D. (2003 A). Liquid dispersion in large diameter bubble columns, with and without internals.*The Canadian Journal of Chemical Engineering*, *81*(3-4), 360-366.

Forret, A., Schweitzer, J. M., Gauthier, T., Krishna, R., & Schweich, D. (2003 B). Influence of scale on the hydrodynamics of bubble column reactors: an experimental study in columns of 0.1, 0.4 and 1m diameters. *Chemical engineering science*, *58*(3), 719-724.

Forret, A., Schweitzer, J. M., Gauthier, T., Krishna, R., & Schweich, D. (2006). Scale up of slurry bubble reactors. *Oil & Gas Science and Technology-Revue de l'IFP*, *61*(3), 443-458.

Fransolet, E., Crine, M., L'Homme, G., Toye, D., & Marchot, P. (2001). Analysis of electrical resistance tomography measurements obtained on a bubble column. *Measurement Science and Technology*, *12*(8), 1055

Fransolet, E., Crine, M., Marchot, P., & Toye, D. (2005). Analysis of gas holdup in bubble columns with non-Newtonian fluid using electrical resistance tomography and dynamic gas disengagement technique. *Chemical Engineering Science*, *60*(22), 6118-6123.

Garnier C., Lance M. and Marie J.L (2002A)., Measurement of local flow characteristics in buoyancy-driven bubbly flow at high void fraction, Exp. Thermal & Fluid Sc., 26 (6-7) 811-815

Garnier C., Lance M., Marie J.L. (2002B) Measurement of local flow characteristics in buoyancy-driven bubbly flow at high void fraction," *Exp.Therm. Fluid Sci*. 26, 811.

Guet, S. & Ooms, G. (2006) Fluid Mechanical aspects of the gas-lift technique. *Annual Review of Fluid Mechanics* 38, 225-249

Guet, S., Fortunati, R. V., Mudde, R. F., & Ooms, G. (2003). Bubble Velocity and Size Measurement with a Four-Point Optical Fiber Probe. *Particle & Particle Systems Characterization*, *20*(3), 219-230.

Guillaume Riboux, Dominique Legendre and Frédéric Risso A model of bubble-induced turbulence based on large-scale wake interactions, J. Fluid Mech. (2013), vol. 719, pp. 362387.

Hey, M. J., & Kippax, P. G. (2005). Surface tensions of mixed aqueous solutions of tert-butanol and n-pentanol. *Colloids and Surfaces A: Physicochemical and Engineering Aspects*, *262*(1), 198-203.

Hubers, J. L., Striegel, A. C., Heindel, T. J., Gray, J. N., & Jensen, T. C. (2005). X-ray computed tomography in large bubble columns. *Chemical Engineering Science*, *60*(22), 6124-6133

Hunt J.C.R., Eames, I., The disappearance of laminar and turbulent wakes in complex flows, J. Fluid Mech. 457, 111-132 (2002).

Jakobsen, H.A., Lindborg, H. Dorao, C.A., 2005. Modeling of bubble column reactors: Progress and limitations, Industrial Engineering Chemistry Research 44, 5107-5151.

Jin, H., Wang, M., & Williams, R. A. (2007). Analysis of bubble behaviors in bubble columns using electrical resistance tomography. *Chemical Engineering Journal*, *130*(2), 179-185.

Kamp, A., Colin, C., Fabre, J., 1995. Techniques de mesure par sondeoptique double en ecoulement diphasique a bulles. Colloque de Mecanique des Fluides Experimentale, Cert Onera, Toulouse, France

Kantarci, N., Borak, F., & Ulgen, K. O. (2005). Bubble column reactors. Process Biochemistry, 40(7), 2263-2283

Kataoka, I., Ishii, M., & Serizawa, A. (1986). Local formulation and measurements of interfacial area concentration in two-phase flow. *International Journal of Multiphase Flow*, *12*(4), 505-529.

Kazakis, N. A., Mouza, A. A., & Paras, S. V. (2006). Bubble size distribution at the entrance of bubble column with pore sparger. In *Proceedings of the 17th International Congress of Chemical and Process Engineering (CHISA), Prague, Czech Republic* (pp. 1-17).

Krishna, R., & Van Baten, J. M. (2001). Scaling up bubble column reactors with the aid of CFD. Chemical Engineering Research and Design, 79(3), 283-309.

Krishna, R., Van Baten, J. M., Urseanu, M. I., & Ellenberger, J. (2001). Design and scale up of a bubble column slurry reactor for Fischer–Tropsch synthesis.*Chemical Engineering Science*, *56*(2), 537-545.

Kuncová, G., & Zahradnik, J. (1995). Gas holdup and bubble frequency in a bubble column reactor containing viscous saccharose solutions. *Chemical Engineering and Processing: Process Intensification*, *34*(1), 25-34.

Laborde-Boutet, C., Larachi, F., Dromard, N., Delsart, O., Schweich, D., 2009. CFD simulation of bubble column flows: Investigations on turbulence models in RANS approach. Chemical Engineering Science 64, 4399-4413.

Lage, P. L. C., & Espósito, R. O. (1999). Experimental determination of bubble size distributions in bubble columns: prediction of mean bubble diameter and gas hold up. *Powder technology*, *101*(2), 142-150.

Lance M. & Bataille J., Turbulence in the liquid phase of a uniform bubbly air-water flow. J. Fluid Mech., 222, 95-118 (1991).

Lau, R., Cui, Z., & Fan, L. S. (2005). Liquid entrainment in high-pressure bubble columns. *Industrial & engineering chemistry research*, *44*(10), 3776-3782.

Lim, K. S., & Agarwal, P. K. (1992). Bubble velocity in fluidized beds: the effect of non-vertical bubble rise on its measurement using submersible probes and its relationship with bubble size. *Powder Technology*, *69*(3), 239-248.

Lindken, R., & Merzkirch, W. (2002). A novel PIV technique for measurements in multiphase flows and its application to two-phase bubbly flows. *Experiments in fluids*, *33*(6), 814-825

Liu, W., & Clark, N. N. (1995). Relationships between distributions of chord lengths and distributions of bubble sizes including their statistical parameters. *International Journal of Multiphase Flow*, *21*(6), 1073-1089.

Liu, W., Clark, N. N., & Karamavruç, A. I. (1998). Relationship between bubble size distributions and chord-length distribution in heterogeneously bubbling systems. *Chemical Engineering Science*, *53*(6), 1267-1276.

Liu, Z., Zheng, Y., Jia, L., & Zhang, Q. (2005). Study of bubble induced flow structure using PIV. *Chemical Engineering Science*, *60*(13), 3537-3552

Maaß, S., Wollny, S., Voigt, A., & Kraume, M. (2011). Experimental comparison of measurement techniques for drop size distributions in liquid/liquid dispersions. *Experiments in Fluids*, *50*(2), 259-269.

Marchisio, D. L., & Fox, R. O. (2013). Computational models for polydisperse particulate and multiphase systems. Cambridge University Press

McClure DD., Norris H., Kavanagh JM, Fletcher DF., Barton GW (2014) Validation of a Computationally Efficient Computational Fluid Dynamics (CFD) Model for Industrial Bubble Column Bioreactors. *Industrial & Engineering Chemistry Research*, 53-37 14526-14543

McClure, D. D., Kavanagh, J. M., Fletcher, D. F., & Barton, G. W. (2013). Development of a CFD Model of Bubble Column Bioreactors: Part One–A Detailed Experimental Study. Chemical Engineering & Technology, 36(12), 2065-2070.

McClure, D. D., Norris, H., Kavanagh, J. M., Fletcher, D. F., & Barton, G. W. (2015). Towards a CFD model of bubble columns containing significant surfactant levels. Chemical Engineering Science, 127, 189-201.

Menzel, T., In der Weide, T., Staudacher, O., Wein, O., & Onken, U. (1990). Reynolds shear stress for modeling of bubble column reactors. *Industrial & engineering chemistry research*, *29*(6), 988-994.

Miyauchi, T., & Shyu, C. N. (1970). Flow of fluid in gas bubble columns. *Kagaku Kogaku*, *34*(958), 661-667.

Mizushima, Y., & Saito, T. (2012). Detection method of a position pierced by a single-tip optical fibre probe in bubble measurement. *Measurement Science and Technology*, *23*(8), 085308.

Mizushima, Y., Sakamoto, A., & Saito, T. (2013). Measurement technique of bubble velocity and diameter in a bubble column via single-tip optical-fiber probing with judgment of the pierced position and angle. *Chemical Engineering Science*, *100*, 98-104.

Mouza, A. A., Dalakoglou, G. K., & Paras, S. V. (2005). Effect of liquid properties on the performance of bubble column reactors with fine pore spargers. Chemical Engineering Science, 60(5), 1465-1475.

Mudde, R. F., Groen, J. S., & Van Den Akker, H. E. A. (1997). Liquid velocity field in a bubble column: LDA experiments. *Chemical Engineering Science*, *52*(21), 4217-4224.

Mudde, R.F. (2005) Gravity-driven bubbly flows. *Annual Review of Fluid Mechanics* 37, 393-423

Pinelli, D., Liu, Z., & Magelli, F. (2010). Analysis of KLa measurement methods in stirred vessels: the role of experimental techniques and fluid dynamic models. *International Journal of Chemical Reactor Engineering*, *8*(1).

Popović, M., & Robinson, C. W. (1987). The specific interfacial area in external-circulation-loop airlifts and a bubble column-I. Aqueous sodium sulphite solution. *Chemical engineering science*, *42*(12), 2811-2824.

Reilly, I. G., Scott, D. S., De Bruijn, T., Jain, A., & Piskorz, J. (1986). A correlation for gas holdup in turbulent coalescing bubble columns. *The canadian journal of chemical engineering*, *64*(5), 705-717.

Rensen, J; Luther, S; Lohse, D The effect of bubbles on developed turbulence, JOURNAL OF FLUID MECHANICS Volume: 538 Pages: 153-187 Published: SEP 10 2005

Riboux, G., Risso, F., Legendre, D. (2010). Experimental characterization of the agitation generated by bubbles rising at high Reynolds number, Journa*l of Fluid Mechanics* 643, 509-539.

Risso F., Roig V., Amoura Z. & Billet A-M., Wake attenuation in large Reynolds number dispersed two-phase flows. Phil. Trans. R. Soc. A, 366, p.2177 (2008).

Rivière N., Cartellier A., Timkin L., Kashinsky O., Wall shear stress and void fraction in Poiseuille bubbly flows: Part II: experiments and validity of analytical predictions, *European Journal of Mechanics* - B/Fluids, Volume 18, Issue 5,

Roig, V. & de Tournemine, L. (2007) Measurement of interstitial velocity of homogeneous bubbly flows at low to moderate void fraction. *J. Fluid Mech*. 572, 87-110.

Ruzicka, M. C., Zahradnık, J., Drahoš, J., & Thomas, N. H. (2001). Homogeneous–heterogeneous regime transition in bubble columns. *Chemical Engineering Science*, *56*(15), 4609-4626.

Saito, T., & Mudde, R. F. (2001, May). Performance of 4-tip optical fiber probe and bubble characterizations by the probe in turbulent bubbly flows. In *Fourth international conference on multiphase flow* (Vol. 27).

Schäfer, R., Merten, C., & Eigenberger, G. (2002). Bubble size distributions in a bubble column reactor under industrial conditions. *Experimental Thermal and Fluid Science*, *26*(6), 595-604.

Schultz, J. S., & Gaden, E. L. (1956). Sulfite oxidation as a measure of aeration effectiveness. *Industrial & Engineering Chemistry*, *48*(12), 2209-2212.

Schweitzer, J. M., Bayle, J., & Gauthier, T. (2001). Local gas hold-up measurements in fluidized bed and slurry bubble column. *Chemical Engineering Science*, *56*(3), 1103-1110.

Simonnet, M., Gentric, C., Olmos, E., & Midoux, N. (2007). Experimental determination of the drag coefficient in a swarm of bubbles. *Chemical Engineering Science*, *62*(3), 858-866.

Simonnet, M., Gentric, C., Olmos, E., & Midoux, N. (2008). CFD simulation of the flow field in a bubble column reactor: Importance of the drag force formulation to describe regime transitions. Chemical Engineering and Processing: Process Intensification, 47(9), 1726-1737.

Spelt, PDM; Biesheuvel, A. On the motion of gas bubbles in homogeneous isotropic turbulence Journal of Fluid Mechanics / Volume 336 / April 1997, pp 221- 244

Suzanne C., Ellingsen K., Risso F. and Roig V. (1998). Local measurements in turbulent bubbly flows. Nuclear Engineering and Design, 184, 319-327

Thorat, B. N., Shevade, A. V., Bhilegaonkar, K. N., Aglawe, R. H., Veera, U. P., Thakre, S. S., ... & Joshi, J. B. (1998). Effect of sparger design and height to diameter ratio on fractional gas hold-up in bubble columns. *Chemical Engineering Research and Design*, *76*(7), 823-834.

Toye, D., Fransolet, E., Simon, D., Crine, M., L'Homme, G., & Marchot, P. (2005). Possibilities and limits of application of electrical resistance tomography in

hydrodynamics of bubble columns. *The Canadian Journal of Chemical Engineering*, *83*(1), 4-10.

Urseanu, M. I., Guit, R. P. M., Stankiewicz, A., van Kranenburg, G., & Lommen, J. H. G. M. (2003). Influence of operating pressure on the gas hold-up in bubble columns for high viscous media. *Chemical Engineering Science*, *58*(3), 697-704.

Veera, U. P., & Joshi, J. B. (1999). Measurement of gas hold-up profiles by gamma ray tomography: effect of sparger design and height of dispersion in bubble columns. *Chemical Engineering Research and Design*, *77*(4), 303-317.

Vejražka, J., Večeř, M., Orvalho, S., Sechet, P., Ruzicka, M. C., & Cartellier, A. (2010). Measurement accuracy of a mono-fiber optical probe in a bubbly flow. *International Journal of Multiphase Flow*, *36*(7), 533-548.

Wilkinson, P. M. (1991). *Physical aspects and scale-up of high pressure bubble columns* (Doctoral dissertation, University of Groningen).

Wilkinson, P. M., Haringa, H., & Van Dierendonck, L. L. (1994). Mass transfer and bubble size in a bubble column under pressure. *Chemical engineering science*, *49*(9), 1417-1427.

Xing, C., Wang, T., & Wang, J. (2013). Experimental study and numerical simulation with a coupled CFD–PBM model of the effect of liquid viscosity in a bubble column. Chemical Engineering Science, 95, 313-322.

Xue, J. (2004). *Bubble velocity, size and interfacial area measurements in bubble columns* (Doctoral dissertation, Washington University).

Xue, J., Al-Dahhan, M., Dudukovic, M. P., & Mudde, R. F. (2003). Bubble Dynamics Measurements Using Four-Point Optical Probe. *The Canadian Journal of Chemical Engineering*, *81*(3-4), 375-381.

Xue, J., Al-Dahhan, M., Dudukovic, M. P., & Mudde, R. F. (2008 A). Four-point optical probe for measurement of bubble dynamics: Validation of the technique.*Flow Measurement and Instrumentation*, *19*(5), 293-300.

Xue, J., Al- Dahhan, M., Dudukovic, M. P., & Mudde, R. F. (2008 B). Bubble velocity, size, and interfacial area measurements in a bubble column by four- point optical probe. AIChE journal, 54(2), 350-363.